

Advanced High Temperature Static Strain
Sensor Development Program

(NASA-CR-179520) ADVANCED HIGH TEMPERATURE
STATIC STRAIN SENSOR DEVELOPMENT Final
Report (United Technologies Research
Center) 205 p Avail: NTIS HC A10/MF A01

N87-25552

Unclas
CSCL 14B G3/35 0082684

C. O. Hulse, K. A. Stetson, H. P. Grant
S. M. Jameikis, W. W. Morey, P. Raymondo
T. W. Grudkowski and R. S. Bailey

United Technologies Research Center

Prepared for
National Aeronautics and Space Administration

NASA Lewis Research Center
Contract NAS3-22126
July 1987

1. Report No. NASA CR-179520		2. Government Accession No.		3. Recipient's Catalog No.	
4. Title and Subtitle Advanced High Temperature Static Strain Sensor Development				5. Report Date August 1986	
				6. Performing Organization Code	
7. Author(s) C. O. Hulse, K. A. Stetson, H. P. Grant, S. M. Jameikis, W. W. Morey, P. Raymondo, T. W. Grudkowski and R. S. Bailey				8. Performing Organization Report No. R86-995875-28	
9. Performing Organization Name and Address United Technologies Corporation United Technologies Research Center East Hartford, CT 06108				10. Work Unit No. 505-62-01	
				11. Contract or Grant No. NASA NAS3-22126	
12. Sponsoring Agency Name and Address Project Manager: F. G. Pollack National Aeronautics and Space Administration Lewis Research Center 21000 Brookpark Road, Cleveland, Ohio 44135				13. Type of Report and Period Covered Final Report	
				14. Sponsoring Agency Code NAS3-22126	
15. Supplementary Notes					
16. Abstract <p>An examination was made into various techniques which might be used to measure static strain in gas turbine liners at temperatures up to 1150 K (1600°F). The methods evaluated included thin film and wire resistive devices, optical fibers, surface acoustic waves, the laser speckle technique with a heterodyne readout, optical surface image and reflective approaches and capacitive devices. An preliminary experimental program to develop a thin film capacitive device was dropped because calculations showed that it would be too sensitive to thermal gradients. In a final evaluation program, the laser speckle technique appeared to work well up to 1150 K when it was used through a relatively stagnant air path. The surface guided acoustic wave approach appeared to be interesting but to require too much development effort for the funds available in this program. Efforts to develop a FeCrAl resistive strain gage system were only partially successful and this part of the effort was finally reduced to a characterization study of the properties of the 25 μm diameter FeCrAl (Kanthal A-1) wire. It was concluded that this particular alloy was not suitable for use as the resistive element in a strain gage above about 1000 K.</p>					
17. Key Words (Suggested by Author(s))			18. Distribution Statement		
- strain gages - elevated temperatures - static strain - laser speckle technique			- electrical resistance - optical sensor - capacitance - strain Unlimited STAR Category 35		
19. Security Classif. (of this report)		20. Security Classif. (of this page)		21. No. of Pages	
Unclassified		Unclassified		211	
22. Price					

FOREWORD

The work described in this report was performed by the United Technologies Research Center for the National Aeronautics and Space Administration under Contract NAS3-22126. The final Principal Investigator was Dr. C. O. Hulse. Mr. S. M. Jameikis served as the initial Principle Investigator and he was followed by Dr. R. K. Erf. Technical assistance was also provided by Mr. H. P. Grant, Mr. W. L. Anderson, Mr. J. S. Przybyszewski and Mr. W. B. Watkins of the Pratt and Whitney Aircraft Group and also by Dr. K. A. Stetson, Dr. T. W. Grudkowski, Dr. E. L. Paradis, Dr. W. Morey, Mr. P. Raymondo, Mr. R. Bailey, Dr. B. Cassenti, Mr. S. Kustra and Mr. R. O. Gavitt from the Research Center. The NASA Technical Project Manager for this effort was Mr. F. G. Pollack.

PRECEDING PAGE BLANK NOT FILMED

PAGE 11 INTENTIONALLY BLANK

TABLE OF CONTENTS

	<u>Page</u>
1.0 SUMMARY	1
2.0 INTRODUCTION	3
3.0 ANALYSIS OF POTENTIAL SENSOR SYSTEMS (TASK 1)	5
3.1 Introduction	5
3.2 Wire Resistance Strain Gages	6
3.3 Capacitive Strain Sensors	24
3.4 Fiber Optic Concepts	28
3.5 Holographic and Speckle Strain Sensing Techniques	38
3.6 Surface Acoustic Wave/Acoustic Guided Wave Concepts	48
3.7 Summary and Recommended Candidates	52
4.0 PRELIMINARY EVALUATION PROGRAMS AND REVIEW (TASKS 2 AND 3)	55
5.0 PRELIMINARY EXPERIMENTAL EVALUATIONS	57
5.1 FeCrAl Resistance Wire Gages (Task 4)	57
5.2 Laser Speckle Technique with Heterodyne Readout (Task 5)	77
5.3 Thin Film Capacitive Sensor (Task 6)	82
6.0 REVIEW AND MODIFICATION OF PROGRAM (TASK 7)	87
7.0 FINAL EVALUATION OF LASER SPECKLE PHOTOGRAPHIC SENSOR (TASKS 8a, 9a, 10a and 11a)	89
7.1 Fabrication and Evaluation of Telecentric Lens	89
7.2 Specklegram Recording and Halo Evaluation System	91
7.3 Arrangement for Testing at Elevated Temperatures	93
7.4 Results of Elevated Temperature Measurements	94
8.0 EVALUATION OF RESISTIVE SENSOR (TASKS 8b, 9b, 10b AND 11b)	99
8.1 Testing Equipment	99
8.2 Testing Procedures	102
8.3 Results of Wire Testing	104
8.4 Analysis of Thermal Strain	113

PRECEDING PAGE BLANK NOT FILMED

TABLE OF CONTENTS (Cont'd)

	<u>Page</u>
9.0 SUMMARY AND CONCLUSIONS	117
10.0 REFERENCES	121
APPENDIX - GOVERNING EQUATIONS FOR THERMAL STRESS ANALYSIS	
FIGURES	

1.0 SUMMARY

A research program was conducted to examine various techniques which might be used to obtain more accurate measurements of static strain at temperatures up to 1150 K (1600°F). The specific application was for test stand gas turbine burner liners where more accurate strain data measurements are needed in order to evaluate and improve the behavior of advanced designs. The initial phase consisted of a review and analysis of various potential concepts - resistive, optical, capacitive and S.A.W. Preliminary experimental programs were conducted to evaluate the laser speckle technique, FeCrAl wire gages and the capacitive sensor. In a subsequent review, the capacitive approach was dropped primarily because of fabrication difficulties and high sensitivities to thermal gradients calculated to occur even when the device was encapsulated in various ways. In a final evaluation program, the laser speckle technique appeared to work well up to 1150 K when used through a relatively stagnant air path. The FeCrAl program was restructured to consist of a comprehensive evaluation of the properties of the wire. It was shown that exposures to temperature of about 1000 K caused the wires to become extremely weak and brittle at room temperatures. The electrical resistivity becomes very sensitive to different rates of heating and cooling when they include exposure to temperatures above about 1030 K. Thermal soaking, especially at temperatures around 1150 K, causes significant increases in the thermal coefficient of resistivity. The strength and elastic limit of .025 mm diameter wire is very low at 1150 K, approximately 169 and 96 MPa, respectively. It was concluded that this particular alloy was not suitable for use as the resistive element in a strain gage above about 1000 K.

2.0 INTRODUCTION

One of the most critical components in the gas turbine engine is the combustor, which suffers failures resulting from the formation of cracks, buckling, and liner burn-through. Instrumentation is needed which can function reliably in the combustor liner environment during testing and provide data to determine the quality of the analytical predictive tools used in designing these combustors. One of the instruments of extreme interest is a sensor system which can measure the static strain of combustor liners. The objective of this Advanced High Temperature Static Strain Sensor Development Program was to establish the technology for making static strain sensors which would survive the harsh environment experienced by gas turbine combustor liners and make valid measurements up to 1150 K. These strain sensors were to be no larger than 12 mm x 12 mm x 1.5 mm thick and be capable of measuring strains to ± 2000 microstrain with total errors not to exceed ± 200 microstrain. These sensors were also to be mounted directly on test specimens and the performance demonstrated under simulated combustor operating conditions.

As different developments and conclusions were reached during the course of the work, modifications were made in the program which increased the costs slightly and lengthened the period of performance. In its' final form, the program consisted of the following sequence of Tasks:

- Task 1: Sensor Analysis of the state-of-the-art technology as applicable to experimental combustor liners and a design analysis of potential sensor systems.
- Task 2: Design of Preliminary Evaluation Program to evaluate the characteristics of candidate systems selected in Task 1.
- Task 3: Review of Tasks 1 and 2.
- Task 4: Fabrication, testing, and post-test analysis of FeCrAl Wire Resistive Gage.
- Task 5: Fabrication, testing, and post-test analysis of High Temperature Speckle Photography with Heterodyne Halo Evaluation Concept.
- Task 6: Fabrication, testing, and post-test analysis of Thin Film Capacitive Strain Sensor.
- Task 7: Briefing to report on results of Tasks 1-6.

PRECEDING PAGE BLANK NOT FILMED

PAGE 2 INTENTIONALLY BLANK

- Task 8a: Design of Optical Sensor and test apparatus.
8b: Development of Wire Sample Test Plan and design of test apparatus.
- Task 9a: Fabrication of Optical Sensor and test apparatus.
9b: Fabrication of Wire Samples and test apparatus.
- Task 10a: Testing of Optical Sensor.
10b: Testing of Wire Samples.
- Task 11a: Post Test Analysis of Optical Sensor.
11b: Post Test Analysis of Wire Samples.
- Task 12: Briefing to Report on Task 1-11 and Final Report.
- Task 13: Monthly Reports

The original Program Manager of this effort was S. M. Jameikis of the Optics and Applied Technology Laboratories, a part of the United Technologies Research Center located in West Palm Beach, Florida. When the main thrust of the program shifted to the experimental tasks which were all being carried out in East Hartford, it was decided that it would be more appropriate to have Dr. R. K. Erf at the main Research Center become the Program Manager. Because of a subsequent change in Dr. Erf's reporting assignments, Dr. C. O. Hulse became the Program Manager for the later portions of the effort.

A parallel effort to develop new, high temperature alloys for use as electrical resistance sensors has been separately funded (NAS3-23169) and a report which describes the results of the first year of that effort is available (NASA CR-174833). A follow-on effort to this program, (NAS3-23690), evaluating the use of the laser speckle technique and the FeCrAl wire gages at lower temperatures on a burner liner on a test stand has also been completed.

3.0 ANALYSIS OF POTENTIAL SENSOR SYSTEMS (TASK 1)

3.1 Introduction

The need for strain gage systems capable of measuring static strains at temperatures in the region of interest for this program (ambient to 1150°K) has existed for many years and a considerable effort has been directed to the problem. The various components of resistive gage systems have been refined so that physical survivability of these components in a combustor type environment is achievable. This was demonstrated for a FeCrAl resistive strain gage system in NASA Contract NAS1-11277. However, none of the existing gage systems and materials suitable for high temperature operation are capable of meeting the static strain accuracy goals of ± 200 microstrains specified in the program requirements.

Task 1 of this Advanced High Temperature Static Strain Sensor program was to analyze the state-of-the art strain sensor technology, and to compare this technology with the environmental constraints imposed by the operating conditions of the gas turbine engine combustor. This part of the effort was carried out by a number of different investigators located at either the Corporate Research Center (UTRC), in the Commercial Products Division (CPD) or in the Government Products Division (GPD) of the Pratt and Whitney Aircraft Group. The work reported in Section 3.2, Wire and Thin Film Resistance Strain Gages, was accomplished by H. P. Grant, W. L. Anderson, and J. S. Przybyszewski of CPD, W. B. Watkins of GPD, and P. Raymodo of UTRC. The work in Section 3.3, Capacitive Strain Sensors, was accomplished by R. O. Gavitt and S. M. Jameikis of UTRC. The work in Section 3.4, Fiber Optic Concepts, was accomplished by W. W. Morey of UTRC. The work described in Section 3.5, Holgraphic and Speckle Techniques, was accomplished by K. A. Stetson of UTRC. The work in Section 3.6, Surface Acoustic Wave/Acoustic Guided Wave Concepts, was done by T. W. Grudkowski and E. L. Paradis of UTRC.

Much of the data presented in this section of the report was taken from an Interim Technical Report, Task 1: Sensor Analysis, prepared by S. M. Jameikis and P. Raymondo of UTRC, dated June, 1980.

3.2 Wire Resistance Strain Gages

3.2.1 Analysis

3.2.1.1 Resistive Strain Gage System: A resistive static strain gage bridge circuit is shown in figure 1, powered from a constant voltage source, E. Each of the four arms of the bridge has a nominal resistance of R ohms.

One arm of the bridge consists of a resistive strain gage whose unstrained resistance is R (ohms) and whose gage factor is G, defined as:

$$G = \frac{\Delta R/R}{\epsilon}$$

where ΔR (ohms) is the resistance change due to strain ϵ (cm/cm). The output voltage, E_{out} , from the bridge can be described by the following equation (see refs. 1 and 2):

$$E_{out} = \frac{E_1 G}{4} \left[\left(\epsilon + \frac{(\Delta R)_{other}}{GR} \right) \left(1 - \frac{1}{2} \frac{(\Delta R)_{other}}{R} \right) + \left(\frac{2}{G} \frac{(\Delta E)_{other}}{E_1} \right) \right] \quad (1)$$

In this equation, $(\Delta R)_{other}$ is any stray resistance change in any arm of the bridge circuit not due to strain in the strain gage. Examples of this change include resistance changes in the lead wires, lead wire connectors, bridge resistors, or resistance changes in the strain gage itself due to temperature effects, metallurgical changes with time at temperature, or changes in the shunting resistance of insulating layers. In particular, the temperature, time, and gage stress may affect the gage resistance itself in several ways, including oxidation effects, change in resistivity of the gage material with temperature, changes in dimension with temperature due to mismatches in expansion coefficients, and slow changes in metallurgical structures.

$(\Delta E)_{other}$ is any stray voltage which may appear in any one arm of the bridge circuit, e.g., stray thermocouple e.m.f., piezoelectric voltages, magnetostrictive voltages, ground loops, or electromagnetic pickup.

In designing and fabricating resistive static strain gage systems, careful attention must be given to minimizing all sources of false strain indication represented by $(\Delta R)_{other}$ and $(\Delta E)_{other}$ in equation 1.

Note that in applying equation 1 to static strain measurement, the actual strain seldom exceeds 0.02 percent. False strain indications must be kept below 0.01 percent for error less than 5 percent of this 0.2 percent.

If a true constant-current bridge is employed in place of the constant voltage bridge, the above effects of stray resistances and voltages are reduced by about a factor of two. In practice, the bridges employed usually lie between constant voltage and true constant-current operation.

3.2.1.2 Resistive Strain Gage System Analysis Matrix: The strain gage system consists of the following elements:

- 1) Burner liner material and surface preparation
- 2) Insulating layer (grown oxide, painted or flame sprayed coating, or sputtered thin film coating)
- 3) Strain gage element (wire, foil, or deposited thin film)
- 4) Lead wire connection
- 5) Protective overcoat layer.

The selection of candidate materials, configurations and fabrication techniques for each of the elements involves considerations of the effect of the engine environment on the accuracy and life of the gage system, including the effects of:

- a) Oxidation
- b) Erosion
- c) Thermal expansion and temperature cycling
- d) Fatigue (vibration, stress cycling).

The selection process must also consider the feasibility of fabrication and calibration, including:

- a) Quality control, sensor to sensor
- b) Reproducibility, facility to facility
- c) Cost.

The five elements of the strain gage system mentioned above are discussed in the above order in the remaining articles in this section.

3.2.1.3 Burner Liner Material and Surface Preparation: The material typical of modern burner liner design is Hastelloy X. Pertinent properties of this material are presented in Table 3.2.1.

TABLE 3.2.1. - PROPERTIES OF WROUGHT SHEET HASTELLOY X

<u>PWA Designation</u>	<u>PWA 1038</u>
Approximate Composition	46 Ni-22 Cr-18.5 Fe-9 Mo-1.5 Co-0.6 W
Maximum Recommended Service Temperature	1400 K
Maximum Heat Treat Temperature	1400 K
Modulus of Elasticity (E), 1140 K	140,000 MPa
TCE (at 1150 K)	16 ppm/K
Approximate Elastic Strain Limit (at 1150 K) (at 300 K)	1000 microstrain 1600 microstrain
Remarks:	Non-hardenable by heat treatment

Good adhesion of flame-sprayed or painted insulation coatings is best achieved on a surface slightly roughened by grit blasting. On the other hand, the best adhesion of grown oxides or nitrides (or of vacuum-deposited layers of oxide-forming materials) is achieved on a highly polished surface (ref. 3).

3.2.1.4 Insulating Layer: To qualify as a candidate, the insulating material must be adherent, have high electrical resistivity at service temperatures and a high dielectric breakdown voltage at service temperatures. The candidate material should also possess both an elastic strain range and a temperature coefficient of linear expansion (TCE) reasonably well matched to the liner material and sensor material. There is appreciable scatter in the data available on elastic strain range and TCE of refractory insulating materials. This is not surprising, since the thermal and mechanical behavior of the material depends on the internal structure, grain size and porosity which in turn depends on fabrication procedure and on the character of the substrate surface.

The insulating layer material must also be chemically compatible with the gage and burner liner materials, for good adherence and stability.

Table 3.2.2 lists approximate properties of high-resistance refractory materials for which favorable experience has been reported. On the basis of thermal expansion matching, none are well matched to Hastelloy X, implying that a ductile precoat may be required, or that reliance must be placed on plastic flow of the burner line material occurring locally to relieve the stress in the insulating layer. Local plastic flow in a ductile precoat or in the burner liner material itself may introduce apparent strains in the strain gage system. Experimentation will be required to evaluate these effects on Hastelloy X.

Table 3.2.3 lists values of the temperature coefficient of linear expansion (TCE) for a variety of materials, for comparison with the insulating layer candidates.

First-hand experience at United Technologies Corporation (UTC) has shown that:

- a. Al_2O_3 can be flame-sprayed or sputtered directly on nickel steel alloys with good adherence and durability to about 1000 K, but these layers crack or spall at temperatures above 1000 K unless a ductile alumina-forming precoat is used. Examples of ductile precoats include the nickel aluminide precoat used in flame-sprayed systems on compressor and turbine blade strain gage installations (Ref. 4) or the MCrAlY coating systems used on turbine blade sputtered thermocouple installations (refs. 3 and 5).
- b. HfO_2 can be sputtered directly on tungsten and is durable at 1470 K on a tungsten-nickel interface.
- c. Si_3N_4 can be sputtered directly on Si, Incoloy 901 steel, and AMS 4928 titanium alloy and provides a dense, hard abrasion-resistant coating at room temperature. It is durable at 1470 K on Si, and to at least 900 K on the steel and titanium alloys.
- d. SiO_2 can be sputtered directly on tungsten, platinum, steel, and titanium alloys with good adherence and durability to about 900 K. Cracking would be expected at temperatures much above 900 K on these materials and on Hastelloy X.

Experience confirms predictions based on TCE matching, which results in an order of preference of Al_2O_3 , HfO_2 , Si_3N_4 , and SiO_2 . All four are candidates for use on Hastelloy X.

Applying the insulating layer at an elevated temperature in order to prestress the layer in the "safe" direction may be a useful technique. However, a number of quality control problems may arise in such a process.

TABLE 3.2.2. - APPROXIMATE PROPERTIES OF
CANDIDATE INSULATING LAYER MATERIALS

	Al_2O_3	Si_3N_4	HfO_2	SiO_2
Resistivity at 900 K, $\mu\Omega\text{-cm}$	10^{15}	10^{13}	10^{12}	10^{12}
Modulus, MPa	360,000	160,000	-	70,000
TCE, ppm/K	7	3	4	1
Dielectric Breakdown, V/cm	5×10^6	10^7	-	-
Differential Thermal Expansion between material and Hastelloy X, 300 K to 1150 K, $\text{K}^{-1} \times 10^{-6}$	7650	11050	10200	12750

TABLE 3.2.3. - APPROXIMATE TEMPERATURE COEFFICIENT OF
LINEAR EXPANSION (TCE) FOR SEVERAL MATERIALS

<u>Material</u>	<u>TCE (ppm/K)</u>	<u>Material</u>	<u>TCE (ppm/K)</u>
PWA 1422	8	Fe	12
AMS 4928	9	Mn	22
PWA 1003	15	Mo	5
Al_2O_3	7	Ni	13
Si_3N_4	3	Pd	12
HfO_2	4	Pt	9
SiO_2	1	Si	3 to 7
Ag	20	Ti	8
Al	24	W	4
Cu	16	Au	14
Cr	6		
NiCoCrAlY	13		
Hastelloy X	16		
Haynes 25	16		

High temperature wire strain gages are typically bonded to substrate surfaces using ceramic cement or flame sprayed ceramic coatings.

Ceramic coatings require a clean, degreased, and roughened substrate surface for good adherence at high temperatures. Grit blasting with a pressure grit blaster and #60 or #120 grit Al_2O_3 normally provides satisfactory roughness. A bond coat of flame sprayed NiAl or NiCrAl (such as Metco 443[†]) can also provide the roughness required for good ceramic adherence.

Common commercial ceramic cements are based on MgO , Al_2O_3 , ZrO_2 or SiO_2 . Although these ceramics have very high electrical resistance, the binders used with them do not and the resistivity of the cement is in the range of 10^4 to 10^5 ohm-cm at 922 K. This level of resistivity is too low for most strain gage applications.

The most successful type of ceramic cement used in high temperature strain gage applications is the AlPO_4 type, which cures through chemical reaction with H_3PO_4 . The resistivity of this cement is about 10^7 to 10^8 ohm-cm at 922 K. The adherence is very good up to at least 1200 K. A commonly used AlPO_4 -base cement is Sermetel P-1.^{††}

Flame sprayed Al_2O_3 based ceramics have been used extensively for strain gage applications up to 1200 K. Because the materials are applied as a semimolten spray, no binder is required and the excellent electrical resistance is retained after application. Although the electrical resistivity of high purity Al_2O_3 is greater than that of low purity, the adherence of the high purity flame sprayed Al_2O_3 is poor. A good compromise is a mixture of 97% Al_2O_3 , 2.5% SiO_2 and .5% other materials.^{†††} The electrical resistance of this coating is slightly higher than that of Sermetel P-1 in the temperature range of 900 K to 1200 K.

3.2.1.5 Strain Gage Element: For survival and calibration stability the sensor material must be electrically stable versus time at operating temperature. For acceptable performance in regions of steep temperature gradients (whether or not a thermocouple or a second bridge element is incorporated for temperature compensation), the strain sensor temperature coefficient of resistance (α) must be reasonably low. These two

[†] Manufactured by Metco, Inc. of Westbury, N.Y.

^{††} Manufactured by Sermetel, Inc. of Limerick, PA.

^{†††} Manufactured by the Norton Co., of Worcester, Mass., Trade Name: Rokide H.

characteristics, resistance stability and α , are the controlling factors in the selection of candidate sensor materials. In equation 1, both of these effects are included in the term $(\Delta R_{\text{other}})/GR$, which has the dimensions of strain. If the gage factor "G" is 2, for example, then an uncertainty of 50 microstrain would result from a 100 ppm drift in resistance R. This is the order of magnitude of stability reported in the literature over several hours for the better high-temperature alloys in wire form (Table 3.2.4). To keep additional uncertainty due to temperature dependence of resistance, below 100 microstrain, assuming a temperature uncertainty of 20 K, requires that the ratio α/G be held below 5 ppm/K. The best (stable) high-temperature wire strain gages produce α/G of about 60 ppm/K at 1150 K, which is ordinarily unacceptable for static strain measurement at 1150 K. The goal of the present program, ± 200 microstrain, is therefore an ambitious objective requiring a major breakthrough in strain measurement technology.

Two other considerations which are not so stringent also affect the selection of gage materials for resistive strain gages. They are the resistivity and the gage factor. A resistivity range of 10 to 200 microhm-cm permits fabrication of strain gages in the 100 to 1000 ohm resistance range in the desired size and thickness range. If the strain gage resistance is above 1000 ohms, insulation leakage to ground becomes a serious problem. If it is below 100 ohms, lead-wire resistances and contact resistances become serious problems. The 10 to 200 microhm-cm range requirement includes virtually every metal and alloy in the literature, and is a weak restraint.

The value of the gage factor itself is not predictable using the present knowledge of the electrical behavior of conductors. However, on the basis of bulk dimensional change, it can be shown that the gage factor would be 1.7 for elastic deformation (with a Poisson ratio of 1/3), and would be 2.0 for constant-volume deformation (Poisson ratio of 1/2). In fact, the gage factor of ordinary alloys is found to lie between 1.5 and 6. A larger value of gage factor would be desirable to reduce the error term, $\Delta R_{\text{other}}/GR$, in equation 1. The gage factor of semiconductors is large and negative (e.g., -100), but no stable semiconductor materials are available for 1150 K service. It is therefore expected that the gage factor of the high-temperature resistance strain gage will be in the 1.5 to 6 range.

It is clear that in any program with the objective of improving high temperature strain measurements, the development of new alloys for high temperature resistive strain sensing elements should be considered. In one such recent program at UTC, (NAS3-21262), Thin Film Strain Gage Development

TABLE 3-2.4. - RESISTANCE STRAIN GAGE-WIRE ALLOYS

Type	Trade Names	Composition at %	Resistivity Microhm cm	TCR ppm/K	Max.		Fatigue Rating (10 = best; from Ref. b19)	Remarks
					Approx. Gage Factor G	Operating Temp. (K) for Dynamic Strain	Operating Temp. (K) for Static Strain	
Ni-Cr	Nichrome V Tophet A	Ni20Cr	110	110	2	1400	600	55
	Nichrome Tophet C	Ni16Cr24Fe	110	150	2	1400	600	75
	Karma Moleculoy	Ni20Cr3Fe3Al	130	±20	2	1100	600	±10
	Evanohm	Ni20Cr3Al3Cu	130	±20	2	700	600	±10
Cu-Ni	Constantan Cupron Advance	Cu45Ni	50	±40	2	600	600	±20
								Oxidation rapid above 600 K
Pt-W	Alloy 479 Platinum- Tungsten	Pt8W	70	240	4	1400	600	38
Fe-Cr-Al	Kanthal A-1 BCL-3	Fe23Cr6Al0.5Co Fe25Cr8Al	150	-35	2	1400	600	18
								10

Note: Values of all quantities listed vary widely with heat treatment and cold work. The values given are typical for wound strain gages in service.

Program, Final Report NASA CR-174707, reference 6, the methodology for developing new alloys was explored. The literature on chemical, physical, and metallurgical mechanisms affecting electrical stability and alpha was reviewed in depth (refs. 7 through 23) and presented. Guidelines for formulating new strain gage alloys were established and a technique was developed for fabrication of strain gages by thin-film sputtering from bulk sources of new alloys (some not workable in fine wire form). The program achieved its limited goal of small thin-film gages for dynamic strain measurement to 900 K, and provided the background analysis and guidelines for use toward the broader goal of higher-temperature static strain alloy development.

One conclusion reached in the above referenced program was that several families of alloys offered promise of achieving the static strain high-temperature goals, but that none was readily available in fine-wire form. These alloys might best be fabricated in sputtered thin-film form. It was planned to pursue the thin-film resistive static strain gage approach further in another program, discussed in Section 3.2.3.4 below.

3.2.1.6 Lead Wire Connection: The lead wire material in any resistive system must be similar in composition to the gage material to avoid thermocouple effects (ΔE_{other} in equation 1). Connection methods already developed and used successfully at UTC in burner and turbine environments for dynamic strain gages may be appropriate for the burner liner static strain installation. Three lead wires are required for each static strain gage in order to cancel temperature dependent lead wire resistance changes. The wire leads may be capacitive discharge welded to strain gage wires or foils in a configuration chosen to avoid transmission of high stress to the connections, and to avoid measurements of stress-induced resistance changes in the lead wires. If sputtered thin film strain gages are employed, the lead wires may be hot compression bonded to the thin films as described in reference 3 or resistance spot welded to pads consisting of thicker films oversputtered at the desired locations. All of these techniques require meticulous care on the part of the strain gage technician. The connection and routing of lead wires is anticipated to be a problem area requiring special attention.

3.2.1.7 Overcoat: In the case of wire or foil strain gages, an overcoat of insulating material is required to bond the gage to the insulation layer on the burner liner. The overcoat may also provide erosion and corrosion protection. Techniques used to apply overcoats to high-temperature dynamic strain gages are appropriate for burner liner static strain gages. These techniques are widely used at UTC (ref. 4) and elsewhere (ref. 10). They usually involve a two or three step sequence of refractory oxide flame spray

operations, the first step being to tack down the gage (temporarily taped in place) and the remaining steps to produce a smoothly formed installation after removing the tape.

3.2.2. FeCrAl Alloy Wire Gages

3.2.2.1 Background: Alloys in the FeCrAl family, such as Kanthal A-1[†] (Table 3.2.4), have special characteristics that offer potential for application in the specific case of static strain measurement on burner liners during engine test cycling. This alloy is commercially available in fine wire form and is notable for its high stability of electrical resistance and its low rate of oxidation at high temperatures (800 K to 1300 K).

The two limitations of FeCrAl as a static strain gage material are the rather large apparent strain due to temperature and the dependence of this apparent strain on cool-down rate in the intermediate temperature range, 600 K to 800 K. Even though the cool-down rate effect is reversible, well documented, and repeatable (ref. 11), these two obvious limitations have discouraged general use.

The special characteristics that still make the FeCrAl gage a candidate for burner liner static strain measurement are:

- a) The apparent strain is smallest at the rapid high cool-down rates typical of engine low-cycle fatigue accel-decel tests (500 K/min.).
- b) The apparent strain curves are repeatable, from reference 11, for any two cool-downs of any one gage, at a given cool-down rate, even when one cool-down cycle is run before and one after cool-downs at other cool-down rates.
- c) In two important ranges of temperature the rate of change of apparent strain (OC/G) with temperature is reasonably low (below 8 $\mu\text{E/K}$). One of the ranges is the low temperature range, below 500 K, typical of burner liner temperatures at engine idle. The other range is the moderately high temperature range, 850 K to 1000 K, typical of burner liner temperatures in some areas at engine cruise to full power. As a result, the measurement of burner liner temperature at the beginning and end of an engine deceleration (during engine cycles such as those conducted for low-cycle fatigue testing), which is required for correcting for effects of temperature, need be accurate only to about ± 12 K to keep uncertainty in strain below 100 microstrain from this source.

[†]Kanthal Corp., Bethel, CT.

The evidence is that, even though the true static strain may not readily be measured accurately, the difference in the static strain in a burner liner between engine high power condition and engine idle condition might be determined with reasonable accuracy using these FeCrAl gages provided that the following conditions are met:

- a) The measurement is confined to engine cycles in which the upper temperature lies above 850 K, and the lower temperature at engine idle lies below 500 K, avoiding end points in the region of most rapid change of apparent strain with temperature.
- b) The temperature of the gage is monitored (± 12 K) by installing a nearby thermocouple.
- c) The apparent strain vs. temperature of each installed gage is established by preliminary calibration, at any one reasonably fast cooling rate (perhaps 50 K/min) on the fully instrumented burner liner.
- d) The apparent strain change during the actual (fast) engine cooling cycle is calculated by applying the information from the calibration run with an adjustment for cool-down rate based on tests of sample batches of the FeCrAl gages on small test bars cycled at both slow and fast cooling rates.
- e) Repeatability during the engine test can be demonstrated by repeating the engine accel/decel cycle before accepting data.

3.2.2.2 Experience at UTC with FeCrAl Gages: Prior to the present contract, UTC conducted bench tests of FeCrAl gages.

The gages, fabricated as shown in figure 2, were installed on a Hastelloy X test bar and subjected to a series of six oven cool-downs from 950 K to room temperature, at cool-down rates from 10 K/min to 450 K/min. The stated rate is the average over the middle 80% of the cool-down temperature range, to avoid ambiguities due to start time and end setting time. Three additional repeat cooling cycles were run at 450 K/min. Thermocouples installed on the bar provided gage temperature information. Apparent strain and temperature were recorded continuously during cool-down.

All test data for one gage (No. 2) at six cool-down rates are shown in figure 3, plotted as apparent strain (ϵ_A) versus temperature. All test data for the fastest and slowest of the six cool-down rates, for all seven gages, are plotted on the same coordinates in figure 4. Apparent strain data of figures 3 and 4 were calculated using an assumed constant gage factor of 2.4, based on a limited number of measurements of gage factor at room temperature.

This value agrees closely with that reported in reference 11 at room temperature. The gage factor, in fact, is known to decrease to about 2.0 at 950 K, and also may vary somewhat from gage to gage due to installation factors affecting strain transfer from burner liner to gage. These factors would alter the results in figures 3 and 4 by amounts up to about 20%, and would need documentation in future testing.

For clarity of presentation, the curves in figures 3 and 4 have been translated up or down vertically as follows:

- a) The curves for any one gage have been made to coincide at 950 K so that any slight zero shift from run to run is not shown.
- b) All curves for any one gage have then been shifted so that again the curve for the fastest cooling rate (450 K/min) is made to pass through a universal reference point - zero microstrain at room temperature.

Figure 3 shows the character of the effect of temperature and cooling rate. Figure 4 displays the similarity of apparent strain curve shape among seven gages, and the striking repeatability from gage to gage of the effect of change in cooling rate. The change in apparent strain with temperature is about the same for five of the seven gages (about $6400 \mu\epsilon \pm 300 \mu\epsilon$ at the fast cool-down rate) and is much larger for the other two (about $7500 \mu\epsilon$ for gage 5 and $10500 \mu\epsilon$ for gage 8). Sampled data has been analyzed in Table 3.2.5. This table provides a listing of observed apparent strain change $\Delta\epsilon_A$ due to temperature for each gage at each of two cool-down rates and a listing of the difference, δ , between the two values of $\Delta\epsilon_A$ for each gage. Averages and differences from averages are also listed. Table 3.2.5 also includes the results of repeatability tests not shown in figures 3 and 4 consisting of the four runs at the fastest cooling rate (450 K/min) on two different days, and a listing of average zero shift at 950 K from run to run for each of the gages throughout all tests.

An examination of Table 3.2.5 leads to three conclusions:

- a) The five "best" gages are closely similar. The worst departure from the average $\Delta\epsilon_A$ among these five is $329 \mu\epsilon$, and the worst departure from average δ (change of $\Delta\epsilon_A$ due to extreme change in cooling rate) is 286 microstrain. The worst repeatability among these five is $182 \mu\epsilon$ (Gage 8).
- b) The other two gages, 5 and 8, lie far afield, with departure from the average $\Delta\epsilon_A$ of $522 \mu\epsilon$ and $3036 \mu\epsilon$ respectively, departure from average δ of $190 \mu\epsilon$ and $62 \mu\epsilon$, and repeatability of $192 \mu\epsilon$ and $405 \mu\epsilon$.

TABLE 3.2.5 - ANALYSIS OF APPARENT STRAIN DATA FOR TWO COOLING RATES
FROM 950 K to 477 K
SEVEN KANTHAL A-1 STRAIN GAGES ON HASTELLOY*

	$\frac{(\Delta\epsilon_A)^{(1)}_{10 \text{ K/min}}}{\mu\epsilon}$	$\frac{(\Delta\epsilon_A)^{(1)}_{450 \text{ K/min}}}{\mu\epsilon}$	$\frac{\delta^{(2)}}{\mu\epsilon}$	$\frac{\text{Repeat-ability}^{(3)}}{\mu\epsilon}$	$\frac{\text{Zero Shift}^{(5)}}{\mu\epsilon}$
Gage 2	11146	6733	4413	67	16
Gage 3	10890	7022	3868	83	-9
Gage 4	10862	6791	4071	165	-13
Gage 5 ⁽⁴⁾	12122	7728	4394	192	-170
Gage 6	10714	6721	3993	78	-202
Gage 7	10833	6406	4227	182	-48
Gage 8 ⁽⁴⁾	14636	10370	4266	405	-210
Average for 7 Gages	11600	7396	4204	167	-91
Extreme-Average for 7 Gages	3036	2974	336		
Extreme-Average for Gage 5	522	332	190		
Extreme-Average for Gage 8	3036	2974	62		
Average, for 5 Gages ⁽⁴⁾	10889	6735	4154	115	-51
Extreme-Average, for 5 Gages ⁽⁴⁾	257	329	286		

NOTES

1. $\Delta\epsilon_A$ = Apparent Strain Change, for Gage Factor = 2.4
The subscripts 10 and 450 indicate the average cooling rate (K/Min) over the middle 80% of the cooling period
2. $\delta = (\Delta\epsilon_A)_{10} - (\Delta\epsilon_A)_{450}$
3. Repeatability = Extreme-Average $\Delta\epsilon_A$ in 4 Repeat Runs @ 450 K/Min
4. Gages 5 and 8 omitted in "5 Gages" Group because these two gages show poorer repeatability (column 4 in the table).
5. Average Zero Shift, Cycle to Cycle, over all tests

- c) The zero drift cycle-to-cycle varied from +16 $\mu\epsilon$ to -210 $\mu\epsilon$, with average for the five best gages of -51 microstrain per cycle. Zero drift at a constant temperature of 950 K was typically only a few microstrain per hour. For comparison, reference 11 also reports only about 20 microstrain per hour at about 1150 K.

The two worst gages of figure 4 and Table 3.2.5, Gages No. 5 and No. 8, are so different in behavior from the other five as to suggest the presence of some uncontrolled parameter in the installation technique. The probability of the large divergence of the data for these two being due to random variations in wire material properties or temperature uncertainty is near zero.

Based on figure 4 and Table 3.2.5, for all gages with the performance envelope of the best five, use of a simple mathematical model incorporating calibration data taken at the 10 K/min cooling rate (after mounting the gage on the burner liner) would permit predicting the apparent strain correction required in an engine test at 450 K/min within about $\pm \sqrt{286^2 + 182^2} = 338$ microstrain.

This uncertainty in apparent strain could be further reduced if the oven calibration run on the actual burner liner could be run at a cooling rate closer to that expected in engine tests. Of course, the probability of attaining uniform cooling of a large burner liner (avoiding thermally induced distortions) decreases as the test cooling rate increases. Nevertheless, a uniform rate in the neighborhood of 50 K/min should be achievable, and this should reduce the apparent strain correction uncertainty to the neighborhood of the desired goal of 200 microstrain.

Further reduction of the uncertainty will require improvement in gage-to-gage scatter through methodical improvement of the fabrication processes.

3.2.2.3 Recommended Further Testing of FeCrAl Wire Gages: To determine whether an acceptable level of uncertainty ($\pm 200 \mu\epsilon$) in burner line strain, at temperatures up to 1150 K and strains up to 2000 $\mu\epsilon$, could be achieved using FeCrAl static strain gage systems further development steps were recommended as follows:

- a) Thermal and mechanical testing of lead wires: The low-resistance nickel-clad-copper lead wire material (fig. 2) was used only to 950 K in the previous tests. Tests of this material were recommended at 1150 K and 2000 $\mu\epsilon$. In addition, the AMS 4772 braze material used previously to 950 K was ruled out at 1150 K because of its 991 K melting (solidus) temperature. Tests of new braze materials or welding methods for the higher temperature were recommended.

- b) Thermal and mechanical testing of complete gage systems: Using the lead wire material and attachment method found best to 1150 K in the lead wire tests, fabrication of a number of complete FeCrAl wire static gage systems on Hastelloy X test bars was recommended. Since it was not known whether the best overcoat (bond coat) material at 1150 K was the Sermetel P-1 cement used previously to 950 K or the flame-sprayed Al_2O_3 -based Rokide H, fabrication of some gage systems with each type of overcoat was recommended. The recommended testing included pre-stabilization at 1150 K, repeated apparent strain tests at two cool-down rates from 1150 K and gage factor tests at several temperatures up to 1150 K, followed by analysis of the results to determine which system was the better and to establish a mathematical model for use in engine tests.

3.2.3 Advanced Alloy Wire and Foil Gages

3.2.3.1 Background: The principles of alloy property prediction discussed in the previously referenced NASA/UTC thin-film dynamic strain gage program (ref. 6) indicate that the most promising untested static strain gage alloy candidates lie in the class of concentrated hard alloys which might be difficult to draw into wire form. Evaluation of these promising alloys may require adaption of new techniques for forming wires or foils having thicknesses in the range of 5 to 50 microns, and subsequent (or simultaneous) shaping into a strain gage element.

One such technique is the thin film sputtering process best suited for simple binary alloys. Other techniques for wire and foil formation include various standard and powder metallurgy processes, which are addressed in this section. These techniques are as well suited for complex (tertiary or higher order) alloys as for the simpler binary alloys.

Specific alloys of special interest already identified in reference 6 are Pt-20W and Pd-30Mo, with possible additions of other atomic species to each to enhance oxidation resistance or electrical stability.

Neither of these alloys has been produced in fine wire form with a high concentration of the alloying species. For example, Pt-8W is available commercially in fine wire, but not Pt-20W. Techniques for fabrication of wire of each of these alloys are examined in the next two sections.

3.2.3.2 Standard Metallurgical Techniques

3.2.3.2.1 Platinum-20 tungsten (Pt-20W) - Knapton (ref. 21) reports no intermediate phases in the platinum-tungsten system. Hultgren and Jaffee (ref. 24) reports the solid solubility of tungsten in platinum to be 35 weight

percent; however, Nemilov, et al., (ref. 25) postulate the existence of a tungsten platinum intermetallic of formula WPt_3 based on an upward trend in the hardness versus composition data at the stoichiometric ratio 25 atomic percent W, 75 atomic percent Pt. Therefore, based on the above data, it can be expected that an alloy of platinum 20 weight percent tungsten should be a face centered cubic solid solution with twelve independent slip systems and could have the required ductility for either rolling into thin foil or drawing into thin gage wire with intermediate temperature anneals.

The platinum tungsten phase diagram from Hanson (ref. 26) is in full agreement with all of the above referenced work in the composition range of platinum to platinum-20 tungsten. The melting point of platinum-20 tungsten alloy is quite high, in excess of 2200 K, therefore requiring that the alloy be melted in a watercooled copper crucible either by arc melting with a non-consumable electrode or through the use of an electron beam gun.

3.2.3.2.2 Palladium-30 molybdenum (Pd-30Mo) - The palladium molybdenum phase diagram taken from Shunk (ref. 27) presents information only at temperatures in excess of 1273 K, and thus leaves some doubt as to the extent of the palladium-rich single phase field at lower temperatures. Raub (ref. 28) reports the limiting solubility of molybdenum in palladium as 33.2 weight percent at a temperature of 1073 K. Based on the preceding two references, it is possible that a palladium 30 weight percent molybdenum alloy will be a random, face centered cubic solid solution.

In the final analysis, in order to determine the feasibility of the subject alloy for use as a high temperature strain gage material, the alloy must be produced and, based on the information in reference 27, homogenized in the single phase field at a temperature in the vicinity of 1470 K. After homogenization, the alloy should then be subjected to a series of isothermal aging treatments at temperatures below 1470 K in order to determine whether the subject alloy remains single phase for the times and temperatures of interest for the intended application. Should the palladium-30 molybdenum alloy indeed be a single phase solid solution, then it is possible that it can also be fabricated into thin foil and/or fine gage wire.

3.2.3.3 Powder Metallurgical Techniques

3.2.3.3.1 Background - The feasibility of producing the subject alloys from elemental powders with homogenization by means of solid state diffusion was also investigated. As stated in Section 3.2.3.2, these alloys can be produced by melting in a water-cooled copper crucible either through the use of non-consumable electrode arc melting or electron beam melting. However, when preparing alloys consisting of elements of greatly differing

melting points, difficulty is often encountered in dissolving the higher melting point constituent. This problem can be alleviated somewhat by using a sintered powder mixture of the constituents as melt feed stock. If the maximum powder particle size of the elemental powders is limited to a reasonably small size, say less than 100 microns, then an alternate fabrication approach is feasible.

That approach, for which supporting calculations follow, is simply to hot isostatically press (HIP) the elemental powders to full density followed by a high temperature homogenization cycle to level the composition gradients in the powder compact.

3.2.3.3.2 Homogenization feasibility - A one dimensional diffusion analysis was made to estimate the times which might be required to homogenize powder metallurgy compacts of Pt-20W and Pd-30Mo. The following assumptions were made:

- (1) The grain size diameter was 100 micrometers.
- (2) No intermediate phases would be present between grains which would act as diffusion barriers.
- (3) The effective diffusion coefficient for homogenization would be the same as the self diffusion coefficient for the major constituent in the alloy.
- (4) The initial compositional variation could be approximated by a sinusoidal variation equal to the particle diameter.

In the case of the Pt-20W alloy, a time of 4.9 hours was estimated to accomplish complete homogenization at 1873 K. In the case of the Pd-30Mo alloy, it was estimated that homogenization in the same amount of time would only require a temperature of 1670 K.

3.2.3.3.5 Summary of Powder Metallurgy Feasibility - The preceding suggests the basic feasibility of producing homogenous alloys of Pt-20W and Pd-30Mo by powder metallurgy techniques. However, the assumptions used in the analysis make the accuracy of these estimates at best one order of magnitude; thus, the homogenization times, at the temperatures specified, could exceed 50 hours. While 50 hours is not an unreasonable time, the homogenization time should be proportional to the square of the segregation distance, i.e., the square of the powder particle size. Thus, experimental difficulties which tend to increase the homogenization time, such as incomplete mixing, might be compensated for by reducing the average particle size of the powder blend.

3.2.3.4 Sputtered Thin Film Resistive Gages: An alternative to the development of procedures for fabrication of fine wires of the special concentrated hard alloys, is to develop further the thin-film fabrication methods based on sputtering thin film gages and insulation layers directly on burner liner segments. Besides permitting fabrication of strain gage elements of special hard alloys, the thin-film approach offers other potential advantages in static strain gage performance due to the smaller total build-up thickness of less than 25 microns (compared with up to 500 microns for wire gages) on the burner line surface. These potential benefits include improved fatigue life because the gage is nearer the neutral axis in bending, improved resistance to erosion because the thin film does not protrude into the particle-laden airstream, and improved accuracy through reduced interference with local aerodynamics, heat transfer, and burner liner structural stiffness and vibration response. One possible problem area is an increased oxidation effect due to the larger surface-to-volume ratio of thin films. The effect might be overcome by use of a protective overcoat layer.

Because the thin-film resistive strain gage approach to high temperature static strain measurement offered these potential advantages, the thin-film approach was incorporated as an important segment of a separate NASA/UTC program, High Temperature Static Strain Gage Alloy Development Program, NAS3-23169, now in progress. Study of the thin-film technology was therefore not continued further in the present program.

3.3 Capacitive Strain Sensors

3.3.1 Commercially Available Capacitive Strain Gages. - The capacitance strain gage is a fairly recent development in which the distance between gage points is mechanically related to the spacing or area between capacitor plates. The change in capacitance is measured and related directly to the strain in the surface on which the device is attached. An advantage of this technique is that, if the dielectric between the plates does not change with temperature, the device can be extremely stable. The problem of metallurgical stability and oxidation is not as critical as it is for wire resistance gages. However, small capacitance changes are, in general, more difficult to measure than are small resistance changes, so some advances in instrumentation are required; typically, a charge amplifier or transformer bridge is used. The three types of gages currently available commercially are the CERL-Planer gage (sold in the U.S. by Hitec), the Hughes gage, and the Boeing gage (also licensed to Hitec).

Table 3.3.1 lists the characteristics of three commercial capacitance gages, from reference 28.

TABLE 3.3.1. - CHARACTERISTICS OF COMMERCIALY AVAILABLE CAPACITANCE STRAIN GAGES

	CERL	Hughes	Boeing
Maximum Temperature	922 K	1227 K	1088 K
Mounting	Weld	Weld	Weld
Gage Length	20.3 mm	12.7 mm	25.4 mm
Resolution	10 $\mu\epsilon$	50 $\mu\epsilon$	1 $\mu\epsilon^4$
Initial Capacitance	1 pf	10 pf	1.5 pf ⁴
Range	1%	0.15%	$\pm 2\%$
Apparent Strain	100 $\mu\epsilon$ @ ¹ 922 K	2000 $\mu\epsilon$ @ 1033 K	300 $\mu\epsilon$ @ 1088 K
Drift	0.2 $\mu\epsilon$ /h @ 866 K	250 $\mu\epsilon$ /h @ 1227 K	0.3 $\mu\epsilon$ /h @ 922 K
Life of Gage	10,000 h ²	N.A. ³	2000 h
Gage-Factor Change	+ 2% @ ¹ 1922 K	$\pm 5\%$ @ 1033 K	$\pm 4\%$ @ 1088 K
Maximum Thermal Shock	N.A.	6 K/s ³	17 K/s ⁴

All data in the table are from manufacuter's literature except as noted.

¹ Private communication from S. P. Wnuk of Hitec.

² Private communication from B. E. Noltingk of the Central Electricity Research Laboratories

³ Private communication from O. L. Gillette of Hughes.

⁴ Private communication from R. L. Egger of Boeing.

Typically, these commercially available capacitance gages do not meet the size or temperature requirements required for the Advanced High Temperature Static Strain Sensor program. Therefore, an investigation was made to determine the feasibility of developing a capacitive sensor capable of measuring $\pm 2000 \mu\epsilon$ with the dimensional constraints of 12 x 12 x 1.5 mm.

3.3.2 Analysis. - The capacitance of a basic parallel plate capacitor is given by:

$$C = \frac{AK \epsilon_0}{d}$$

where C = Total Capacitance (neglecting fringing)
 A = Area of plate
 d = Separation between plates
 K = Relative dielectric constant of material between plates
 $\epsilon_0 = 8.855 \times 10^{-12}$ farads/meter

For the purpose of analysis several potential capacitive sensor configurations were examined. With the full scale strain given as ± 2000 microstrain ($\mu\epsilon$), the maximum movement within the 12 mm limit of the sensor caused by this strain, will be 2.4×10^{-2} mm. The central problem with the approach is to discover configurations which will result in the maximum amounts of plate surface and ways by which to maximize the amounts of motion between these plates per unit of substrate strain within the limits of the dimensional constraints mentioned above.

Figure 5 shows a possible configuration in which the motion between the plates has been maximized by attaching the device to the substrate only at the corners of the maximum available area. If "d" is the separation between the plates and the total motion (see fig. 5) span is 12 mm then for $\pm 2000 \mu\epsilon$ the growth or shrinkage between the plates will be:

$$\Delta d = d(\mu\epsilon) = 2.4 \times 10^{-4} \text{ mm}$$

and the range of the gap will vary as follows:

$$0.076 \text{ mm} \leq d \leq 0.124 \text{ mm}$$

which should result in values of capacitance:

$$\begin{aligned} C_{\max} &= 2.966 \text{ pf} \\ C_{\min} &= 1.818 \text{ pf} \\ \Delta C &= 1.147 \text{ pf} \end{aligned}$$

Data of this magnitude is detectable and could be processed.

Consider next the device concept B illustrated in figure 6. Here the total plate area has been increased considerably resulting in the following values:

$$\begin{aligned}C_{\max} &= 6.905 \text{ pf} \\C_{\min} &= 6.629 \text{ pf} \\ \Delta C &= 0.276 \text{ pf}\end{aligned}$$

The values of capacitance are higher, but Δd is a function of Δd , the change in plate separation, which is smaller in this case.

The simple analysis indicates that, in order to achieve the most practical values of capacitance and capacitance change, we have A , ΔA , d , Δd , and ϵ at our command. We have to make as many of these as possible to contribute ΔC , and to make these contributions as large as possible.

Now consider the device concept C shown in figure 7. This represents a variable, parallel plate capacitor, with a solid dielectric material between the six plates. In this particular device, the dielectric material, the larger plate area and the multiple plates all act to raise the overall value of capacitance. The motion of one set of plates with respect to the other acts to produce the change in capacitance and the spacing between plates remains constant. To maximize the motion, the space between attachment points was made 10 mm long and a linkage assembly with 5X distance amplification, has been provided in order to drive the movable plates.

Reasonable variables for purposes of computation are as follows:

$$\begin{aligned}A &= 80 \text{ mm}^2 \leq A \leq 90 \text{ mm}^2 \\d &= 0.005 \\n &= 6 \text{ (number of plates)} \\K &= 6 \text{ (dielectric coefficient, } K = \frac{\epsilon}{\epsilon_0} \text{ , mica)}\end{aligned}$$

The capacitance of a multiplate capacitor is given by:

$$C = \frac{AK\epsilon_0}{d} (n - 1)$$

The capacitance of this device for the extreme values of A noted above are:

$$\begin{aligned}C_{\max} &= 134.4 \text{ pf} \\C_{\min} &= 93.8 \text{ pf} \\ \Delta C &= 40.58 \text{ pf}\end{aligned}$$

Taking advantage of sensor concept C brings the capacitance values into the measurable range. The resolution of 100 μ in./in. (5% of full scale) requires the ability to measure $\Delta C \approx \pm 1.008$ pf. This change is detectable and can be processed.

It is anticipated that the detection of the signal from this capacitive device would be accomplished by exciting the capacitor with a known frequency, letting the capacitor serve as a charge source, and then detecting and amplifying its output. The same excitation frequency would be used as a reference in synchronous detection of the signal. The environmental conditions in which this device will have to operate have not been investigated empirically. The most significant sources of apparent strain errors will be from changes in sensor component sizes due to changes in temperature and changes in dielectric constant due to changes in temperature and pressure. It was felt that by monitoring the temperature and the pressure of the sensor during initial tests, a correction algorithm could be derived which would reduce these effects to within acceptable limits. Vibration could also pose a more serious problem. Environmental measurements would be signal conditioned using standard techniques. The processing of the sensor and correction-factor signals could accomplish either by analog or digital techniques.

3.3.3 Summary. - Capacitive devices contained within the 12 mm x 12 mm x 1.5 mm package could conceptually be made to produce readily detectable capacitance and capacitance changes to satisfy the strain measurement range and sensitivity. It is virtually impossible, however, to assess the practicality of such devices without empirical effort and data. The main challenge would lie in the selection of appropriate materials and a mechanically ingenious design which enable this device to function unimpaired within the harsh combustor liner environment.

3.4 Fiber Optic Concepts

3.4.1 Overview. - There are two classes of sensors which use optical fibers: those that use an optical fiber directly as the sensing element, and those sensors that use an optical property of another device attached to the liner, and optical fibers or a bundle of fibers deliver and receive the optical information signal from the sensing device.

The first class of sensors, those that place fibers on the combustor liner, will not withstand the maximum temperatures encountered on a liner in an operating engine. New developments in producing crystal fibers from sapphire or YAG (yttrium aluminum garnet) could change this perspective, however. For these sensors, there will always be the problems of mounting the fibers and providing sufficient protection for the fiber on the burner can.

The second class of sensors utilizes reflection, diffraction, or interference of an optical beam incident on a device or reflecting pattern that has been attached to the combustor liner. These sensors require the transfer or imaging of an optical signal through the high density turbulent atmosphere that surrounds the liner. The amount of optical distortion from the rapidly-moving, hot, dense gas probe a sensor device or pattern on the liner is not precisely known. Previous experiments that have used a fiber optic probe to view a combustor liner could identify cracks as small as 0.25 mm, with 2 mm diameter, f/3.8, and 10X magnification imaging optics (ref. 28). The resolution of the fiber optic probe was over 100 times the diffraction limit. Some of the resolution loss in this instance could have been due to video camera detection system. It may be possible in many instances to average out the turbulence distortions with a sufficient integration time if required.

3.4.2 Optical Fiber Strain Sensors

3.4.2.1 Optical Coupling Between Fibers: The coupling of optical power between the ends of opposing fibers could be used to detect very small displacements. The optical coupling is related to the off-center alignment, diameter, and spacing of the fiber cores. The sensitivity of the optical coupling to displacement would depend on the size of the fibers and their spacing. Single mode fibers, for instance, have core diameters of a few microns and could detect displacements much smaller than 1 μm . The size of the fiber to use would depend on the range of strain to be covered with 1.0 to 0.1 percent of range being a reasonable sensitivity to measure.

Figure 8 shows an example of a fiber coupling strain gage that might be used on a combustor liner. The gage consists of two independent arms attached to the liner at two points along the line of expansion to be measured. An optical fiber that carries light from an LED or laser source is brought into

one of the arms of the gage. The light emitted by the input fiber is picked up by two adjacent receiving fibers placed opposite to the input fiber on the second arm. As the combustor liner expands, the opposing fibers are displaced crossways, and one pick-up receives more light than the other. By ratioing the two signals from the receiving fibers, the crossways displacement of one arm relative to the other can be measured.

The most serious problem in applying optical fiber strain sensors to the combustor liner is the temperature limitation of the fibers. Data from Amersil Inc., a fused quartz (silica) manufacture, indicates that the maximum temperature at which to use fused quartz for continuous life is 1223 K; and the maximum temperature for limited life is 1473°K. The new fluorinated silica clad, fused silica core filters may be able to handle the required combustor liner temperatures. For proper protection of the fiber surface, these fibers would have to be coated with a metal film. Fibers that have a glass or fused quartz cladding require a doped core glass that lowers the maximum operating temperature of the fiber from that listed above for fused silica. Corning graded index fiber, for example, which has a high silica content, has a strain point temperature of 1040 K. This temperature is about 100 K short of the required temperature capability of the sensor. New developments in making a clad-crystalline fibers from materials such as sapphire or yttrium aluminum garnet (YAG) could make the optical fiber strain sensors more attractive for the high temperature applications.

3.4.2.2 Fiber Optic Mach-Zender Interferometer: Other fiber strain sensors which have been discussed in the literature include the fiber-optic Mach-Zender interferometer (ref. 29). This sensor measures the difference in phase of a coherent optical signal in two single mode fiber arms by measuring the fringe shift of the interferring signals from the output of the arms. If a section of the fiber in one arm is placed under a stress, then a shift in the optical signal occurs which in turn produces a detectable fringe shift. This sensor, which is very sensitive to strain, is also very sensitive to small temperature and pressure changes (ref. 30). The two fiber arms of the sensor would have to lie within close proximity to avoid differences in temperature and pressure that could mask the strain measurement.

3.4.2.3 Fiber Bending Loss Sensor: Another fiber strain could be based on microbending loss associated with fibers. The optical signal in a fiber is trapped in the fiber core by total interval reflection at the core/cladding interface. If the fiber is placed under a small enough bend, then total internal reflection no longer occurs and some of the optical signal can leak from the core into the cladding, where it is eventually lost due to scattering and absorption at the outside boundary of the fiber. The amount of signal loss is related to the radius and number of bends placed on the fiber. Such a device has been proposed as a sensitive pressure sensor (ref. 31) and might in principle be modified to measure a strain induced pressure on the fiber.

3.4.3 Expansion of Grating. - Diffraction gratings were first proposed by J. F. Bell in 1956 to measure dynamic strain in metals under impact loading (ref. 32). The diffraction grating strain gage has been applied to both static and dynamic measurements, but the major interest has been in the measurement of strain in moving specimens undergoing constant velocity impact. Typical gratings were ruled on cylinders with a precision lathe. A 0.25 mm long grating with 1200 lines/mm rulings gave strain measurement accuracies of 500 μ strain and strain measurements have been made to within 20°C of the melting temperature of the base material. These results were obtained by Bell and reported in a review article by W. L. Bingham (ref. 33).

Some laboratory tests have also been made with grating sensors by G. G. Smith of Pratt & Whitney Aircraft's instrumentation group (ref. 34). Photographic recording techniques were used, and the reflectivity of the grating surface was found to be a strong function of temperature due to oxide buildup and erosion on the grating surface.

Figure 9 illustrates how a particular diffraction grating sensor would work. A laser source is injected into an optical fiber and then expanded at the end of the fiber transmitting link with a lens onto the grating surface at normal incidence. The diffracted beam is returned at an angle $\pm \beta$ and reimaged onto one of a pair of return fibers. As the strain in the liner increases, the grating expands and the angle β becomes slightly smaller causing the return image spot to shift to the second fiber. With proper choice of fiber core/clad diameters and lenses, the ratio of light in the return fibers could be made to make a continuous change as the combustor liner went from zero to full-scale strain.

Let us consider a specific case. The first order grating equation is:

$$\pm \sin \beta = (\lambda/a) - \sin \alpha,$$

and the displacement at the receiving fibers is:

$$\delta_s = - \frac{\lambda f}{a \cos \beta} \frac{\delta \ell}{\ell}$$

where f is the focal length of the lens, $(\delta \ell / \ell)$ the strain, " a " the line spacing of the grating. For a 1000 ℓ/mm grating ($a = 1.0 \mu\text{m}$), $\beta = \pm 58^\circ$ ($\alpha = 0$), $f = 50 \text{ mm}$, $\lambda = .85 \mu\text{m}$, and $(\delta \ell / \ell) = 2 \times 10^{-4}$, which corresponds to 200 μ strain. For the above parameters, we would have to detect a displacement, δ_s , of 16 μm at the pair of fiber receivers over a range of about 160 μm . This displacement would not be difficult to detect in practice in a controlled laboratory environment with proper choice of fiber sizes.

Because we are detecting the diffraction angle of a monochromatic light source, any vibration that causes a comparable angle change between the grating and sending/receiving optics will give an error in the reading of the strain component of the angle change. If small enough, the error induced by the vibration can be cancelled by incorporating two receiving pairs of fibers in opposite sides of the grating normal as shown in figure 9. The rotation of the grating will cause the spots to shift in the same direction, while a grating expansion will cause the spots to shift in opposite directions.

The sensitivity of the diffraction angle β to strain ϵ can be shown to be:

$$\delta\beta = \epsilon \tan \beta$$

In the example above $\beta = \pm 58^\circ$. If a smaller ruling spacing is used, or a higher order diffraction, then larger diffraction angles would be generated and the sensitivity of the grating for strain measurements would be enhanced.

In practical application to combustor liners, however, the larger diffraction angles may be difficult or impossible to implement. Smaller diffraction angles would be easier to work with, but would decrease the sensitivity for strain measurements.

Actual implementation of the diffraction grating strain sensor to the combustor liner will require overcoming problems of fabrication and attachment of the grating to the liner. The liner has a curved surface that has to be polished, ruled, and overcoated with a reflective material. P&W, for instance, has used platinum with 10% rhodium as a reflective coating material on a flat sample that was made for a laboratory test. Sharp and Martin have tested a variety of reflecting overcoats, such as chromium and platinum, on superalloys at high temperatures (ref. 35). They found different results for different alloys, and that sometimes a preoxidized surface prior to overcoating was an aid in maintaining the reflectivity at high temperatures. The bare alloy with no overcoat would completely lose reflectivity at temperature of 870 K.

A section of the liner could be cut out, polished, ruled, and coated, and then welded back in place on the liner. Ruling the curved liner piece or liner itself may become an expensive special operation. A more attractive method of etching the grating on the liner could also be explored. Such etching may also become an expensive research project by itself, however.

The grating could be expected to survive for a reasonable period of time in the combustor environment. While oxidation and abrasion will deteriorate the rulings in time and significantly change the grating efficiency, the ruling spacing and, hence, the diffraction angle, will remain the same. Some

effort would have to be made to determine a good coating that will retain a reasonably reflectivity over the entire temperature range.

In summary, the diffraction grating in theory and laboratory practice is a feasible way to measure large strains on the order of 2000 μ strain to the required accuracy. Fabricating a survivable grating on a combustor liner, however, could prove a more formidable task than covered by the current program.

3.4.4 Vibrating Drumhead. - A small vibrating sensor, whose vibrating frequency depends on the applied tension, could be attached to the combustor liner. The sensor device could be attached to the combustor liner at two points and be designed in such a manner that it would be driven into its lowest order or fundamental mode of vibration by the broad spectrum of vibration frequencies present in the operating engine. The sensor would be stretched between its two attachment points and its frequency of vibration would depend on the applied tension. A strain displacement of the attachment points will cause a change in tension and consequently a change in the fundamental mode frequency of the sensor. Laser heterodyne techniques which have been well developed at the United Technologies Research Center (ref. 36) could be used to detect such vibration frequencies.

Figure 10 is an illustration of a possible vibration strain sensor. A central mass is attached at the center of a much thinner flexing strip. The ends of the flexing strip are attached to mounting posts on the liner. A restoring force, F , will be exerted from a small downward displacement, δy , of the flexing strip. The restoring force is related to the displacement by the relation:

$$F = \frac{8Ewh^3}{L^3} \delta y,$$

where E is the modulus of elasticity, w and h the width and thickness of the flexing strip, and L the length of the flexing arm between the mounting post attachment and the central mass.

If a tension is applied to the flexing strip from a strain displacement ϵ , then an additional restoring force will be added, namely:

$$F = - \frac{\epsilon Ewh}{L} \delta y$$

The frequency of vibration of the sensor is given by $1/2\pi$ times the square root of the sum of the restoring force constants divided by the mass, m , or:

$$f = \frac{1}{2\pi} \sqrt{\frac{whE}{mL} \left(\frac{8h^2}{L^2} + \epsilon \right)}$$

For a typical example, consider $w = 2.5 \text{ mm}$, $h = 50 \text{ }\mu\text{m}$, $L = 4 \text{ mm}$, $m = 150 \text{ mg}$, $E = 1.4 \times 10^{11} \text{ N/m}^2$ (Hastelloy X) then:

$$f = 962 (1 + \epsilon/1250)$$

where ϵ is in microstrain. At zero μ strain, $f = 962 \text{ Hz}$ and at the maximum strain of $2000 \text{ }\mu$ strain, $f = 1551 \text{ Hz}$.

The principal difficulty with this vibrating sensor would be that it would not work in compression and, consequently, would have to be mounted under a bias tension. In either case it could not cover the entire range of $\pm 2000 \text{ }\mu\epsilon$ and stay within the elastic limit of the sensor. In addition, the sensor would have to be made from the same material as the combustor liner in order to avoid net displacement due to temperature expansion which could also easily exceed the elastic range of the sensor.

3.4.5 Time of Flight. - A small spot of light from a laser could be focused on to the combustor liner and made to repetitively scan across two reflecting grooves that have been scribed or etched into the combustor liner. The grooves could be overcoated with a protective metallic coating, as discussed previously, to reflect the laser at a specified angle when the spot traverses the grooves. The time of arrival between successive reflections at a photodetector giving rise to electrical pulses would be a measure of the groove separation. The separation or time between the electrical pulses would have to be measured to 1 part in 5000 to obtain the required sensitivity of $200 \text{ }\mu$ strain. If the reflecting groove spacing is 10 mm , then we would have to measure a spatial resolution of $2 \text{ }\mu\text{m}$ on the liner.

The generated electrical pulses produced by the optical detector could trigger a counter with a constant-fraction-of-pulse-height trigger, so that any amplitude changes in the pulse would trigger the counter at the same instant of time. The first pulse would initiate the counter to count a standard crystal oscillator signal, and the second pulse would turn the counter off so that a fixed number of cycles from the oscillator have been counted. The number of cycles counted corresponds to the distance between the reflecting grooves. This number could be stored in a minicomputer and the process repeated several times a second until a sizeable group of spacing measurements have been measured.

The electromechanical beam scanner would have to be stable and repeatable to 1 part in 5000. This might be accomplished by a stable oscillator driven synchronous motor. The motor could turn a circular wedged window to deviate the laser beam back and forth at a precisely repeatable rate.

The experiment just described, to measure the distance between two narrow grooves on a combustor liner, could be carried out in a laboratory environment with the proper optical and electronic processing equipment. There are problems that would arise, however, in a combustor environment. One problem could be caused by the expansion of the reflecting grooves with increasing temperature and possible erosion of the groove edges, which would change the pulse shape and consequently change the timing of the trigger to turn on the counter.

Another problem might arise if the liner shifted position during the transit of the scanning spot between the grooves. A shift of 10 to 50 μm might be expected from vibrations of the liner, although the exact amplitude of the vibrations is not known at the present time. By averaging over several scans, one could obtain an average separation of the grooves; but if the vibrations are as large as 50 μm , it would be hard to resolve 2 μm for the 200 μ strain accuracy required.

The vibration problem with the scanning spot sensor could be solved by scanning the groove spacing with two focused laser spots. The spots would be scanned, at identical rates, in opposite directions. If the pulses were simultaneous on the initial groove crossing, then they would also be simultaneous on the second groove crossing. If the combustor liner shifted during the transit of the beam spots, then the pulses would not be simultaneous on the second groove crossing. The separation in time of the arrival of the second groove crossing pulses would give a measure of the shift in position of the liner during the scan time. The groove spacing could then be computed by taking an average separation between the pulses.

3.4.6 Hinged Reflector Concept. - Of the several optical sensors considered, the hinged reflector appears most promising for application to the combustor liner strain measurement. This sensor has over one order of magnitude more angular sensitivity per unit strain than the diffraction grating for small reflection angles, and it can be conveniently accessed with an input beam at normal incidence and return beams at small angles to the normal. The sensor could be made rugged enough to withstand the combustor environment. Moreover, if the sensor is made from the same material as the substrate, the elongation due to temperature expansion will not affect the sensor output provided both substrate and sensor are at the same temperatures.

The strain sensor consists of two small hinged reflectors that form a dihedral angle. The reflectors would be attached to two posts which in turn would be mounted on a substrate for which the strain is to be measured. The reflectors are tilted slightly from the surface of the substrate and in opposite directions. An example of such a device is illustrated in figure 11. The reflecting pieces of the sensor are attached to each other and to the mounting posts by thin sections of metal which act as the hinges. The reflecting section of the sensor remains plane and the dihedral angle is relatively free to bend at the thinner joining sections.

A collimated beam of light incident on the sensor and normal to the substrate surface is reflected as two beams at equal angles about the normal as shown in figure 11. A lens system can image the two reflected beams to small spots in the focal plane of the lens. The separation between the two spots in the focal plane would be a measure of the dihedral angle. If the substrate is strained in compression or tension, then motion of the sensor posts together or apart will be registered by an opposite change in the separation of the two beam spots in the focal plane.

The beam spot separation should be independent of small vibratory motions between the incident beam and sensor. The imaging lens would focus parallel light to the same position in the focal plane. Translations would shift the position of the beams, but the beam angles will be the same. A small rotation between the incident beam and sensor will make an angular shift in both of the reflected beams. The shift will be in the same direction and by the same amount, moving the spots in the focal plane, but keeping the separation between them constant. Vibrations, then, between sensor and optical beam, averaged over a period of time, may increase the size of the focal spots; but the distance between centers of the spots will still measure the dihedral angle.

The beam reflector tilt angle, β , can be calculated in terms of the strain, ϵ . If x represents half the distance between the mounting posts and l the length of one of the reflecting arms, then:

$$x/l = \cos \beta$$

By differentiation, the small changes in angle β can be related to small changes in the strain, $\epsilon = \delta x/x$ by:

$$\delta \beta = \epsilon / \tan \beta$$

For small angle β this expression is inaccurate, since $\tan \beta \rightarrow 0$, and second order terms in the derivation of $\delta \beta$ must be considered. When we consider second order terms the shift in angle becomes:

$$\delta\beta = \tan\beta [1 - (1 - 2\epsilon/\tan^2\beta)]^{1/2}$$

which, if $2\epsilon/\tan^2\beta \ll 1$, reduces to the first expression for $\delta\beta$. The deflection angle of the incident optical beam, ϕ , is twice the tilt angle β .

Another formula for the deflection angle can be derived from the expression:

$$(x + \delta x)/l = \cos\beta$$

From this expression

$$\phi = 2\cos^{-1} [(1 + \epsilon) \cos \beta_0]$$

where β_0 is the tilt angle at zero strain.

Figure 21 shows a calculated plot of ϕ vs strain for $\beta_0 = 3.6^\circ$. For this case, at maximum strain in tension, namely $\epsilon = 2000$ microstrain, the dihedral angle is completely opened, and the reflectors are normal to the incident beam.

The hinged reflector concept, described above as a potential optical beam reflecting sensor, is an outgrowth of UTRC's corporate-sponsored novel sensor development program. A simple laboratory demonstration model has been fabricated under this program to verify the principles involved, and has been successfully tested. The hinged reflector was a simple strip of 0.076 mm stainless steel shim stock, onto which thicker reflecting pieces are mounted. This strip was spot welded to posts welded to a stainless steel bending specimen. Loads corresponding to over 1000 μ strain have been applied, and the changes in the separation of the reflected spot were quite easily measured.

The proposed optical beam deflecting sensor measures strain displacements in the direction of the line between the two mounting post centers by a corresponding change in the dihedral angle between the reflectors. If there is a strain displacement at an angle to the line between centers, the two reflectors would be made to twist about the line of centers in opposite directions, as well as producing a change in the dihedral angle. The twist would produce a deflection of two reflected beams in an opposite sense away from the line of centers. The twisting motion would represent a shearing stress on the normal plane between the mounting posts. The change in the dihedral angle along the line of centers would correspond to the normal component of the stress.

By monitoring the direction and magnitude of the change in position of the beam spots in the focal plane of the lens system, we can determine the

direction and magnitude of the strain. The ends of the mounting posts on the sensing element can be set normal to the substrate and polished to provide additional reflected beam and corresponding beam spots in the image plane with which to reference the more complex motions of the sensor when both shearing and normal strain occur.

Another change that effects the reflected beams from the sensor would be a bending of the substrate surface. A small bend in the substrate can have an amplified effect on the dihedral angle between the sensor reflectors. A bending of the substrate surface could be determined by observing additional reflections from the two mounting posts. Reflections from the posts would shift in opposite directions when a bend occurs in the substrate.

A more generalized sensor could be made, then, that also allows for twisting of the reflectors. By monitoring four reflected beams from the sensor, we could determine strain and bending of the substrate surface. Two of the beams would come from the tilted, hinged reflectors and their angular deflections perpendicular to and along the line of centers would indicate shearing and normal strain. The other two reflected beams would come from polished ends of the two mounting posts. A change in angle of these reflected beams indicate that a bend occurred on the substrate surface.

The bending and twisting forces required to actuate the deflecting beam sensor must be small enough, of course, so as not to significantly affect the strain conditions in the substrate. A basic trade-off with this sensor is to make it flexible enough to monitor the strain without causing a significant effect on the strain deformation in the substrate itself. It also must be rugged enough to withstand the vibrations and hostile environment inside gas turbine engines for which the sensor is proposed.

3.5 Holographic and Speckle Strain Sensing Techniques

3.5.1 Survey of Optical Methods. - Whereas electrical strain gages have a fairly good history of reliability, accuracy and convenience, they have, nonetheless, a number of disadvantages. They must be well bonded to the surface of the test object or else they do not give accurate measurement. It is easy for their fine electrical structures to become damaged by mechanical contacts, and they are intrinsically temperature sensitive. Furthermore, at high temperatures and in harsh environments their components may become physically, electrically or chemically unstable.

Because of the problems associated with electrical strain gages, considerable effort has been put forth to develop optical methods as alternatives. Perhaps the earliest work was done by Ennos (ref. 37) with holographic reconstructions of a stretched membrane. This technique was put forth for subtracting the out-of-the-plane displacements of a stretched membrane from those containing both in-plane and out-of-plane deformations to yield only in-plane components. This was further pursued by Wilson (ref. 38), and Wallach et. al, (ref. 39), and eventually generalized by Sciammarella and Gilbert (ref. 40). Bending strains have been obtained by taking second derivatives of the out-of-plane displacements for plate-like structures by Brandt and Taylor (refs. 41 and 42), Stetson (ref. 43), Sollid and Stetson (ref. 44) and MacBain (ref. 45). Holographic moiré techniques were introduced by Boone (ref. 46) and further developed by Sciammarella, et. al. (refs. 47 and 48). Finally, techniques based upon fringe localization have been developed by Schumann and Dubas (ref. 49) and by Stetson (ref. 50) and based upon fringe parallax by Stetson and Pryputniewicz (refs. 51, 52, and 53).

After the technique of speckle interferometry was introduced by Leendertz in 1969 (ref. 54), and speckle photography by Archbold et. al. in 1970 (ref. 55), many people came to feel that the ultimate answer to optical strain measurement lay in speckle metrology. This arose from the fact that many techniques of measurement using speckles were sensitive to displacements transverse to a viewing direction, which could be set parallel to an object surface normal. A thorough exposition of this technology is available in the recent book edited by Erf (ref. 56).

Generally speaking, however, no truly satisfactory optical method of strain measurement has yet been developed. The greatest problems encountered with optical methods are lack of accuracy, impractically large gage lengths, cumbersome data extraction and processing requirements, and difficulties in dealing with curved surfaces. Most of these difficulties are brought about by the use of systems which record images, such as hologram interferometry or speckle photography. Although strain information could be recorded at once by

these methods over an entire object surface, in practice the images must be scanned to generate data for strain analysis.

3.5.2 Optical Strain Sensor Technique. - In response to the above needs the United Technologies Research Center has conceived a real-time system that operates by means of coherent illumination of two nearby points on an object surface. Preliminary experiments have confirmed that surface strains may be extracted in an easy, straightforward manner from the Fourier transform of the fields scattered from two such illuminated points. From this starting point, it is possible to envision an optical system for strain measurement that could obtain high accuracy and rapid readout using an optical heterodyne technique. Such a system could have significant advantages over electrical strain gages for measuring static strain on combustor liners. By eliminating the need for mechanical attachment to the part under test and for electrical connections to the strain gage, the optical strain sensor could eliminate many of the problems involved with making high temperature strain measurements on non-rotating components.

3.5.2.1 System Concept: The concept of the real-time Optical Strain Sensor can be explained by means of figure 12. Two narrow light beams are obtained from a laser and directed by a small mirror, M, so as to illuminate two nearby points on an object, A and B. The surface, being rough, will scatter light in wide, conical angles from its illuminated regions. The field from each illuminated point will be speckled due to the random scattering within each region illuminated on the subject.

A lens is placed a distance of one focal length away from the object surface in order to collimate the fields scattered from each point. At a distance of one focal length from this lens, a recording is made of the interference pattern that results from the coherent addition of the two fields. The field at this recording plane is the optical Fourier transform of the field at the object surface. Because of the lateral separation of the two points, the two fields at the transform plane will be inclined at an angle to one another, causing a fine interference pattern to appear where the speckles of the two fields overlap. An example of such a pattern is shown in figure 13.

If, after it has been developed, the recording is relocated back in the same position it occupied during exposure, a black-silver image will occupy the illuminated areas, while the transparent portions of the recording will not be illuminated. This will result in a minimum of light transmitted through the recording. If the phases of the illuminating beams are shifted by 180° relative to one another, the fine interference pattern will shift by one-half cycle relative to the recording at the transform plane. The transparent areas of the recording will not be illuminated, and this will result in a

maximum of light being transmitted through the recording. This beating of a pattern of illumination with its photographic replica is often referred to as moiré interference.

Moiré interference at the transform plane of the system, can be used quite effectively to measure strain on the object surface. If the object surface is strained so that points A and B increase their separation, the angle between the two fields at the transform plane will increase. This, in turn, will increase the spatial frequency of the fine interference fringes relative to the recording. If this frequency increase is small relative to the spatial frequency itself, its effect will be to generate a spatially cyclic change of phase between the two patterns, which will cause a spatially cyclic fluctuation of light transmitted through the recording. This will appear to the observer as a fringe pattern. The spatial frequency of the moiré fringe pattern in the ω_x direction is proportional to the x strain.

It is quite simple to verify that no other motion of points A and B in figure 12 will yield a moiré pattern that could be confused with that caused by strain. First, translation in the x and y directions (up to x and out of the plane of the drawing for y) will change the phase of both fields by equal amounts and will not change their relative inclination angles in the transform plane, i.e., both field angles will change by the same amount. Translation along the z-axis (to the right or left) will also change the phase of both fields by the same amount and will add curvature to the fields at the transform plane. To first order, this curvature will be equal for both fields and will not change the angle between them. Translations, therefore, will not generate a moiré fringe pattern in the transform plane.

Rotation of the object about the x-axis (through A and B) will obviously also not create a moiré fringe pattern, because the points A and B do not move. Rotation about the y axis will change the phase of one field relative to the other, but it will do so uniformly, i.e., the angle between the two fields in the transform plane will not change. Such a rotation will cause the moiré fringe pattern to cycle from maximum to minimum, and, therefore, cause it to scan across the transform plane. Rotation about the z-axis will simply rotate the pattern in the transform plane. This will generate moiré fringes, but they will be parallel to the ω_x -axis and, therefore, be at right angles to those generated by x strain (which are parallel to the ω_y -axis). Shear parallel to the x-axis, like x-axis rotation, will have no effect, since points A and B do not move. Shear parallel to the y-axis will create moiré fringes identical to those of z-axis rotation. The greatest effect that can occur by a combination of strain, translation, rotation, and shear is that the fringes may translate and tilt; however, their spatial frequency in the ω_x direction will always be proportional to strain parallel to the x direction.

Figure 14 shows the results of strain measurements performed with a system of the type shown in figure 12. The objective was an aluminum bar under three-point bending to which a resistive strain gage had been fastened. This allowed both a theoretical and experimental check on the optical strain measurements. The illuminated spots were 3.8 mm apart, and the lens was 100 mm in diameter with a 180 mm focal length.

3.5.2.2 Combustor Liner Strain Measurement: Application of the optical strain sensor to the measurement of strains on actual combustor liners is straightforward. First, the surface of the liner must be checked to assure that it reflects light with suitable diffusivity. If not, the surface may be coated with a diffusely reflecting refractory material. Secondly, provision must be made for repeatably loading the liner if strain values obtained at one location are to be compared with those at another. Finally, a means of scanning the liner past the sensor, or the sensor past the liner, must be provided if strain distributions are to be recorded. The scanning system should not interfere with either the operation of the strain sensor or the loading system.

3.5.2.2.1 Three Dimensional Surfaces - A problem encountered with actual combustors arises from their three-dimensional surfaces. The operation of the optical strain sensor depends upon having the system aligned with the normal to the object surface. If it is not, the indicated strain will include contributions from the other surface strains, shear, and rotations of the object. Let us consider an x, y, z coordinate system for the strain sensor with x along the line connecting the two illuminated points, z toward the illumination, and y orthogonal to x and z . Let us also consider an x', y', z' coordinate system on the object surface, with z' axis along the surface normal. The indicated strain, ϵ_x , is expressed in terms of the surface strains, shear, and rotations x ($\epsilon_{x'}$, $\epsilon_{x'y'}$, $\epsilon_{y'}$, $\theta_{x'}$, and $\theta_{y'}$) by:

$$\begin{aligned} \epsilon_x' = & \epsilon_{x'} \cos^2 \sigma_{xx'} + \epsilon_{x'y'} \cos \sigma_{xy'} \cos \sigma_{xx'} + \epsilon_{y'} \cos^2 \sigma_{xy'} \\ & + \theta_{x'} \cos \sigma_{xz'} \cos \sigma_{xy'} - \theta_{y'} \cos \sigma_{xz'} \cos \sigma_{xx'} \end{aligned}$$

where $\sigma_{xx'}$, $\sigma_{xy'}$, and $\sigma_{xz'}$ are the angles between the x axis and the x' , y' , and z' axes, respectively. Typically, the x' axis would be assumed to lie in the x - z plane so that, for small misorientations, $\sigma_{xx'}$ would be small, and both $\sigma_{xy'}$ and $\sigma_{xz'}$ would be near 90° . Thus, the contributions from the unwanted terms are on the order of the sine or the sine squared of the misorientation angle. If the misalignment is held to within 1° , the effects of these terms may be kept to less than 1.7 percent of their maximum values.

Perhaps the simplest method that could be used for aligning the strain sensor with the surface of the object would be to place a small piece of shiny black tape on the object surface. The reflection from the surface of the tape can be used to assure that the illumination is directed along the surface normal. Preliminary checks have shown that this method can be used to align a surface to within 0.5° of the normal, or better.

3.5.2.2.2 Incandescence - Another consideration for high temperature application of the optical strain sensor is the fact that the material under study may be hot enough to emit visible radiation. In the actual operation of the sensor readout, this would not create much effect. The optical system would use laser radiation at a single wavelength which can be separated from the background by an interference filter.

3.5.2.2.3 Gas Flow - The flow of gases between the strain sensor head and the surface of the object will cause phase fluctuations in the fields whose interference is sensed by the sensor. These fluctuations will be, generally, random functions of time and their effect will be to create noise in the moiré pattern. There may also be steady-state gradients of refractive index. Some study will be required to determine if such gradients actually exist in the measurement environment.

3.5.2.2.4 Surface Degradation - If, during the operation of the optical strain sensor, the object surface changes significantly, the field it scatters to the Fourier transform plane will change its amplitude and phase pattern. This will cause a loss of the signal used for the detection of strain. If this happens, a new recording will be required at the transform plane in order to continue the strain measurement. Such a new recording, however, would effectively reset the system, and any further measurement of strain would be relative to the state of the surface when the new recording was made. If a strain history is required over a long cycle of operating conditions during which there has been a substantial build up of dirt or corrosion, the system would have to be reset periodically. With a rapid recording system, this might mean the loss of only ten or fifteen seconds of measurement time.

3.5.2.2.5 Thermal Expansion - One important feature of the optical strain sensor is that it will simply and faithfully indicate all changes in surface expansion or contraction, regardless of the way in which they are generated. Thermal expansions, therefore, will appear directly equivalent to strain even though no load is applied to the part. Effects may also be read as strain due to differential expansion of components of the strain sensor. Care should be taken, therefore, to make the system components from glasses with ultra low coefficients of expansion, to keep these effects negligible.

3.5.2.2.6 Mechanical Vibration - Perhaps the most serious problem facing the optical strain sensor in measuring the strains of combustor liners would be mechanical vibration. The points on the object illuminated during the transform plane recording must remain illuminated during the readout. Motion of the object relative to the sensor head must be kept to less than $1/5$ the spot diameters, and similar restrictions exist on the allowable tilting of the object. These two issues are in conflict in that the larger the spot diameters, the less allowable tilt; and the smaller the diameters, the less allowable displacement. Good mechanical coupling to the test object would be required.

3.5.3 Heterodyne Optical Strain Sensor Techniques. - For the experimental case illustrated in figure 14, the parameters of the optical system set both the: 1) minimum strain (approximately 500 microstrain) that could be detected, by the need to have one fringe across the transform plane; and 2) the accuracy (approximately 50 microstrain) of the measurement, by the fraction of a fringe to which the fringe center could be located. Clearly, what would be preferable is to measure the number of moiré fringes between two locations at the extremities of the transform plane to a small fraction of an order and starting directly from zero. This can be done most effectively by means of heterodyne interferometry.

3.5.3.1 Heterodyne Interferometry: One of the most important developments in the last decade in the field of interferometry is the emergence of heterodyne readout of fringe data. For generations, the data presented by interferometers has been pictorial. An interferometer divides light beams, directs them through or onto objects under test, and then recombines them to form fringes. Fringes are bands of constructive and destructive interference in a wave front that presents the equivalent to a topographical map of optical phase changes between two beams. With the introduction of holography into the field of interferometry, it has been possible to associate fringe patterns with deformations of diffusely reflecting, three-dimensional objects. For qualitative inspection, the pictorial display of fringe patterns is quite useful, but for accurate metrology, they offer a disadvantage. Whereas the conditions that correspond to dark fringes, for example, correspond to exact object displacements, the locations of the centers of the dark fringes may not be precisely defined. Furthermore, the use of dark or bright fringes as data points eliminates many points in the field of view from the measurement process. Because heterodyne methods effectively solve many problems of this sort, they are becoming increasingly important.

Figure 15 illustrates the principle of heterodyne interferometry. The configuration is that of a conventional Mach-Zender Interferometer. A laser beam is partially reflected and partially transmitted by a beam splitter, and the resulting beams are redirected by mirrors to a second beam splitter that

serves to recombine the beams. Before recombination, both beams have been expanded by telescopes, and one has passed through a test object. Changes in optical phase introduced by the test object appear as fringes in the output field. To implement heterodyne readout, a device for constantly changing the phase of one beam is placed in one leg of the interferometer, thereby shifting the optical frequency of this beam. This causes the fringes to scan across the field of view in a constant direction. A detector placed anywhere in the field of view will generate a sinusoidal voltage at the shift (or heterodyne) frequency. The phase of this signal, however, will correspond exactly to the phase change introduced by the test object. Two detectors may be used, one kept stationary, and the other scanned across the output field. Electronic circuitry exists that can measure the phase difference between the two signals to within $2\pi \times 10^{-3}$ radians, and, in the language of conventional interferometry, this would mean dividing each fringe into 1000 parts.

The advantages of the heterodyne readout are that data may be taken with high precision anywhere in the image field, with near immunity to variations in light intensity, and in a rapid, machine-readable format.

3.5.3.2 General Description of Optical System: A possible heterodyne optical strain sensor system is illustrated in figure 16. Such a system can be fabricated to investigate implementation of this strain sensor to the measurement of static strain under adverse conditions, such as in a combustor liner.

Two separate lenses are used to transform two portions of the fields scattered by the object. This would make it possible to sample the fields within angles of approximately $\pm 45^\circ$ to the surface normal without requiring a lens of exceptionally high numerical aperture. (Such a lens would exhibit severe aberrations.) Mirrors would be used to bring these two field transforms to adjacent regions of a recording plane. Photodiode detectors would be placed behind these two regions on the recording plane, and their outputs would be connected to a phase meter. The recording should be made on a material that can be processed in place to avoid time delays and repositioning errors. The two input beams would be put through a heterodyne modulator to continuously increase the phase difference between them before they enter the strain sensor.

Operation of the heterodyne strain sensor would be as follows. The heterodyne modulator is turned off, and a recording is made of the transform fields. The heterodyne modulator is turned on, and the detectors will generate sinusoidal voltages at the heterodyne frequency. With no disturbance of the object, the signals from the two detectors will be exactly the same in phase. When stress is applied to the object, any resulting strain will change the phase between the detector signals by an amount directly proportional to the strain. To measure strain at a different location on the object, either

the object or the strain sensor would be moved until that location is illuminated, a new recording made, stress applied, and the resulting phase difference between the detector signals measured. Filtering and averaging techniques can be applied to the signals to reduce or eliminate the effects described in Section 3.5.3.2.

3.5.3.2.1 Transform Plane Recording System - The operation of the heterodyne strain sensor depends upon the recording of a photographic pattern at the Fourier transform plane. This recording step can be thought of as detecting and storing the initial phase information of the interference patterns within a large number of speckles in the transform plane. Although these phases are randomly distributed from speckle to speckle, they all change by an equal amount when the object surface is strained. Rotations of the surface, however, cause translations of the speckles, and this adds a random variation to the phase change of the interference pattern within each speckle. This random error differs from speckle to speckle, but adds to zero over a large number of speckles. A rough estimate indicates that, to reduce the error to 0.1 percent, the signal should be averaged over about 1000 speckles. If two regions in the transform plane are considered, this would require 2000 sampled points and storage units. The cost effectiveness of doing this electronically would be low.

There are several possibilities for the photographic storage system. The most straightforward is in-situ development of a photographic plate exposed in a liquid gate. Cycling time for this method can be as low as two or three minutes per recording. A wide variety of photographic materials are available that are suitable for this method. A more rapid alternative would be a system based on the Kodak Ektavolt photoconducting material. This is a reasonably priced transparent film, consisting of a base material coated with a transparent conductor layer and a transparent photoconductor layer. The material is charged by corona discharge, exposed to light, and developed with a liquid toner. Cycling time can be a matter of seconds, the material is red sensitive, can resolve 400 cycles/mm, and requires as little as 45 erg/cm² for exposure. It is possible that the liquid toner could be applied as an aerosol spray.

3.5.3.2.2 Heterodyne Modulator - A number of methods exist for generating a continuously increasing phase difference between two light beams. Perhaps the most popular device for this is the acoustooptic modulator, which employs an acoustic wave in a transparent medium to diffract light. Light diffracted into the first diffraction orders by such a device will be shifted from the original optical frequency by the acoustical frequency in the modulator, usually around 40 megahertz. Such devices are most useful for obtaining high-frequency heterodyne signals. They also require considerable electronic instrumentation to operate.

Heterodyne signals of lower frequencies, about 150 Hz, can be generated by a system of properly arranged polarizers, retarding plates, and a Wollaston prism. Such a signal generator would be more suited to a laboratory environment.

3.5.3.3 Signal Detection and Processing System

3.5.3.3.1 Light Levels - Experimental measurements have shown that 50 mW of HeNe laser power illuminating a matte aluminum surface, generates on the order of 2 mW/cm² at a distance of 180 mm. This is sufficient energy for convenient exposures of a variety of photo-sensitive materials. For example, solid state detectors are available that give high signal-to-noise ratios when exposed to nanowatts of irradiance. Sufficient light energy can be produced at the output plane of a heterodyne optical strain sensor, therefore, to allow high-precision phase measurements.

3.5.3.3.2 Static Strain - Static strain on the object surface will be directly proportional to the difference in phase of the heterodyne signals detected by the two photodiodes indicated in figure 16. This phase difference may be obtained by direct evaluation of the two signals by an electronic phase meter. Commercially available instruments usually operate by amplifying the two input signals and hard limiting them to convert them to square waves. The elapsed time is measured between the leading edge of one square wave and the leading edge of the other, and this is then divided by the time period of one cycle. This measurement may be averaged over a number of cycles to improve accuracy. Strain may be obtained by multiplying this phase difference by an appropriate scale factor, corresponding to the geometric parameters of the system used.

If it is assumed that ϕ is the phase difference (in degrees) measured between the two signals, then d is the separation of the two illuminated points on the object surface, and θ is the angle between the surface normal and the directions in which the transform fields are sampled, then the surface strain ϵ , would be given by the equation:

$$\epsilon = [\lambda / (d \sin \theta)] \phi / 360 \quad (1)$$

where λ is the wavelength of light and ϵ is the surface strain. Figure 17 shows a plot of spot separation, σ (gage length), versus θ , the half-angle subtended by patterns that fall on the detectors. The range of measurement is determined by the illuminated spot sizes, and two factors compete in this choice. For the range of strain measurement, the displacement of the object surface under one illuminated spot should not exceed 1/5 of the spot diameter. Thus, the range may be estimated as:

$$\epsilon_{\max} = S/5d,$$

where ϵ_{\max} is the maximum strain, S is the spot diameter, and d is the gage length. If the illuminated spots are 0.1 mm in diameter, $\epsilon_{\max} = 20,000$ microstrain/mm gage length. Rotations, however, will shift the speckle patterns that fall on the detectors, and these must not move by more than 1/5 of a characteristic speckle diameter (S). Thus, the maximum rotation allowed would be on the order of:

$$\sigma_{\max} = \lambda/5S,$$

where σ is the rotation of the object surface. With illuminated spots of 0.1 mm, $\sigma_{\max} = 1,200$ microradians, independent of gage length. In designing a practical system, some range in strain measurement would probably be sacrificed to obtain less sensitivity to rotations by the choice of a smaller illumination spot.

3.5.3.4 Limitations of the Method: The foremost limitation on the real time optical strain sensor is that the spots illuminated would have to remain under the illuminating beams during the entire cycle of measurement. This limitation is in a way analogous to the requirement for proper bonding of a resistive strain gage. In addition, the surface under measurement would have to retain its integrity of microstructure during the measurement; i.e., little, if any, erosion or build-up of dirt can be tolerated. Finally, any phase changes in the transparent medium between the sensor and the surface would be tolerated only if they were homogeneous, or if their inhomogeneities were random functions of time. If a strain distribution were required, the loading would have to be repeated for each positioning of the strain sensor.

3.6 Surface Acoustic Wave/Acoustic Guided Wave Concepts

3.6.1 Sensor Approach. - The sensing of physical variables such as pressure and temperature using acoustic wave phenomena has been successfully demonstrated in prior work. The Surface Acoustic Wave (SAW) pressure sensor, for example, relies on the SAW velocity change produced when a pressure differential is applied across a thin diaphragm. Since a SAW delay line is fabricated directly on the diaphragm, the resulting change in SAW phase delay provides a precise indication of the applied pressure. The phase change is translated into a frequency change by using the SAW delay line to control the frequency of a simple oscillator circuit.

The approach considered for strain sensing is similar to that of the SAW pressure sensor. A strain-induced change in acoustic propagation velocity, or time delay, would be utilized to directly control an oscillator frequency. However, unlike the SAW sensor, the harsh surface environment for the present application prohibits the use of an acoustic wave which propagates at an exposed surface. As surface contaminants build up over a period of time, they would not only produce a time varying change in SAW time delay greater than the strain-induced effect, but would also tend to attenuate the SAW. In order to avoid effects caused by surface contaminants, another form of acoustic wave must be utilized; one which would propagate within the interior of the film coating.

One such wave is the Stonely Wave which propagates at the interface between two semi-infinite media (refs. 57 through 60), as shown in figure 18a. These waves have been found to exist for only 30 out of 900 combinations of materials which satisfy certain density and stiffness requirements. Another form of AGW, which will be termed a Modified Stonely Wave, may also exist for a wider range of materials if a three layer media is considered as shown in figure 18b. The existence of this wave would require that the central layer have an acoustic velocity lower than that of the adjoining layers. While the existence of either of the above AGW types may be satisfied by materials appropriate to the present application, proof of existence has yet to be achieved.

In addition to the above restrictions, related to acoustic wave propagation, the constituent materials forming a composite coating would have to satisfy the following additional requirements:

- 1) Temperature stability to 1150 K,
- 2) Correct piezoelectric polycrystalline film orientation to medium 1,

- 3) Resistance to surface attack by ambient contaminants,
- 4) Smooth surface quality allowing the photolithographic fabrication of interdigital transducer electrodes at the interface.

3.6.2 Discussion. - The thickness of mediums 1 and 2 of figure 18a must exceed the acoustic wavelength in order to avoid surface contaminant effects for medium 1 and shorting out of the transducers by the underlying metal base for medium 2. Medium film thicknesses are therefore determined by the resolution achievable in fabricating the interdigital transducer electrodes. If the linewidth resolution is limited to 7 μm , then the acoustic wavelength of 30 μm would require films at least that thick and preferably thicker. If an acoustic wave velocity near 6×10^5 cm/sec is assumed, then an operating frequency near 200 MHz would result.

The material combination which has the highest probability for satisfying the above requirements is the aluminum nitride (medium 1)/aluminum oxide (medium 2) system. Piezoelectric AlN films, 2 microns thick, have been previously sputter deposited at UTRC in single crystal form on single crystal Al_2O_3 substrates for SAW device applications (ref. 61). The AlN is deposited at a temperature near 1523 K and is relatively impervious to chemical attack.

Since depositing the AlN films referenced above, UTRC has designed (under IR&D), a new planar magnetron sputtering cathode. This apparatus has enabled material to be deposited several times faster than with a conventional sputtering cathode. Not only does the planar magnetron have an enhanced deposition rate, but, because of the presence of strong magnetic fields, secondary electron bombardment to the substrate is greatly reduced. High secondary electron bombardment had degraded the quality of the crystal being grown. With the use of the planar magnetron, it is felt that high quality piezoelectric aluminum nitride layers 30 μm or more thick could be grown by sputtering in a reasonable amount of time.

The modified Stonely Wave system shown in figure 18b might be formed using the same techniques as described above. The piezoelectric AlN medium 1 and the Al_2O_3 medium 2 could both be deposited using the planar magnetron sputtering source. The intermediate layer medium 2, either SiO_2 or a metal film having a slower acoustic wave velocity, could also be deposited using the planar magnetron sputtering cathode. This intermediate layer would be deposited between the interdigital transducers, and would be the same material as the transducer electrodes.

For the combustor liner application considered in this program, the intermediate layer medium 3 would have to be a high temperature metal to satisfy the environmental requirements. The deposition of such metal films onto insulating Al_2O_3 layers is a well established procedure. However, the

growth of oriented piezoelectric aluminum nitride films on metal layers is not as well established.

The United Technologies Research Center has had considerable success in growing oriented piezoelectric zinc oxide films on metal electrodes. The procedure used has been to first grow a thin (600 Å) layer of titanium, followed immediately by a thicker (1500 Å) layer of gold. This combination has provided a well adhered oriented metal on which oriented ZnO can be grown. The titanium layer has a dual purpose. First, since it is a highly reactive metal, it adheres very well to oxide and other surfaces to form a good bond to the substrate. Second, it has a hexagonal structure which causes it to grow with its basal plane parallel to the substrate, i.e., in the (0001) direction. However, because titanium is a very reactive metal, it quickly forms an oxide layer when exposed to the atmosphere, therefore a thick gold layer is applied over the titanium to prevent the oxide from forming and to assure good electrical conductivity. Under the proper growing conditions, the crystalline orientation of the gold layer will follow the 3-fold symmetry of the underlying titanium layer and the gold will grow oriented in the (111) direction. The oriented gold provides a suitable substrate on which to subsequently grow oriented ZnO.

The growing of single crystal aluminum nitride requires a substrate temperature of 1520 K and ammonia as the sputtering gas. Zinc oxide, on the other hand, requires a substrate temperature of only 620 K and a 20 percent oxygen doped argon sputtering gas. Since titanium diffuses rapidly in gold and forms an intermetallic at approximately 770 K, it is doubtful if this metallization system will work with AlN. Platinum has been used as a diffusion barrier between titanium and gold. It is conceivable that platinum could be used in place of gold on which to grow AlN. Like gold, platinum has a face centered cubic structure, so that it is likely that platinum will follow the orientation of the underlying titanium and grow oriented in the (111) direction.

Other metals which have a hexagonal structure themselves would also be candidates for electrode materials. Osmium, ruthenium and rhenium all have melting points above 2700 K and have a hexagonal structure. These metals do not form stable high temperature oxides or nitrides, and should be acceptable as a surface on which to grow the AlN layer, without danger of surface oxidation during processing. However, they may not be adherent enough to the Al_2O_3 substrate. As a result, it may still be necessary to deposit an underlying adherent layer like titanium to assure adequate bonding of the electrodes and subsequently deposited AlN.

Oriented films of AlN have been successfully deposited on gold-film substrates by rf reactive planar magnetron sputtering (ref. 62) at temperatures from 320 K to 770 K. These films have c-axis oriented properties

similar to zinc oxide on similar substrates. Surface acoustic waves have been generated within these AlN films, though at much lower frequencies and of much poorer quality than such waves in films grown at UTRC. The technology for such a Modified Stonely Wave does appear to exist, although further development is needed.

In summary, potential candidate metals including osmium, ruthenium, and rhenium have been identified for use as an intermediate layer for providing acoustic wave guiding between Al_2O_3 and AlN. This metal layer would also serve as the material for fabricating acoustic wave interdigital transducers. All candidate metals and metal combinations have been chosen for their ability to withstand high temperature and their tendency for providing the desired 3-fold crystal symmetry for oriented piezoelectric AlN film growth. Process development would be required to optimize the Al_2O_3 , AlN, and metal film surface smoothness and crystalline orientation. This development would include optimization of the sputter deposition conditions such as pressure, temperature, rate, etc. The optimum metallization system would also have to be determined experimentally.

3.6.3 Acoustic Guided Wave Stress Sensor. - The acoustic guided wave shown in figure 18b, as well as a stress sensor based upon this Modified Stonely Wave, as illustrated in figure 19, remained unproven concepts after the analysis undertaken in this program. While computer-based analytical programs to determine the existence and characteristics of surface acoustic waves in various material combinations are available, they are quite costly to run and would still require experimental verification of the actual parameters.

The simpler method of determining the existence of a Modified Stonely Wave and its characteristics for the materials proposed as a strain sensor would be the fabrication and experimental testing of a three-layer AGW medium similar to that shown in figure 18b. The funding and scope of the Advanced High Temperature Static Strain Sensor program precludes the implementation of such an experimental effort in this contract program.

3.7 Summary and Recommended Candidates

An examination has been made of the state-of-the-art of static strain sensor technology which has included analyses of a number of sensor types and concepts, encompassing the general sensor areas of:

- Wire resistive sensors,
- Thin film resistive sensors,
- Capacitive sensors,
- Optical sensors, and
- Acoustic wave device sensors.

The primary considerations used in the analysis were:

- Measurement accuracy,
- Reproducibility over several thermal cycles,
- Survivability,
- Minimum perturbation of surface stress, and
- Minimum perturbation of normal gas flow.

The "Design and Environmental Guidelines", Exhibit B of the RFP3-188132, served as criteria for a selection process in the form of the "Evaluation Matrix" presented in Table 3.7.1. The "Evaluation Matrix" is set up as follows:

The decision criteria listed at the left of the table were subdivided into: "Parameter" and "Goal". The maximum temperature, maximum strain, accuracy, and sensor size and thickness were considered absolute requirements. The remaining goals were considered as desirable objectives.

Several values were provided for the evaluation process:

- HI: Will satisfy or has high probability of satisfying the particular parameter and goal. Some testing may be required.
- MOD: Has moderate probability of satisfying the particular parameter and goal. Testing is definitely required to verify.
- LO: Will not satisfy or has low probability of satisfying the particular parameter and goal value.

One of these values was assigned to each parameter for each sensor type. A value of "LO" in any of the absolute requirements eliminated the candidate from further consideration. In the desirable objectives portion of the matrix, HI, MOD, and LO carried respectively decreasing values, and in general more than two values of "LO" eliminated that particular candidate.

Beyond this point the elimination process relied on the general thrust of the program toward promising novel concepts and on the practical limits imposed by program funding. There was a certain redundancy in consideration of the two thin film alloys and wire gages of the same alloys. The thin film gages approach, being more novel, was chosen.

As a result of this analysis, the recommendation was made that the following devices be considered for the preliminary evaluation program:

- FeCrAl wire,
- Pt20W and Pd30Mo thin film,
- Capacitive Sensor concept C (fig. 16)
- Hinged Reflector, and
- Optical Strain Sensor (Section 3.5.2)

It was anticipated that the work with the Kanthal wire would be fairly straightforward and would require minimum effort. Contact with Ailtech indicated that this firm might also have a potential candidate, and, if possible, this device might be worked into the preliminary evaluation program. Standard commercially available capacitive devices did not meet size or temperature requirements. Our limited analysis showed that it should be possible to construct small capacitive devices with sufficient sensitivity to produce a reliable sensor. The optical techniques appeared very promising, and their apparent simplicity made them attractive candidates.

The only area where the state-of-the-art had not progressed sufficiently to consider for this application was in the acoustic wave devices. It was felt that this was a very promising technique and with a corporate IR&D development program in progress, a separately funded development program might be appropriate.

ORIGINAL PAGE IS
OF POOR QUALITY

TABLE 3.7.1. - EVALUATION MATRIX

ORIGINAL PAGE IS
OF POOR QUALITY

ORIGINAL PAGE
OF POOR QUALITY

SENSOR TYPES		WIRE RESISTANCE GAGES			THIN FILM RESISTIVE GAGES		CAPACITIVE DEVICES		FIBER OPTIC CONCEPTS							HOLOGRAPHIC AND SPECKLE TECHNIQUES										SAW/AGW DEVICES	
PARAMETER	GOAL	KANTHAL WIRE	P138 W WIRE	P138Mo WIRE	P120W THIN FILM	P138Mo THIN FILM	A	B	GRATING EXPANSION	PULSE TIMING	OPTICAL COUPLING	FIBER MACH ZENDER INT.	FIBER BENDING LOSSES	VIBRATING DRUMHEAD	HINGED REFLECTOR	MOIRE METHODS	HOLO - GRAPHIC TECHNIQUES	FRINGE LOCALIZATION	FRINGE PARALLAX	SPECKLE INTERFEROMETRY	SPECKLE PHOTOGRAPHY	OPTICAL STRAIN SENSOR	METRIC - DYNAMIC STR. SENSOR	AGW STRAIN SENSOR			
MAXIMUM TEMPERATURE	1150 K	HI	HI	HI	HI	HI	MOD	MOD	MOD	MOD	LO	LO	LO	MOD	HI							HI	HI	MOD			
STRAIN AT MAX. TEMP.	2000µε	HI	MOD	MOD	MOD	MOD	LO	MOD	MOD	MOD	MOD	MOD	MOD	LO	HI							HI	HI	HI			
ACCURACY	± 200µε	MOD	MOD	MOD	MOD	MOD	LO	MOD	HI	LO	MOD	MOD	MOD	LO	HI							HI	HI	MOD			
SENSOR SIZE	12mm x 12mm	HI	HI	HI	HI	HI	HI	HI	HI	HI	LO	MOD	MOD	MOD	HI							HI	HI	HI			
SENSOR THICKNESS	≥ 1.5mm	HI	HI	HI	HI	HI	HI	MOD	HI	HI	LO	MOD	MOD	MOD	MOD							HI	HI	HI			
COMPATIBILITY w/HAZARDOUS	—	HI	MOD	MOD	MOD	MOD	HI	HI	MOD	MOD	MOD	MOD	MOD	MOD	HI							HI	HI	MOD			
PRESSURE	10, 20, 40 SIN	HI	HI	HI	HI	HI	HI	HI	HI	HI	MOD	LO	LO	MOD	HI	LACK OF ACCURACY						LO	LO	MOD			
FLOW	≤ MACH 0.1	HI	HI	HI	HI	HI	HI	MOD	MOD	MOD	MOD	MOD	MOD	LO	MOD							LO	LO	MOD			
THERMAL CYCLES	100 1HR @ MAX T	MOD	MOD	MOD	MOD	MOD	MOD	MOD	MOD	MOD	LO	LO	LO	MOD	HI	LARGE RAD. LENGTH						MOD	MOD	MOD			
STEADY STATE THERMAL	8 HR.	MOD	MOD	MOD	MOD	MOD	MOD	MOD	MOD	MOD	LO	LO	LO	MOD	HI	NUMERATIVE DATA EXTRACTION						MOD	MOD	MOD			
VIBRATION	10g AT 0.1-0.5 KHZ	MOD	MOD	MOD	MOD	MOD	MOD	MOD	MOD	MOD	MOD	LO	MOD	LO	MOD							LO	MOD	MOD			
SENSOR MOUNTING	ON LINER	HI	HI	HI	HI	HI	HI	HI	E	E	E	E	E	E	E							E	E	HI			
LEVEL OF DEVELOPMENT	—	HI	MOD	MOD	MOD	MOD	LO	LO	LO	MOD	LO	LO	LO	LO	MOD	DIFFICULT SIGNAL PROCESSING						MOD	LO	LO			
GAGE FACTOR*	OPTIMUM	MOD	MOD	MOD	MOD	MOD	LO	MOD	HI	HI	HI	HI	MOD	LO	HI	PROBLEMS WITH SURFER SURFACES						HI	HI	HI			
ADHESION	OPTIMUM	MOD	MOD	MOD	MOD	MOD	HI	HI	MOD	MOD	MOD	MOD	MOD	MOD	MOD							HI	HI	MOD			
CORROSION	OPTIMUM	MOD	MOD	MOD	MOD	MOD	LO	MOD	LO	LO	MOD	MOD	MOD	LO	MOD							LO	MOD	MOD			
EROSION	OPTIMUM	MOD	MOD	MOD	MOD	MOD	LO	MOD	LO	LO	LO	LO	LO	LO	MOD							LO	MOD	LO			
FATIGUE	OPTIMUM	MOD	MOD	MOD	MOD	MOD	MOD	MOD	MOD	MOD	LO	LO	LO	LO	MOD							HI	HI	MOD			
LEADWIRE ATTACHMENT	OPTIMUM	MOD	MOD	MOD	MOD	MOD	MOD	MOD	MOD	MOD	MOD	MOD	MOD	MOD	MOD							MOD	MOD	MOD			

SYMBOLS
 HI WILL MEET OR HAS A HIGH PROBABILITY OF MEETING REQUIREMENTS; MORE TESTING REQUIRED
 MOD HAS A MODERATE PROBABILITY OF SATISFYING REQUIREMENTS; MORE TESTING REQUIRED
 LO WILL NOT MEET OR HAS A LOW PROBABILITY OF SATISFYING REQUIREMENTS
 E PROBE HEAD REMOTE FROM LINER MOUNTED ELEMENT
 * STRAIN SENSITIVITY FOR NON-RESISTIVE DEVICES

2 FOLDOUT FRAME

3 FOLDOUT F.

1 FOLDOUT FRAME

PRECEDING PAGE UNK NOT FILMED

4.0 PRELIMINARY EVALUATION PROGRAMS AND REVIEW (TASKS 2 AND 3)

A part of each of the analytical investigations of the different approaches examined in Task 1 involved suggestions for further experimental evaluations. These were discussed along with the results of these preliminary analyses at the NASA review meeting which constituted Task 2 of the program. Three candidate approaches were selected for additional experimental evaluation.

1. Wire Resistance Sensor
2. Optical Speckle Technique
3. Capacitive Sensor

It was also indicated at the review meeting that the Surface Acoustic Wave approach was also worthy of additional effort, but not within this program.

Discussions were held during the presentation of optical methods for strain measurement to NASA personnel that dictated a change in approach to optical methods for strain measurement. A primary assumption was made during the analysis phase of this contract that the techniques involved must operate in real time and provide nearly instantaneous strain data on the test surface. Based upon this assumption, photogrammetric methods were devalued as potential candidates for development under this contract.

Discussions with NASA personnel made it apparent that geometrical distributions of strain were more important than real-time operation. Consequently, techniques that offered the potential for area analysis were to be rated higher than techniques that allowed only pointwise measurement. A cooperative program between UTRC and P&W had been carried out concurrently with this contract that demonstrated a new technique for strain measurement using singly-exposed speckle photographs and a heterodyne photogrammetric comparator. The decision was made to change from the optical strain sensor approach described in the analysis section of this report to the method of speckle photogrammetry described hereafter.

The Preliminary Evaluation Program adopted for the Wire Resistor Sensor consisted of laboratory testing of FeCrAl (Kanthal A-1) wire strain gages. Thermal and mechanical tests on lead wires and on complete strain gage systems were to be performed to determine lead and splice durability, apparent strain, drift and gage factors at temperatures up to 1150 K and strain levels to $\pm 2,000$ microstrains. Previous work at United Technologies had been limited to 950 K. Specimen fabrication, drift testing, leadwire evaluations and some of the effects of thermal cycling on apparent strain were to be performed by

the P&W Commercial Products Division (CPD) Instrument Group. The other mechanical testing work was to be done at the United Technologies Research Center.

The Preliminary Evaluation Program for the optical speckle technique was to use dual photographs of laser speckle patterns (before and after strain) and also to include a halo heterodyne readout system in a new configuration which would include provisions for the independent adjustment of the system parameters so that the sources of systematic error could be determined. Also, a telecentric lens system was to be designed and then built (at Corporate expense). This was to be used to demonstrate the use of this technique to measure strains at room temperatures from zero to 1,000 microstrains. Finally, the ability of the laser system to sense and record the appropriate halo interference patterns on Hastelloy X at elevated temperatures was to be demonstrated.

As a result of the program review and subsequent discussions, the capacitive sensor approach described in Section 3.3 was revised to consist of plans to fabricate by sputtering a capacitive plate system in which one of the plates lay parallel to the substrate surface but was raised slightly above that surface. Strain in the substrate would then result in the "free standing" plate moving closer or further away from the substrate resulting in a change in capacitance. This approach was more consistent with the thin film technology available for preparing sputtered coatings and would result in a sensor system less sensitive to surface contamination. After fabrication, these sensors were to be used to demonstrate the measurement of surface strains at ambient temperatures to $\pm 2,000$ microstrains.

5.0 PRELIMINARY EXPERIMENTAL EVALUATIONS

5.1 FeCrAl[†] Resistance Wire Gages (Task 4)

5.1.1 Test Description

5.1.1.1 Overview: The testing program was separated into three parts: 1) thermal and mechanical testing of lead wires, 2) thermal cycle testing of complete systems and measurements of apparent strain, and 3) mechanical testing of complete strain gage systems (including lead wires) at various temperatures. Parts 1 and 2 were performed by the P&WA Instrument Group (H. P. Grant). Part 3 was performed by the United Technologies Research Center Materials Testing Group (C. O. Hulse). Two test bars, each with three lead wire installations were fabricated for lead wire testing. Four test bars with four strain gages each were fabricated for the testing of complete strain gage systems. The substrate materials were all Hastelloy X.

5.1.1.2 Lead Wire Testing: The lead wire testing consisted of measuring with an ohmmeter the loop resistance of the lead circuits during:

- A. Ten thermal cycles to 1150 K.
- B. Ten strain cycles at 1150 K at each of the following approximate strain levels: ± 800 , ± 1400 , and ± 2000 microstrain.

The resolution of the ohmmeter was $.1 \Omega$ and the measurements were intended only to show gross changes and open circuits.

The Hastelloy X test bars for lead wire testing were 19.6 cm long (7.6 cm active length mounted in the test fixture), 3.5 cm wide and .65 cm thick. Bending loads were applied using a Budd cantilever bending beam fatigue machine as a means of deflecting the beam to a constant static strain level. The machine utilized a small Marshall furnace for elevated temperature testing.

Strain levels were substantiated at room temperature using commercial strain gages (estimated uncertainty of $\pm 5\%$ based on previous experience). Strain levels at elevated temperature were established by applying the same bar deflections as those at room temperature. For further discussion of the strain levels attained at high temperatures see Section 5.1.5, "High Temperature Strain Verification".

[†]The FeCrAl Alloy used throughout was Kanthal A-1, Kanthal Corp., Bethel, CT. Vendor specified composition in wt %: Fe-72.5, Cr-22.0, Al-5.0, Co-0.5.

5.1.1.3 Strain Gage Testing: Four bars were instrumented with four strain gages each which were all located on the same face of the bar. Testing consisted of:

- A. Measuring (recording on strip chart) apparent strain during 5 rapid cooling cycles from 1150 K.
- B. Measuring drift (change in no load output with time) during 48 hours at 1150 K.
- C. Measuring the gage factor at 290, 920, 1030 and 1150 K. A minimum of 4 strain cycles were to be run at each temperature.

Testing in four-point bending was the approach selected by the Research Center to examine the behavior of FeCrAl wire resistance strain gages under load at various temperatures. A discussion of the reasons for this decision, together with some experimental verifications of the assumptions required to properly determine strain in this mode of testing, are included in Section 5.1.4.2, High Temperature Strain Verification.

Strain calculated from deflection measurements were compared strains measured with commercial strain gages at room temperature. The differences were less than 4 percent.

5.1.1.4 Post-Test Inspection: To obtain a better understanding of the yield characteristics of the bar in the test setup, the permanent deflection of the bar for each strain cycle was measured to determine the amount of inelastic strain which had occurred.

Each lead wire and strain gage was subjected to a post-test, microscopic examination to determine where possible the location and mode of any distress or failure.

5.1.2 Samples and Test Fixtures. - Two test bars were prepared for lead wire testing using the layout shown in figure 20. Both bars used a bond coat of flame-sprayed Metco 443 (NiCrAl) and a precoat of Rokide H (Al_2O_3). On each bar, three lead wire loops of 0.76 mm diameter chromel wire were installed as shown in figure 20 with a Sermetel P-1 ceramic cement overcoat (cured 1 hr. at 620 K). Two extension cables of three-conductor Ni-clad Cu were strap welded to each bar. The diameter of the Ni-clad copper conductors was (.25 mm) and the sheath diameter was 1.5 mm. The cable sheath material was AISI 304 stainless steel with MgO insulation inside. The total length of the sheathed cable 46 cm.

The splices on the first specimen were brazed with gold braze filler AWS type B Au-4 (AMS 4787, 82% Au/18% Ni, 1223 K eutectic temperature). The splices on the second specimen were brazed with nickel braze filler AWS BNi-7 (Microbraz 50, 77% Ni/13% Cr/10% P, 1160 K eutectic temperature). The splices were overcoated with GA-100 ceramic cement (cured 1 hr. 620 K). The typical loop resistance was about 15 ohms including the long sheathed cable and 14 ohms in the Chromel portion alone. The ends of the sheathed cable on the first specimen were sealed with Cerama-Dip 538 (cured 1 hr at 300 K, then 3 hrs at 355 K) and Aremco-Seal 529 (cured 1 hr at 300 K, 1 hr. 450 K) and those on the second specimen with Cerama-Dip 538 only.

All four test bars were prepared for testing of complete strain gage systems using the strain gage arrangement shown in figure 21. For gage factor testing, the test bars were mounted in a four-point bending fixture (fig. 22). The layout of the strain gages on each test bar is shown in figures 23 and 24. Comparisons of the behavior of the same strain gage in tension and in compression were obtained by turning the samples over and bending them in the opposite sense. In order to avoid any possibility that these lead wires might be loosened by twisting forces, the lead wires were positioned with sufficient length on the sample to contain a 90° turn. Spot welded straps across sections of the lead wires running at 90° to each other were used to eliminate the possibility that a twist force around the axis of a lead wire could be transmitted to the junction between the strain gages and the leads. In order to have a sufficient area for the lead wire attachment plan just described, the two upper loading pins, each included two slots. The lead wires passed through these slots and exited from the side surfaces of the sample outboard of these loading pins when the strain gages were on the compression surface of the sample. The strain gages were fabricated from .025 mm diameter FeCrAl alloy wire. An overcoat of Sermetel P-1 was used on bars 1 and 2 and an overcoat of Rokide H on bars 3 and 4. The Ni-clad Cu sheathed extension cable was end sealed with Cerama-Dip 538. The splices were brazed with AWS BNi-7 (Microbraz 50), which was obtained in powder form and mixed with AWS 3A flux to form a paste in approximately equal parts by volume. The brazing was done in air using a miniature hydrogen/oxygen torch.

5.1.3 Results of Lead Wire Tests. - Prior to any strain gage system testing, lead wire testing was conducted to determine whether the proposed lead systems could withstand the strain and temperature environments (2000 microstrains and 1150 K). Testing was conducted on the two differently instrumented Hastelloy X bars each having three lead wire loop installations.

On the first bar, all three installations failed (open circuits) after six cycles at 800 microstrain. On the second bar, all installations

successfully completed 10 thermal cycles to 1150 K and 10 strain cycles at 1150 K at each of the following strain levels: ± 800 , ± 1400 and ± 2000 microstrain (about 20 hours of total test time).

After thermal cycle testing of the first bar, both the room temperature loop resistance and the 1150 K loop resistance had increased slightly as follows:

<u>Test</u>	<u>Temperature</u>	<u>ΔR</u> <u>Circuit 1</u>	<u>ΔR</u> <u>Circuit 2</u>	<u>ΔR</u> <u>Circuit 3</u>
Thermal	295 K	+ 1.3 Ω	+ 1.0 Ω	+ 2.2 Ω
	1150 K	+ 2.3	+ 2.0	+ 1.7

After heat up to 1170 K in preparation for strain testing, the loop resistances had increased dramatically:

1170 K	164 Ω	112 Ω	165 Ω
--------	--------------	--------------	--------------

After six strain cycles to 800 microstrain (tension) all loop resistances were infinite. After strain cycle and thermal cycle testing of the second bar, the room temperature loop resistance had decreased slightly but the 1150 K resistance had increased in most cases:

<u>Test</u>	<u>Temperature</u>	<u>ΔR</u> <u>Circuit 1</u>	<u>ΔR</u> <u>Circuit 2</u>	<u>ΔR</u> <u>Circuit 3</u>
Strain	295 K	- 1.0 Ω	- 1.0 Ω	- 2.3 Ω
	1150 K	+ .4	+ .4	- .6
Thermal	295 K	- .1	- .2	- .1
	1150 K	+ .7	+ .6	+ .9

Splices on both bars showed some oxidation, but were still mechanically sound. The electrical open circuits on bar #1 were at or near the splice. It is not known why the open circuit occurred on bar #1; it is clear that partial failure occurred during the final heat up before strain was applied (resistance increased to greater than 100 ohms) and final failure occurred during the strain testing. The test results show that the first type of installation is unacceptable and that the second type survived all testing.

5.1.4 Results of Tests of Complete Strain Gage Systems

5.1.4.1 Apparent Strain and Drift Testing: Apparent strain and drift testing at temperatures up to 1150 K was conducted on two of four instrumented Hastelloy X specimens, each with 4 gages. The other two specimens were saved for gage factor testing at UTRC. Apparent strain testing consisted of the measurement of apparent strain during rapid cooling to room temperature from various temperatures over the range of 950 K to 1150 K. Drift testing consisted of the measurement of zero strain output during several hours exposure to each of several temperatures over the range of 950 to 1150 K. The combined test time for the two specimens was about 230 hours.

Testing of the first specimen (#4, Rokide overcoat) was intended to show whether the apparent strain behavior up to 950 K was consistent with previous tests and to learn something about apparent strain behavior up to 1150 K. The results are shown in figure 25 and are also summarized here. More detailed comments are presented later. Apparent strains during a rapid cooling cycle from 950 K, curve A for example, were similar to previous experience: between 3,000 and 7,000 microstrain. For a rapid cooling cycle from 1150 K, however, the apparent strain was much greater than expected: between 10,000 and 18,000 microstrain. In a repeat of the cooling cycle from 950 K it was found that the apparent strain had increased to 10,000 to 14,000 microstrain. During additional 1150 K cooling cycles, the total change in apparent strain during cooling progressively increased to 16,000 to 30,000 microstrains.

Drift testing at 950 K for 10 hours resulted in drift rates of -100 to -200 microstrain per hours. This rate was much higher than the 1 to 5 microstrain per hour drift rates observed for samples early in 1980. Drift testing at 1150 K for 8 hours indicated rates of 100 to several hundred microstrain per hour.

A more detailed examination of the curves shown in figure 25 follows:

The apparent strain during cooling from 950 K (curve A) agreed well with previous results.

After one cycle to a higher temperature (to about 1100 K) the apparent strain upon cooling from 950 K became larger (curve B).

Apparent strain increased and the character changed, including some zero non-return, as the temperature increased (curve C). The drift rate of -97 to -229 microstrain per hour is much greater than the 5 microstrain per hour at

950 K from previous tests. After the 10 hour 950 K drift test, the apparent strain at 1150 K had increased significantly (curves D, E & F). The 1150 K drift test ended after 9 hours because all the gages were opened or had large changes in resistance.

The conclusion from the testing of specimen #4 is that the apparent strain increases and the negative slope at the lower temperatures disappears when the operating temperature was increased from 950 to 1150 K. The drift rate was also higher than expected.

Because of these results, a different test sequence was used in testing of the second specimen (#1, Sermetel P-1 overcoat) to investigate drift and apparent strain at intermediate temperatures between 950 and 1150 K. The test history of specimen #1 is shown in figure 26. Two apparent strain sequences were conducted, the first after a long (44 hr) soak at 950 K and the second after a long (46 hr) soak at 1150 K.

The drift rate at 950 K was high even after 44 hours but it was positive rather than negative. (The drift of specimen #4 had been negative after prior exposure to 1150 K.) After the first exposure to 1150 K, the drift rates at 950, 1030 and 1090 K were reduced.

The final drift test at 1150 K again showed the excessive negative drift rate. The test ended after 20 hours because all the gages opened or had large resistance changes.

The apparent strain of specimen #1 did not increase greatly up to 1150 K (curves A through G) and the negative slope at low temperatures was retained. Later apparent strain tests (curves H through K) at 1090 K showed an increase, but also a closer grouping.

The conclusion from the testing of specimen #1 was that the apparent strain is high but fairly stable and that the drift rate is low at 1190 K. There was no significant difference in the 950 K apparent strain between the Sermetel P-1 and the Rokide H overcoat gages (this was the only temperature at which they could be compared because of their different test histories). The Sermetel P-1 overcoating was the more durable by a factor of 3 or 4. It is not known whether the durability of the gages coated with Rokide H would have been improved by a prestabilization heat treatment. The possible beneficial effects of mechanical strain cycles on durability, drift and apparent strain were also not examined.

5.1.4.2 High Temperature Strain Verification: It was a requirement of this program that the behavior of the strain gages developed be experimentally examined over the strain range of $\pm 2,000$ microstrains ($\pm 0.2\%$) from room

temperatures to 1150 K. This requirement presented some significant testing difficulties because, in general, the optimum test samples for use in compression are quite different from those used in tension.

The approach used to overcome this testing problem was to perform the experimental evaluation in the four-point bending mode. In this case, a uniform state of stress and strain exist at the external surfaces of the sample between the two inner loading pins. The samples needed for this type of testing are simple flat plates, requiring a minimum amount of effort and cost to fabricate. The behavior of the same strain gage in either tension or compression can be evaluated by simply turning the sample over in the test fixture.

While this mode of testing provided significant advantages, it also presented potential difficulties when the evaluation must be done at elevated temperatures. At room temperatures, commercial strain gages could be used as a basis of comparison between the correct values of strain and the strain as measured by the experimental strain gages. At elevated temperatures, however, where commercial gages would not survive, we had to resort to measurements of beam deflections as the input measurements from which to calculate the correct values of strain present at the experimental strain gage.

At 1150 K the elastic modulus of Hastelloy X is 127×10^6 MPa and the 0.2% offset yield strength is only 109×10^3 MPa. If we assumed only elastic behavior, an apparent stress of 253×10^3 MPa would be needed to reach 2,000 microstrain, which is well beyond the above mentioned yield stress. Not only will some plastic yielding occur, but deformations by creep processes will also occur. For example, at 1140 K, Hastelloy X will creep about 0.1% in one hour at a stress of only 27.5×10^3 MPa.

The fact that some plastic yielding would occur during the testing, especially at 1150 K, implied that simple elastic equations should not be used to calculate the strains present at the experimental strain gages at elevated temperatures.

A practical solution to the question of how to measure the strain present at the beam surfaces when some plastic flow has occurred is suggested by reference to figure 27. This figure shows how the stress and strain vary through the beam after a small amount of plastic yielding occurs (ref. 9). When the beam yields, it does so at the surfaces most distant from the neutral axis. The distribution of stress through the beam becomes non-linear and the maximum stresses present at the free surfaces can no longer be

calculated from simple elastic theory. Because of geometrical requirements, however, the distribution of strain through the beam still tends to remain linear. This suggests that the elastic equations used to calculate outer fiber strains in a bent beam should still apply with reasonable accuracy even after some plastic flow has occurred.

In order to examine and demonstrate the validity of the above assumptions prior to the actual testing of our samples with their experimental strain gages, a series of four-point bending experiments were made at room temperature. In these experiments, strains measured by a commercial strain gage located at the center of the lower span were compared to the simultaneously obtained strains calculated using the output of deflection measuring equipment which contacted the sample adjacent to the gage. The term "span" is used to denote the distance between the centers of the pins applying the bending load on either the upper or lower surface of the sample. The deflection strain was calculated using the following elastic equation valid when the lower span is twice the upper span:

$$\epsilon = \frac{192h(\Delta y)}{44S^2} \quad (1)$$

where ϵ = lengthwise strain on surfaces within the upper (smaller) span
 h = thickness of bar sample
 S = lower (bottom) span
 (Δy) = deflection at center of lower span.

The samples used in these experiments were 6061-T6 aluminum. Aluminum was selected as a test material because it would show some plastic flow in the strain range of interest at room temperatures. The dimensions of the sample were also close to those of the samples already selected for use in this program with the exception that a range of thicknesses were examined -- .82, .163 and .318 mm. Samples of different thickness were examined because the shear stresses present at the ends of the beam in four-point bending compared with the maximum tensile or compressive stresses present at the beam surfaces at mid-span, vary with the span to thickness ratio as:

$$\frac{\sigma}{\tau} = \frac{3}{2} \frac{S}{h} \quad (2)$$

where σ = outer fiber normal stress
 τ = shear stress
 S = lower span
 h = thickness of bar sample

The upper and lower spans used were 36 mm and 72 mm respectively, the same as those selected for use in the rest of this program.

Examples of some of the experimental results from these bending experiments are presented in figures 28 and 29. These figures compare the strains measured by commercial strain gages with the strains calculated from deflection measurements using the above equation. The data indicate that the equations for elastic behavior can be used to fairly accurately estimate the correct values of strain even when some plastic flow has occurred. The limits of purely elastic behavior for a number of the different aluminum test samples examined is also shown in these plots. The data also indicated that any plastic flow due to the shear stresses developed at the ends of the bend samples did not affect in any significant way the measurement of strain calculated from beam deflections.

5.1.4.3 Gage Factor and Strain Testing Results: Four-point bend tests of instrumented Hastelloy X test specimens were made to establish gage factor and performance characteristics of the FeCrAl wire gages. Gages were tested under a variety of loads and temperatures up to ± 2000 microstrain and 1150 K, respectively. Gages overcoated with Sermetel P-1 ceramic cement showed better performance than did gages overcoated with flame-sprayed Rokide H.

Specifications for the two samples subjected to four-point bend tests, are presented below:

<u>Sample</u>	<u>Test Gages</u>	<u>Surface Prep</u>	<u>Precoat/Insulation</u>	<u>Overcoat</u>
#2	5, 6, 7, 8	Metco 443	Rokide H	Sermetel P-1
#3	9, 10, 11, 12	Metco 443	Rokide H	Rokide H

The Metco 443 and Rokide H layers were applied via flame-spraying, while the Sermetel P-1 cement was applied with a brush.

During the testing of the first sample, #3, the sheathed connector wires were bent down along the lower loading ram, to exit below the furnace. When the sample was turned over to change the direction of strain, it was

convenient to reverse the bend in these connectors so that they again came out of the bottom of the furnace. The sequence of tests was arranged to minimize the number of times this bending would be required. In testing the second sample, #2, the three-piece split furnace was wired together so that it was slightly open. This permitted these connectors to be brought out from the furnace in the horizontal plane so that only a small amount of rebending was required when the samples were turned over. No significant differences in results were noted between these two different procedures.

The deflection of the bend sample in the test apparatus was determined by the use of an LVDT transducer system attached to the two loading rams just where they exited the furnace. After simplification, the elastic equation for the outer fiber strain in four-point flexure reduces to:

$$\epsilon = \frac{6 h y_a}{S^2} \quad (3)$$

where ϵ = strain
h = sample thickness
 y_a = relative vertical motion between upper and lower loading pins
S = lower span

Note that in this equation, y_a is the relative movement of the loading pins, not the mid-span deflection.

In order to determine the motions due only to the deflection of the sample, it was necessary to make separate preliminary calibration runs at each test temperature to determine the contributions to the data due to the compliance of the apparatus (loading rams and fixtures). In these pretest runs, a one-half inch thick block of alumina was substituted for the sample and "stress-strain" curves run up to the appropriate loads. The apparent deflections for these various loads were then subtracted from those observed when an actual test sample was tested. The maximum full load deflection of this block was less than 1×10^{-6} cm at any temperature of interest in this program.

Three x-y plotters were used simultaneously during the testing of an experimental strain gage. One plotter recorded the LVDT sample deflection as a function of the load. The loads were continuously measured by a load cell in line with the axis of the loading columns. The second x-y plotter recorded the output of the commercial strain gage on the sample with a Vishay BAM-1 strain gage conditioner and amplifier box versus the same loads. This output

was used to define the LVDT deflection which corresponded to a strain of $\pm 2,000$ microstrains. The third x-y plotter recorded gage output versus load for an experimental strain gage.

The four test gages on each sample were all connected to a Vishay P-350 switch and balance box. The output of this box was connected to a second Vishay BAM-1 strain gage conditioner and amplifier box which fed the data to the third x-y plotter. All of the gages were individually balanced to zero on the x-y plotter prior to any testing using individual balance knobs on the P-350 box.

The P-350 was also used to select which gage would be tested. The data from only one test gage was recorded each time the sample was loaded. In further work at elevated temperatures, two gages were tested simultaneously, because the commercial gage had been destroyed during the first heating which permitted use of the other BAM-1 on a test gage.

The samples were soaked about 10 to 15 minutes at each test temperature prior to testing in order to obtain thermal equilibrium. All tests were conducted in an argon atmosphere. The rate of loading was selected so that the full load to a deflection corresponding to 2,000 microstrains was reached in about 40 seconds. The sample was immediately unloaded, at the same speed, once this deflection had been obtained.

A summary of test results and the sequence of experiments followed for sample #3 are presented in Table 5.1.4.3-1. The testing began with a series of tests in compression at room temperature. One of the gages failed on its first test. The sample was subsequently turned over and the same tests were done in tension. Tests in tension were next made at 920 K and 1090 K. A second gage was lost in the 1090 K test series. The sample was then soaked for 2 hours at 1090 K under no load and the gages tested again at 1090 K. This soaking apparently had very little effect. The sample was then cooled to 920 K and again tested. The third gage failed at this point in the test series. The sample was then cooled to room temperature, and tested in tension and compression. The test series was finished by tests in compression of the one remaining gage at 920 K and then at 1090 K.

Table 5.1.4.3-1 also contains permanent strain measurements deduced from the deflection data. At these elevated test temperatures, there was evidence of a small amount of plastic yielding. It was felt that this effect was due to plastic flow in the Hastelloy X substrate in general agreement with the available mechanical data for this alloy at these temperatures.

Figure 30 presents a summary plot of all the gage factors measured during the test series on sample #1 as a function of test temperature. The data

TABLE 5.1.4.3-1
STRAIN GAGE TEST RESULTS AND RUN SEQUENCE FOR SAMPLE #3
HASTELLOY-X, ROKIDE H, 0.025 mm DIA FeCrAl, 2000 $\mu\epsilon$

RUN #	GAGE #	TEST TEMP (°K)	TYPE STRAIN	GAGE FACTOR	AVERAGE* G.F.	1-STD. DEV.** OF G.F.	TOTAL ACCUMULATED PERMANENT STRAIN*** (×10 ⁻⁶)
1	9	RT	COMPRESSION	2.800	2.4	0.3	0
2	10	RT	COMPRESSION	2.573			0
3	11	RT	COMPRESSION	GAGE FAILED			0
4	12	RT	COMPRESSION	2.031			0
5	9	RT	TENSION	2.251	2.2	0.4	0
6	10	RT	TENSION	2.549			0
7	11	RT	TENSION	OMIT			0
8	12	RT	TENSION	1.811			0
9	9	1200°K	TENSION	1.933	1.8	0.1	+ 66
10	10	1200°K	TENSION	1.818			+ 66
11	11	1200°K	TENSION	OMIT			+ 66
12	12	1200°K	TENSION	1.564			+ 66
13	9	1500°K	TENSION	1.040	0.9	0.1	+ 123
14	10	1500°K	TENSION	GAGE FAILED			+ 123
15	11	1500°K	TENSION	OMIT			+ 123
16	12	1500°K	TENSION	0.873			+ 123
SOAKED FOR 2 HOURS AT 1500°F, WITH NO LOAD APPLIED							
17	9	1500°K	TENSION	1.116	1.0		+ 123
18	10	1500°K	TENSION	OMIT			+ 123
19	11	1500°K	TENSION	OMIT			+ 123
20	12	1500°K	TENSION	0.882			+ 123
21	9	1200°K	TENSION	2.222	2.2		+ 123
22	10	1200°K	TENSION	OMIT			+ 123
23	11	1200°K	TENSION	OMIT			+ 123
24	12	1200°K	TENSION	GAGE FAILED			+ 123
25	9	RT	TENSION	2.607	2.6		+ 123
26	10	RT	TENSION	OMIT			+ 123
27	11	RT	TENSION	OMIT			+ 123
28	12	RT	TENSION	OMIT			+ 123
29	9	RT	COMPRESSION	2.400	2.4		+ 123
30	10	RT	COMPRESSION	OMIT			+ 123
31	11	RT	COMPRESSION	OMIT			+ 123
32	12	RT	COMPRESSION	OMIT			+ 123
33	9	1200°K	COMPRESSION	1.849	1.8		+ 123
34	10	1200°K	COMPRESSION	OMIT			+ 123
35	11	1200°K	COMPRESSION	OMIT			+ 123
36	12	1200°K	COMPRESSION	OMIT			+ 123
37	9	1500°K	COMPRESSION	1.636	1.6		+ 40
38	10	1500°K	COMPRESSION	OMIT			+ 40
39	11	1500°K	COMPRESSION	OMIT			+ 40
40	12	1500°K	COMPRESSION	OMIT			+ 40

* — G.F.-GAGE FACTOR

** — STANDARD DEVIATION

*** — CALCULATED FROM DEFLECTION MEASUREMENTS USING ELASTIC EQUATIONS

°F = K

RT = 290

1200 = 920

1500 = 1090

indicates a significant decrease in gage factors at 1090 K. Examination of the data also indicates that the gage factor generally tended to increase in proportion to the amount of exposure the gages had had to elevated temperatures.

Table 5.1.4.3-2 summarizes the data of a similar series of tests for sample #2, gages 5, 6, 7 and 8. This sample differed from sample #3 in having an overcoating of Sermetel P-1 instead of Rokide "H". Some data is also included from deflection measurements indicating again that some plastic flow has occurred. In these tests especially, the visual permanent bending of the sample after the elevated temperature testing provided evidence that the Hastelloy-X underwent permanent plastic flow under these conditions of loading. Sample #2 apparently experienced more plastic flow than sample #1 because it was tested to higher temperatures.

Figure 31 is a summary plot of all the gage factor measurements made in the test series on sample #2. The data for sample #2 shows a much more linear decrease of gage factor with temperature and much better behavior at elevated temperatures in terms of gage survival. Again, the data indicates that the gage factors tended to become higher in proportion to the amount of exposure the systems had had to elevated temperatures. At higher temperatures, the ceramic components of the gage system may sinter and develop more strength so that they can transfer strain more effectively to the FeCrAl wires.

Although the pre-curing of strain gages before use, to temperatures slightly above their intended use temperatures, is common practice with lower temperature commercial gages, we did not elect to do this with these gages because of uncertainty about the survivability of the gages. The fact that the gage factors tended to be higher in proportion to the amount of exposure to elevated temperature suggests that the behavior of these gages might have improved had we done so.

The significantly improved behavior observed for the gages overcoated with Sermetal P-1 (specimen #2) instead of Rokide "H" (specimen #3) requires comment:

- (a) The Sermetel is probably more compliant, i.e., has a lower elastic modulus, than the alumina. This means that lower stresses would be seen by the bond between the substrate and the ceramic,
- (b) the strength of the sintered Sermetel ceramic is probably lower than that of the alumina which is formed directly from the molten state so that, again, lower stresses could be transmitted to the bond between the substrate and the coating, and

TABLE 5.1.4.3-2
STRAIN GAGE RESULTS AND RUN SEQUENCE FOR SAMPLE #2
HASTELLOY-X, SERMENTAL P-1, 0.025 mm Dia. FeCrAl

RUN #	GAGE #	TEST TEMP °K	TYPE STRAIN	GAGE FACTOR	AVERAGE* G.F.	1-STD. DEV.** OF G.F.	TOTAL ACCUMULATED PERMANENT STRAIN*** (10 ⁻⁶)
1	5	290	COMPRESSION	2.442	2.5	0.10	0
2	6	290	COMPRESSION	2.720			0
3	7	290	COMPRESSION	2.502			0
4	8	290	COMPRESSION	2.493			0
5	5	290	TENSION	2.365	2.3	0.06	0
6	6	290	TENSION	2.336			0
7	7	290	TENSION	2.340			0
8	8	290	TENSION	2.236			0
9	5	920°K	TENSION	1.360	1.5	0.3	0
10	6	920°K	TENSION	1.956			0
11	7	920°K	TENSION	1.200			0
12	8	920°K	TENSION	1.589			0
13	5	1090°K	TENSION	1.871	1.6	0.6	0
14	6	1090°K	TENSION	1.929			0
15	7	1090°K	TENSION	—			0
16	8	1090°K	TENSION	0.900			0
SOAKED FOR 2 HOURS AT 1090°F, WITH NO LOAD							
17	5	1090°K	TENSION	1.900	1.9	0.05	0
18	6	1090°K	TENSION	1.933			0
19	7	1090°K	TENSION	GAGE FAILED			0
20	8	1090°K	TENSION	1.824			0
21	5	1150°K	TENSION	1.911	1.9	0.1	+ 91
22	6	1150°K	TENSION	2.022			+155
23	7	1150°K	TENSION	OMIT			+155
24	8	1150°K	TENSION	1.796			+215
SOAKED FOR 2 HOURS, AT 1150°F, WITH NO LOAD							
25	5	1150°K	TENSION	1.911	1.9	0.1	+275
26	6	1150°K	TENSION	2.036			+360
27	7	1150°K	TENSION	OMIT			+360
28	8	1150°K	TENSION	1.844			+420
29	5	920°K	TENSION	2.476	2.3		+420
30	6	920°K	TENSION	2.126			+420
31	7	920°K	TENSION	OMIT			+420
32	8	920°K	TENSION	GAGE FAILED			+420
33	5	290	TENSION	GAGE FAILED	2.4		+420
34	6	290	TENSION	2.422			+420
35	7	290	TENSION	OMIT			+420
36	8	290	TENSION	OMIT			+420
37	5	290	COMPRESSION	OMIT	2.2		+420
38	6	290	COMPRESSION	2.169			+420
39	7	290	COMPRESSION	OMIT			+420
40	8	290	COMPRESSION	OMIT			+420
41	5	920°K	COMPRESSION	OMIT	1.9		+420
42	6	920°K	COMPRESSION	1.893			+366
43	7	920°K	COMPRESSION	OMIT			+366
44	8	920°K	COMPRESSION	OMIT			+366
45	5	1090°K	COMPRESSION	OMIT	1.7		+227
46	6	1090°K	COMPRESSION	1.742			+227
47	7	1090°K	COMPRESSION	OMIT			+227
48	8	1090°K	COMPRESSION	OMIT			+227
49	5	1150°K	COMPRESSION	OMIT	1.6		+76
50	6	1150°K	COMPRESSION	1.604			+76
51	7	1150°K	COMPRESSION	OMIT			+76
52	8	1150°K	COMPRESSION	OMIT			+76

* — GAGE FACTOR

** — STANDARD DEVIATION

*** — CALCULATED FROM DEFLECTION MEASUREMENTS USING ELASTIC EQUATIONS

- (c) the thermal expansion of the Sermetel is "probably" higher than that of the alumina. It is probably significant that a number of the gages failed upon cooling. Because the true relationships between the various relevant properties are not known, one cannot properly evaluate these differences or suggest how to optimize the advantages of the properties of the materials which we have.

Figure 32 presents machine traces of gage #6 (specimen #2) recorded at room temperature, 920 K and 1150 K. The outputs appear to vary linearly with load except for some definite indications of plastic flow at the higher loads at the elevated temperature.

The fact that some yielding occurs raises the question of whether this effect is due to yielding of the sample, yielding of the strain gage wire or both. We know from the load/deflections data that the Hastelloy X sample is undergoing some plastic straining at the elevated temperature. We do not know, however, the elastic limits of the FeCrAl gage wires at these temperatures.

In order to further examine the possible effect of this yielding on the accuracy of the strain gages at 2000 microstrains, the load/deflection curve and the load/strain gage output curve for gage #5 at 1150 K are both presented in figure 33. The deflection data is reported here as strain using formula (3) presented earlier in the section. The strain gage output data is also reported as strain using a gage factor of 1.9 where

$$\text{Gage Factor} = \frac{\Delta R/R_0}{\Delta l/l_0} \quad (4)$$

The data from figure 33 has been replotted in figure 34 as the strain determined from deflection versus the strain determined by the strain gage using the load as the transfer function. The slope of this curve is a direct measure of the gage factor. It can be seen that the small amount of yielding which occurred at 2,000 microstrain and 1150 K had little or no effect on the gage factor of this gage.

Data plots prepared in the same way as shown in figures 33 and 34 for the other experimental gages were similar to those presented here for gage #5.

5.1.4.4 Post Test Analysis of Strain Gages: Sixteen experimental gage systems were examined after completion of all preliminary evaluation testing.

Eight of the gages had been subjected to drift and apparent strain testing and the remaining eight to gage factor and performance tests. The specimens were visually inspected under a microscope to note the conditions of the gage systems and system components. Gage resistance was checked with an ohmmeter across selected points, after removing the overcoat layers, to determine locations of electrical failure. Of the 16 tested gages, 3 remained electrically intact.

No open gage element grids were found. Reductions in gage resistances were observed which could have resulted from the oxidation of the Cr and Al, resulting in an alloy closer to pure Fe (lower resistivity), but no compositional analyses were made in order to verify this. Three of the eight gages with the Rokide overcoat had separated from the precoat. None of the eight gages with Sermetel P-1 overcoat had separated from the precoat.

Open circuits were found in the .076 mm Chromel leads of nine gages. In three cases, the break was located where the lead met the braze (possibly weakened by over-heating during brazing). Several leads appeared to be broken at cracks in the GA-100 cement. All braze joints appeared solid and there were no indications of melting or deformation.

Open circuits in the .25 mm Ni-clad copper leads were found on seven gages, between the braze joint and the entrance to the sheath (about 6.3 mm) where bare Ni-clad copper wire was not enclosed in the sheath. Protection is provided by GA-100 ceramic cement on this bare wire. Many appeared to be oxidized in this area.

No open circuits were found inside the sheathed cable. The sheathed cable had been cut from the specimens used in the gage factor tests so that only about 3.3 cm remained. On the other specimens, the full 46 cm length was checked.

Cracking and looseness of the GA-100 cement used to overcoat the leads and splices was found on many leads. One specimen (Gages 1-4) was an exception having very solid and well adhering GA-100. There was no obvious difference in appearance except that the non-cracked GA-100 may have been slightly thinner. Most of the leads were covered by thicker layers of cement than were necessary to cover the splices.

Table 5.1.4.4 presents a summary of the inspection results.

5.1.5 Conclusions and Recommendations for FeCrAl Resistance Gages. - The preliminary lead wire tests showed that the AWS BNi-7 braze material was more durable than the AWS BAu-4 braze. Electrical failures (open circuits) occurred at or near all AWS BAu-4 brazed connections. AWS BNi-7 is reported

TABLE 5.1.4.4. - POST TEST INSPECTION OF FeCrAl SPECIMENS

NO.	OVERCOAT	TESTING	GRID RESISTANCE	% CHANGE	GRID ADHERENCE	3 MIL LEADS	BRAZE JOINT	10 MIL <input type="checkbox"/>	GA-100	GA-100
								LEAD UNDER		
1	Sermetel P-1	Drift & App. ϵ (187 hrs)	115.3 Ω	-6.7%	Good	Good	Good	2 Open	Good	
2			112.8	-9.5%	Good	Good		1 Open		
3			119.5	-6.4%	Good	2 Open		2 Open		
4			*	-	Good	Good		2 Open		
5		Gage Factor	117.4	-3.1%	Good	1 Open Δ		Good	Loose	
6			118.3	-2.6%	Good	Good		Good		
7			117.2	-5.3%	Good	2 Open Δ		1 Open		
8			117.6	-4.2%	Good	2 Open Δ		Good		
9	Rokide H	Gage Factor	118.3	-4.3%	Good	Good		Good		
10			117.6	-4.2%	Good	1 Open		Good		
11			Not Measured	-	Loose	Not Checked		Not Checked		
12			118.9	-4.0%	Loose	2 Open X		Good		
13		Drift & App. ϵ (43 hrs)	103.9	-15.1%	Good	2 Open		Good		
14			108.9	-12.2%	Loose	1 Open		1 Open		
15			107.6	-11.9%	Good	1 Open		Good	Fair	
16			112.4	-9.6%	Good	Good		2 Open		

* Damaged during inspection.

 Δ Broken at braze joint.

X May have been broken during inspection, but looks oxidized.

☐ Checked only to cut off point (about 3.3 cm) on the specimens subjected to gage factor testing: Gages 5 thru 12.

to have better oxidation resistance at 1150 K than AM5 BAu-4 in the braze literature, so that internal oxidation may have contributed to the AWS BAu-4 failures. Recommended practice is to use the AWS BNi-7 braze material. There were no failures of the FeCrAl wire gage grids or lead wire splices, either in the gage element to .076 mm Chromel wire splices, or the .076 mm Chromel wire to .25 mm Ni-clad Cu wire splices. There was no evidence of severe oxidation of the gages or the .076 mm Chromel lead wires. Significant reductions in gage resistance were found: 10 to 15% on the specimen with the longest temperature exposure and 3 to 5% on a specimen of short exposure.

The four failure modes and recommended corrective actions are as follows:

- (a) Some .076 mm Chromel leads failed due to cracks in GA-100 cement. The cracks occurred only in areas where the cement thickness was over .25 mm.

Recommended corrective action is to keep GA-100 cement thickness in the .1 to .2 mm range.

- (b) Three .076 mm Chromel leads failed near the brazed connection to the .25 mm Ni-clad Cu leads. Overttemperature during brazing (due to difficulty in controlling the minature water welder torch flame) is believed to be the cause.

Recommended corrective actions are to provide better fixturing and to shield the .076 mm wire during welding. Laser welding should be considered as an alternative. Laser welders with spot size of less than .1 mm diameter are available.

- (c) Three of the gages showed loss of adherence to the test bar (separating from the precoat of Rokide H). All of these were on specimens overcoated with Rokide H. There were no adherence failures on the eight specimens precoated with Rokide H and overcoated with Sermetel P-1.

Recommended procedure is to overcoat with Sermetel P-1 on all future specimens, and to maintain carefully the specified surface preparation required in the Rokide H flame-spray procedure instructions.

- (d) Deterioration of the .25 mm Ni-clad Cu lead wires occurred under the GA-100 cement after prolonged exposure at 1150 K, even in some cases where the cement was completely free of cracks or voids and the wire was completely coated. Examination after scraping away the cement

showed the copper core of the lead wire to be dull gray and powdery in the failed areas, suggesting oxidation or some other chemical or metallurgical transformation.

Recommended corrective actions are a) investigate better sealing of the end of the sheath of the lead wire cable (where the three Ni-clad Cu conductors emerge) using GA-100 cement without the Cerama-Dip 538. This would include investigating optimum fabrication procedures to form an impermeable overcoat, such as proper thickness and firing conditions, as well as the use of ceramic transfer tapes. b) Review again the possibility of using .25 mm Chromel extension leads instead of the Ni-clad Cu, and correcting for the static strain error resulting from temperature gradients along these high resistance leads.

5.2 Laser Speckle Technique with Heterodyne Readout (Task 5)

5.2.1 Introduction. - The objective of this task in the Preliminary Evaluation program was to evaluate the technique of dual speckle photography for high-temperature strain measurement over the F.O.V. with potential application to jet engine combustor liners. Dual speckle photography involves photographing an area on an object lit by laser light before and after strain and determining the relative speckle motions in the image due to object strains. The recent introduction of heterodyne readout of halo fringes, facilitated by recording single exposures on separate plates rather than double exposures, allows for the accurate measurement of strain over the F.O.V. even in the presence of significant object displacements and rotations. The results of the experimental demonstration and the analyses performed in this task recommended the application of this technique for additional development.

5.2.2 Major Problems. - During the preliminary investigation of this technique, the experimental system exhibited repeatable errors in strain measurement when examined on a scale of 0.1 to 0.2 mm gage length. While these errors could be removed by averaging over lengths 10 to 20 times longer, it was found that the error was systematic and it was dependent upon system alignment. Therefore the sources of these systematic errors needed to be identified and alignment procedures needed to be established to eliminate such errors.

Speckle photography itself has an inherent problem in that most camera lenses have spherical perspective. With such a perspective, out-of-plane object motions yield image magnifications that appear as isotropic strains. The potential solution to this problem lies in the design and use of a telecentric lens for speckle photography.

Very little work has been done to date with speckle photography of objects at elevated temperatures. Problems may be encountered with speckle decorrelation due to surface oxidation and other changes in its microstructure. Distortions due to refractive index changes in the gas surrounding the object may also generate errors in apparent strain. In addition, heating of the lens system used to record the specklegram may cause problems unless sufficient working distance can be provided. Finally, any windows through which light must enter the heated region and through which the camera must look could be a source of trouble due to thermal and optical distortion.

PRECEDING PAGE BLANK NOT FILLED

5.2.3 Approach. - The sources of systematic error were to be determined by setting up the halo heterodyne readout system with a new configuration and which included provision for independent adjustments of the system parameters. Evaluations were then to be conducted with specklegrams recorded with simulated isotropic strains from zero to 1000 microstrains.

Two approaches were taken to the problem of spherical perspective in speckle photography. First, fabrication was planned for a telecentric lens system from existing lenses, which would provide approximately a 25 mm diameter field of view. This lens system would be used to record specklegrams of a test specimen subjected to four-point bending and monitored by a strain gage. This test was to confirm that a telecentric lens system would solve the problems of out-of-plane displacements in speckle photography. Second, work was planned for the design of a telecentric lens system with larger aperture, i.e., up to 100 mm diameter. The OSLO lens design program, which is available at UTRC, was to be used to perform this task.

The problems of speckle photography at high temperatures were to be approached by a study of speckle correlation in specklegrams recorded of high-temperature samples at zero strain (only thermal expansion stains present). This could be done both in air and within an oven to evaluate the problems of working with and without an intervening window. Finally, specklegrams would be recorded of samples under strain at elevated temperatures, provided the previous tests have proved successful.

5.2.4 Heterodyne Readout System. - A system for heterodyne readout of halo fringes was fabricated and tested for halo alignment procedures and for system errors. The system is shown in figure 35. The two beams B_1 and B_2 are from the heterodyne interferometer. They are directed by mirrors M_1 and M_2 through lenses L_1 and L_2 and through specklegrams S_1 and S_2 . The specklegrams diffract light away from the directions of the incident beams to form what are referred to as halos. The halos from the two specklegrams are recombined at the beamsplitter BS forming a fringe pattern in the detector plane. One halo is directed to the beamsplitter by mirror M_3 and the other through a path extender formed by two corner reflectors CR_1 and CR_2 .

The adjustments which were provided in this system were: gimbaled two-axis rotations of the beamsplitter, two-axis rotations of the path extender, two axis rotations of CR_1 , in-plane orthogonal translations of S_1 , in-plane rotation of S_2 , and two-axis rotations of M_1 and M_2 . Both S_1 and S_2 were mounted on a common translation stage denoted by T.

The rate of change of phase difference between the signals obtained from detectors D_1 and D_2 as the pair of specklegrams is translated, is proportional to the relative expansion or dilation between the two patterns, which can be related directly to strain.

Considerable experimentation with the setup showed that the two-axis rotations provided to the path extender appeared to be redundant adjustments and they were eliminated in the interest of stability. Also, the two lenses L_1 and L_2 were replaced with a single lens prior to the division of the two beams. This assured identical waveforms for the two incident beams. The errors that remained were random fluctuations of the output phase due to seismic noise on the optical table and a gradual drift in time due to thermal drift. These two effects were reduced by taking data over a section of the specklegram pair several times while translating back and forth and summing the data for each point.

Figure 36 shows a sample of data taken in the manner described above. The total translation in this case was 2.5 mm with data points taken at .125 mm intervals. Above the data plot is a set of five lines whose slopes correspond to strains from zero to two thousand microstrain. As can be seen, the data shows very little system error. Linear regression of the data gives a line whose slope corresponds 2.1 microstrain. The worst possible calculation, based upon the most abrupt change between neighboring points, gives 250 microstrain; however, this corresponds an extremely short gage length of 0.125 mm.

Data was also taken over a longer gage length: 12.5 mm at 0.625 mm intervals. This is shown in figure 37, and it is clear that on this scale a systematic error is now evident. The sources of this error were not investigated because the errors on this scale represent still relatively small inaccuracies. Regression of the data yielded an error of 12 microstrain.

At this point the investigation of the systematic errors of the halo evaluation system was regarded as complete, the errors having been reduced to a level acceptable for high temperature specklegram evaluation.

5.2.5 Telecentric Lens System. - A telecentric lens system to record specklegrams over large areas on a surface was designed. Camera lenses typically exhibit a spherical perspective, which causes out-of-plane motions to yield image magnifications that appear to be isotropic strain. A telecentric lens eliminates this spherical perspective since the lens design achieves flat object and image planes, to prevent defocusing at the edges of the field. The design was performed upon only one-half of the lens system for an object assumed to lie at infinity. The lens was taken to be two complementary halves centered about a common aperture.

The earlier design effort had also not fully exhausted the possibilities of fabrication using a cemented doublet. Additional effort using the OSLO lens design computer program resulted in the design shown in figure 38. The lenses themselves would mount in either end of a tube 110 mm diameter by 510 mm long, with the aperture in the center of the tube. The cost of this lens design was minimal compared to the previous design, although the object to image length is doubled (1058 mm) and had slightly more field curvature. However, the fabrication cost was significantly reduced so that these difficulties were considered acceptable. A system of this design was fabricated for use on this and other programs using Corporate Funds.

5.2.6 Analysis of Thermal Inhomogeneities. - An analysis was performed to evaluate the effects that may be encountered when speckle photographs are recorded through heated air. Whereas the air temperature, per se, has no effect on speckle photography, changes in distribution of air temperature between successive specklegrams may generate image distortions that will be indistinguishable from mechanical distortions. These image distortions result from the bending of light rays as they travel through the optically inhomogeneous air. The analysis may be summarized in the following way.

Let the unit vector tangent to a light ray be \hat{s} . Let the radius of curvature of the ray, R , be used to define a curvature vector, \vec{K} , pointing inward along the radius and with magnitude equal to $1/R$. Let P_s be the matrix transformation that transforms a vector into its shadow on the plane normal to S . Let n be the distributed index of refraction of the air. The ray curvature may be related to the index of refraction by

$$\vec{K} = P_s \nabla \log n$$

where ∇ is the gradient operator. This relationship shows that rays are bent only by those gradients of refractive index that lie at right angles to their propagation. The integral of ray curvature, along the ray, gives its angular deviation. If the angle of ray deviation changes across the field of view, the image may appear distorted. This leads to the conclusion that apparent strain (i.e., linear distortion) will be related to the second derivatives of refractive index at right angles to the propagation direction.

Physically, a refractive index distribution that exhibits quadratic variations in a transverse plane will appear to be like a lens. Thus, quite logically, it will be the lens-like character of the optical inhomogeneities of the air through which the object is observed that will distort its image and cause apparent strain.

5.2.7 Speckle Photographs of Heated Hastelloy X. - The foregoing suggested a simple physical setup that could allow evaluation of speckle photography on heated Hastelloy X samples. This is shown in figure 39. The sample rests on top of a ceramic cylinder and is heated from above by a propane torch. A thermocouple is fitted into a hole drilled into the side of the sample. A mirror below the cylinder makes it possible to observe the sample through the cylinder, while a small mirror and lens make it possible to illuminate the sample from below with laser light. The cylinder allows the heated air below the sample to form a stable temperature inversion such that the gradient of refractive index lies mainly along the direction of view.

Speckle photographs were recorded on film (for ease of handling and processing) with the sample at the following temperatures: 295, 505, 605, 894, 994, and 1016 K. Three exposures (1, 1/2, and 1/5 sec) were recorded at each temperature using a lens aperture of f/4, Kodak SO 253 holographic film and a system magnification of 4. The specklegrams were observed by placing pairs in contact, aligning their images, and passing a narrow laser beam through the pair. If the pair exhibited correlation, their combined halos would exhibit fringes.

The results of this study, shown in figure 40, were extremely encouraging; some degree of correlation was exhibited between all pairs including the one between room temperature and 1016 K. With temperature differences of up to 477 K, fringe quality was excellent, with good visibility over the entire extent of the f/4 halo. With temperature differences of approximately 588 K, good visibility extended only out to what would correspond to a f/10 halo. In general, the greater the temperature difference, the poorer, and smaller extent of, the halo fringes. The results confirm, however, that successive speckle photographs can be used to record and evaluate the changes in surface deformation of a sample over a large temperature variation. Even though a red HeNe laser was used, and the specklegrams were recorded on red sensitive film, the reflected laser light was sufficiently intense to eliminate any masking problems which might have been caused by the incandescence of the sample. In addition, neither the darkening of the sample nor the oxidation of its surface presented a problem. It was concluded at this point that: 1) speckle photography does not face any major barriers in its application to high-temperature strain measurement; and 2) heterodyne halo evaluation can be employed to obtain accurate strain distributions over the F.O.V. from pairs of single-exposure specklegrams.

5.3 Thin Film Capacitive Sensor (Task 6)

5.3.1 Design. - In order to better exploit the capacitance approach, the original Preliminary Evaluation Plan was revised and approved to fabricate a series of bridge devices which would be drawn closer to the substrate when the gage length was deformed in tension. In this design, the two plates of the capacitor would lie parallel to the surface of the burner can. Figure 41 presents a schematic side view of one of the bridges together with a listing of the various bridge widths to be examined.

The two ends of the bridge contained sections at 45 degrees to the surface of the substrate. These thin metal sections would deflect to move the surface of the bridge closer to the substrate when the surface of the burner can was deformed in tension and further away when the surface was deformed in compression.

5.3.2 Fabrication. - The fabrication process for the capacitive sensors consisted of the following sputtering deposition steps:

1. Deposit Electrical Insulation Layer (SiO_2)
2. Sacrificial Metal Deposition (Aluminum)
3. Metal Etch
4. Deposit Bridge Metal Asymmetrically in Two Steps (Nickel)
5. Bridge Metal Etch
6. Contact Metal Deposition (Gold)
7. Metal Etch
8. Removal of Sacrificial Metal by Etching.

Metal masks were used with the sputtering process to lay down the bridges of nickel across the strips of sacrificial aluminum, which remained after the initial etching process. A low rate of aluminum deposition was used in order to avoid a coarse surface texture from being present on the underside of the nickel bridges. An interface layer of Cr (500 to 600 Å thick) was deposited between the nickel and the silica layers in order to improve adhesion. The nickel was deposited in steps in order to enhance its deposition on the sloping edges of the aluminum.

One of the fabrication problems which developed was maintaining good film integrity at the corners of the partially free standing bridges of nickel. This problem was overcome by a modification of the sputtering process to make it a two-step asymmetric process. The substrate, prepared with the proper masks in place over the already deposited aluminum filler material, was placed at the edge of the circular nickel sputtering target. The film deposited in this step would form about one-half to two-thirds of the bridge film. The substrate would then be moved to the opposite edge of the target and the remainder of the film

deposited. The final shape and thickness of the device was established during a post-deposition etch process.

Other problems in the fabrication process were related to the experimental determination of the proper etching procedure so that the final integrity of the structure was not damaged by these processes. Figure 42 shows two views of the sensor system. The relative position and form of the dielectric gap can be seen in the magnified view of the device.

5.3.3 Thermal Gradient Problem. - One of the attractive features of the thin film capacitive strain sensor was the potential of making a strain sensor which would be temperature insensitive. This could be done by fabricating the thin film device of the same material as the work piece whose strain is to be measured. In this way, if both the thin film and the work piece were at the same temperature, there would be no strain induced in the sensor due to a difference in thermal expansion.

As part of the program to investigate the thin film capacitive strain sensor, a series of computer calculations using the Pratt and Whitney Aircraft (P&WA) temperature distribution program "TCAL" was undertaken. Jet engine combustor operating conditions were obtained from analysts in the P&WA Burner Group. Analyses were done for a variety of encapsulations of the thin film sensor as well as an unencapsulated case.

The first case run was that of the device with no protective cover, and an outline of the model, conditions, and the temperature in the center of the bridge film are shown in figure 43. The temperature difference between the liner and film is about 973 K, which produces a capacitance change of 100 picofarads and an apparent strain of 700-1500 microstrain. This is totally unacceptable and indicated the device must be capped so that a uniform temperature could be maintained around the device.

A simple cap design was chosen and analyzed. The cap was a simple T05 header used extensively in microelectronics. One material selected was nickel, and the resulting temperature distribution is shown in figure 44. The 70 K temperature difference produces an error of 350 microstrain; better, but still far from the 200 microstrain goal. Another material analyzed was a dielectric with a reflective metallic film on the inside surface. The temperature distribution calculated was similar to that for the nickel cap.

The analysis showed that not only is encapsulation necessary, but that the design of the cap was important so as not to produce a severe local temperature perturbation in the burner can. This latter consideration is important for any sensor which may be attached to the outside of the burner can.

The initial results were calculated on an estimated model of the temperature distributions in the vicinity of the burner liner, and did not take the film coefficient of the burner liner into account. The temperature distribution for a device protected by a double-wall, vacuum-insulated cap was also calculated using this early model.

The design of the caps used for encapsulation was based on the size and shape of a T05 header cap. Three cases were run using this simple configuration. One case was with the cap made of stainless steel, another was with the cap made of copper and the third was with the cap made of an insulating material. Three other cases were run with a modification to the T05 cap. These caps were a double-wall configurations which was evacuated and sealed in the manner of a Dewar flask. The inner wall was about three times thicker than the normal wall thickness of a T05 cap. The outer wall was the same thickness as the T05 cap for two cases and the same thickness as the inner wall for one case.

Table 5.3.1 summarizes the three temperature differentials calculated for the different cap configurations. The combustor-film ΔT is the drop in temperature from the center of the thin film sensor to the combustor wall directly beneath the center of the film; the film gradient is the drop in temperature from one edge of the film to the center of the film; the hot spot is the rise in temperature from the unperturbed outer combustor wall to the outer combustor wall beneath the center of the thin film sensor. These temperature differentials are the primary causes of film movement, and hence, error, due to temperature gradients normal to the surface of the burner liner.

TABLE 5.3.1. - CALCULATED TEMPERATURE DIFFERENCES FOR DIFFERENT CAP DESIGNS

Cap Configuration	Combustor Film ΔT , K	Film Gradient ΔT , K	Hot Spot ΔT , K
None	389	100	61
Insulating Thin Cap	67	34	591
SS Thin Cap	98	50	418
CU Thin Cap	71	36	250
SS-Vacuum-Thick CU Cap	18	7	422
CU-Vacuum-Thick CU Cap	29	12	159
Thick CU-Vacuum-Thick CU Cap	28	11	151

Clearly the configuration that simultaneously minimizes all three of the temperature differential columns is the most desirable. The cap configuration which comes closest to this is the cap with the thick double copper walls. It would be desirable to reduce all three temperature differentials even further; however, it appears that the lower limit on the hot spot ΔT is 61K as seen from the unencapsulated case. The calculated values of these thermal gradients and the corresponding error strains which they would cause together with the fact that the presence of the device might generate undesirable thermal discontinuities on the surface of the burner can lead to serious questions about the feasibility of continuing with this approach.

6.0 REVIEW AND MODIFICATION OF PROGRAM (TASK 7)

A program review was held at the completion of Task 6 in order to select the two best candidate for continued development after the preliminary experimental program had been completed. It was decided that further efforts to develop the capacitance type sensor should be discontinued and that efforts should continue to develop the dual photographic laser speckle technique and the resistive strain gage approach.

The results from the preliminary experimental studies of the laser speckle technique were considered quite encouraging. It was decided that in the remainder of the program, the effort should concentrate on the design and fabrication of a practical measurement system based upon this concept. After the system had been evaluated for optical quality, it would be used to demonstrate strain measurement over the range from ambient to 1150 K.

The results of the work in the resistance strain gage effort led to the conclusion that the effects of a number of variables were all probably playing some part in what had been observed. It would be difficult to understand the whole system without having good characterizations of each of the components by themselves. For example, the sensitivity of the apparent strain to temperature change and to the rate of temperature change could be reflecting the effects of several thermal expansion mismatch problems, reactions with the environment or a change in state of the component. Examples of the latter type could be strain relief and grain growth in the insulation subcoat layer or curing of the overcoating cement.

It was concluded that probably the most important component of the system was the strain gage resistance wire itself. It was decided that further work on the resistive approach should concentrate on determining the thermal expansion, the mechanical and the electrical resistance properties of FeCrAl wires, 0.025 mm in diameter. Because a major effort was being made on a companion contract, NAS3-23169, to discover new alloy systems, it was inappropriate to duplicate that type of work in this contract. An additional effort should also be made in this program to evaluate analytically the possible magnitudes of the isothermal strains present due to the differences in thermal expansions of the different materials present.

In order to accommodate these changes in emphasis, a change in the work statement was required. The program began again in August 1, 1981 with the new task outline given below:

PRECEDING PAGE BLANK NOT FILMED

PAGE 86 INTENTIONALLY BLANK

- Task 1: Sensor Analysis of the state-of-the-art technology as applicable to experimental combustor liners and a design analysis of potential sensor systems.
- Task 2: Design of Preliminary Evaluation Program to evaluate the characteristics of candidate systems selected in Task 1.
- Task 3: Review of Tasks 1 and 2.
- Task 4: Fabrication, testing, and post-test analysis of FeCrAl Wire Resistive Gage.
- Task 5: Fabrication, testing, and post-test analysis of High Temperature Speckle Photography with Heterodyne Halo Evaluation Concept.
- Task 6: Fabrication, testing, and post-test analysis of Thin Film Capacitive Strain Sensor.
- Task 7: Briefing to report on results of Tasks 1-6.
- Task 8a: Design of Optical Sensor and test apparatus.
8b: Development of Wire Sample Test Plan and design of test apparatus.
- Task 9a: Fabrication of Optical Sensor and test apparatus.
9b: Fabrication of Wire Samples and test apparatus.
- Task 10a: Testing of Optical Sensor.
10b: Testing of Wire Samples.
- Task 11a: Post Test Analysis of Optical Sensor.
11b: Post Test Analysis of Wire Samples.
- Task 12: Briefing to Report on Task 1-11 and Final Report.
- Task 13: Monthly Reports

7.0 FINAL EVALUATION OF LASER SPECKLE PHOTOGRAPHIC SENSOR (TASKS 8a, 9a, 10a and 11a)

7.1 Fabrication and Evaluation of Telecentric Lens

As discussed earlier, the fabrication of a special telecentric lens system was required for use with the laser speckle technique in order to avoid errors associated with the distortions of images dependent upon the distances of the image from the axis of the lens. This system, which was constructed under corporate funding, consisted finally of a tube 560 mm long with lenses at each end which were 96 mm in diameter.

The following tests were conducted to evaluate the various aspects of the telecentric lens system performance:

7.1.1 Point Source Imaging. - Light transmitted through a 10 micrometer pinhole was directed toward the input side of the lens, and the image formed at the output side was examined with a microscope. Both white light and laser light were utilized in this phase of the evaluation. Although the lens was not designed for color correction, examination in white light indicated that it was not badly corrected in this respect. Thus, it is quite possible that the lens could be used at a variety of laser wavelengths with little or no loss of performance. Examination under laser light showed that the image quality was excellent at the edge of field, as per the design, but that aberrations did exist over the central portion, being particularly significant at 70 percent of the field. However, in subsequent tests it was demonstrated that these aberrations would not be sufficient to adversely affect the performance of the lens in speckle photography.

7.1.2 Helical Motion Recording. - An aluminum plate was affixed to a translation device capable of generating a helical motion (consisting of 0.0835 revolutions per cm of axial movement), and double-exposure laser specklegrams were recorded before and after plate translation. Such specklegrams are generally sensitive to lens aberrations in that they may exhibit: a) curved halo fringes in the presence of spherical aberration; and b) a loss of fringe contrast in the presence of astigmatism. The amount of these aberrations existent in the telecentric lens system was not sufficient to affect the quality of the halo fringes, although slight field curvature was noticeable.

7.1.3 Telecentricity. - The telecentric imaging quality of the lens was checked by recording a double-exposure specklegram; one exposure before, and one after, a 2.5 mm axial translation of the lens. For a nontelecentric lens with an equivalent working distance (250 mm), 2.5 mm of translation would cause an apparent strain of 10,000 microstrain. An analysis of the halo fringes generated in the present test indicated that, in fact, the image had undergone an apparent strain of only 175 microstrain. This residual error may be adjusted by changing the spacing of the two lenses. However, in the present investigations, this will not be attempted because the axial displacements of the object must be kept below 0.2 mm to avoid loss of correlation due to depth of focus limitations. This constraint will limit any apparent strain to less than 14 microstrain.

7.1.4 Lateral Motion Recording. - The effect of lateral object translation was evaluated by recording two single-exposure specklegrams; one before and one after 1 mm of translation. Subsequent to processing, these specklegrams were placed in the halo interferometer, aligned, and halo fringes obtained; thereby demonstrating more than sufficient tolerance to lateral object motion.

7.2 Specklegram Recording and Halo Evaluation System

A new photodetector circuit was designed and fabricated for heterodyne fringe evaluation. It made use of photoconductive cells whose sensitivity and frequency responses eliminated the need for high gain amplifier circuits. This made it practical to design a four-channel detector for measurement of changes in fringe pattern in both the vertical and horizontal directions. A four-channel detector was installed in the halo interferometer and successfully evaluated.

In addition, zero-strain test plates were recorded using the telecentric lens system and used to check out the halo interferometer which had been equipped, with the compensated beamsplitter, x, y, θ adjustments, and set up in a symmetrical co-planar configuration. Both the differential x displacement (δx) and the differential y displacement (δy) were recorded as the pair of specklegrams (zero-strain test plates) were translated. The differential y displacement showed quite large fluctuations. This was not surprising because the δy displacement may be created by rotations of the translation stage about an axis parallel to the transmitted beams.

Finally, the procedure for alignment of the halo interferometer was systematized so that repeatable results could be obtained rapidly. It was determined that the system must be aligned so that the primary rays all lie in a horizontal plane in order to avoid an optical rotation of the two halo patterns.

Figure 45 is a schematic of the specklegram read-out system while Fig. 46 shows the actual device as seen from the sample being measured. Light from a suitably coherent source (e.g., a HeNe laser) enters from the left and passes through a rotating halfwave retarder ($\lambda/2$) followed by a quarterwave retarder ($\lambda/4$). These two components convert the linearly polarized light into equal vertical and horizontal components that are up and down shifted in frequency by twice the rotation frequency. The frequency shifted light then passes through a lens that brings it to focus at the plane of the two detectors on the right. A polarization beamsplitter (PBS) reflects one polarization that is subsequently rotated 90 deg by an additional halfwave retarder ($\lambda/2$) and transmits the other. A set of six mirrors (M) and a compensated beamsplitter (BS) complete the interferometer. The photograph does not include the rotating halfwave retarder, quarterwave retarder, and lens which are off to the right and left of the figure. As indicated in the photograph, the two specklegrams are fastened to a common translational stage (SCHNEEBERGER), and each is provided with an independent set of translation stages for vertical and horizontal (N.R.C. 405), as well as rotational (N.R.C. 470A) adjustment during alignment.

The two specklegrams are placed in the interferometer of figure 46, as shown, and properly aligned to diffract nearly identical fields. If the pair of specklegrams are translated by equal amounts, any differential displacement between the two will cause a displacement to appear between corresponding details in the newly illuminated regions. Because of the Fourier transform relationship between the planes of the specklegrams and the output plane (created by the convergence of the light beams), the differential displacements will correspond to an increase or decrease in the number of fringes between the two detectors. When the interferometer is operating in the heterodyne mode, the change in the number of fringes between the two detectors will correspond to a change in phase between the two output signals. Electronic phase meters are available that can measure such phase changes to one part in 1000 and thereby make very precise measurement of the differential displacements, or strain, between the two specklegrams.

7.3 Arrangement for Testing at Elevated Temperatures

A laboratory furnace was set up with the telecentric lens system so that a sample could be illuminated, with HeNe laser light, and observed through the lens. Figure 47 shows a sketch of the experimental test apparatus. The sample was placed inside the furnace on top of a ceramic tube, and a first surface mirror was located beneath the tube at a 45 deg angle. The telecentric lens system, positioned in front of the mirror, forms an image of the sample at the plane of a plate holder. The illuminating laser beam comes in beneath the furnace at right angles to the lens axis, and is reflected toward the 45 deg mirror by another, much smaller mirror located near the edge of the lens. A small negative lens is used to diverge the beam to illuminate the bottom of the test sample. The mirror and lens, for the incoming laser beam, are positioned toward the edge of the field of the recording (telecentric) lens so that they do not obstruct the field of view in recording the specklegram.

The effects on image quality of air currents inside the tube may have been reduced because the sample acted as a closure at the top of the ceramic tube. The changes in strain brought about by heating this sample would be caused by the thermal expansion of the plate.

A bimetallic strain sample, shown in figure 48, was also fabricated in an attempt to produce higher levels of strain in the Hastelloy X. Incoloy 901 has a slightly higher coefficient of thermal expansion (by 1.25 from room temperature to 1150 K) than Hastelloy X. This difference should be capable of generating 1120 microstrain in the Hastelloy X in a suitably constructed bimetallic sample. Although slightly above the elastic strain limit of 700 microstrain, the strain created by the use of Incoloy 901 in combination with Hastelloy X was less than that which could have been achieved with other compatible metals.

7.4 Results of Elevated Temperature Measurements

7.4.1 Flat Plate Sample. - Specklegrams were recorded of a small test piece of Hastelloy X at room temperature in order to establish the correct exposure for the light level available and the plates being used (Kodak 131 holographic plates). The plates were developed in pyrocatechol whose tanning action promotes emulsion stability. Transform fringes could be observed from pairs of these specklegrams, when held in tandem, and this confirmed their suitability for heterodyne halo analysis.

Two more specklegrams were then recorded with the furnace in operation at temperatures of 1156 K and 1045 K. Transform fringes were also observed with this pair of specklegrams, when held in tandem and illuminated with laser light (correlation), thus confirming that the system possessed adequate stability. It should be noted that at the higher temperature, the incandescence from the sample was within one-half of the irradiance of the reflected laser light. Consequently, use of this technique at still higher temperatures would require either narrow band filtering or use of a blue laser and films insensitive to red light.

The pair of specklegrams that had been recorded, one at 1156, and the other at 1045 K were placed in the halo interferometer and analyzed for differential displacements of their corresponding speckle patterns. These differential displacements should be the result of thermal expansion of the Hastelloy X sample due to the change in temperature. The thermal expansion coefficient of Hastelloy X is $16 \times 10^{-6}/K$ which, times 111 K gives a thermal strain of 1776 $\mu\epsilon$. If the sample temperatures were uniform in both situations, analysis of the differential displacements between the two specklegrams should yield 1776 $\mu\epsilon$ apparent strain, independent of direction.

The resulting measurements are shown in figure 49 in isometric projection. The specklegram image is shown lying in the x, y plane, and the points at which strain was measured are indicated on the x and y axes. Strains in the x direction were measured along the x axis and strains in the y direction along the y axis. The measured strains are shown as elevations above the x, y plane, with a pair of axes showing the plane at 1776 $\mu\epsilon$. Each strain measurement was based on a 2.5 mm scan of the specklegram pair.

The errors between the measured values and the theoretical value are plotted in figure 50, in percent. The large circle on each axis shows where the x scan crosses the y scan. The entire x scan and half of the y scan show measurements that are within 10 percent of the theoretical value, even with a gage length of 2.5 mm (which is five times shorter than required). The end of

the y scan, which lies in the center of the image, shows strain values about 20 percent too low, and these values were duplicated by a second scan.

The low values of strain near the center of the image could be caused either by a real variation in temperature of the sample, or by thermal lensing of the air. The variation in temperature of the sample could be due to greater radiation cooling from the center than from the edges. The thermal lensing could be due to conductivity of heat from the air column into the walls of the ceramic tube that surrounds it. Calculations of the thermal variation on the sample, needed to generate the approximate 300 $\mu\epsilon$ error, indicate that it need only be on the order of 11 K. Calculations of the thermal gradient needed in the air column indicate nearly 220 K/inch are required. It seems most likely, therefore, that the sample variations in temperature are the cause, and that the measured variation in strain is real.

7.4.2 Comparisons Between the Flat Plate and Bimetallic Test Samples. - A sequence of twelve specklegrams were recorded of stressed and unstressed Hastelloy X samples, side by side, in the laboratory furnace. Because of the length of time required to return the furnace to room temperature, the terminal temperatures were 470 K. The specklegrams were recorded at the following temperatures: 470 K, 720 K, 930 K, 1140 K, 1150 K, 1150 K, 1151 K, 1150 K, 1150 K, 930 K, 720 K, 470 K. Ten minute intervals were allowed between the 6 specklegrams at the maximum temperature.

The specklegram data was reduced and several problems identified. The primary problem identified was that the samples underwent a noticeable tilting as they were heated (for reasons not identified) and this resulted in a poor correlation between some of the pairs of specklegrams. For this reason, a complete thermal cycle could not be examined.

The second problem identified was that the bimetallic sample had not performed as expected but appeared to put the sample surface examined into compression rather than into tension. An examination of the cold sample revealed that the strip of Hastelloy X was bowed outward by 0.508 mm in the center. Apparently plastic deformation had taken place at the high temperature and the surface had become permanently elongated. This bowing may flatten out as the temperature increases which would effectively decrease the surface strain. It is also possible that the Incoloy 901 does not heat through evenly and expands more on the side facing the heating element which is away from the Hastelloy X. This could cause the Incoloy to bow and compress the sample. In any case, the expansion of the bimetallic sample fell about 30 percent short of that for the unstressed Hastelloy X as measured by

the specklegrams. This result was confirmed by independent measurements using the heterodyne optical strain sensor, which measured strain on the bimetallic sample in real time. The real time strain sensor also confirmed the tilting of the sample surface in the original test configuration.

The third problem identified was the presence of a considerable local fluctuation in the measured strain in the specklegrams, when two samples at 1150 K were compared. These variations were repeatable and did not appear to be related to the readout system.

Pairs of successively recorded specklegrams were then recorded during separate heating and cooling runs of an unstressed plate of Hastelloy X and the bimetallic sample. During these measurements, each sample was symmetrically positioned on the top of the ceramic tube. Strains were measured using the UTRC halo heterodyne interferometric comparator in both the x direction (long dimension of the sample) and in the y direction (short dimension of the sample). For the bimetallic sample, the stress on the sample was applied in the x direction. Strains were measured by determining the relative speckle displacements at the end points of five successive intervals, each of which was 1 mm long. The average of these strains was computed which gave an effective gage length of 5 mm in both the x and y directions. The thermally induced strain, based upon the average linear coefficient of expansion, was also computed. Figure 51 shows a plot of the thermally induced strain of the free Hastelloy X sample plotted as a function of the specklegram-pair numbers. (Note specklegrams 1 and 2 are pair No. 1, etc.). The circles are the average of the x and y strains measured from the specklegrams and the triangles are the values calculated from the measured temperatures. On this scale, the x and y values are not discernably different. The line connecting pair 0 to pair 11 is the strain measured between specklegram 1 and 12.

Figure 52 shows the results obtained for the bimetallic sample. The circles are the optically measured strain in the x direction, the squares in the y direction, and the triangles are the values calculated using the coefficients of thermal expansion. Again the line connecting the pair 0 to 11 is the strain measured between the first and last specklegram. Note that pair No. 1 is missing. The reason this pair is missing is because the second specklegram was recorded with the emulsion accidentally facing the wrong way and had to be eliminated. Fortunately the correlation between specklegrams 1 and 3 was good and this allowed this gap to be passed over. Figure 53 shows plots of the difference between the thermal and the optical strain measurements so that comparisons can be more easily made.

The results presented in figure 51 show the optical measurements of thermally induced strain to be quite close to those calculated from the

C-2

thermal coefficients of expansion. It is particularly impressive that the difference between the strains measured between the first and last specklegrams (3047 microstrains) is less than 100 microstrain from the value accumulated through the 11 successive pairs (2958 microstrains). The upper pair of curves in figure 53 show the difference between the optically measured strains (both ϵ_x and ϵ_y) and those determined from thermal expansion coefficients on an expanded scale for the free standing Hastalloy sample. It is clear that while the temperature of the oven is increasing, the results are less than the thermally predicted values, and while it is decreasing, they are above the predicted value. These errors are very likely an artifact of the way in which the temperature was measured. The thermocouple was fitted into a hole in a 5 cm square by 3 mm thick piece of Hastalloy X, which lay upon top of the actual sample which was 6.5 cm x 2.5 cm x 1.5 mm. A 355 gram block of Incoloy 901 lay on top of both, to hold them in place. The heat source was suspended above this. The actual temperature of the sample from which the specklegrams were recorded was not measured directly. Also, both surfaces of the sample should have been measured in order to assure that no gradient existed across it which might have caused buckling. Without further refinement of the temperature measurement, and without specific measurement of the coefficients of expansion of the particular sample used, it is difficult to assert that the optically measured strains are not correct.

The results presented in figure 52 show that the Hastalloy X portion of the bimetallic sample underwent significantly less strain than should be expected based upon thermal calculations. The difference on an expanded scale between the thermal calculations and the optical measurements, shown as the lower two curves of figure 53, reaches a maximum at pair number 5 when the sample had just reached the maximum temperature. It is clear that the Incoloy 901 was not putting the Hastalloy X into tension, as it should have based upon its higher coefficient of thermal expansion. Most likely, the top of the Incoloy block, which was near the heating element, was hotter than the bottom. As a result, it warped and bent the center of the sample upward. This could easily put the bottom surface of the Hastalloy X sample into compression relative to its top surface. It was also noticed that the Hastalloy X portion of the bimetallic sample was not glowing as brightly orange as the Incoloy 901, when visually observed during the tests. It seems reasonable to conclude that optical measurements are very likely correct and that they do indicate the mechanical stresses present on the sample. The compressive stresses occurred because the sample was cooler than the thermocouple location and because the Incoloy 901 was bent upward.

8.0 EVALUATION OF RESISTIVE SENSOR (TASKS 8b, 9b, 10b AND 11b)

8.1 Testing Equipment

8.1.1 Thermal Expansion. - Thermal expansion measurements were made using a typical quartz dilatometer consisting of a quartz tube, which contained the sample inside a furnace, and a central quartz rod which sensed the changes in length of the sample as it was heated and cooled. A Linear Variable Differential Transformer (LVDT) was fixed via a water-cooled mount to the quartz tube while the moveable central core of the transformer was supported by the central quartz rod.

In normal use, the central quartz rod rests with a small compressive force on the top of the sample. In this particular dilatometer, a removable quartz plate is normally pressed squarely against the sample end of the tube by means of quartz side rods loaded in tension by springs located above the furnace. For the case of a 25 μ m diameter fiber, a compressive load could not be applied and the arrangement shown in figure 54 was developed. The end of the central quartz rod was made into a hook and a centered hole made in the bottom plate. The ends of the fine wire sample were wrapped around a small FeCrAl crossrod and a loop fed up through the hole in the bottom plate and caught by the quartz hook. A one gram load applied to the upper end of the quartz rod with the hook on its end served to keep the test sample taut throughout the tests.

The quartz fixtures were all contained within a sealed Hastelloy tube and the electrical measuring system was inside a bell jar so that the system could be evacuated with a mechanical pump and backfilled with argon. Thermal expansion experiments were run in both line argon and with air permitted to enter the Hastelloy tube.

8.1.2 Electrical Resistance Measuring Facility. - In order to make resistance measurements of the 25 μ m diameter wire at various rates of heating and cooling, a thermal cycling apparatus, initially developed to thermal cycle gas turbine material by self resistance heating, was modified into a tube heater. The heater tube was approximately 35 cm long with 2.5 cm at each end clamped into water-cooled power electrodes. The 2.5 cm I.D. heater tubes of either stainless steel or Hastelloy X used in this program were split into halves lengthwise in order to facilitate positioning of the wire samples inside the tubes. A diagrammatic view of this facility is presented in figure 55. The furnace system was all contained inside a large plastic box which was continuously purged with a positive flow of line argon in order to reduce any effects due to oxidation.

PRECEDING PAGE BLANK NOT REPRODUCED

The electrical connections to the test wires were made by physically clamping the two ends of the test wires between bars of B-1900 nickel-base superalloy material. All four of these bars were at the same end of the tube furnace so that the length of free test wire was about 25 cm long. An upper and lower layer of two mil platinum sheet was placed between the test wire and the clamps to facilitate good electrical contact. Voltage drops across the test wires were measured using platinum wires which were welded to these platinum sheets. The B-1900 clamps also helped to support the ends of the wire to be close to the center line of the heater tube. The B-1900 bars were long enough so that they extended approximately 5 cm inside the tube furnace. A bolt just outside the furnace could be tightened to apply a load to the contact end of each wire of at least 220N over the whole range of the temperatures involved in the tests.

During the resistivity measurements, the FeCrAl test wires were loosely supported by a pair of alumina pins which protruded into the furnace from the end opposite the two sets of B-1900 clamps. These were supported by a flexure system to make sure that no loads were ever placed on the wires due to thermal expansion effects during the measurements. The temperatures reported were sensed by a type K thermocouple made of 50 μ m diameter wires which was located with the bare bead within approximately 1.5 mm from the test wire near the center of the furnace. Control of the furnace temperature during cycling was accomplished using a Research, Inc. Controller and an associated Data Track card type programmer.

A D.C. power supply, typically set to deliver about 6 volts, was used to supply a continuous flow of approximately 3 ma of current through both the test sample and an adjustable precision resistor box in series with the wire being tested. The voltage generated across the test wire and that across the precision resistor were amplified and fed through a scanner system to a strip chart recorder. The voltages to the recorder were suppressed with a stable D.C. power supply so that the strip chart recorder was usually run at 200 MV full scale. Use of a more sensitive scale permitted the detection of much smaller variations in voltage, and hence resistivity, to be detected. The estimated uncertainty of this measurement system was about $\pm 500 \mu\Omega/\Omega$.

8.1.3 Tensile Testing Facility. - A new device capable of simultaneously measuring the tensile and electrical resistance properties of 25 μ m diameter wires in a purged argon atmosphere was constructed for use in this program. A schematic of this facility is shown in figure 56. It was fabricated primarily of stainless steel parts which were contained inside an alumina tube which was purged with argon. A clam-shell furnace was placed around the alumina tube for testing at elevated temperatures. The clam shell furnace and the Tinius Olsen Universal testing machine are not shown in figure 56.

The loads on the sample were continuously measured with a 500 gm, capacity Instron load cell coupled to a Vishay BAM-1 read out. Load calibrations were made using Ohas balance weights of 20 and 50 grams.

Sample deflections were measured using a Trans-Tek model 201-001 DC-DC displacement transducer in axial alignment with the load cell. Calibrations of this transducer were accomplished using an Instron extensometer calibrator. Typical sample gage lengths were about 11 cm. Temperature measurements were made using two Omega type S thermocouples positioned about 7.5 cm apart and about 0.3 cm from the wire test samples. The thermocouple readings were typically within one degree K of each other. The estimated accuracy of this measurement system was about $\pm 200 \mu\Omega/\Omega$. The major source of error, as later discovered, was the thermal sensitivity of the resistors in the decade resistance box.

Resistance measurements were by connecting the sample wire across a Vishay BAM-1 using a standard quarter bridge 3-wire strain gage hook up. A decade resistance box was used in place of a fixed external balance resistor thereby allowing quick and easy bridge balancing throughout a test.

8.2 Testing Procedures

8.2.1 Electrical Measurement Procedure. - All of the FeCrAl wire samples used in this work were 25 μm in diameter and all were taken from the same spool of wire. This spool was obtained from the Pratt and Whitney Division who had purchased it from the Kanthal Corp. and used it as the materials source in their earlier work. The length of wire tested was typically about 25 cm long and had a resistance of about 1000 ohms. Before starting each run, the chamber was purged with argon for 20 minutes.

Before the thermal cycling was begun, the resistance of the sample was estimated and a series reference resistor was set to approximately the same value. Measurements of the voltage drop across the reference resistor and the sample then permitted a precise calculation of the current through the sample to be determined and from that the resistance of the sample. The reference resistor box was then set to this value of resistance so that there would be only a very small difference between the sample and reference resistor. The same zero suppression voltage was then used on both voltages so that the measured voltages could appear on the most sensitive strip chart range. An automatic scanner was used to measure successively these two voltages. The scanner was set so that the voltage across the precision reference resistor was 15 seconds while that across the sample was 30 seconds so that there would be no confusion about which voltage was being measured.

Heating and cooling cycles were then made to 1150 K at 10, 50 and 250 K/min. On the 250 K/min runs, the programs had had a slight delay at the top temperature because the temperature slightly lagged behind the program. On the 50 and 250 K/min cooling cycles, cooling jets of Helium were used at the lower temperatures to force the system to maintain the rate at the lower temperatures.

8.2.2 Mechanical Testing Procedure. - Two significant problems had to be overcome in order to satisfactorily test these fine wire specimens. The first problem arose because of mechanical noise and small friction forces in the system which became important, especially at elevated temperatures, because of the small loads involved.

The initial arrangement had a loading rod which slid in a tube with loose guide bearings at the top and bottom of the tube. The friction and noise problem was overcome primarily by removing these bearing (sliding) surfaces so that the only guidance the rod attached to the load cell had was the clearance restrictions inside the LVDT motion sensor.

The second type problem involved finding the best approach to use in making good electrical contact at the grips. Initially, the test wires were

simply wrapped around a small alumina rod supported at right angles to the length of the wire. Several wraps of platinum foil between the alumina and the wire provided a means of making electrical contact. A variety of different clamps were examined in the program before this difficulty was, to a large degree, overcome with a bolted "clothspin" type external clamp.

8.3 Results of Wire Testing

8.3.1 Chemical Analysis. - A chemical analysis of the 25 μm diameter FeCrAl wire was made by atomic absorption using the standard addition technique. Unfortunately, the intensities of the absorption lines for Al can be in error because of overlap with the lines for Cr and Fe so that the initial analysis had to be repeated.

The final results presented in Table 8.3-1 agree well with expected compositions. This table gives the results for not only the 25 μm diameter FeCrAl wire, but also the results for some 50 μm diameter wire also purchased from the Kanthal Corp.

TABLE 8.3.1. - CHEMICAL ANALYSIS OF FeCrAl WIRE

UTRC Analysis Corp.			Kanthal
Element	25 μm Dia.	50 μm Dia.	Handbook
Percent by weight			
Al	5.78	5.59	5.0
Cr	21.80	21.50	22.0
Co	0.26	0.55	0.5
Fe	72.16	72.36	72.5
Minor impurities	Parts per Million		
Mn	0.1	0.1	
Cu	0.3	0.3	
Ni	0.6	0.6	
Zr	< 0.01	< 0.015	

The above measurements for Al, Co and Cr were by atomic absorption using the matrix matching technique. The concentrations of Fe were obtained by difference. The concentrations of Al were also confirmed gravimetrically. The presence and amounts of minor impurities were measured by emission spectroscopy.

8.3.2 Thermal Expansion Results. - During the initial thermal expansion experiments, the sample wire was wrapped around a quartz cross rod and erratic data traces were obtained. Apparently the large differences in thermal expansion between the quartz and the FeCrAl wire caused small amounts of tightening and loosening during heating and cooling and the wire slipped on the rod to adjust to these differences. This effect was eliminated by the substitution of a FeCrAl cross rod in place of the quartz.

The first thermal expansion runs were made in argon with the wire in the as-received state. At about 870 K, the slope of the thermal expansion versus temperature plot decreased from a constant value of about 9 microstrains/K to about 2 microstrain/K. Upon cooling, the wire showed a hysteresis effect, actually expanding slightly before finally coming back to a slope equal to the original slope of about 9 microstrain/K. In both of the runs made at this condition, the sample finished by being slightly shorter in length than the original length by approximately 200 microstrains/cycle. These observations of shrinkage are believed to be real effects because the most likely sources of uncontrolled error should have given indications of an opposite sense, if they had occurred. These effects would include local yielding of the wires associated with their points of attachment and creep of the wires.

The same wire, again without being touched or adjusted in any way in the apparatus, was then completely annealed for 2 hrs at 1140 K in argon. The thermal expansion was again measured in argon with essentially the same results upon heating and cooling.

The same wire, without being touched or physically adjusted in any way, was subsequently heated and cooled through the same cycle in air. The results, shown in figure 57, were about the same as in argon except that at the end of the cycle, the wire had permanently expanded in length by approximately 200 microstrains. The wire was again heated in the apparatus in air to 1140 K. The total expansion attained at 1140 K was less by about 500 microstrains than was attained in the first heating in air to this temperature. The wire sample was then presoaked in air for 2 hrs at 1143 K which resulted in a growth in length of about 50 microstrains. Upon cooling to room temperature, the sample again did not completely contract, by approximately 200 microstrains, to the length it had come back to after the first heating in air. The net effect of the two heatings in air was a total apparent decrease in length of approximately 400 microstrains.

A clear explanation for the thermal expansion results is not available. Important changes in electrical properties (see fig. 61) and mechanical properties (see fig. 68) were seen at similar temperatures in that work. One unusual feature of these fine wire samples is that they have a very large

exposed surface area to total volume ratio. This could result in surface effects, normally not seen in bulk samples, becoming more important.

One explanation for the effects observed by heating in air could be to attribute the effects as due to the buildup of an oxide coating. Soaking the wire at an elevated temperature could have resulted in an apparent lengthening of the wire as this oxide coating was being formed. The failures to completely contract back to the initial lengths upon cooling could be due to the lower thermal expansion coefficient of the oxide sheath material. The oxide sheath effectively resists, in part, the efforts of the metal core to contract upon cooling. The resultant effect of this process would be to create at room temperature a tensile stress within the metal wire and a compressive stress in the oxide sheath.

At elevated temperatures, the reverse effect may occur to reduce the total thermal expansion of the wire. At high temperatures, the sheath should be in tension which would impose a compressive strain in the metallic core of the wire.

It was found in other experiments using line argon with FeCrAl sputtered films that the use of argon from this source had not been sufficient to prevent some oxidation attack. The similar change in the coefficient of thermal expansion in argon at about 870 K may also have reflected the presence of an oxide coating on the wire. Handbook values for the coefficients of thermal expansion for FeCrAl and aluminum oxide are about 12.5 and 8.5 microstrain/K, respectively. These values suggest some correlation with the idea that an oxide coating may have been an appreciable influence on the coefficient of thermal expansion measured for these fine wires. The effects of the formation of an oxide sheath may also extend to having an influence on other properties such as strength, strain to failure and changes in thermal sensitivity of resistance at different rates of heating and cooling or after different pretest anneals.

Unfortunately, no thermal expansion measurements were made using the 50 μm diameter FeCrAl wire. Because of the smaller surface to volume ratio, one would predict that, with this wire size the thermal expansion traces would have more nearly resembled those reported for bulk FeCrAl.

In earlier corporate funded work prior to this contract, thin foils were made from 0.012 mm thick sheet stock pieces of FeCrAl which had been cooled from 950 K to 280 K in 60 seconds and 60 minutes. Other foils were also examined from the same stock which had been cooled from 811 K to 533 K over a period of 5 days. No significant second phase precipitates were seen in any of these foils when examined in the transmission electron microscope. In other terms, no evidence was found that heating and cooling this alloy

resulted in the solution and precipitation of internal planes which might have had different densities or coefficients of thermal expansion.

8.3.3 Electrical Properties. - In this section all of the data obtained under Task 10b is reported by means of the data plots presented in figures 58 through 67. This data is also available in tabular form from the authors. Table 8.3.3 contains a general summary of all of the samples and thermal cycles run during which measurements of resistance were made. Table 8.3.3 also describes the annealing conditions used, the rates of temperature change for each run, the test atmospheres, the maximum temperatures reached and cross-references between the various figures.

8.3.3.1 Effects of Preannealing in Argon at Different Temperatures: The effects on apparent strain of heating and cooling the as-received FeCrAl wire #1 at 250 K/min to 1140 K are given in figure 58. As this figure shows, even at these high speeds there is apparently time for internal changes to occur within the wire because the first cycle cooling curve shows a much greater sensitivity to temperature than did the curve produced during heating. By the third cycle, the material has begun to more reproducibly repeat this higher sensitivity to temperature during both the heating and cooling parts of the cycle.

Figure 59 present data for test wire #2 obtained for different rates of heating and cooling after being preannealed for 2 hrs at 1140 K in argon. This data indicates that the resistivity of this wire has developed an even greater sensitivity to temperature change and that the degree of this sensitivity is dependent upon the rate of heating and cooling. In contrast with the earlier data obtained at Pratt and Whitney for a complete strain gage system installed on a Hastelloy X substrate, this data does not show an increase in apparent strain occurring at the lower ends of the cooling curves, shown in figure 3 of this report.

Data for the test wire #3 which was preannealed at 1150 K for 2 hrs in argon and then heated and cooled at different rates is presented in figure 60. Again the resistance of the wire has developed a high sensitivity to change in temperature and this sensitivity varies with the speed at which it is heated and cooled. The ten degree increase in the preannealing temperature has apparently caused a dramatic increase in the thermal sensitivity of this wire.

Figure 61 presents data which compares the total amounts of apparent strain from room temperature to 980 K for wire #2, #3, #7, and #8 which had been preannealed at different temperatures. The maximum effect of these preannealing treatments in increasing the apparent strain appears to occur at about 1150 K and to be more significant for wires which had been exposed to previous cycling at 250 K/min.

TABLE 8.3.3. - SUMMARY OF RESISTANCE TESTING OF FeCrAl WIRES

<u>Wire #</u>	<u>Run #</u>	<u>Annealing*</u> <u>Condition</u>	<u>Rate</u> <u>(K/min)</u>	<u>Test</u> <u>Atmosphere</u>	<u>Max.</u> <u>Temp.</u> <u>(K)</u>	<u>Figure</u>
1	1	As Rec.	250	Argon	1140	58
	2	"	250	"	"	-
	3	"	250	"	"	58
2	1	As Rec.	250	"	"	-
	2	1140 K/2 hrs	250	"	"	-
	3	"	250	"	"	-
	4	"	250	"	"	59
	5	"	50	"	"	-
	6	"	50	"	"	59
	7	"	10	"	"	-
	8	"	10	"	"	59
3	1	As Rec.	250	"	"	-
	2	1150 K/2 hrs	250	"	"	-
	3	"	250	"	"	-
	4	"	250	"	"	60
	5	"	50	"	"	-
	6	"	50	"	"	60
	7	"	10	"	"	-
	8	"	10	"	"	60
4	1	1150 K/2 hrs	50	"	"	-
	2	"	50	"	"	62
	3	"	50	Air	570	-
	4	"	50	"	820	-
	5	"	50	"	1140	62
5	1	1150 K/2 hrs	50	Argon	1140	-
6	1	1470 K/2 hrs	Broke during heat up			-
7	1	970 K/6 hrs	50	Argon	980	-
	2	"	50	"	980	63
	3	"	50	"	1140	-
	4	"	50	"	1140	63
	5	"	50	"	1270	63
	6	"	50	"	1270	63

*All Annealing done in Argon.

TABLE 8.3.3 (Cont'd). - SUMMARY OF RESISTANCE TESTING OF FeCrAl WIRES

<u>Wire #</u>	<u>Run #</u>	<u>Annealing Condition</u>	<u>Rate (K/min)</u>	<u>Test Atmosphere</u>	<u>Max. Temp. (K)</u>	<u>Figure</u>
8	1	1270 K/2 hrs	50	Argon	980	64
	2	"	50	"	1140	64
	3	"	50	"	1270	64
	4	"	50	"	1270	64
	5	"	50	"	1270	64
9	1	810 K/2 hrs	250	Argon	1140	-
	2	"	250	"	"	-
	3	"	250	"	"	65
	4	"	50	"	"	-
	5	"	50	"	"	65
	6	"	10	"	"	-
	7	"	10	"	"	65
10	1	"	250	"	"	-
	2	"	250	"	"	-
	3	"	250	"	"	66
	4	"	50	"	"	-
	5	"	50	"	"	66
	6	"	10	"	"	-
	7	"	10	"	"	66
11	1	"	250	"	"	-
	2	"	250	"	"	-
	3	"	250	"	"	67
	4	"	50	"	"	-
	5	"	50	"	"	67
	6	"	10	"	"	-
	7	"	10	"	"	67

Figure 62 presents apparent strain results for wire #4 which had also been preannealed for 2 hrs in argon at 1150 before testing. As shown in figure 62, the thermal sensitivity is much less for this wire and is essentially identical for cycles run in argon and in air. The reasons for the marked contrast between the data shown in figures 60 and 61 is not understood but it may reflect a sensitivity to prior thermal history. Wires #2 and #3 which evidenced higher sensitivities to temperature had experienced initial thermal cycles at 250 K/min while wires #4, #7 and #8 had not.

8.3.3.2 Effects of Cycling to Successively Higher Temperatures: Data is presented in figure 63 for wire #7. This wire was preannealed for 6 hrs at 970 K in argon and then cycled while measurements were being made at 50 K/min to 970, 1140 and 1270 K. Figure 63 shows that as the exposure to higher temperatures is increased, the thermal sensitivity of the apparent strain increased significantly.

Figure 64 show data for wire #8 which was preannealed for 2 hrs at 1270 K in argon. The expected high sensitivity of apparent strain to temperature shown for wire #7 was not seen in this wire. Apparently, the presoak of wire #7 at 973 K somehow preconditioned it to be much more sensitive to being changed by an exposure to temperatures of 1270 K.

8.3.3.3 The Effect on Apparent Strain of Prestraining the Kanthal Wire: Figure 65 presents data for wire #9 which was preannealed for 2 hrs in argon at 810 K and then strained 4% in pure tension at room temperature. As shown in figure 65, the resistivity of this wire also showed a sensitivity to the rate of heating and cooling. When heated and cooled at 250 K/min, this wire had a total apparent strain sensitivity which was similar to (but somewhat less than) that shown in the results for the as-received wire in figure 58.

Wire #10 was also preannealed for 2 hrs in argon at 810 K and then strained 4 percent in tension. After this plastic strain step, the wire was annealed for 4 hrs at 1200 K. As the data in figure 66 show, this wire was also sensitive to the rate of heating and cooling, showing a behavior similar to that presented for the unprestrained wire #2 in figure 59.

Wire #11 was given the same pretest treatments as wire #10 and the test results obtained are given in figure 67. This wire showed a greater sensitivity of apparent strain to temperature and it was also sensitive to the rate of change of temperature. The results obtained for this wire were similar to those obtained for wire #3, shown in figure 60, where that wire was not plastically deformed prior to testing.

8.3.4 Mechanical Properties. - In an attempt to identify an optimum annealing temperature, a series of as-received wires were heated for two hours in air at different elevated temperature and then deformed in tension at room temperatures until failure. The results of these annealing treatment on the mechanical properties of 25 μ m diameter wire is shown in figure 68. The maximum values of ultimate strength and strain to failure observed were 950 MPa and 7 percent, respectively. Both maximum values were associated with annealing at about 780 K. Above that temperature, the strength and ductility decreased steadily with maximum values of strain being less than 0.5 percent above 1100 K when heated in either air or argon. These results may reflect changes in the internal structure of the metal alloy or the effects of forming a relatively brittle surface coating.

Figure 69 presents some stress strain curves for 25 μ m diameter FeCrAl wires at different temperatures. At 920 and 1100 K the ultimate strengths have decreased to about one-sixth of the value obtained at room temperature. At 1100 K, the strain to failure is only about 1.5 percent. Table 8.3.4 presents a summary of the mechanical data. As can also be seen in this table, the strain to failure of the as-received wire as measured at UTRC was only about 7 percent. This strain is less than the 10 percent calculated as the maximum outer fiber strain required to bend the wire around 0.025 cm diameter pins in order to form a strain gage grid. As shown in figure 68, preannealing the wire in air does not increase the plastic strain capacity of the FeCrAl wire.

TABLE 8.3.4. - MECHANICAL PROPERTIES OF 25 μ m DIAMETER FeCrAl WIRE

Condition	Test Temp. K	Yield MPa/(ksi)	Ultimate Strength MPa/(ksi)	Failure Strain, %	Gage Factor	
					Elastic	Plastic
As Rec'd	297	711/(103)	919/(133)	5.8	-	-
As Rec'd	297	754/(109)	924/(134)	8.1	2.74	2.30
Annealed	297	754/(109)	967/(140)	7.1	2.33	2.04
Annealed	920	67.7/(9.8)	174/(25)	23.6	1.88	1.88
Annealed	1030	87.1/(12.6)	150/(21.8)	2.0	2.01	2.18
Annealed	1100	96.8/(14.0)	169/(24.6)	1.5	1.94	1.94

Some simultaneous measurements of the changes in the lengths of the wires and their changes in electrical resistance are shown in figure 70. The gage factors of these wires in both their elastic and plastic ranges can be evaluated from the slopes of these lines. The gage factors from these experiments would be for the wire alone, completely independent of any restraints or influences from such factors as protective overcoats or interactions with substrates which would be involved in any gage factor evaluations from complete strain gage installations. As can be seen from the values tabulated in Table 8.3.4, there was not much difference between these values and those determined earlier for complete systems (see figs. 30 and 31) except that the gage factors for the wire alone may not have decreased as rapidly as the temperature was raised.

One additional factor of interest for the free wires is that there was very little difference between the gage factors observed in the elastic and the plastic ranges. It could have been predicted that the increase in Poissons Ratio in the plastic range and the creation of many more electron scattering centers from dislocation created by plastic flow should have resulted in a higher gage factor after mechanical yielding. This effect was not observed.

The strains corresponding to the beginning of plastic flow in the wires are indicated by arrows on the plots in figure 70. Once plastic flow began, all of the plots gave linear data. The data was less linear in the elastic range which probably reflected the fact that the loads were changing rapidly and the electrical contact resistances may also have been changing as the wires became better "seated" in the platinum foils at the grips. The presence of oxide films on the wires may also have contributed to these complications.

In an attempt to examine reproducibility, one wire was repeatedly loaded to yield at 1100 K in air to give the results shown in figure 71 where the traces have been transposed to be on top of one another. As indicated by the one gram scale, these wires were not only difficult to see but the measurable loads involved at elevated temperatures provided an experimental challenge. As shown in this figure, the elastic range at these temperatures is only of the order of 800 microstrain. While this elastic strain range might be increased by alloying, the fact that the FeCrAl wires appeared to continue to function as strain sensors in the plastic range might be used to advantage. However, if cyclic strains are present which go beyond the elastic range, the rapid accumulation of plastic strain damage might take away this possibility.

8.4 Analysis of Thermal Strain

An analysis was performed to estimate the magnitude of the strains which would result from the mismatches in thermal expansion in an isothermally heated model FeCrAl high temperature strain gage installation on a Hastelloy X substrate. The analysis provides a quantitative assessment of the accuracy of the FeCrAl gages. The mathematical model idealized the structure as a one-dimensional problem in the through thickness direction wherein the edges of the strain gage were infinitely far from the strain gage center compared to the thickness. The model provided for variations in stresses, strains and displacements as a function of through thickness position. The model also assumed that a zero stress state exists in all materials at room temperature and that all of the materials in the system behaved in an elastic manner. This analytical model was taken from reference 64 and is summarized in the Appendix.

Figure 72 illustrates an idealized strain gage layup, and Table 8.4-1 summarizes the geometries considered. Also included in Table 8.4-1 is a list of the material properties assumed. The fact that the elastic modulus for bulk, completely dense alumina was used in this analysis would tend to maximize the magnitudes of any thermal expansion mismatch strains. The results of the analysis are presented in Table 8.4-2 for a Hastelloy X thickness of 30 mils, and Table 8.4-3 for a Hastelloy X thickness of 60 mils. These results show that an overcoat of SermeTal® has no influence on the FeCrAl strains. Much greater effects are caused by the presence of a layer of Rockide H (Al_2O_3).

An examination of figure 73 shows that the strain gage does not experience the same strain as the Hastelloy X substrate metal without the gage installed on its surface. This difference "error" in the strain for the particular configuration of figure 73 is approximately -5000 microstrains. There is also a significant local compressive strain induced in the substrate itself due to the gage installation. Because the thermal expansion of the FeCrAl alloy is considerably greater than that of Hastelloy X and the alumina, the gage would also be restrained in compression by perhaps another -6000 microstrains. If the gage were completely encapsulated in the alumina so that a state of hydrostatic compression existed, the situation would be more complex.

It might be assumed that the surface straining effects resulting from the installation of a strain gage could be avoided by using a noncontacting optical measurement approach. In fact, a similar situation would exist because the reading would still be taken on the outside surface of an oxide coating.

TABLE 8.4-1. - LAYUP CONFIGURATIONS, THICKNESS GEOMETRIES AND MATERIALS PROPERTIES USED IN THE ELASTIC ANALYSIS OF STRAIN GAGE SYSTEMS

<u>Layup Configuration</u>		
<u>Layer No.</u>	<u>Configuration</u>	
	<u>No. 1</u>	<u>No. 2</u>
1	Hastelloy-X	Hastelloy-X
2	Metco	Metco
3	Al ₂ O ₃	Al ₂ O ₃
4	Kanthal A-1	Kanthal A-1
5	SermeTel ^R	Al ₂ O ₃

<u>Strain Gage Thickness Geometries</u>				
<u>Geo. No.</u>	<u>Thickness for Layer No. (μm)</u>			
	<u>2</u>	<u>3</u>	<u>4</u>	<u>5</u>
	METCO	HL ₂ O ₃	FeCrAl	SERMETEL/Al ₂ O ₃
1	130	130	8	130
2	190	130	8	130
3	250	130	8	130
4	130	190	8	130
5	130	250	8	130
6	130	130	8	190
7	130	130	8	250
8	0.0	0.0	0.0	0.0
				Hastelloy-X only (i.e. no strain gage)

<u>Materials Properties</u>				
<u>Material</u>	<u>α(1/K)</u> <u>@ 290 K</u>	<u>E (MPa)</u> <u>@ 290 K</u>	<u>dα</u> <u>1</u> <u>dT</u> <u>K²</u>	<u>dE</u> <u>MPa</u> <u>dT</u> <u>K</u>
Hastelloy	13x10 ⁻⁶	21x10 ⁴	3.2x10 ⁻⁹	78
Metco	18x10 ⁻⁶	14x10 ⁴	0.0	0.0
Al ₂ O ₃	8x10 ⁻⁶	38x10 ⁶	1.6x10 ⁻⁹	0.0
FeCrAl	20x10 ⁻⁶	20x10 ⁴	6.5x10 ⁻⁹	0.0
SermeTel®	12x10 ⁻⁴	.7x10 ⁴	0.0	0.0

TABLE 8.4-2. - ELASTIC STRAINS CREATED BY THERMAL EXPANSION
DIFFERENCES AT VARIOUS ISOTHERMAL CONDITIONS
HASTELLOY-X THICKNESS = .76 mm

Conf. No.	Geometry No.	FeCrAl Strain ($\mu\epsilon$)		
		420 K	920 K	1250 K
1	1	1400	7300	11500
	2	1400	7500	11700
	3	1500	7600	11900
	4	1300	6600	10500
	5	1200	6100	9700
	6	1400	7300	11500
	7	1400	7300	11500
2	1	1300	6600	10600
	2	1300	6700	10700
	3	1300	6900	10900
	4	1200	6300	10100
	5	1100	6000	9700
	6	1200	6600	10600
		Hastelloy-X Strain ($\mu\epsilon$)		
		8	1760	9640 1580

TABLE 8.4-3. - ELASTIC STRAINS CREATED BY THERMAL EXPANSION
DIFFERENCES AT VARIOUS ISOTHERMAL CONDITIONS
HASTELLOY-X THICKNESS = 1.52 mm

Conf. No.	Geometry No.	Kanthal A-1 Strain ($\mu\epsilon$)		
		420 K	920 K	1250 K
1	1	1500	8000	12700
	2			
	3			
	4			
	5			
	6			
	7			
2	1			
	2			
	3			
	4			
	5			
	6			
	7			
		Hastelloy-X Strain ($\mu\epsilon$)		
		8	1760	9640 15800

Figure 74 shows the corresponding stress states which exist at 1250 K in the different materials for the strains presented in figure 73. The most notable stresses are those present in the alumina which are over 1380 MPa. This could result in cracking unless there were some nonelastic deformation occurring in the Metco layer. The formation of cracks or deformation of the metallic substrate would also reduce the 380 MPa compressive stress in the FeCrAl.

The stress state for an installation of Geometry 1 but in configuration 2 is presented in figure 75 at 420 K (300°F). In this configuration, the top layer of SermeTel® cement has been replaced with one of alumina. With twice as much alumina, the degree of compressive stress in the Metco layer becomes approximately equal to the maximum tensile stress present in the alumina layer. Also, with more alumina the relative compressive stress present in the strain gage is greater than the maximum stress present in the alumina. Built in compressive stresses due to differential thermal expansions could function to increase the elastic strain range of the strain gage in tension, while decreasing the range available for measurements in compression.

The situations described above might be used to create apparent strain effects which could assist in the creation of a strain gage system which is relatively insensitive to changes in temperature. It is not clear that an optimum strain gage material will be one with a thermal coefficient of resistivity of zero. It may be more desirable to have a material whose coefficient is linearly negative. The particular optimum values could also be affected by the relative thermal expansion coefficients of the substrate, the insulation, the alloy, and the thicknesses of the substrate and the insulation coatings. Differences in the strain state between the substrate and the strain gage, the formation of cracks in the insulation layer and/or plastic deformation in the metallic bonding layer might be avoided if the coefficient of thermal expansion of the oxide layers had a better match with that of the substrate. The signs and the values of the stresses and strains present in the installation may also be varied depending upon the temperatures present in the substrate at the time the various layers are applied.

9.0 SUMMARY AND CONCLUSIONS

Listed below are the major conclusions and accomplishments which resulted from this program.

1. A variety of different approaches which might be developed to measure strains to ± 2000 microstrains in a jet engine burner liner during ground testing at temperatures up to 1150 K were examined. The methods evaluated included thin film and wire resistive sensors, optical fibers, surface acoustic waves, optical surface image and reflective approaches, and capacitive devices.
2. Following the use of an evaluation matrix and additional discussions, three candidates were selected and examined in a further preliminary experimental evaluation: a) the laser speckle technique, (b) wire resistance and c) a capacitance sensor approach.
3. The surface guided acoustic wave approach was judged to be a novel approach, worthy of additional effort but too undeveloped for inclusion in this program.
4. Work on the capacitance approach was discontinued primarily because of the discovery by calculation that large thermal gradients would occur within the device which would result in unacceptable errors in apparent strain. None of the various encapsulation possibilities examined were adequate to eliminate this problem.
5. A telecentric lens system was designed and built for use in experiments to evaluate the laser speckle technique. An experimental analysis of its quality showed acceptable behavior.
6. A laser speckle recording system, also capable of making very accurate interferometric readings between pairs of films, was successfully designed and constructed for use in this program.
7. The laser speckle technique was used to successfully measure strains on Hastelloy X surfaces up to 1150 K through a relatively stagnant column of air. The accuracy of these measurements was determined to be approximately ± 10 percent. It was felt that these errors were primarily due to errors in the measurements of sample temperatures and that the real measurement errors were much smaller.

8. In a limited study of two braze alloys used to attach lead wires to resistance strain gages, it was concluded that gold braze filler, AWS Type B Au-4 (AMS 4748), gave acceptable service while the nickel braze filler, AWS type BNi-7 (Nicrobraz 50), was not acceptable.
9. In studies of complete strain gage systems of FeCrAl wires up to 1150 K, it was concluded that SermeTel P-1 was superior to Rokide H for use as a strain gage overcoat layer.
10. Further work should be done to develop new resistance strain gage alloys. The final effort in this program concentrated on determining the thermal expansion, electrical and mechanical properties of 25 μ m diameter FeCrAl wire.
11. A tensile testing facility was successfully developed to measure the stress strain characteristics of wires 0.0025 cm in diameter up to 1150 K in a purged argon atmosphere.
12. The yield stress, ultimate strength and strain to fracture of 25 μ m diameter Kanthal wires decreases from about 750 MPa, 940 MPa and 7 percent, respectively, at room temperatures to about 97 MPa, 169 MPa and 1.5 percent, respectively, at 1100 K.
13. Heating the 25 μ m diameter FeCrAl wires above about 1000 K results in embrittlement and significantly reduced strengths at room temperatures.
14. Above about 870 K the thermal expansion of these wires decreased from about 9 microstrain/K to 2 microstrain/K. It was felt that these effects were due, at least in part, to oxidation of the wire.
15. Heat treatments above about 975 K cause the thermal coefficient of resistivity of Kanthal wires to increase and the wires become much more sensitive to rates of heating and cooling. The maximum effect of high temperature exposure on increasing the thermal sensitivity of the resistance occurs at about 1150 K.
16. The gage factors determined from the behavior of free wires agreed fairly well with gage factors determined for complete resistive strain gage systems installed on Hastelloy X. The gage factors decreased from about 2.4 at room temperatures to about 1.8 at 1150 K.

17. It was shown experimentally that equations assuming completely elastic behavior can be used to estimate surface strains in four point bending even when some plastic yielding occurs.
18. Use of the FeCrAl alloy as a strain gage above about 1000 K is not recommended because its resistance appears not to be reproducible, and to be very sensitive to prior thermal history.
19. An analysis of the potential effects of differential thermal expansions assuming all materials only behave elastically resulted in very high calculated stress levels for relatively small changes in system temperatures. These high levels of stress may not be valid because the elastic modulus for completely dense alumina was used in the analysis.

10.0 REFERENCES

1. Perry, C. C., and H. R. Lissner: The Strain Gage Primer. McGraw-Hill, 1965.
2. Dally, J. W., and W. F. Riley: Experimental Stress Analysis. McGraw-Hill, 1965.
3. Grant, H. P., and J. S. Przybyszewski: Thin Film Temperature Sensor Program Phase I Final Report. NASA-CR-15982, 1979.
4. Dolleris, G. W., H. J. Mazur, and E. Kokoszka: Strain Gage System Evaluation Program. Final Report NASA-CR-159486, March 1979.
5. Dils, R., and P. Follansbee: High Temperature Sputtered Surface Sensors. Proc. 21st Int'l Inst. Symp., ISA, Philadelphia, PA, May 1978, p. 127-132.
6. Grant, H. P., J. S. Przybyszewski, W. L. Anderson, and R. G. Claing: Thin Film Strain Gage Development Program Final Report, NASA CR-174707, December 1983.
7. Bertodo, R.: "Platinum Metal Alloys for the Measurement of Strains at High Temperature." Engelhard Industries Tech. Bulletin, v. 9, n. 2, 1968, 37-49.
8. Easterline, K. E.: "High Temperature Resistance Temperature Strain Gages." British Journal of Applied Physics, 1963.
9. Pitts, J. W., and D. G. Moore: Development of High Temperature Strain Gages. NBS Monograph 26 (96).
10. Weise, R. A., J. H. Foster, and G. B. Hadesty: High Temperature Strain Gage System for Application to Turbine Engine Components, Phase I Interim Report. G.E. Co./USAF F33615-76-C-2075, 1977.
11. Lemcoe, M. M.: Development of Electrical Resistance Strain Gage System for Use to 2000°F. ISA Paper 75-572, 1975.
12. Fuschillo, N., and R. A. Lindberg: Electrical Conductors at Elevated Temperatures. ASTIA ASD-TDR-62-481, 1963 (456 pages).
13. Marks, L. S.: Mechanical Engineers Handbook. McGraw-Hill, 1951, p. 588.
14. Alloy Handbook of Electrical Resistance. Wilbur B. Driver Co.

PRECEDING PAGE BLANK NOT FILLED

15. Willard, C. L.: Resistance and Resistors. McGraw-Hill, 1960.
16. Savitsky, E. M.: The Influence of Temperature on the Mechanical Properties of Metals and Alloys. Stanford University Press, 1961.
17. Masterton, W. L., and E. J. Slowinski: Chemical Principles, 4th Ed., W. B. Saunders Co., 1973.
18. Metcalfe, H. C., J. E. Williams, and J. F. Castra: Modern Chemistry. Holt, Reinhart, and Winston, Inc., 1974.
19. Mooij, J. H.: "Electrical Conduction in Concentrated Disordered Transition Metal Alloys." Phys. Stat. Sol. (a) 17, 521 (1973).
20. Masumoto, H., S. Skowkachi, and K. Michio: "Elinvar Properties of Mn-Pt Alloys." Trans. J. I. M., v. 19, 1978, p. 390-394.
21. Knapton, A. G., J. Inst. Metals, 87, 1958-1959, 28-32.
22. Teed, P. L.: "The Influence of Metallographic Structure on Fatigue," in Fatigue and Fracture of Metals: A Symposium. The Technology Press of M.I.T., 1950.
23. Gensamer, M.: "General Survey of the Problem of Fatigue and Fracture." op. cit.
24. Hultgren, R. and R. I. Jaffee, J. Appl. Phys. 12, 1941, 501-502.
25. Nemilov, V. A. and A. A. Rudnitskii, Izvest. Sektora Platiny, 21, 1948, 234-238.
26. Hansen, M.: Constitution of Binary Alloys. McGraw-Hill, NY, 1958.
27. Shunk, F. A.: Constitution of Binary Alloys. Second Supplement, McGraw-Hill Book Co., New York, 1969.
28. Private Communication, W. Drinkuth, Pratt & Whitney Aircraft, Engineering Instrumentation, Commercial Products Division.
29. Butter, C. D. and G. B. Hocker: Appl. Opt. 17, 2867 (1978).
30. Hocker, G. B.: Appl. Opt. 18, 1445 (1979).

31. Fields, J. N. et al: Talk WD3, Topical Meeting on Optical Fiber Communication. 6-8 March 1979, Washington, DC.
32. Bell, J. F.: Journal of Appl. Physics 27, 1109 (1956).
33. Bingham, W. L.: Advanced Experimental Techniques in the Mechanics of Materials, ed. Francis and Lindholm, p. 295-312.
34. Smith, G. B.: Private Communication, P&WA/CPD Instrumentation Group.
35. Sharpe, W. N. and D. R. Martin: Final Report AFML-TR-77-153, September 1977, Air Force Materials Laboratory (LLN) Wright-Patterson Air Force Base, Ohio.
36. Mongeon, R. J. et al: Digital Aircraft Function Monitors Utilizing Passive Fiber Optic Sensors. Final Report R78-922820-4, NASC AIR-52022, Washington, DC.
37. Ennos, A. E.: Measurement of In-plane Surface Strain by Hologram Interferometry. J. Sci. Instrum. 1, p. 731-746 (1968).
38. Wilson, A. D.: Inplane Displacement of A Stressed Membrane with a Hole Measured by Holographic Interferometry. Appl. Opt. 10, p. 908-912 (1971).
39. Wallach, J., J. M. Holeman, and F. A. Passanti: Holographic Strain Measurement on A Tensile Specimen. Proc. SPIE Symp. on Eng. Appl. of Holography, p. 167-175 (1972).
40. Sciammarella, C. A. and J. A. Gilbert: Strain Analysis of a Disk Subjected to Diametral Compression by means of Holographic Interferometry. Appl. Opt. 12, p. 1951-1956 (1973).
41. Taylor, L. H. and G. B. Brandt: An Error Analysis of Holographic Strains Determined by Cubic Splines. Exp. Mech., 12, p. 543-548 (1972).
42. Brandt, G. B. and L. H. Taylor: Holographic Strain Analysis using Spline Functions. Proc. SPIE Symp. Eng. Appl. Holog. p. 123-131 (1972).
43. Stetson, K. A.: Moiré Method for Determining Bending Moments from Hologram Interferometry. Opt. Laser Technol. 2, p. 80-84 (1970).
44. Sollid, J. E. and K. A. Stetson: Strains from Holographic Data. Exp. Mech. 18, p. 208-214, (1978).

45. MacBain, J. C.: Displacement and Strain of Vibrating Structures using Time-Average Holography. Exp. Mech., 18, p. 361-372 (1978).
46. Boone, P. M.: Holographic Determination of In-plane Deformation. Opt. Technol. 2, p. 94-98 (1973).
47. Sciammarella, C. A. and J. A. Gilbert: A Holographic-Moiré Technique to Obtain Separate Patterns for Components of Displacement. Exp. Mech. 16, p. 215-220 (1976).
48. Sciammarella, C. A. and S. K. Chawla: A Lens Holographic-Moiré Technique to Obtain Components of Displacements and Derivatives. Exp. Mech. 18, p. 373-381 (1978).
49. Dubas, M. and W. Schumann: On Direct Measurement of Strain and Rotation in Holographic Interferometry Using The Line of Complete Localization. Opt. Acta 22, p. 807-819 (1975).
50. Stetson, K. A.: Holographic Strain Analysis by Fringe Localization Planes. J. Opt. Soc. Am. 66, p. 627 (1976).
51. Stetson, K. A.: Homogeneous Deformations: Determination by Fringe Vectors in Hologram Interferometry. Appl. Opt. 14, p. 2256-2259 (1975).
52. Pryputniewicz, R. and K. A. Stetson: Holographic Strain Analysis: Extension of Fringe-Vector Method to Include Perspective. Appl. Opt. 15, p. 725-728 (1976).
53. Pryputniewicz, R.: Holographic Strain Analysis: An Experimental Implementation of the Fringe Vector Theory. Appl. Opt. 17, p. 3613-3618 (1978).
54. Lerendertz, J. A.: Interferometric Displacement Measurement on Scattering Surfaces Utilizing Speckle Effect. J. Phys. E: Sci. Instrum., 3, p. 214-218 (1969).
55. Archbold, E., J. M. Burch, and A. E. Ennos: Recording of In-plane Surface Displacement by Double-Exposure Speckle Photography. Opt. Acta, 17, p. 883-898 (1970).
56. Erf, R. K.: Speckle Metrology, (Academic Press, New York, 1978).
57. Lim, T. C., and M. J. P. Musgrove: Stonely Waves in Anisotropic Media. Nature, Vol. 225, p. 372, January 1970.

58. Stonely, R.: Proc. Roy. Soc., Vol. 245A, p. 372, January 1970.
59. Maerfeld, C., and P. Tournois: Pure Shear Elastic Wave Guided by the Interface of Two Semi-Infinite Media. Appl. Phys. Lett., Vol. 19, p. 117, 1971.
60. Owen, T. E.: Prog. Appl. Mat. Res. (GB), Vol. 6, p. 64, 1964.
61. Shuskus, A. J., T. M. Reeder, and E. L. Paradis: rf Sputtered Aluminum Nitride Films on Sapphire. Appl. Phys. Lett., Vol. 24, p. 155, February 1974.
62. Shiosaki, T., et al.: Low Temperature Growth of Piezoelectric AlN Film by rf Reactive Planar Magnetron Sputtering. Appl. Phys. Lett., Vol. 36 (8), p. 643, April 15, 1980.
63. Popov, E. P.: Mechanics of Materials, Prentice Hall, p. 111 (1952).
64. Cassenti, B. N., A. M. Brickley and G. C. Sinko: Thermal and Stress Analysis of Thermal Barrier Coatings, AIAA Paper No. 81-1482, presented at the AIAA/SAE/ASME 17th Joint Propulsion Conference, Colorado Springs, Colorado, July 27-29, 1981. Also JT9D Thermal Barrier Coating Analysis Informal Report PWA-5515-135, Pratt & Whitney Aircraft Group for Contract NAS3-20630, Sept. 1980.

APPENDIX

GOVERNING EQUATIONS FOR THERMAL STRESS ANALYSIS

Consider a uniform multilayer plate of total thickness h in the x - y plane. Assume that plate edges, given by

$$f(x,y) = 0 \quad (1)$$

are far from the region of interest, then: (1) the stresses will not vary in the x or y direction, and (2) the stress state is isotropic in the x - y plane. Assume there are no loads on the surfaces

$$z = \pm \frac{h}{2} \quad (2)$$

The equilibrium equations and the boundary conditions then imply the stress state, in each layer i , is given by

$$\sigma_x^i = \sigma_y^i = \sigma^i(z) \quad (3)$$

where $\sigma^i(z)$ is a function to be determined, and the other stress components vanish.

Hooke's Law requires

$$\epsilon_r^i = \epsilon_\theta^i = \frac{1}{E_i} (1-\nu_i) \sigma^i(z) + \alpha_i [T(z) - T_{0i}] \quad (4)$$

$$\epsilon_z^i = -\frac{2\nu_i}{E_i} \sigma^i(z) + \alpha_i [T(z) - T_{0i}] \quad (5)$$

$$\gamma_{r\theta}^i = \gamma_{\theta z}^i = \gamma_{rz}^i = 0 \quad (6)$$

PRECEDING PAGE BLANK NOT FILMED

where E_i is Young's Modulus for Layer i
 ν_i is Poisson's ratio for Layer i
 T_{0i} is the "Stress Free Temperature" for Layer i , and
 α_i is the coefficient of expansion for Layer i

where the coordinates have been transformed from rectangular (x,y,z) to polar (r,θ,z) . The strain displacement relations are the

$$\begin{aligned} \epsilon_r^i &= \frac{\partial u^i}{\partial r} & \gamma_{rz}^i &= \frac{\partial u^i}{\partial z} + \frac{\partial w^i}{\partial r} \\ \epsilon_\theta^i &= \frac{u^i}{r} & \gamma_{\theta z}^i &= 0 \\ \epsilon_z^i &= \frac{\partial w^i}{\partial z} & \gamma_{\theta r}^i &= 0 \end{aligned} \quad (7)$$

where u is the radial displacement
 w is the axial displacement, and
 v is the circumferential displacement which vanishes by symmetry.

The displacements can be found from equations 4 through 7 to be

$$u^i(r,z) = C_2^i r z + C_1^i r \quad (8)$$

$$w^i(r,z) = F_z^i(z) - \frac{1}{2} C_2^i r^2 \quad (9)$$

where

$$F_z^i(z) = \int_{z_{i-1}}^z \epsilon_z^i(z) dz + F_z^{i-1}(z_{i-1}) \quad (10)$$

and

$$F_z^0(z) = 0$$

The displacements are continuous at the interfaces of the layers and, therefore, all of the C_1^i are identical as well as the C_2^i or

$$C_1^i = C_1 \quad (11)$$

$$C_2^i = C_2 \quad (12)$$

The remaining two constants C_1 and C_2 are found by requiring that the total in plane force and moment are zero or

$$\int_{-h/2}^{h/2} \sigma_r(z) dz = 0 \quad (13)$$

$$\int_{-h/2}^{h/2} z \sigma_r(z) dz = 0 \quad (14)$$

Equations 13 and 14 result in

$$\begin{aligned} A_{22}C_2 + A_{21}C_1 &= b_2 \\ A_{12}C_2 + A_{11}C_1 &= b_1 \end{aligned} \quad (15)$$

where

$$\begin{aligned} A_{11} &= \sum_{i=1}^N \frac{E_i(z_1 - z_{i-1})}{(1-\nu_i)} \\ A_{12} = A_{21} &= \sum_{i=1}^N \frac{E_i(z_i^2 - z_{i-1}^2)}{2(1-\nu_i)} \end{aligned}$$

$$A_{22} = \sum_{i=1}^N \frac{E_i (z_i^3 - z_{i-1}^3)}{3(1-\nu_i)}$$

$$b_i = \sum_{i=1}^N \frac{\alpha_i E_i}{1-\nu_i} \left\{ \int_{z_{i-1}}^{z_i} T(z) dz - T_{O_i} (z_i - z_{i-1}) \right\}$$

$$b_2 = \sum_{i=1}^N \frac{\alpha_i E_i}{1-\nu_i} \left\{ \int_{z_{i-1}}^{z_i} T(z) z dz - \frac{1}{2} T_{O_i} (z_i^2 - z_{i-1}^2) \right\}$$

and H_i is the thickness of layer i .

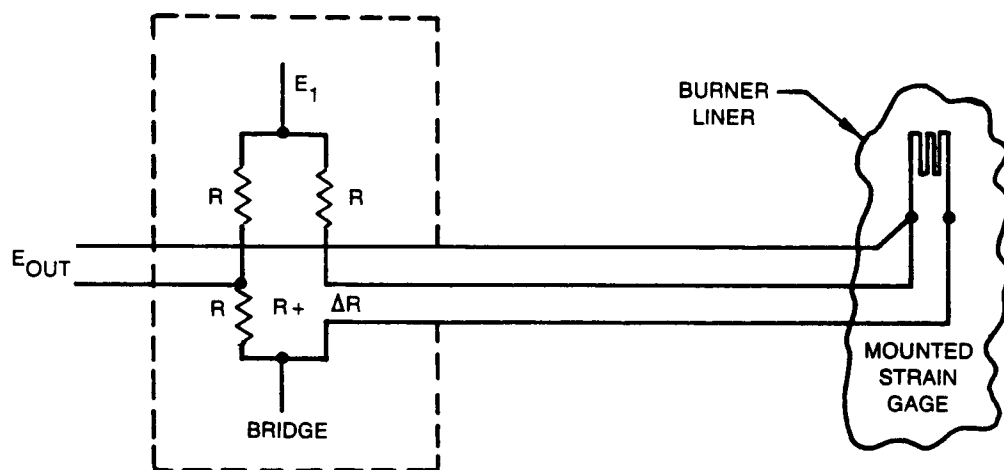
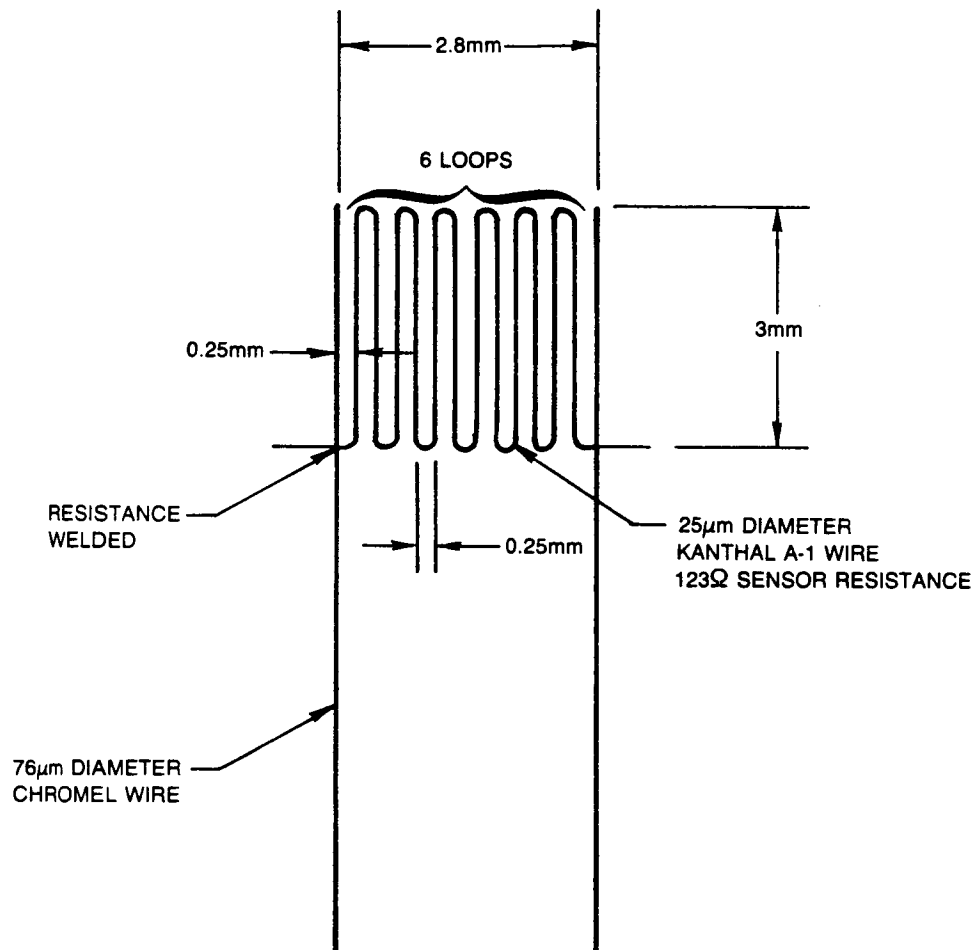


Figure 1. A Resistive Strain Gage System



INSTALLATION:

SURFACE PREPARATION: NiCrAl (METCO 443) FLAME SPRAYED

PRECOAT: Al_2O_3 (ROKIDE "H") FLAME SPRAYED

OVERCOAT: $AlPO_4$ (SERMETEL P-1) CERAMIC CEMENT

EXTENSION LEADS: 3c Ni CLAD Cu WIRE WITH 1.6 mm DIAMETER

S/S SHEATH AND 0.25 mm in. DIAMETER CONDUCTORS
CABLE IS STRAP WELDED TO SUBSTRATE AND SPLICES
ARE BRAZED WITH AMS 4772

Figure 2. Kanthal A-1 Wire Strain Gage Description

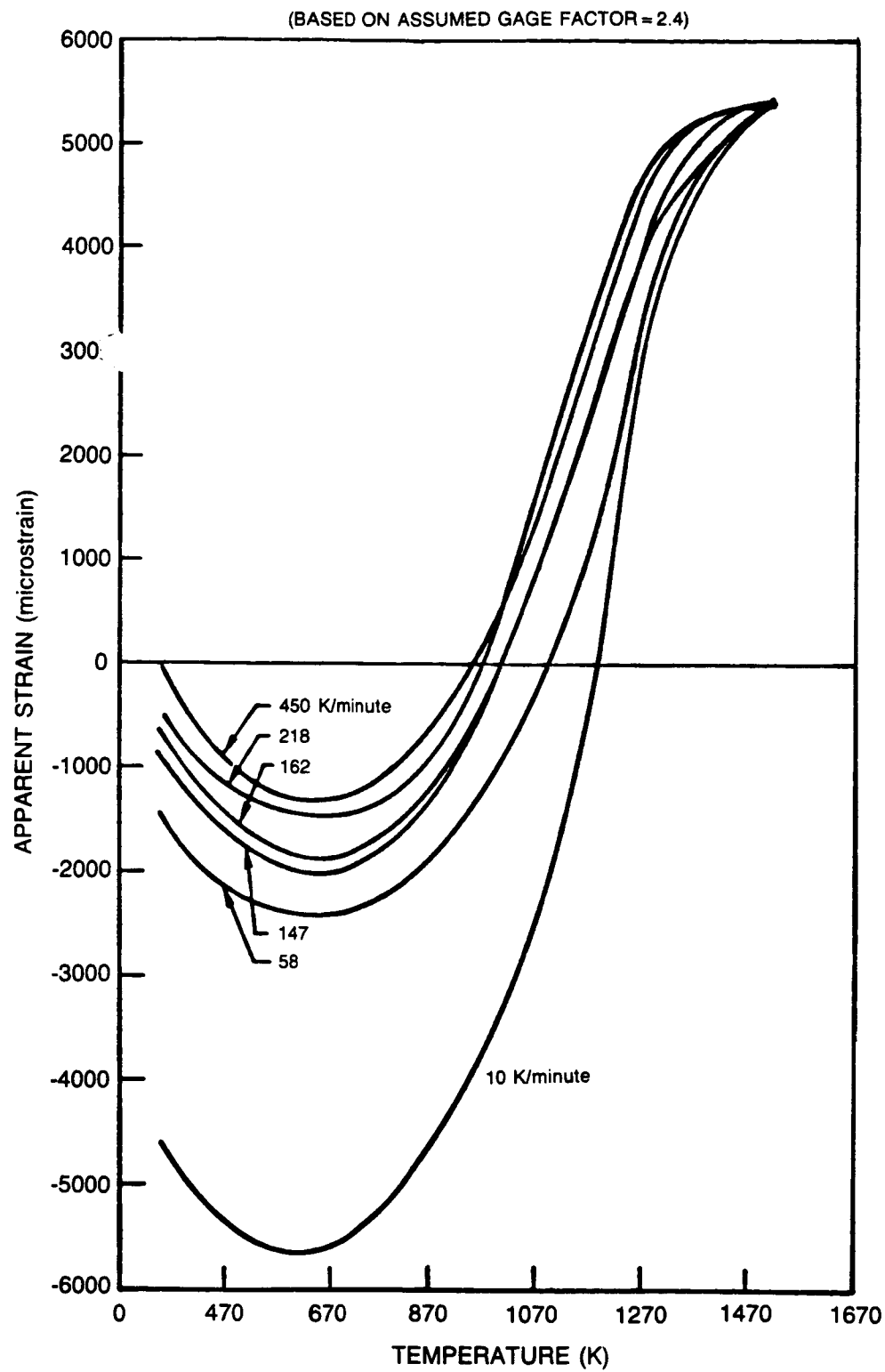


Figure 3. Apparent Strain of Kanthal A-1 Wire Strain Gage for Various Cooling Rates

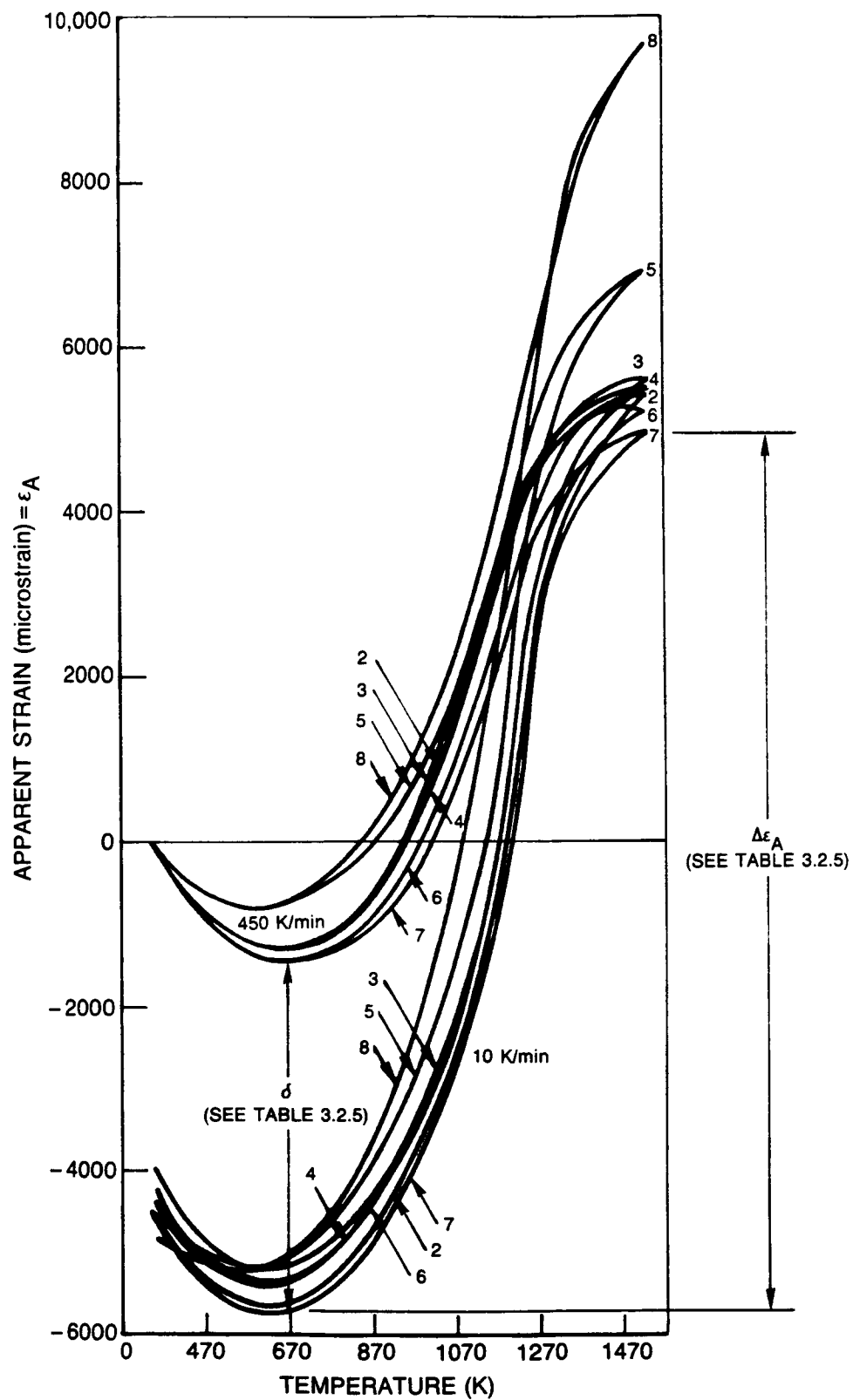


Figure 4. Apparent Strain of Kanthal A-1 Wire Strain Gages

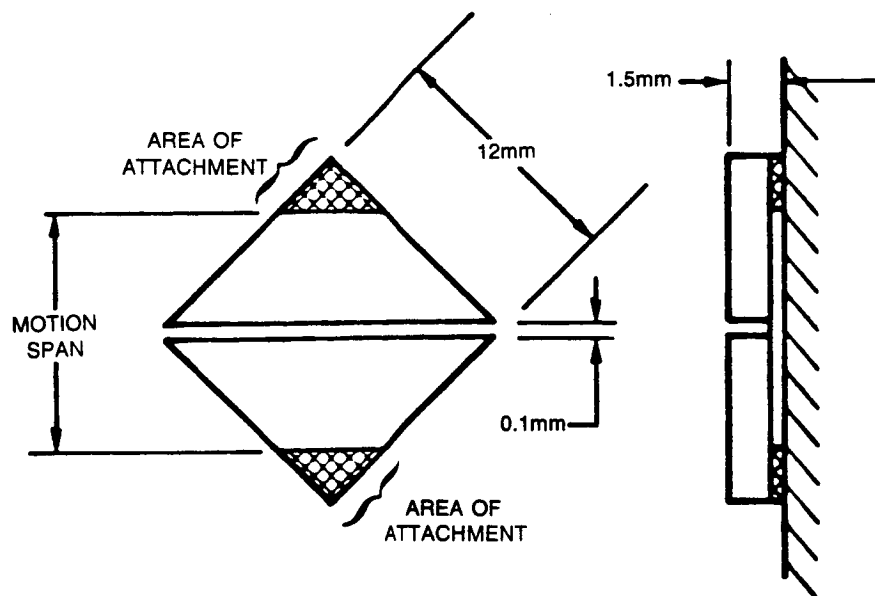
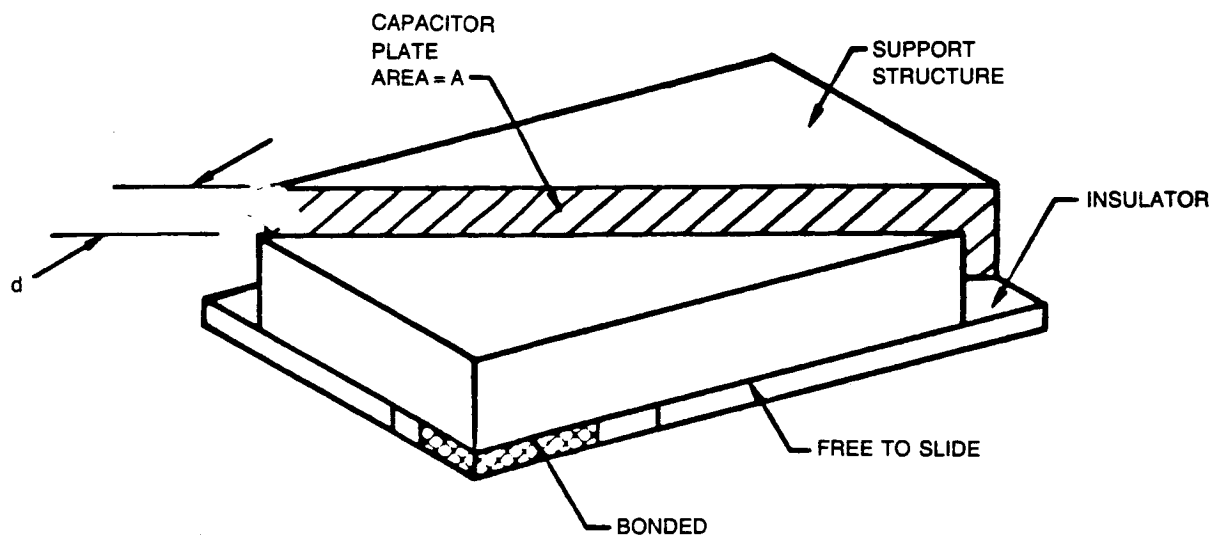


Figure 5. Complex Capacitive Concept A

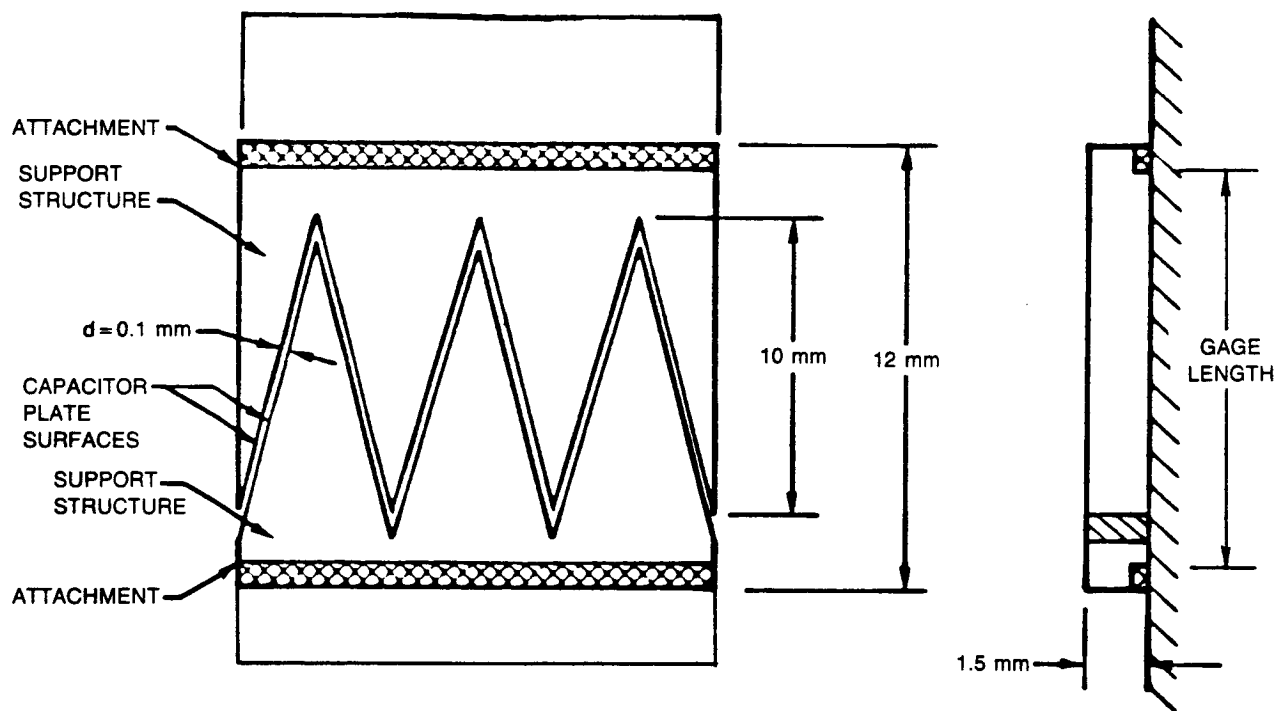


Figure 6. Capacitive Sensor Concept B

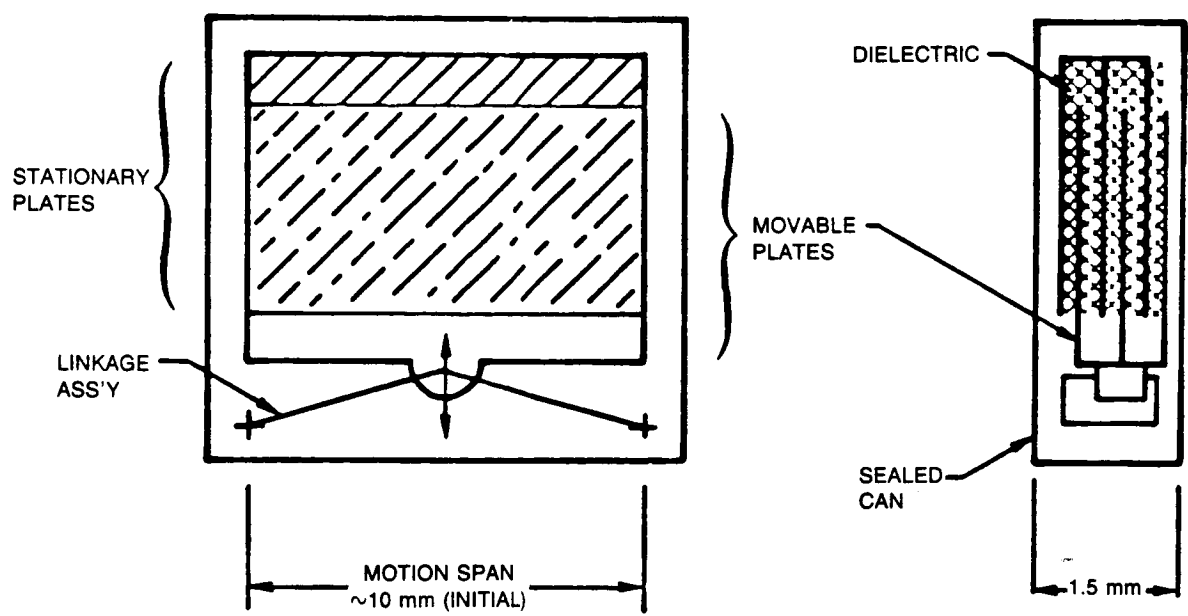


Figure 7. Capacitive Sensor Concept C

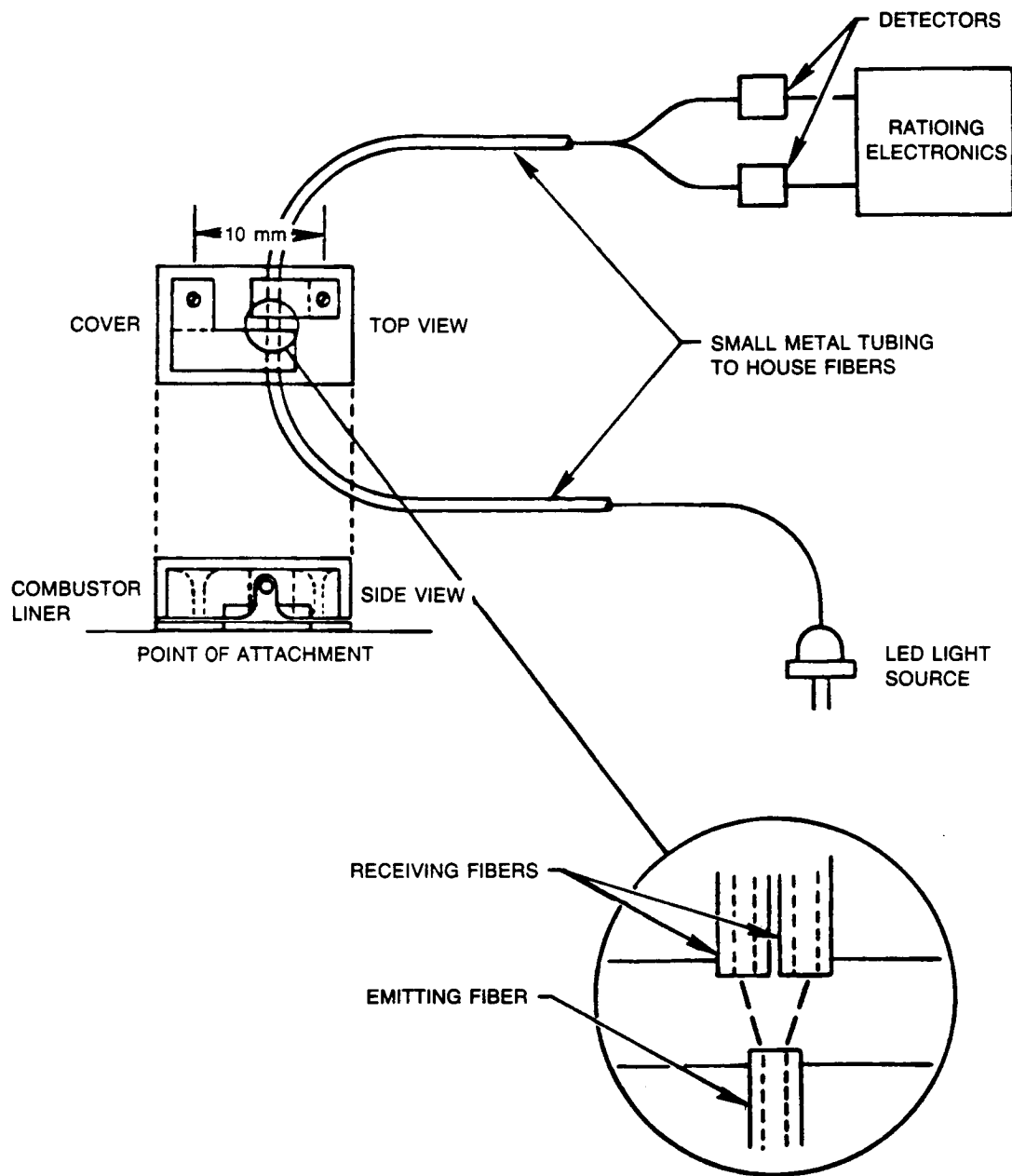


Figure 8. Optical Coupler Concept

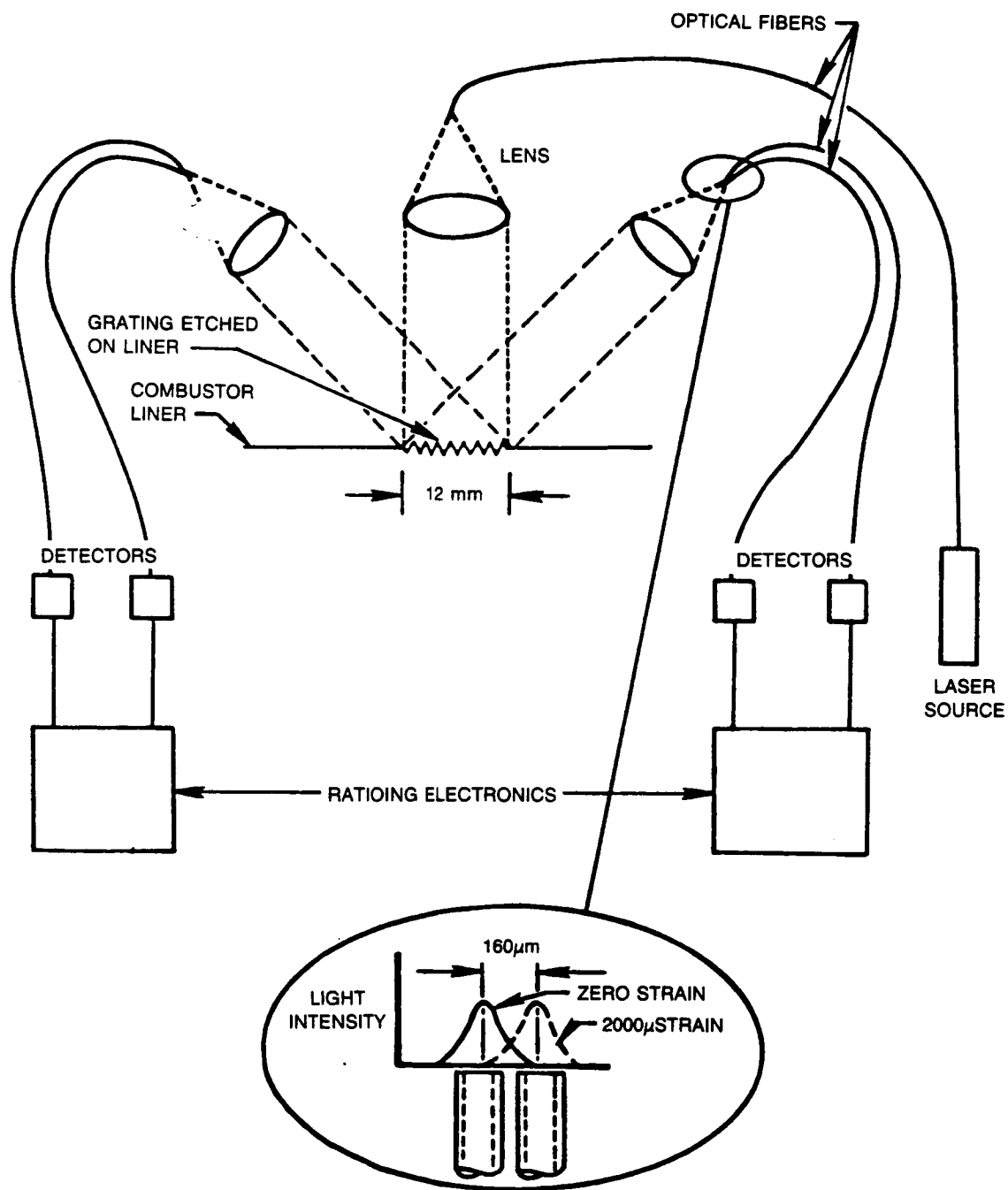


Figure 9. Diffraction From a Grating

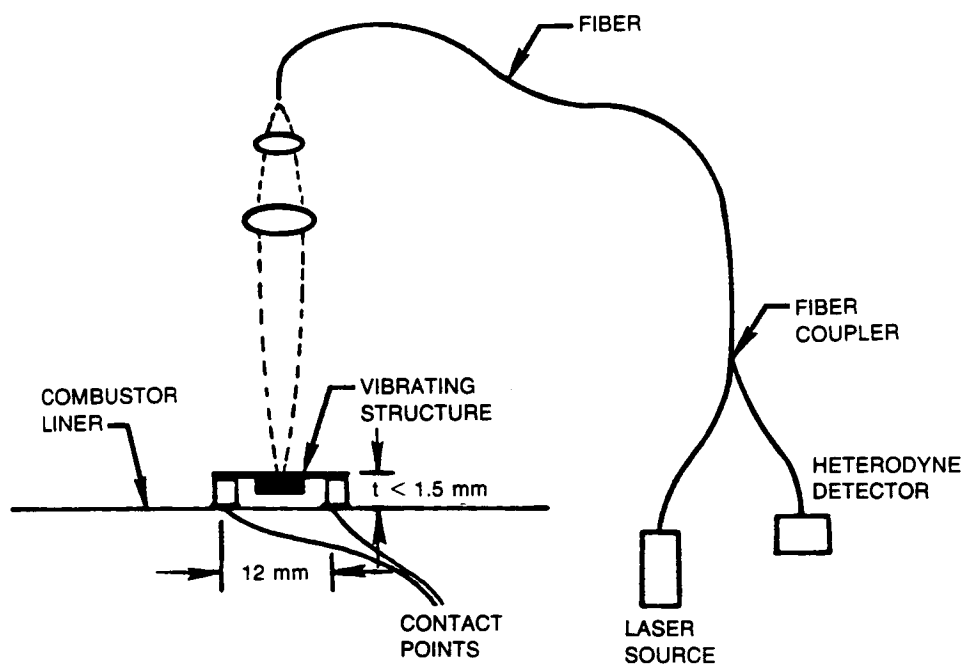


Figure 10. Vibration Strain Sensor

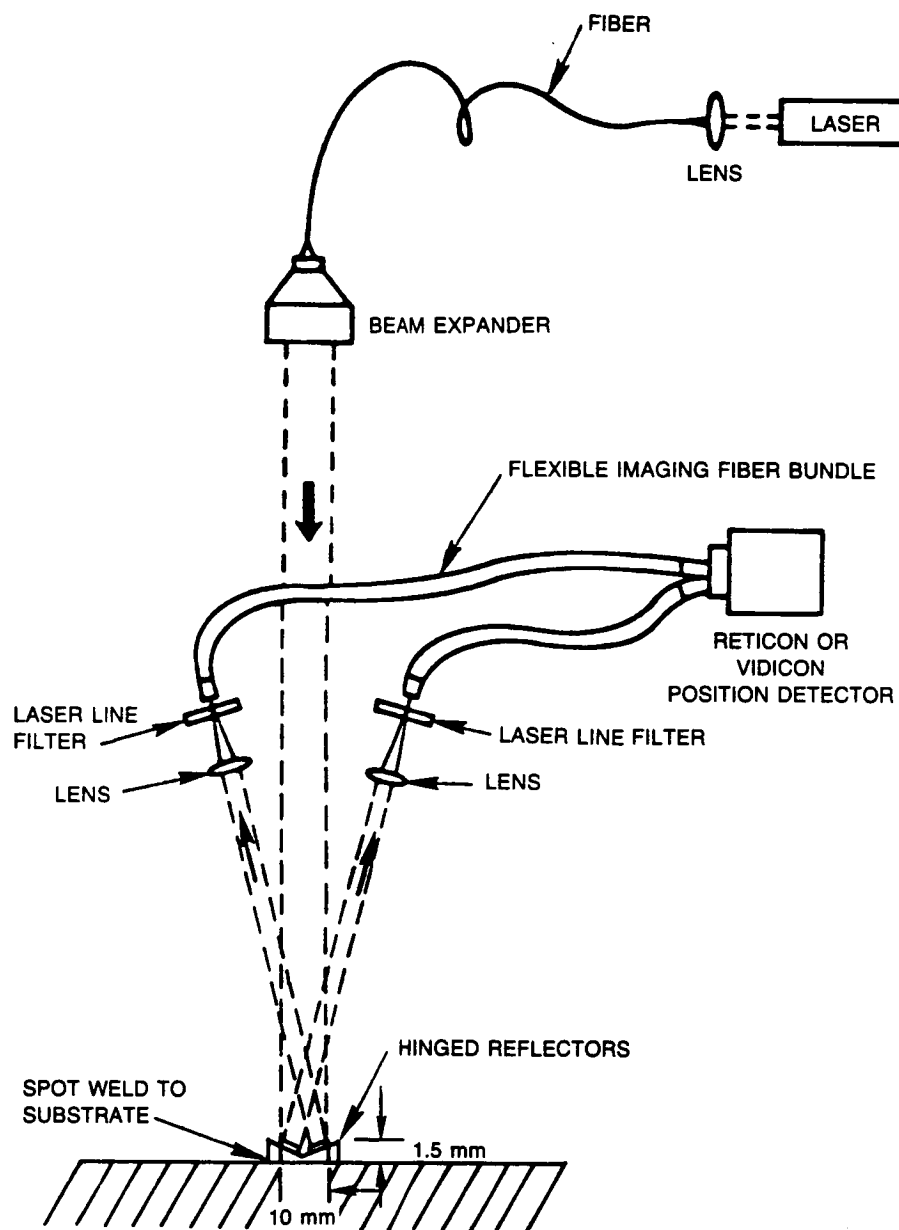


Figure 11. Hinged Reflector Strain Sensor

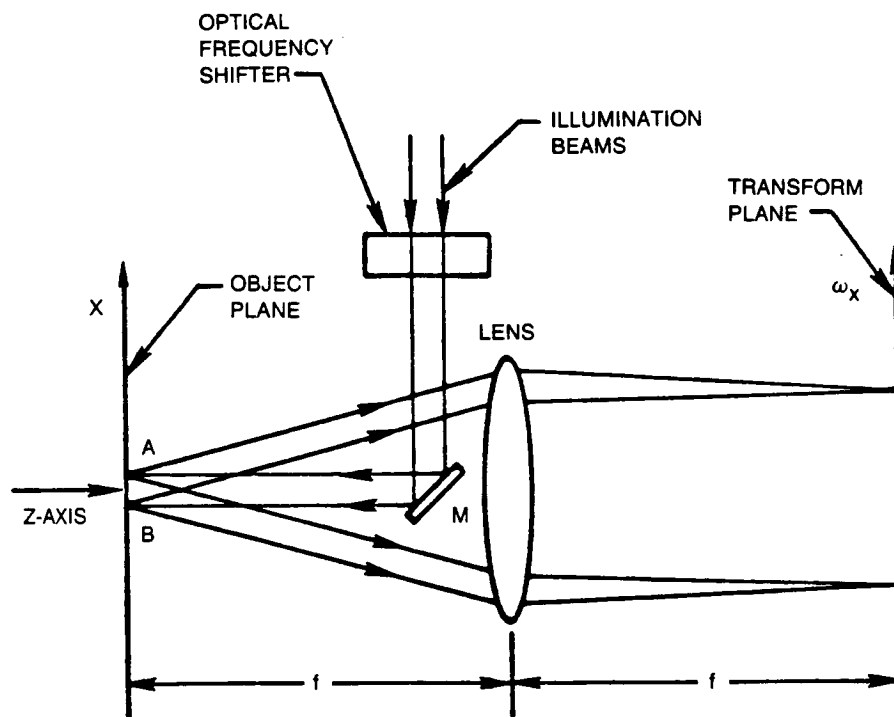


Figure 12. Optical Strain Sensor Concept

ORIGINAL PAGE IS
OF POOR QUALITY

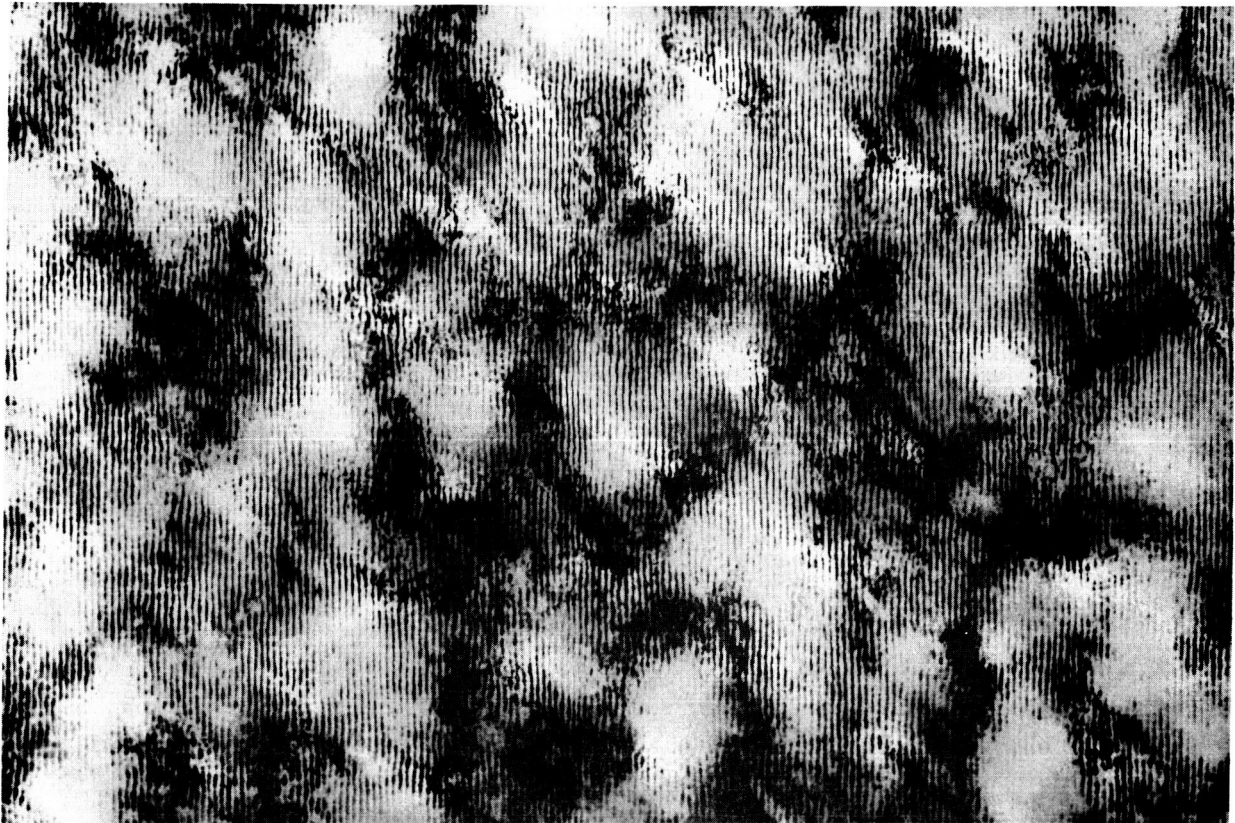


Figure 13. Interference of Two Inclined Speckle Fields

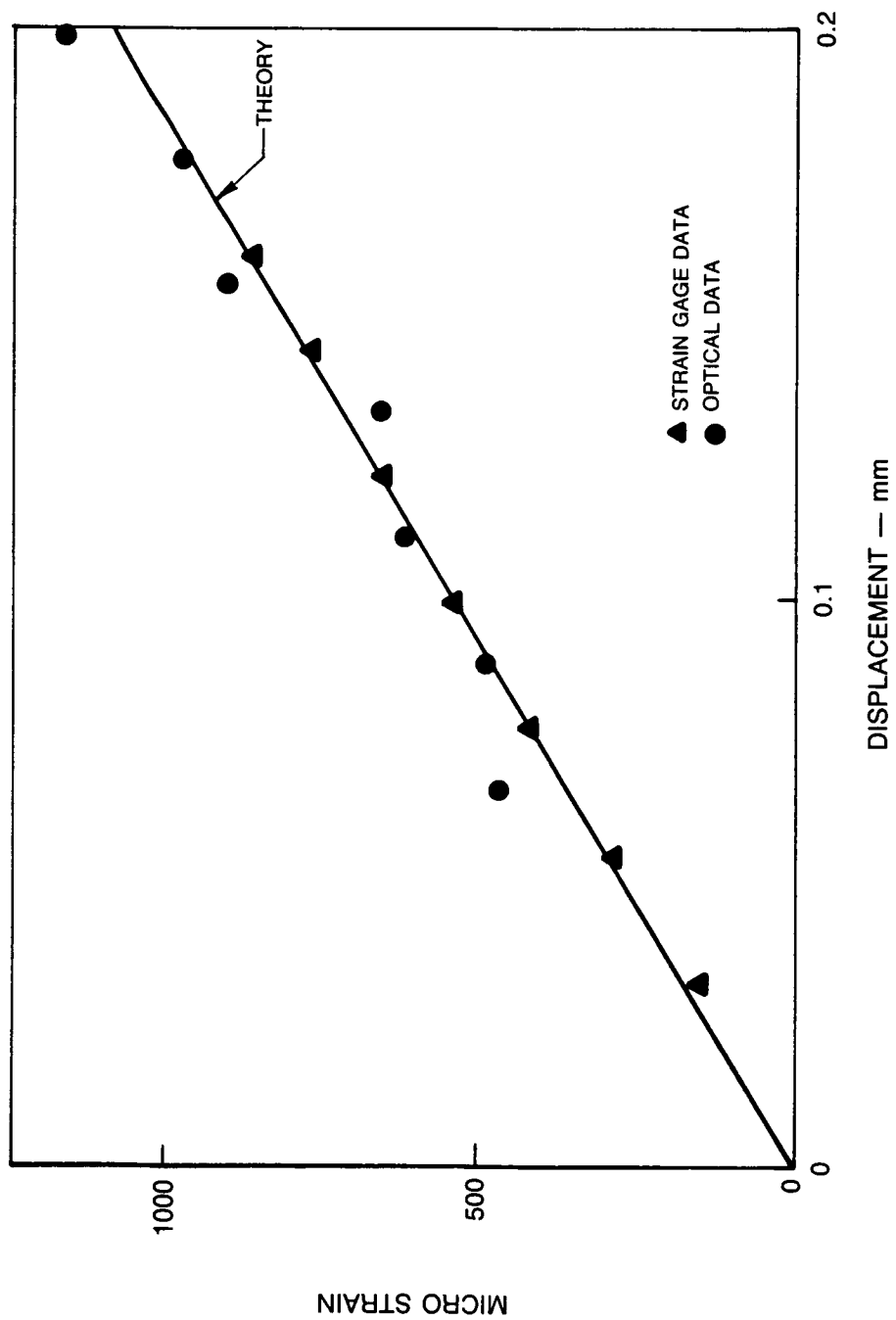


Figure 14. Measured Strain Versus Displacement for a Beam Under 3 Point Bending

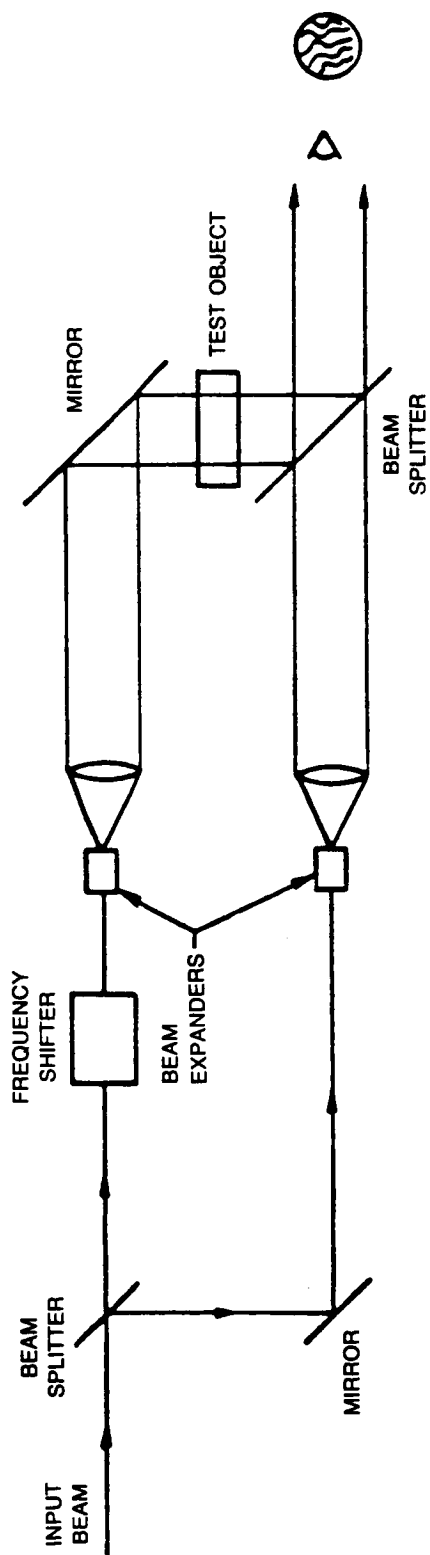


Figure 15. Heterodyne Interferometer

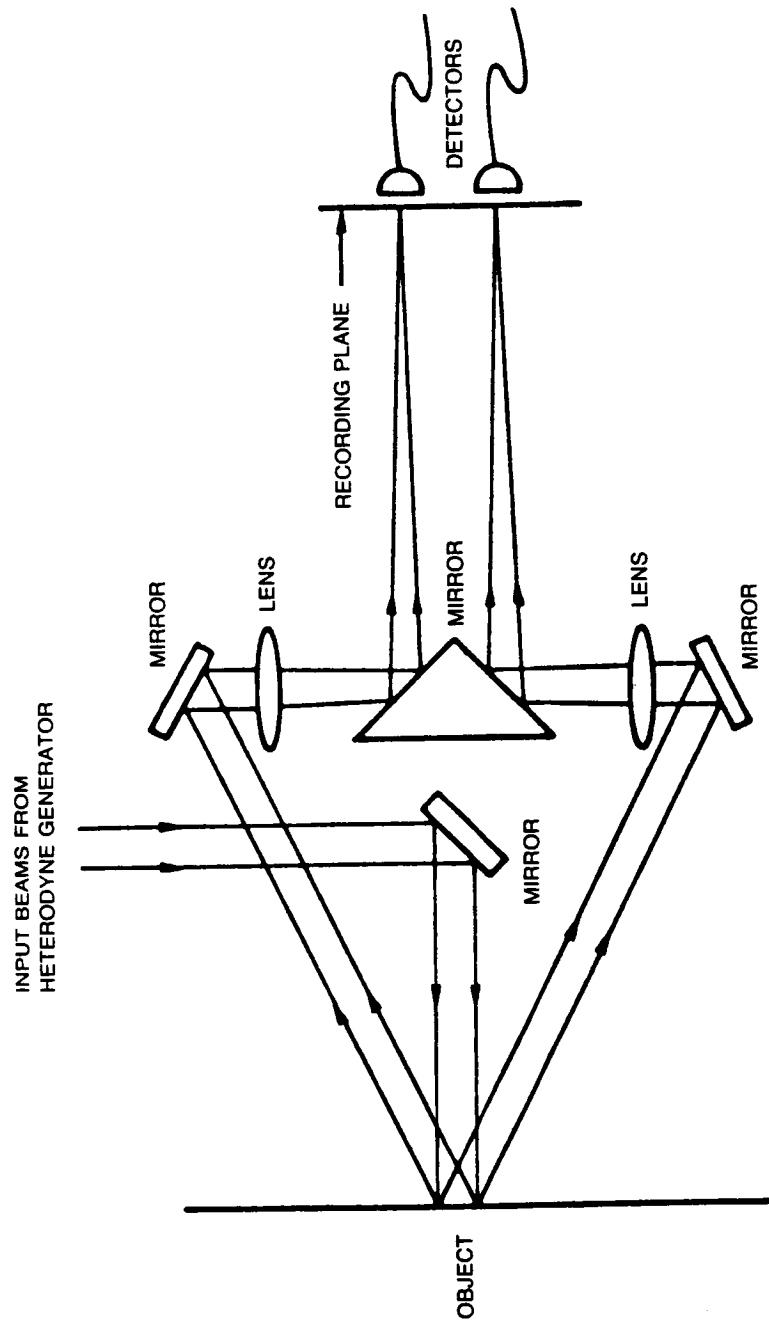


Figure 16. Heterodyne Optical Strain Sensor

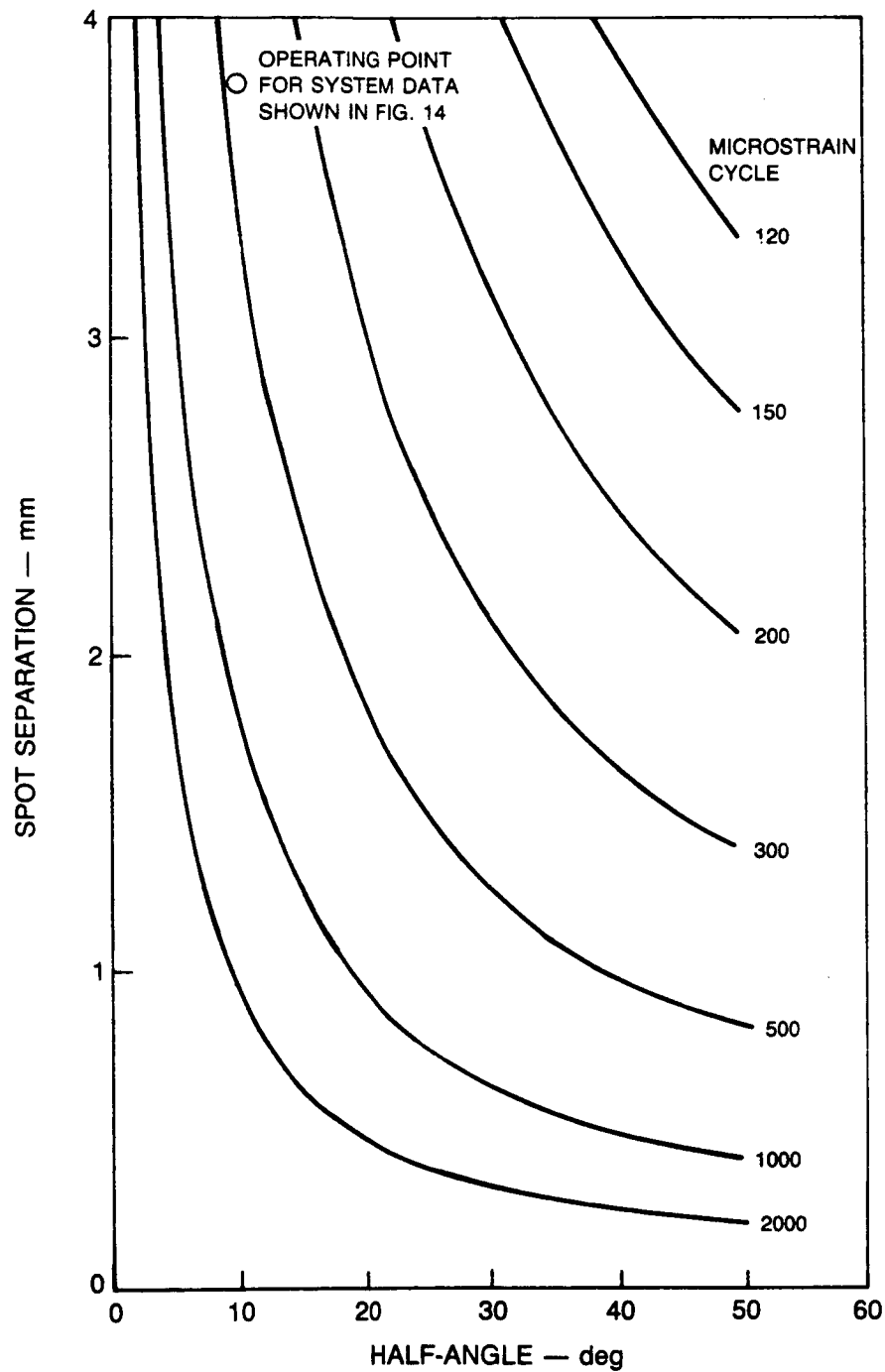
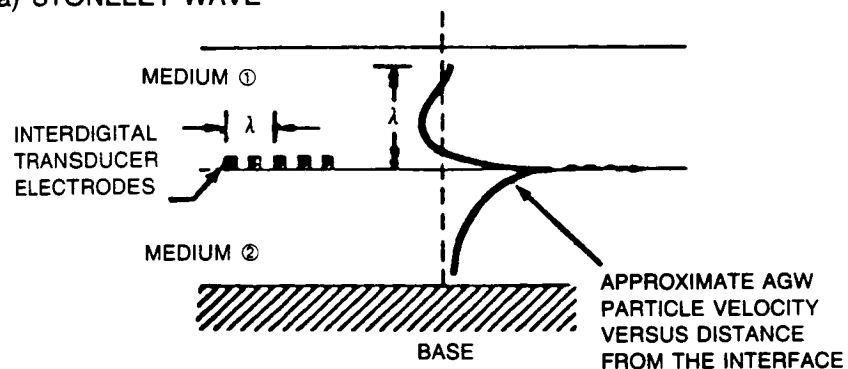


Figure 17. LOCI of Constant Sensitivity

a) STONELEY WAVE



b) MODIFIED STONELEY WAVE

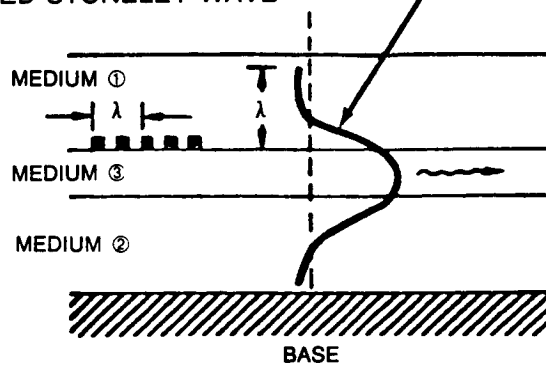


Figure 18. Acoustic Guided Waves Confined Within a Composite Coating

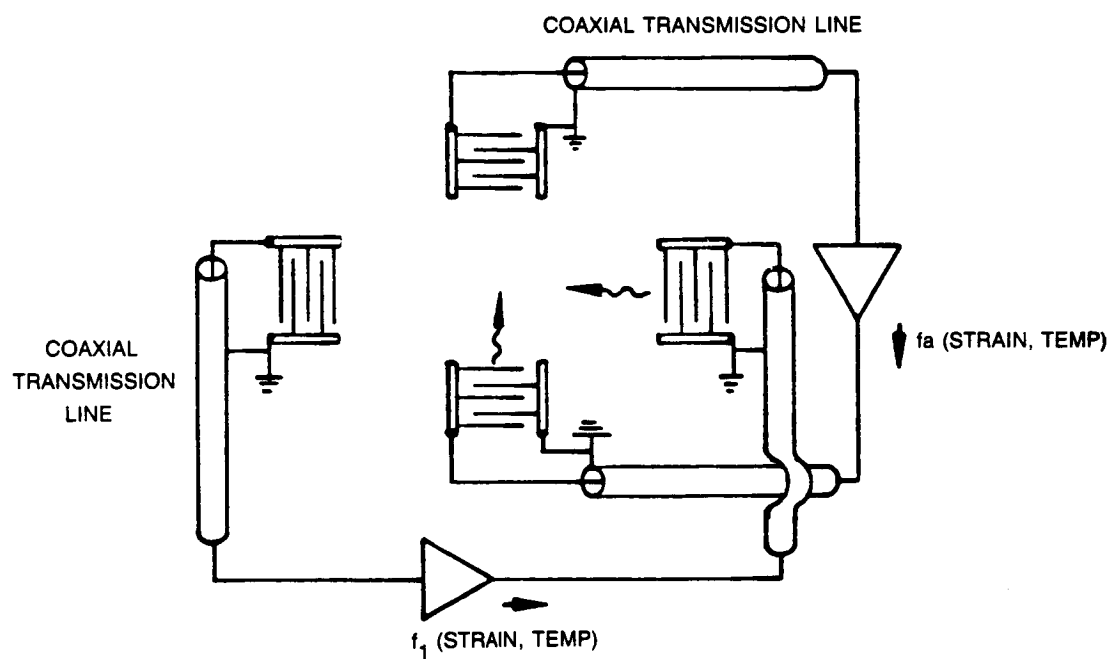
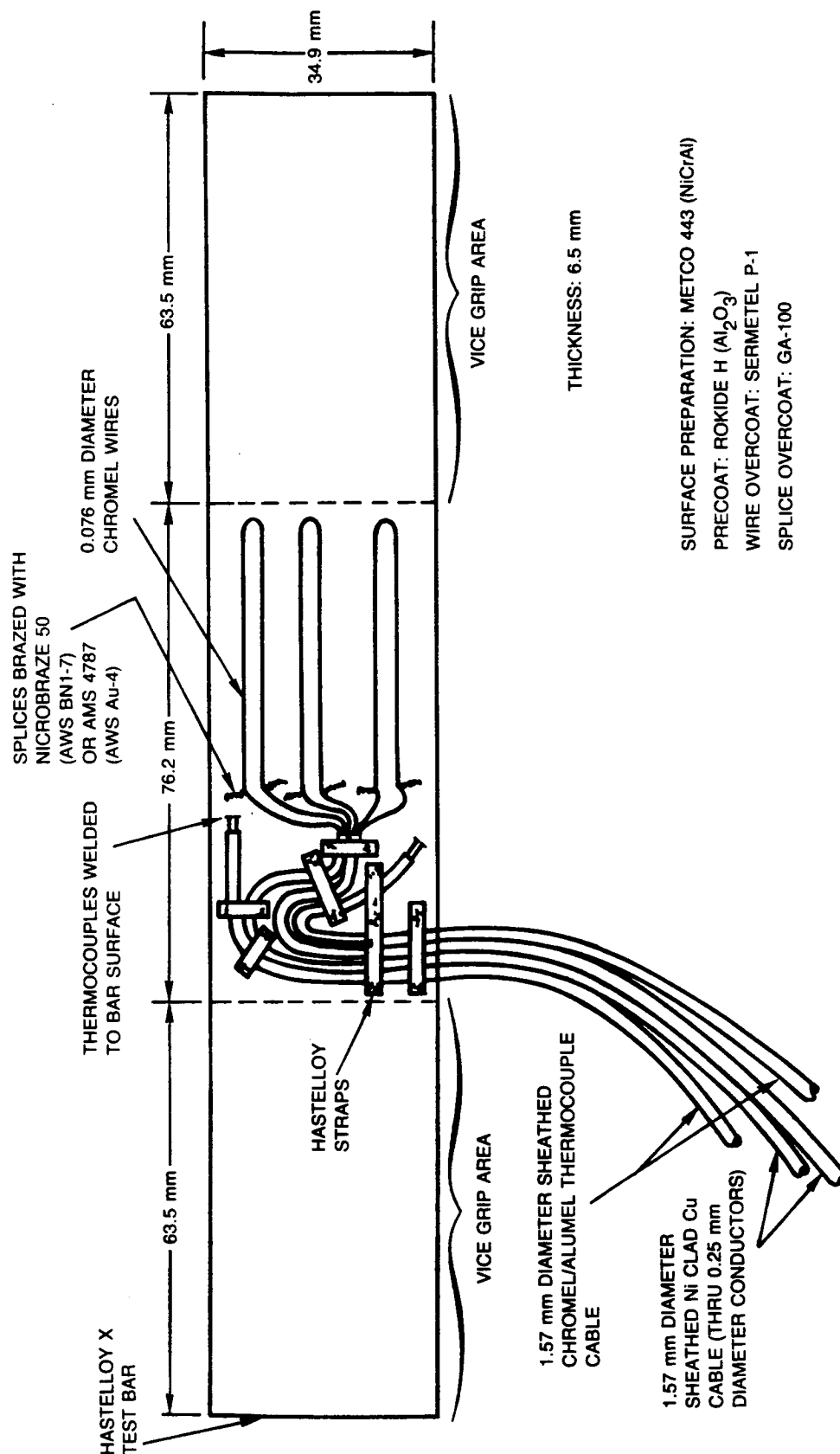
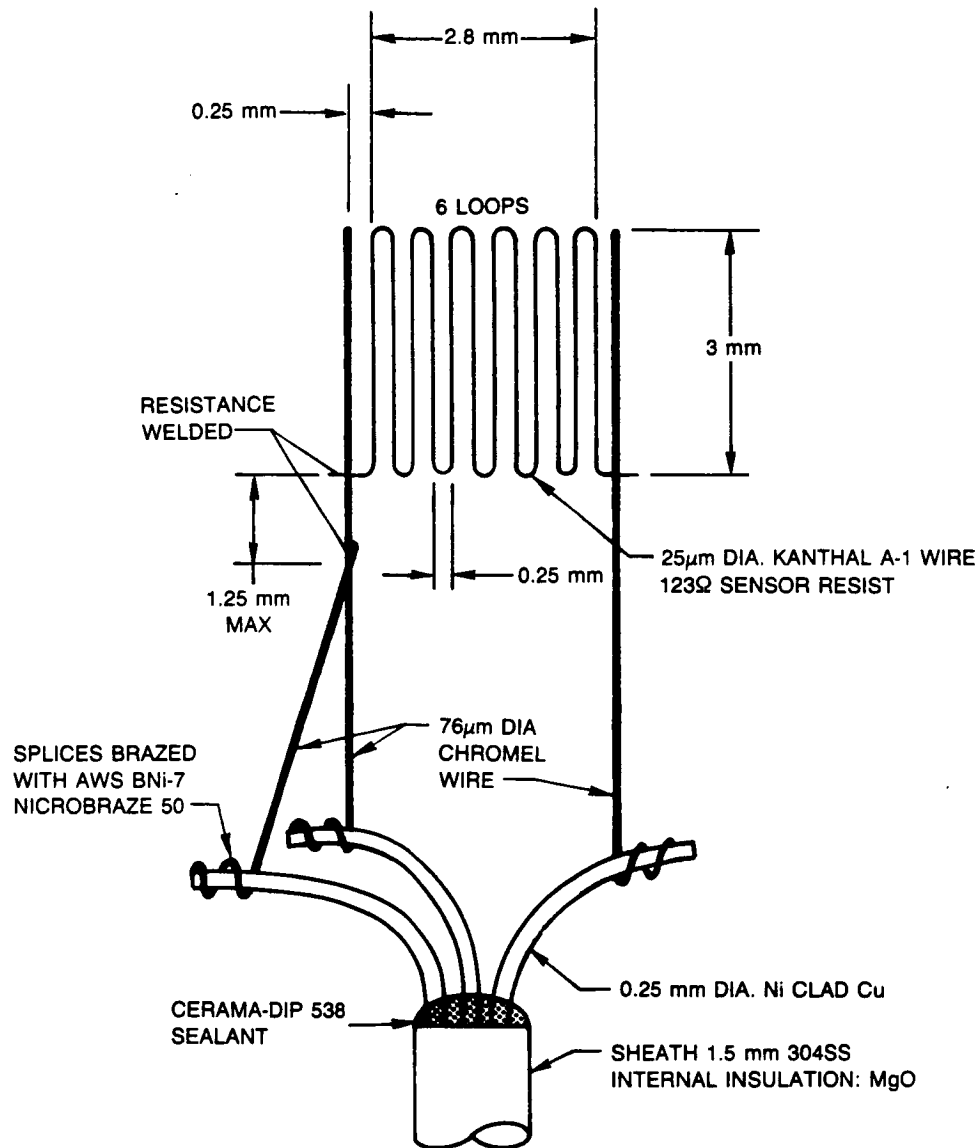


Figure 19. Frequency Output Sensor Configuration Having Two Orthogonal AGW Channels



SURFACE PREPARATION: METCO 443 (NiCrAl)
 PRECOAT: ROKIDE H (Al_2O_3)
 WIRE OVERCOAT: SERMETEL P-1
 SPLICE OVERCOAT: GA-100

Figure 20. Leadwire Test Specimen



INSTALLATION

SURFACE PREPARATION: NiCrAl (METCO 443) FLAME SPRAYED

PRECOAT: Al_2O_3 (ROKIDE "H") FLAME SPRAYED

OVERCOAT: $AlPO_4$ (SERMETEL P-1) CERAMIC CEMENT OR Al_2O_3 (ROKIDE "H") FLAME SPRAYED

EXTENSION LEADS: 3c Ni CLAD Cu WIRE WITH 1.55 mm DIAMETER S/S SHEATH AND 0.25 mm DIAMETER CONDUCTORS. CABLE IS STRAP WELDED TO SUBSTRATE AND SPLICES ARE BRAZED WITH AWS BNi-7 MICROBRAZE 50

Figure 21. FeCrAl Wire Strain Gage Description

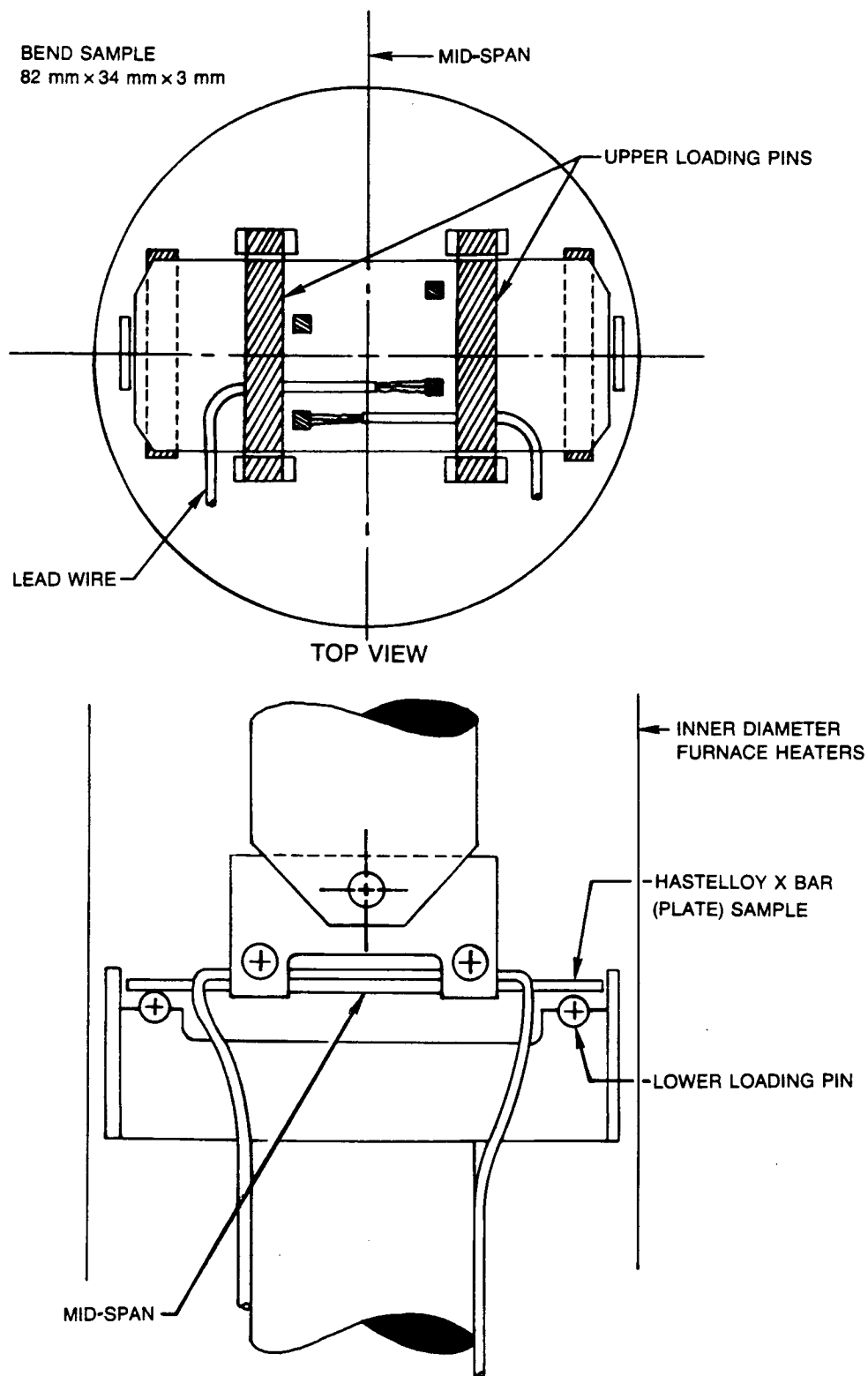


Figure 22. High Temperature Strain Gage Test Sample in Position

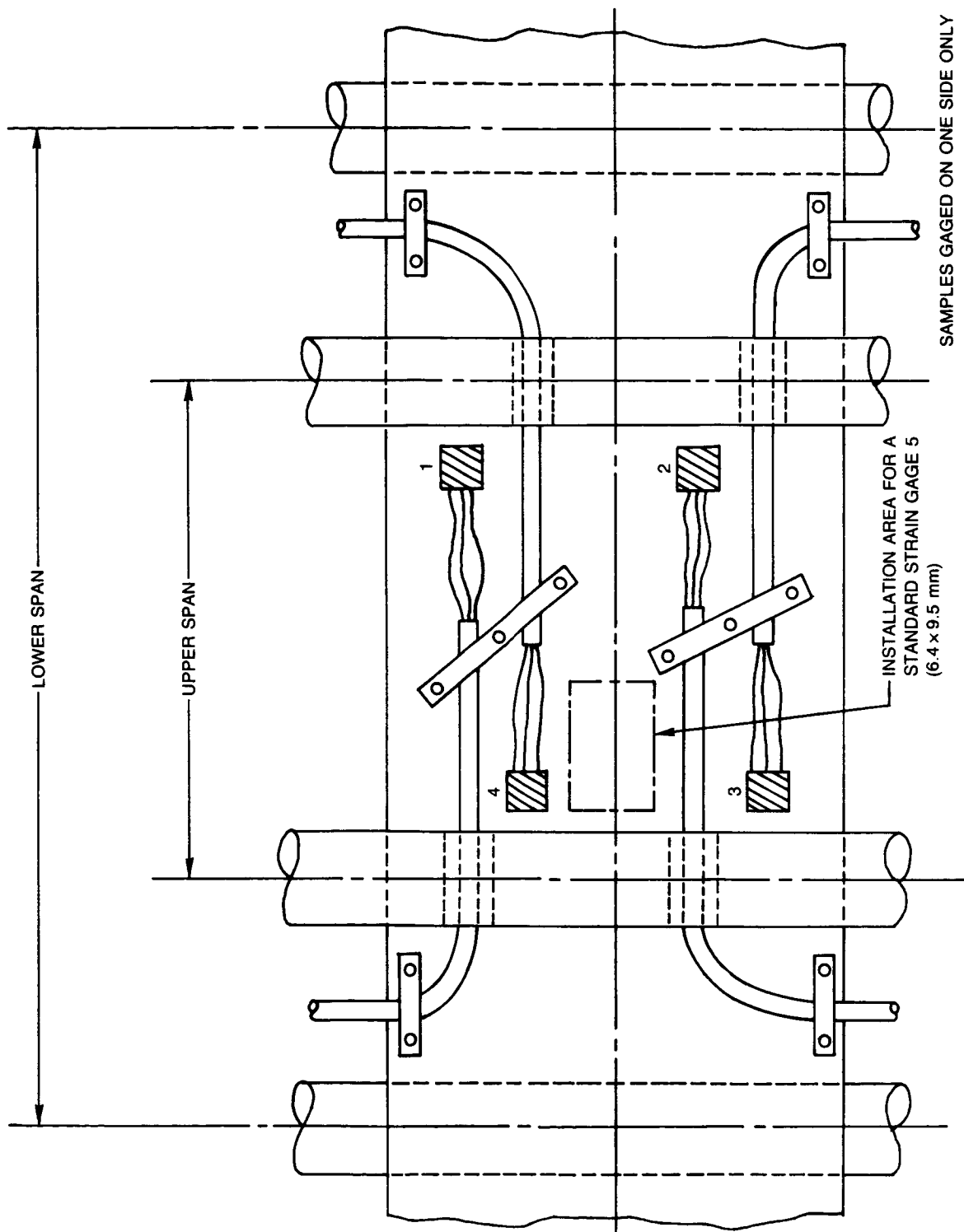


Figure 23. Strain Gage Wiring Layout for 4-Point Bend Samples

ORIGINAL PAGE IS
OF POOR QUALITY

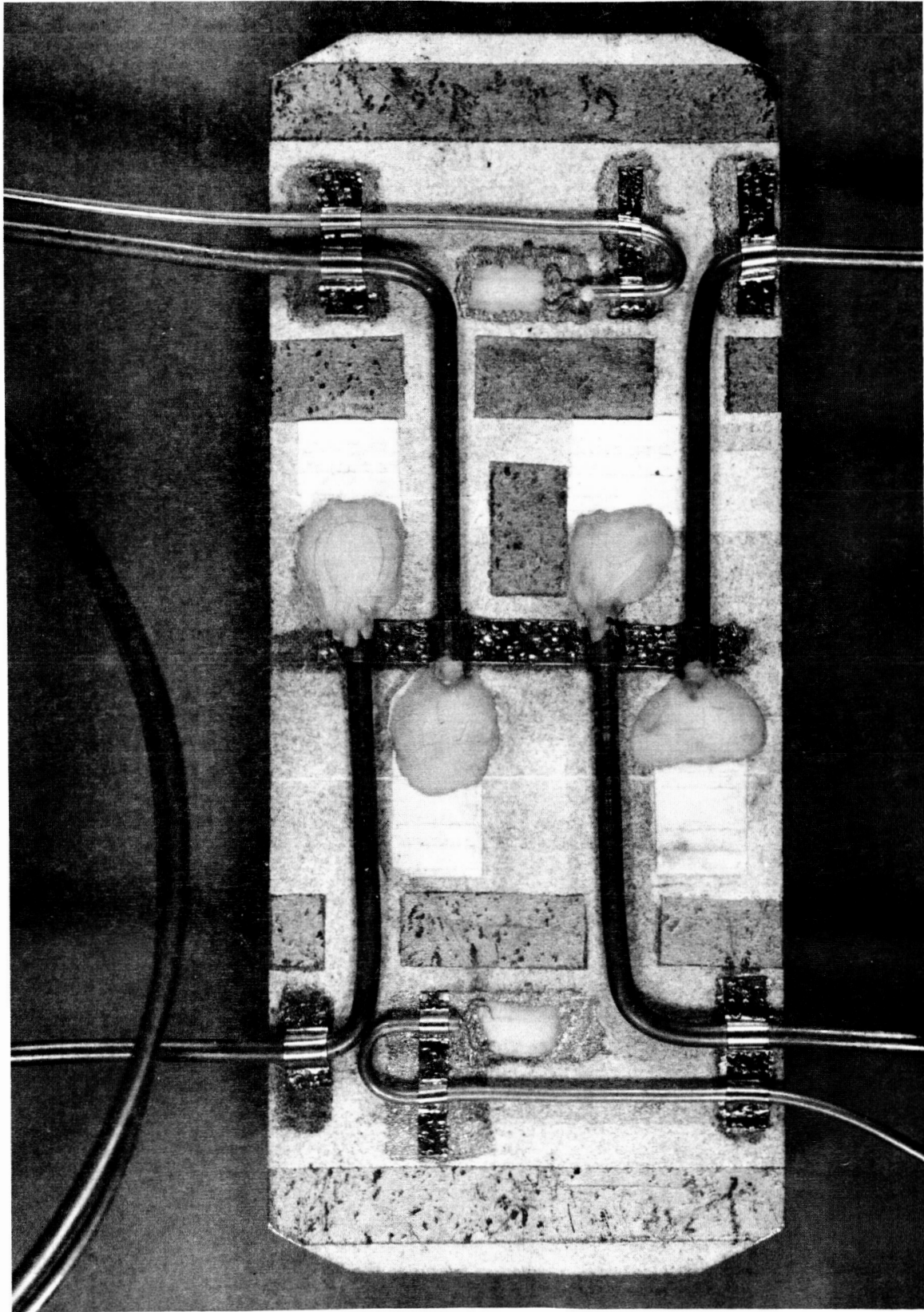


Figure 24. Strain Gage Test Specimen — For Four-Point Bend Testing

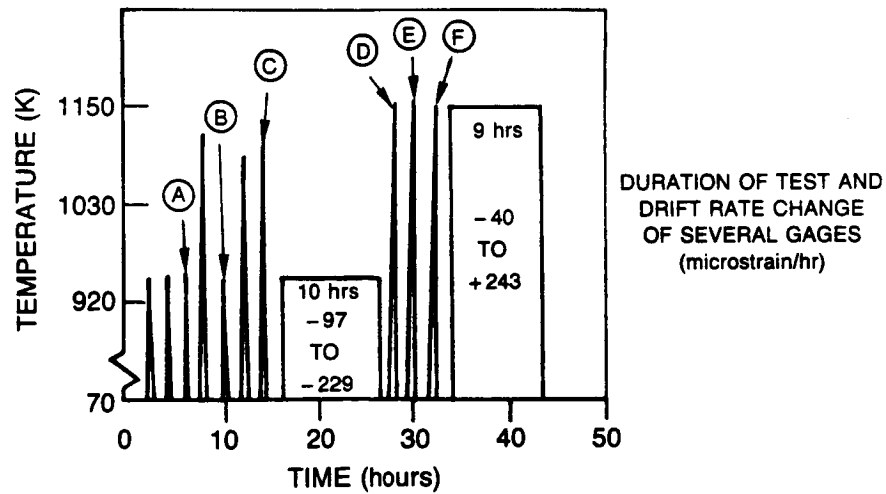
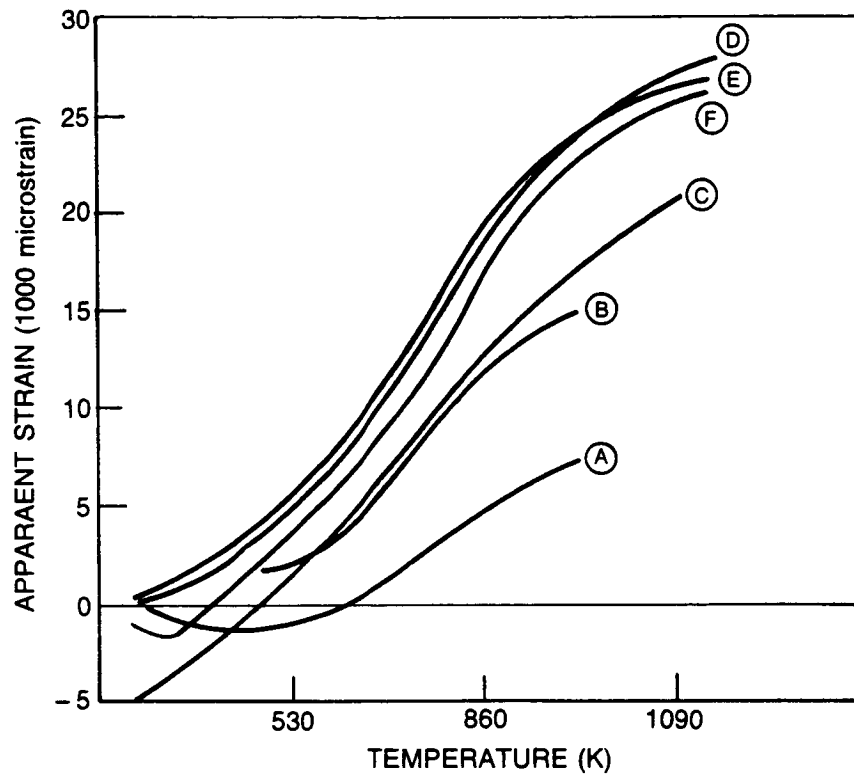


Figure 25. FeCrAl Wire Gage, Rokide H Overcoat (Specimen #4)

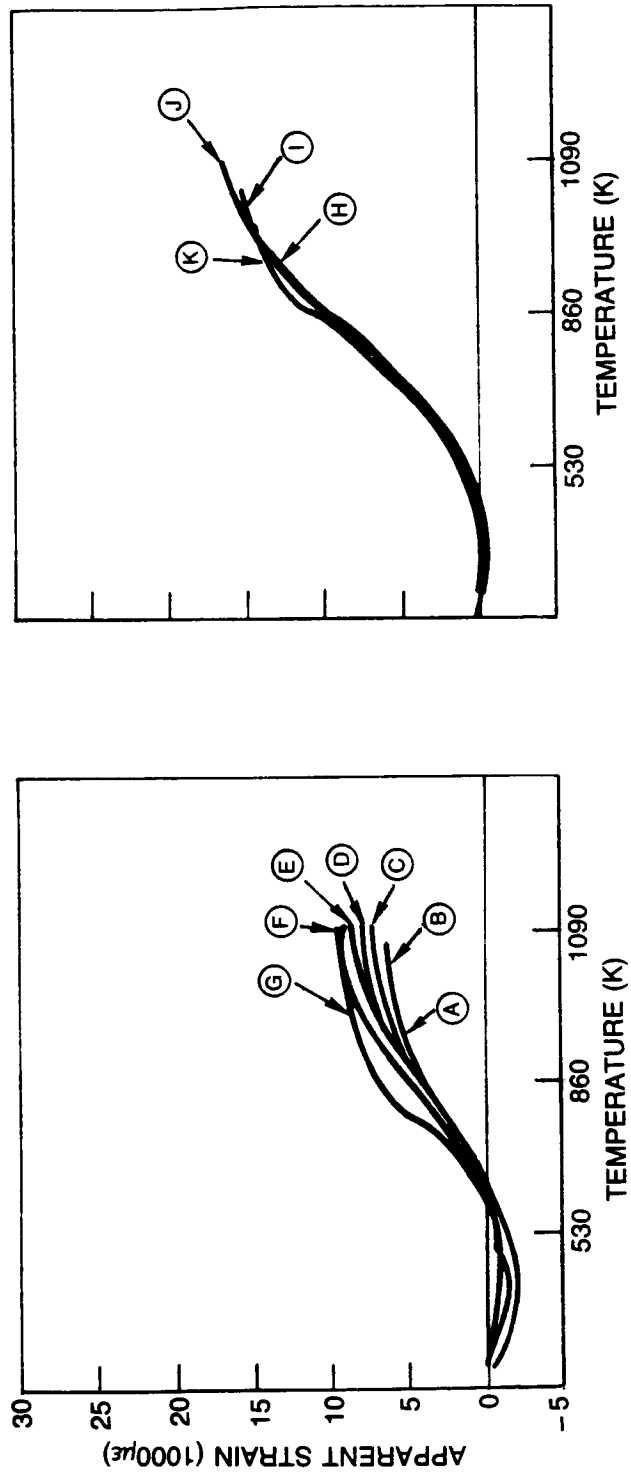
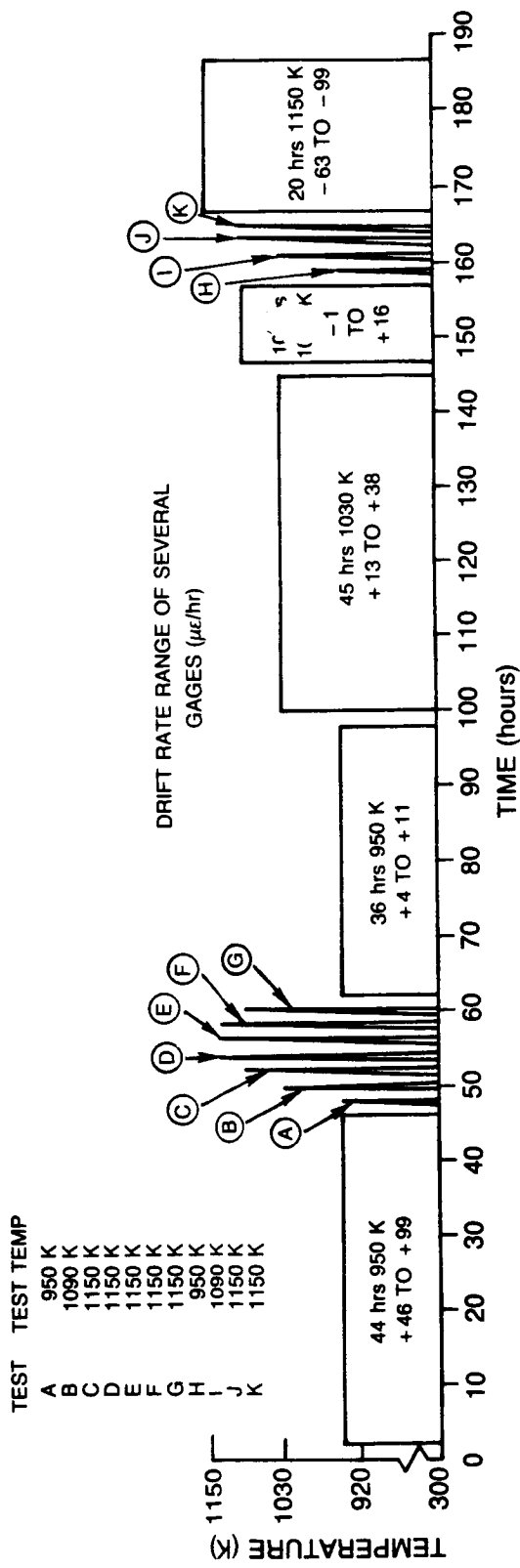


Figure 26. Kanthal A-1 Wire Gage, Sermetel P-1 Overcoat (Specimen #1)

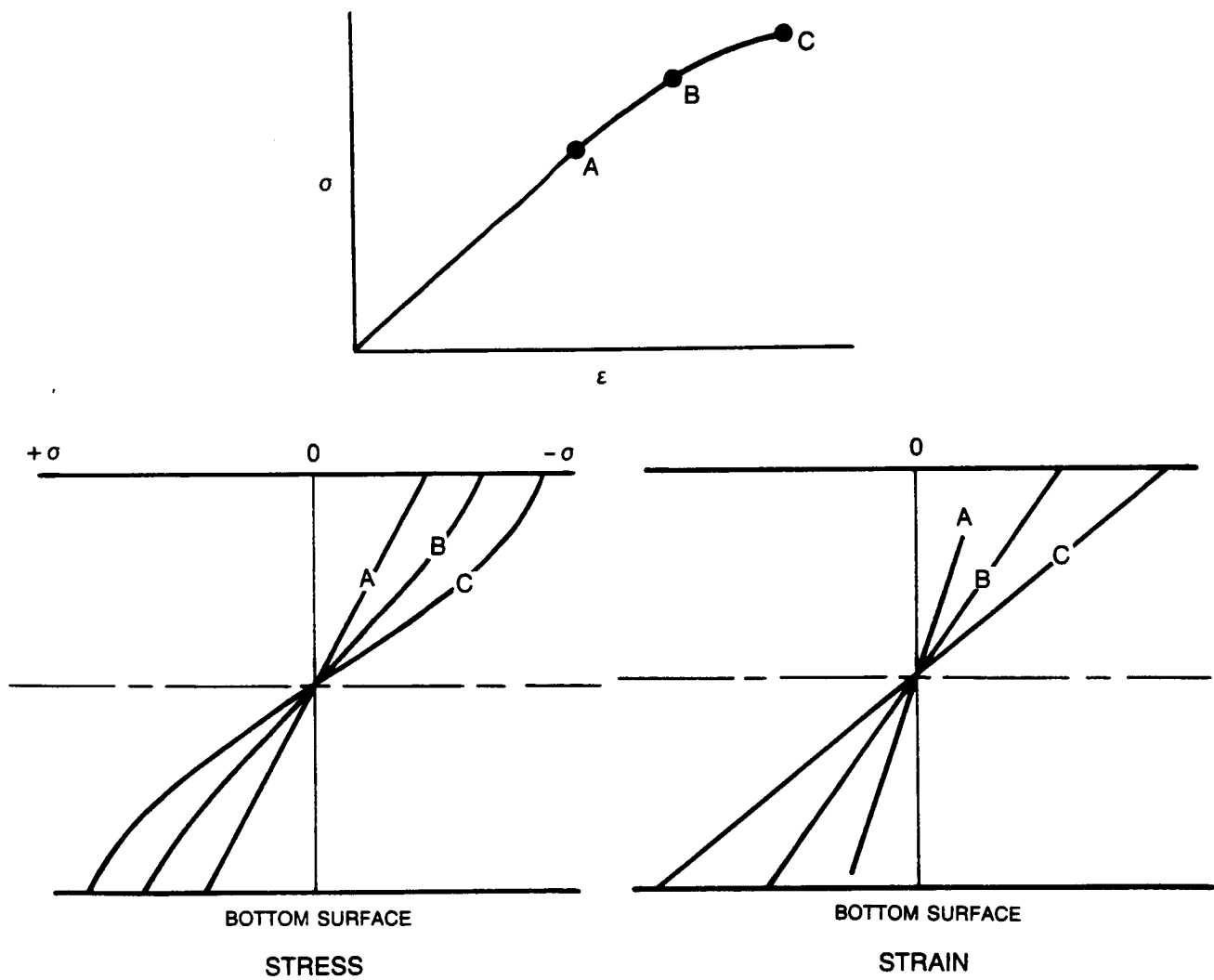


Figure 27. The Change in Stress and Strain with Distance from the Neutral Axis of a Beam Before and After a Small Amount of Plastic Yielding in Bending

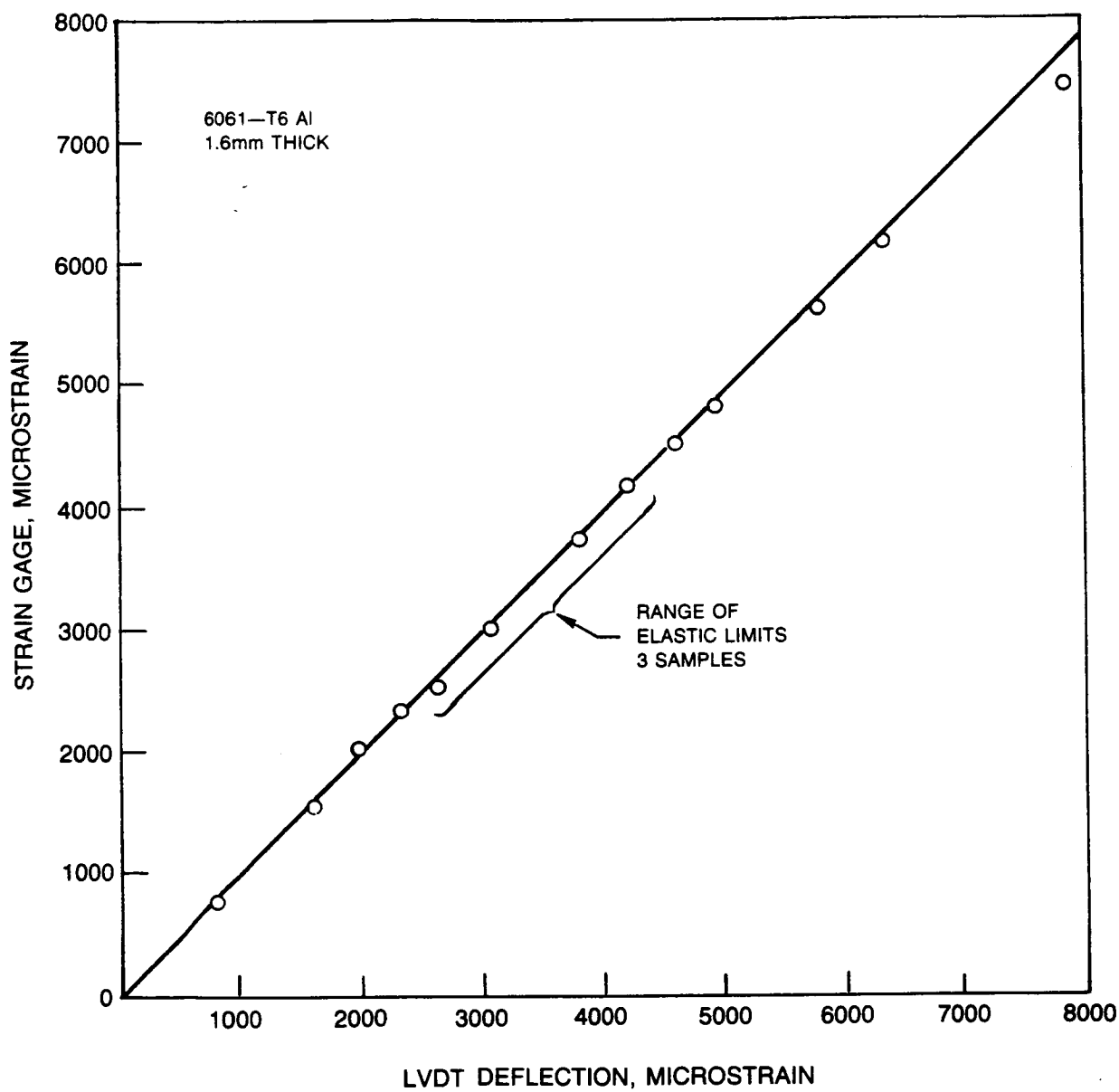
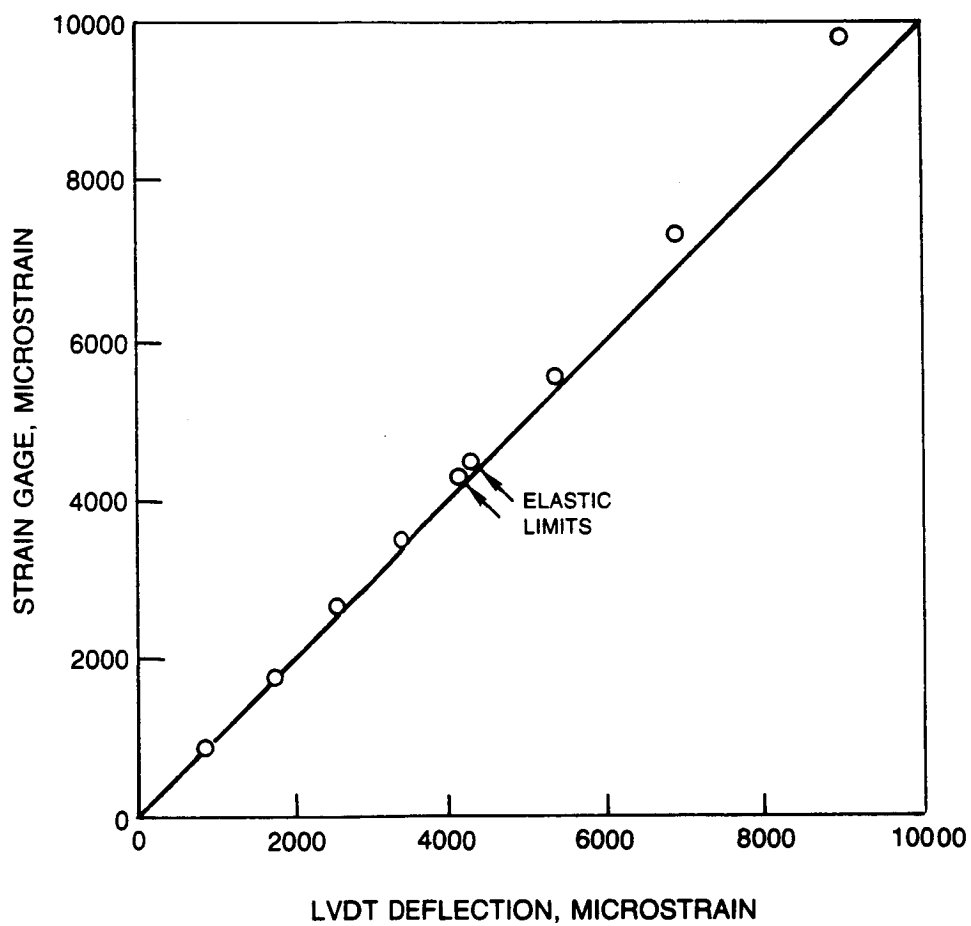


Figure 28. Comparison of Strain as Measured by Midspan Deflection and Strain Gage



**Figure 29. Comparison of Strain as Measured by Midspan Deflection and Strain Gage
2 Samples, 6061-T6 Al, 3.2 mm Thick**

SAMPLE #3, $\pm 2,000 \mu\epsilon$, KANTHAL A-1, ROKIDE "H"

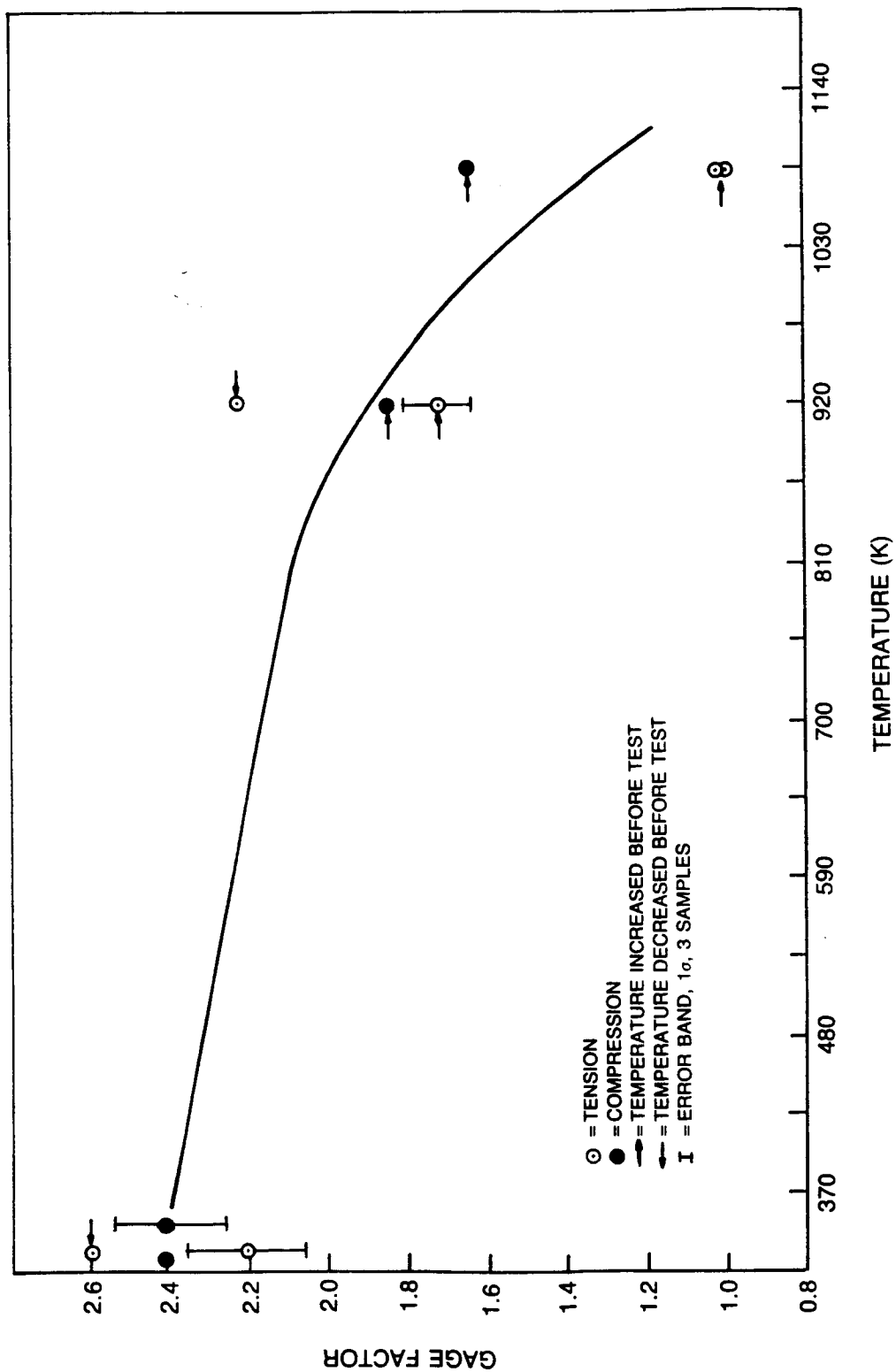


Figure 30. Gage Factor vs Temperature

SAMPLE #2, $\pm 2000\mu\epsilon$, KANTHAL A-1, SERMETAL P-1

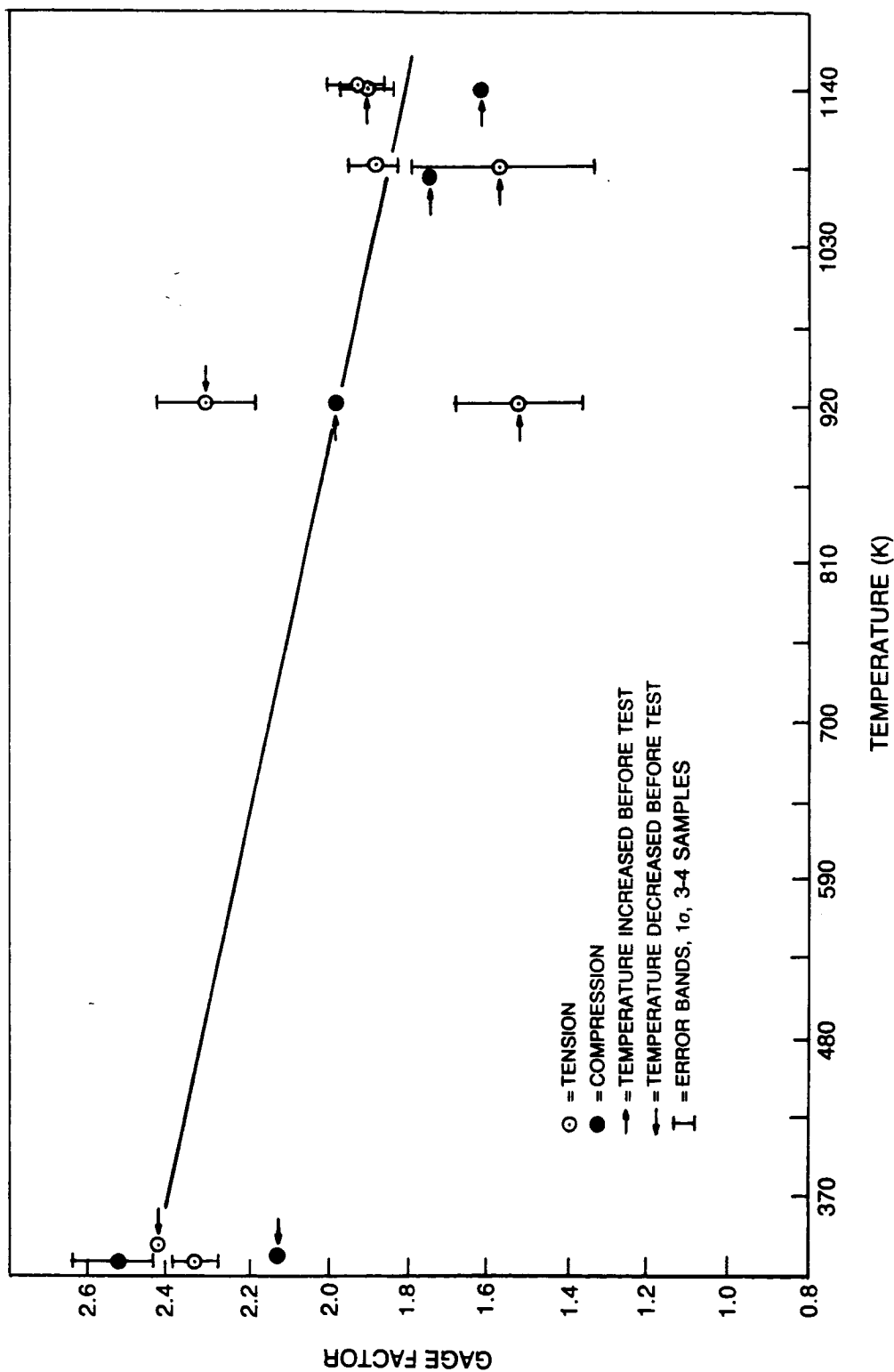


Figure 31. Gage Factor vs Temperature

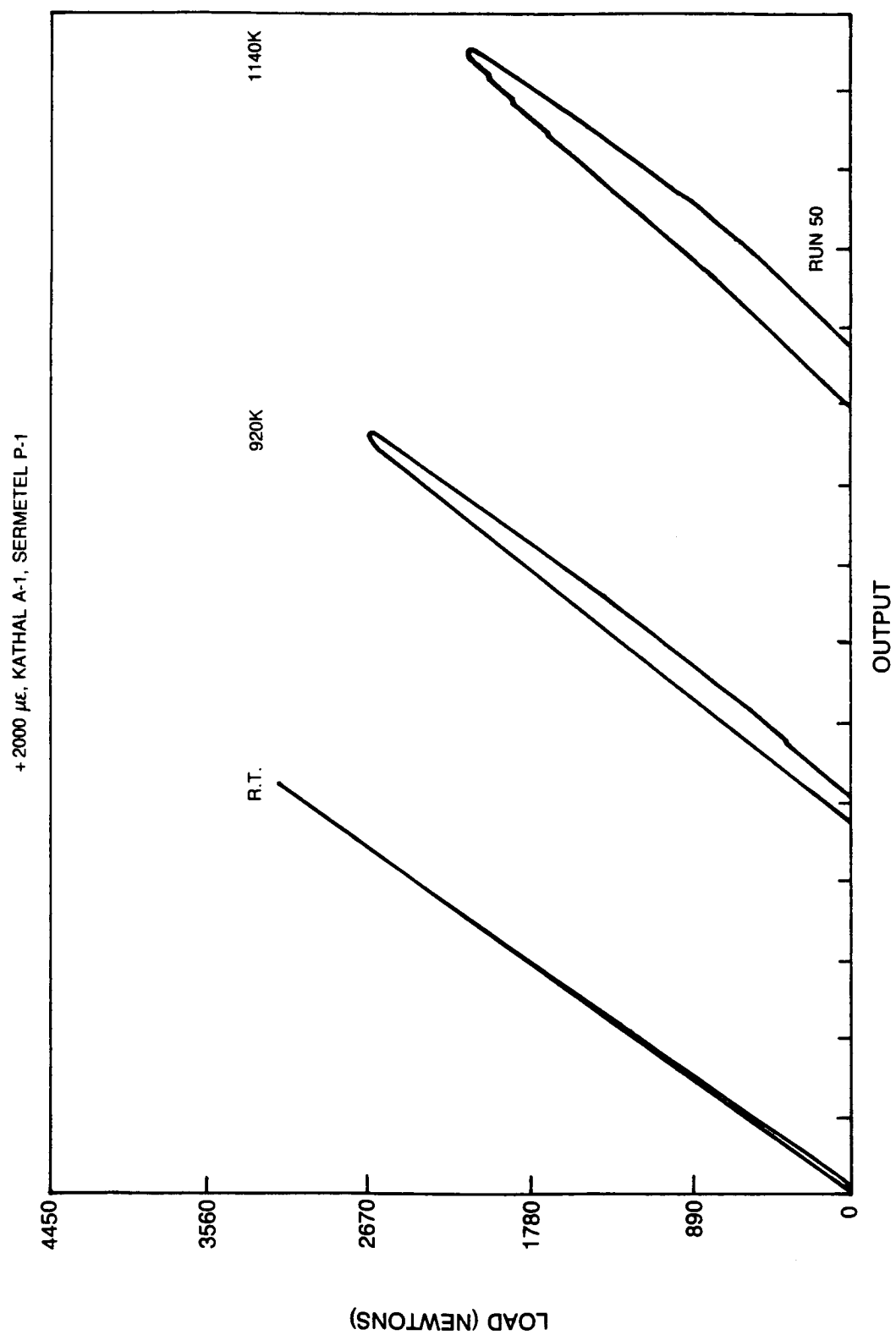


Figure 32. Data from Strain Gage #6

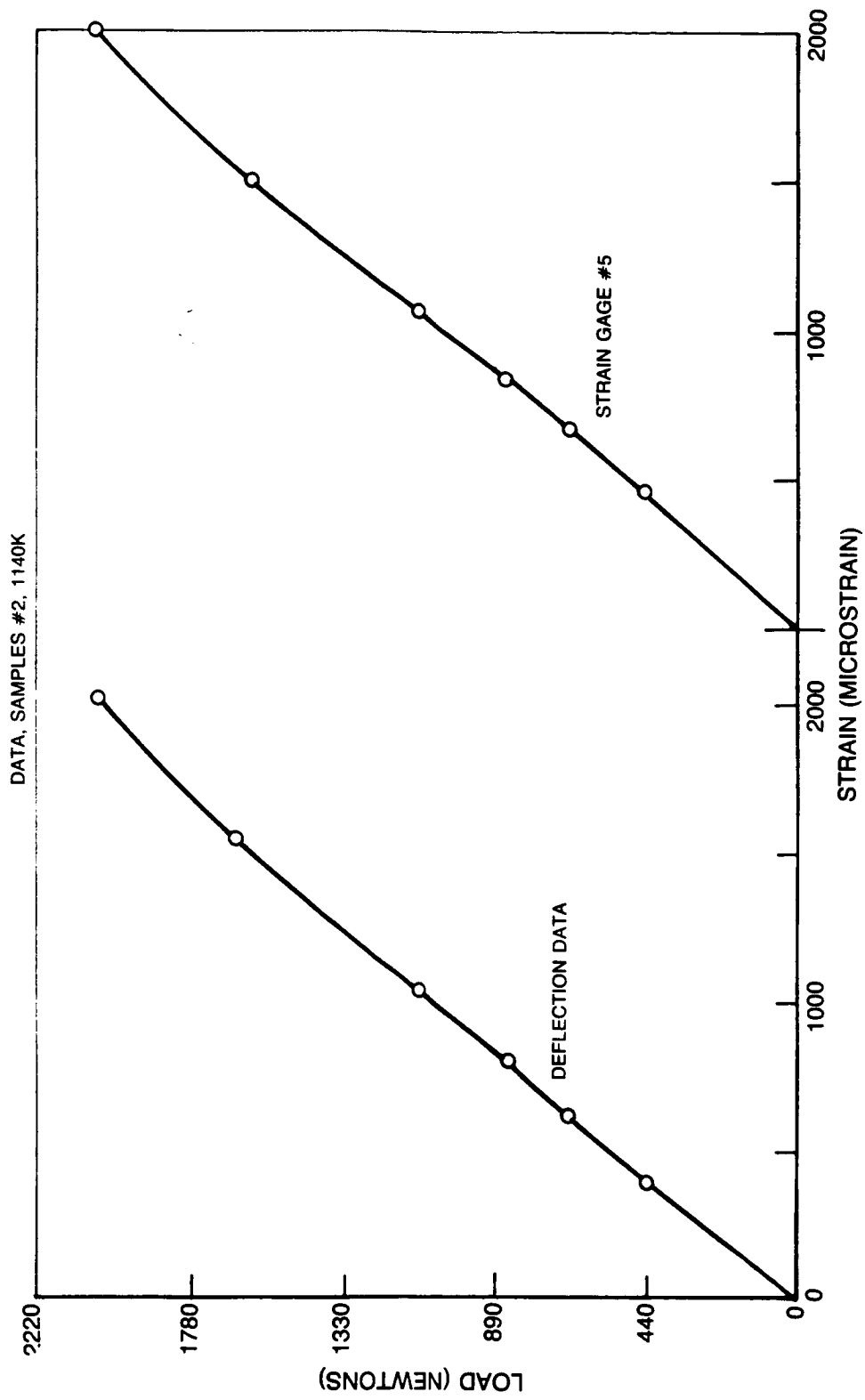


Figure 33. Stress/Strain Comparison Between Deflection and Strain Gage

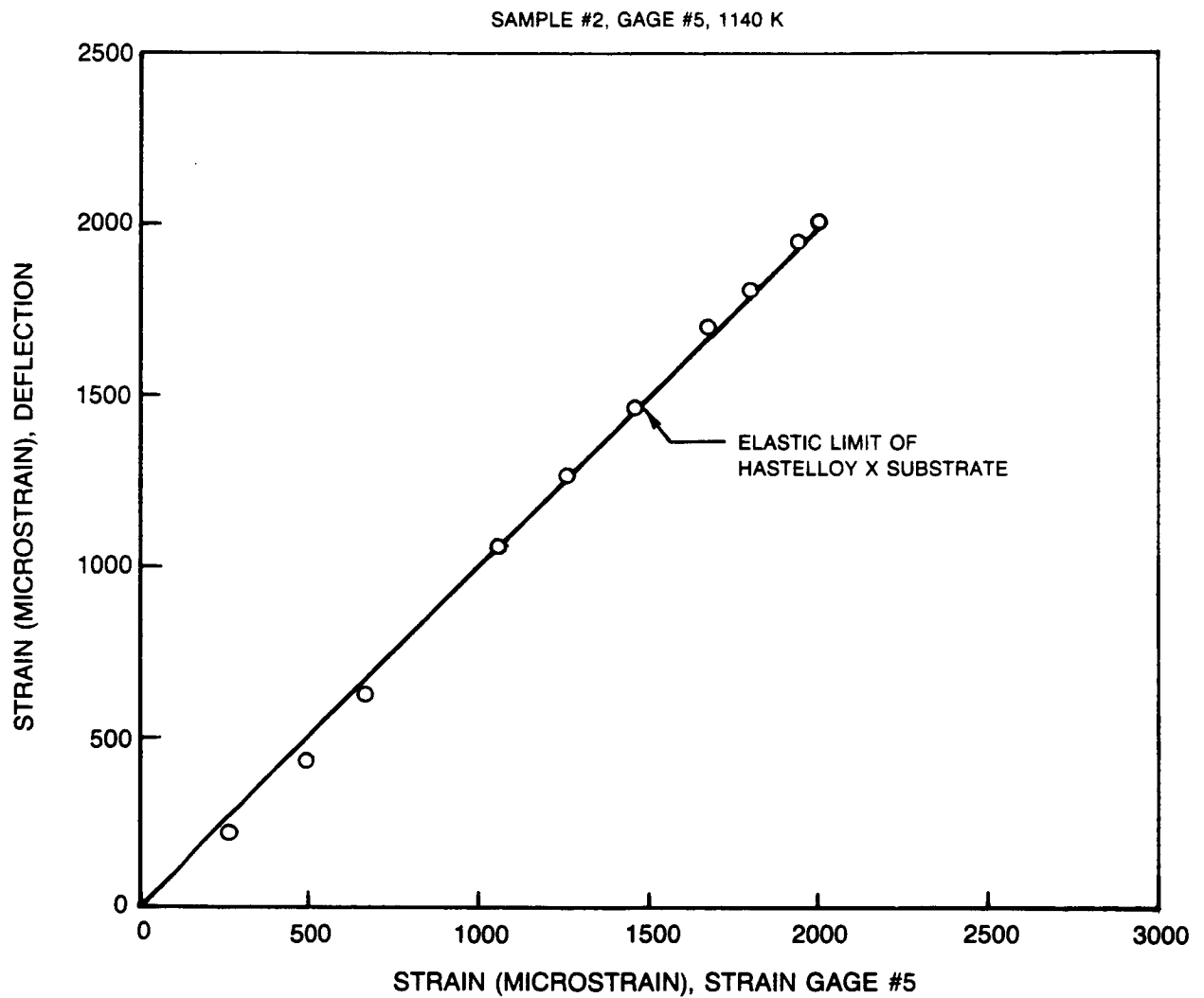


Figure 34. Relationship Between Strain From Deflection and Strain From Gage

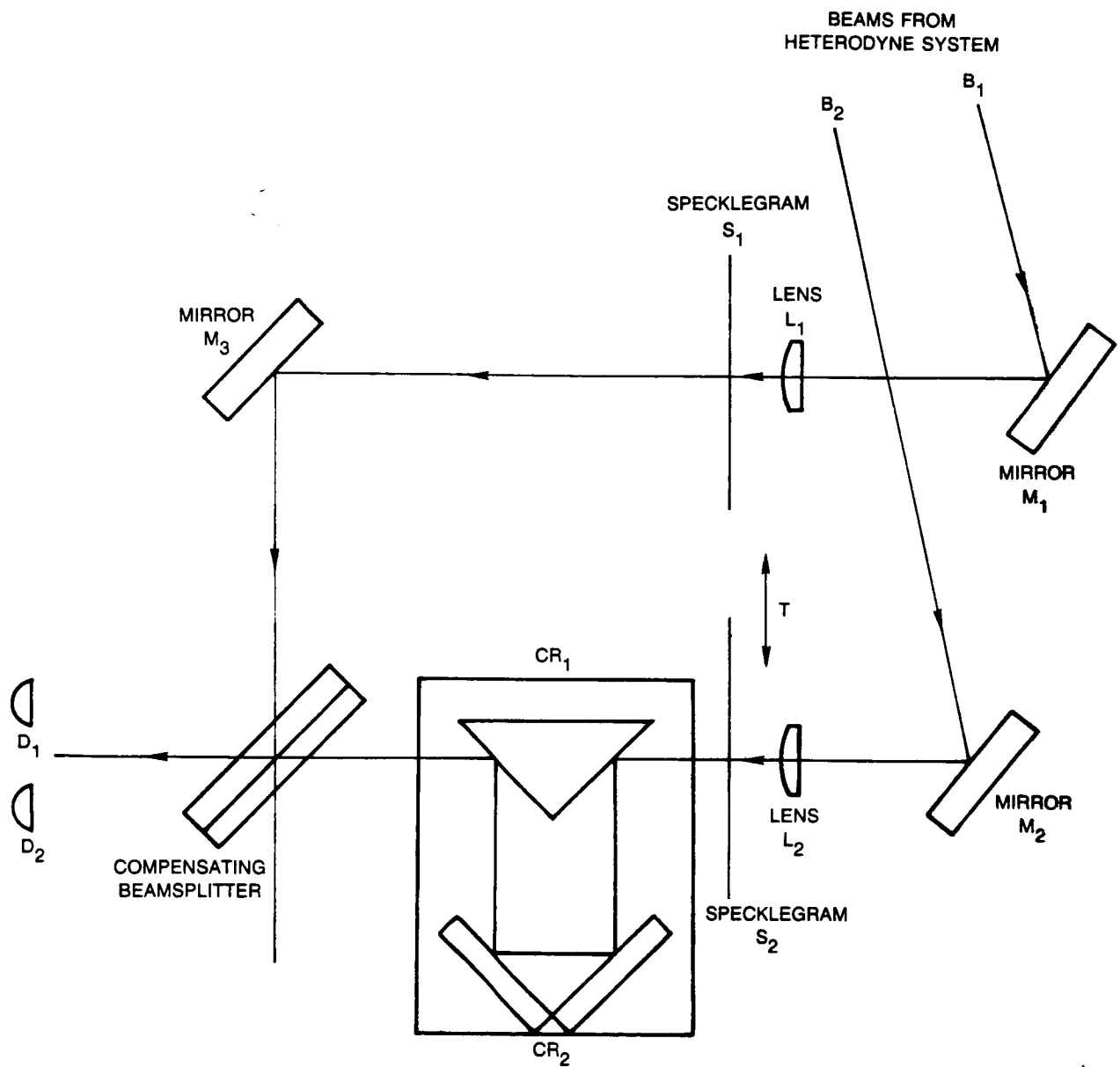


Figure 35. Heterodyne Readout System

GAGE LENGTH: 2.5mm

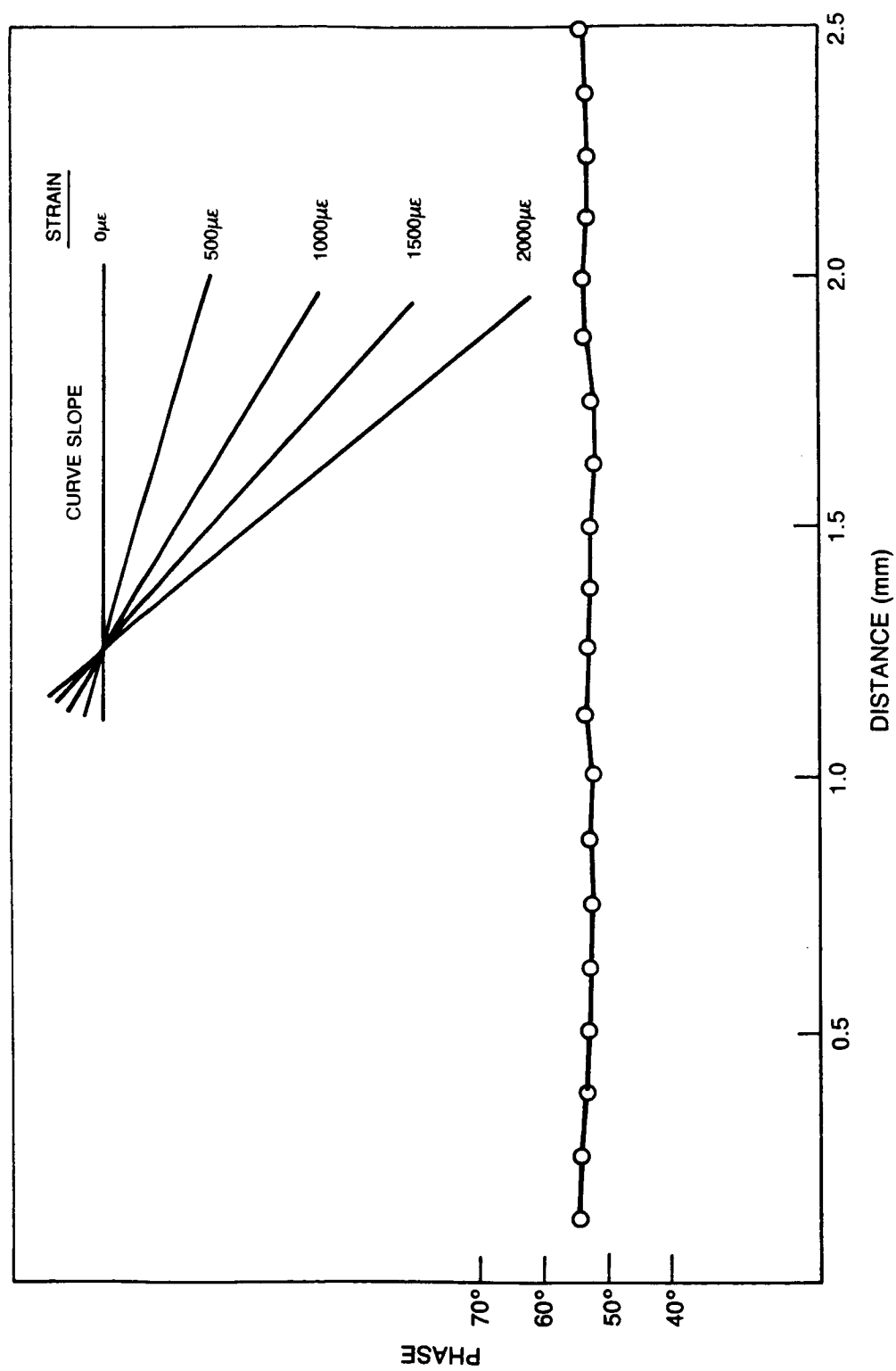


Figure 36. Phase Versus Translation of Specklegram Pair

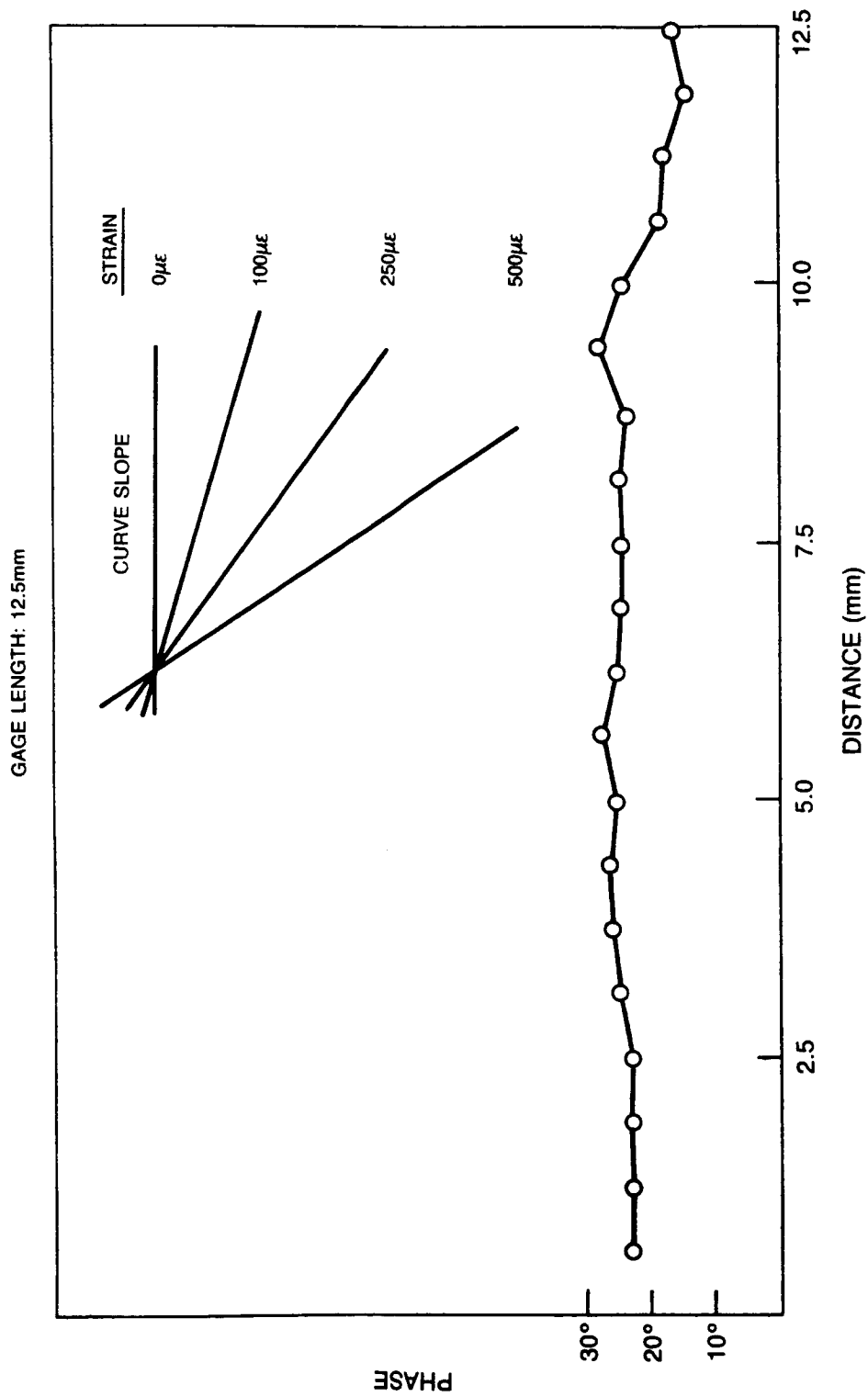


Figure 37. Phase Versus Translation of Specklegram Pair

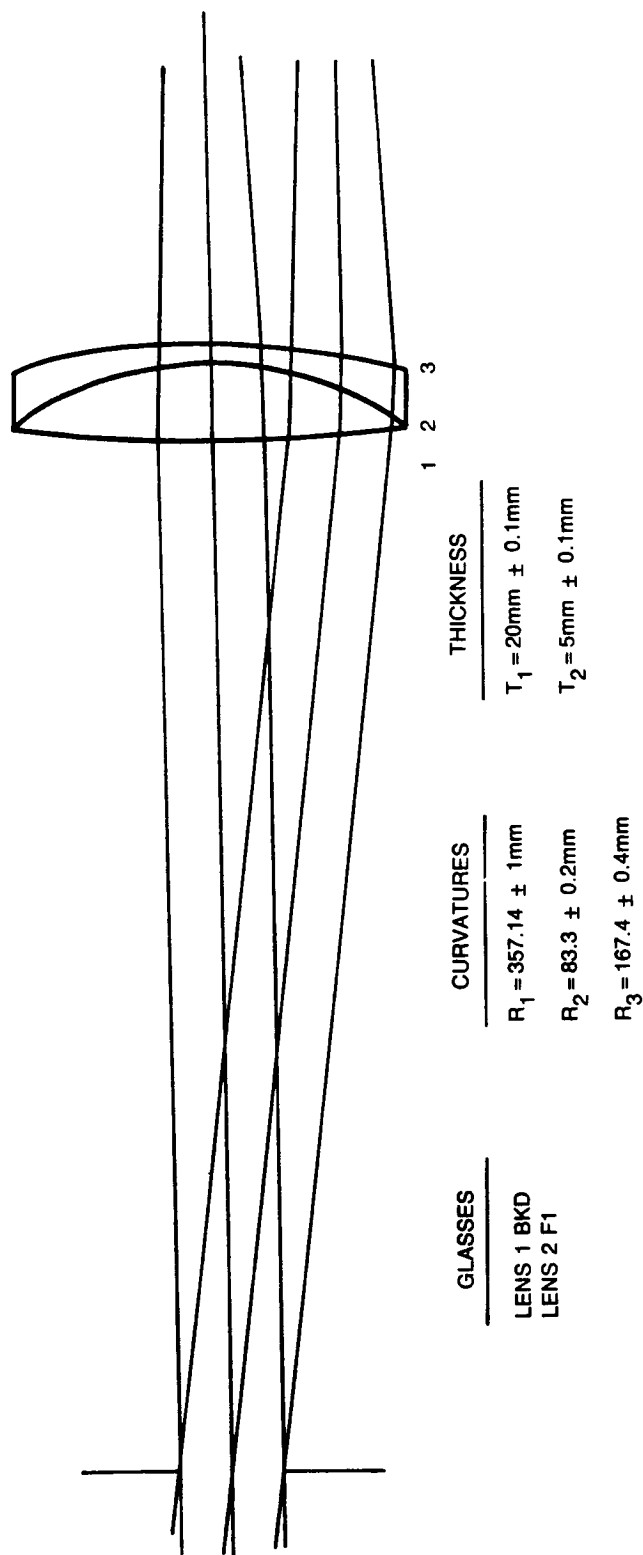


Figure 38. Telecentric Lens Design

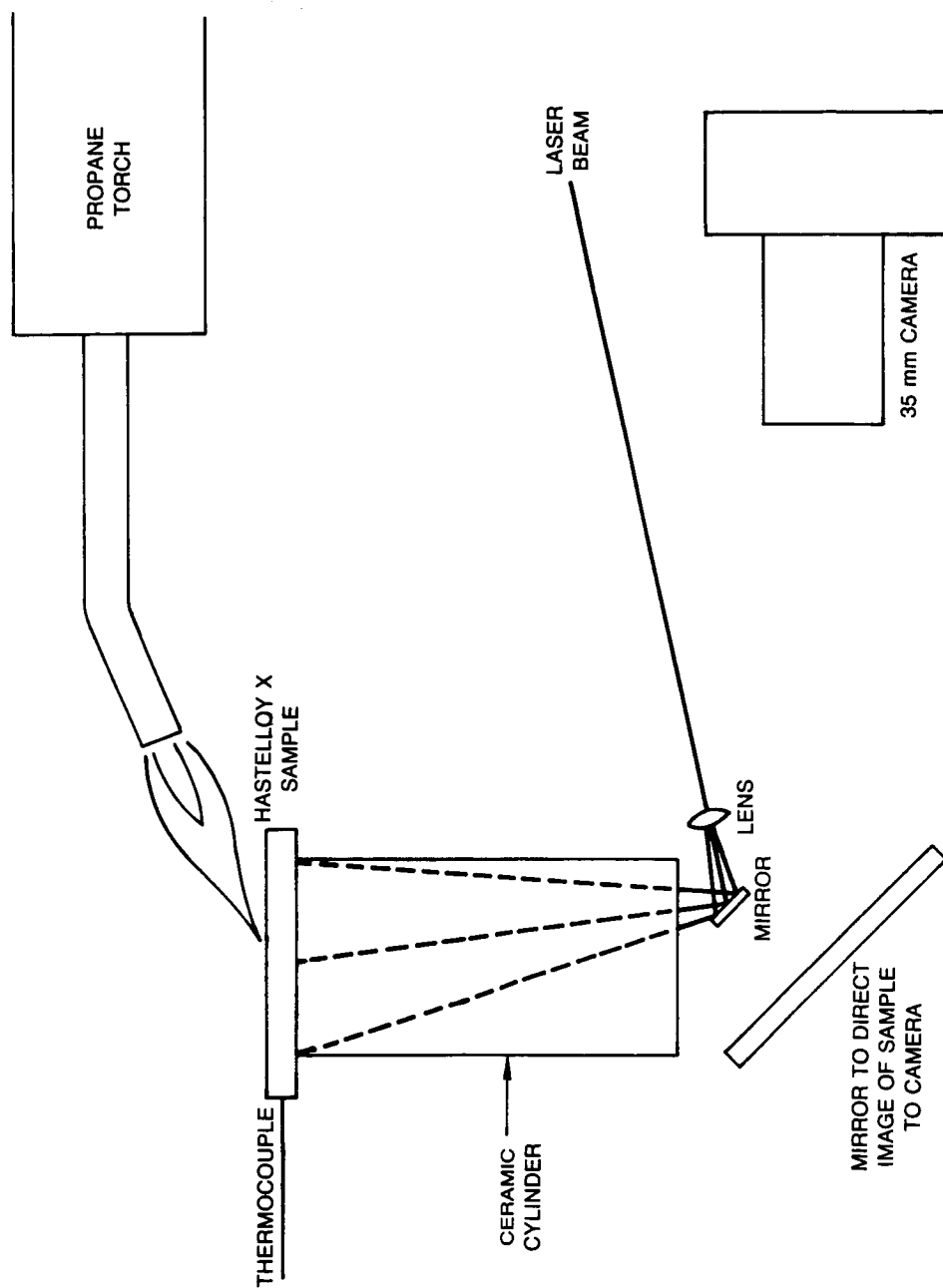


Figure 39. Experimental Set Up to Record Specklegrams from Heated Hastelloy X

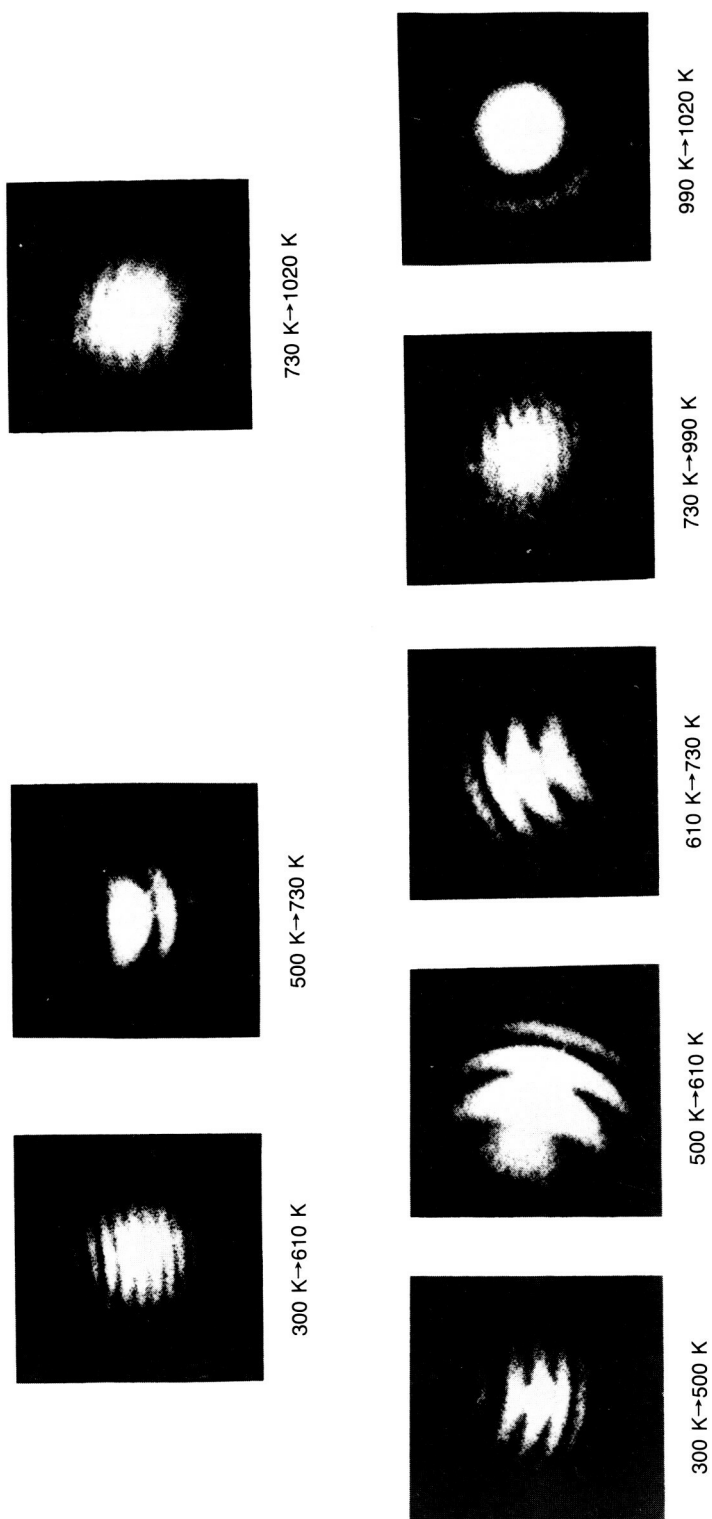


Figure 40. Correlation of Specklegrams at Different Temperatures

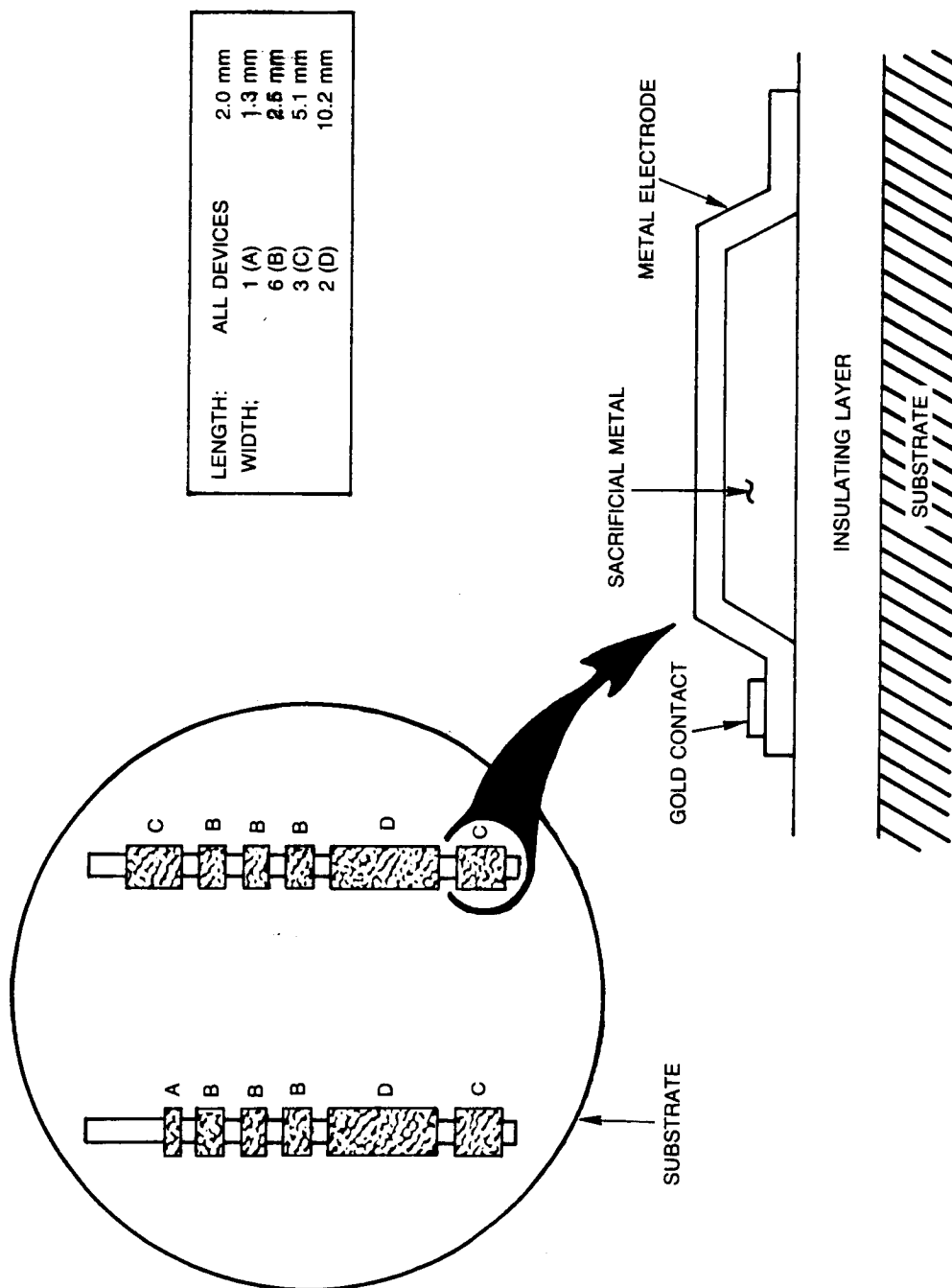


Figure 41. Thin Film Capacitive Sensor Test Sensor Design

ORIGINAL PAGE IS
OF POOR QUALITY

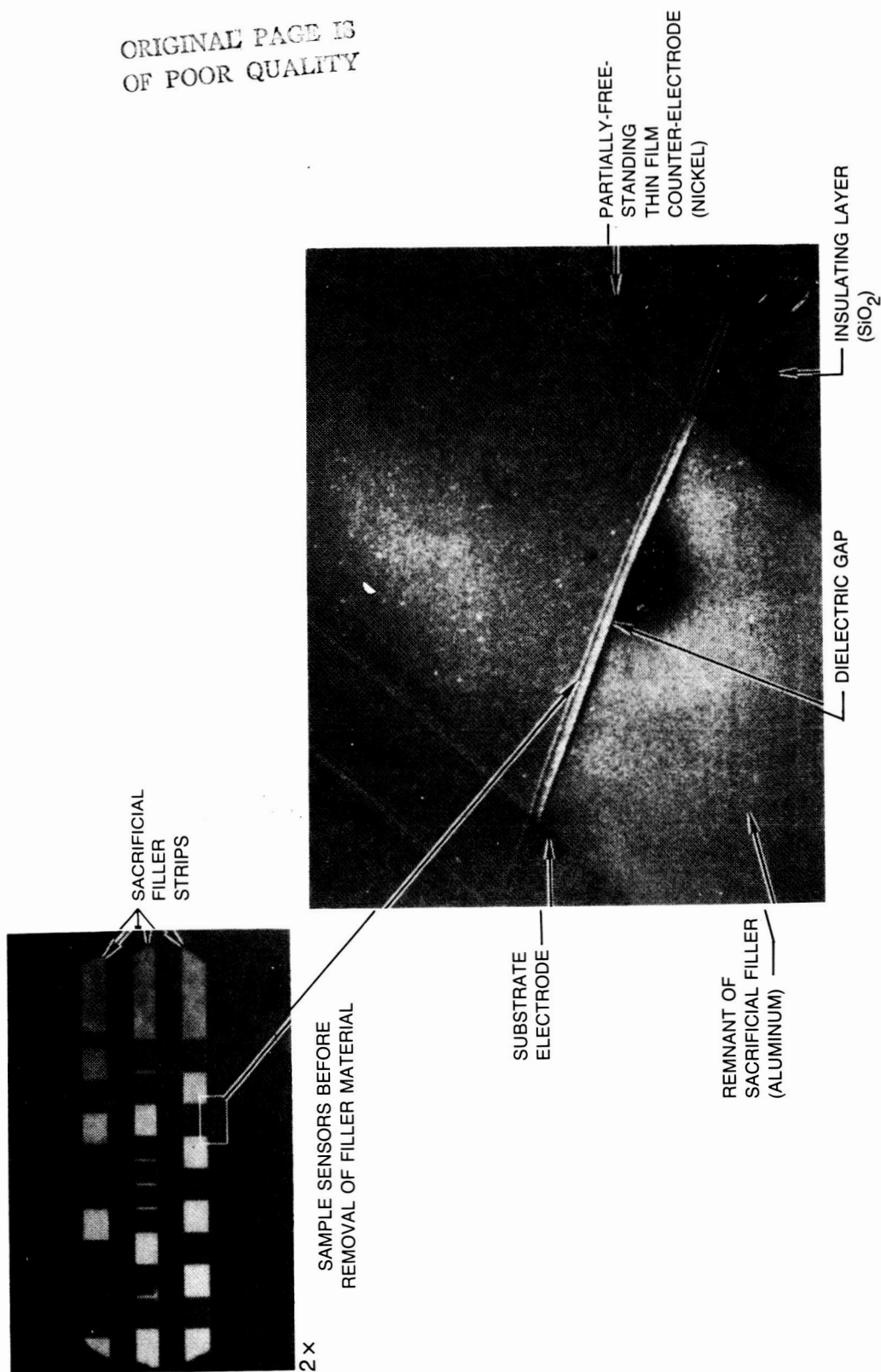


Figure 42. Thin Film Capacitive Sensor

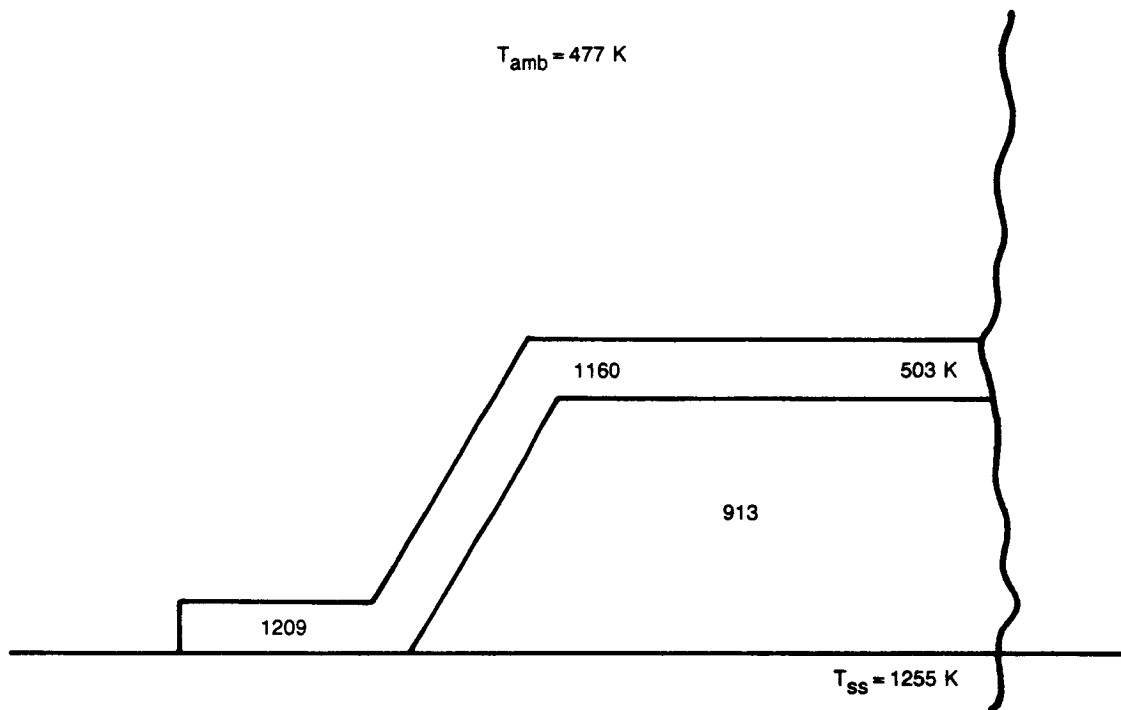


Figure 43. Temperature Distribution for Uncapped Device

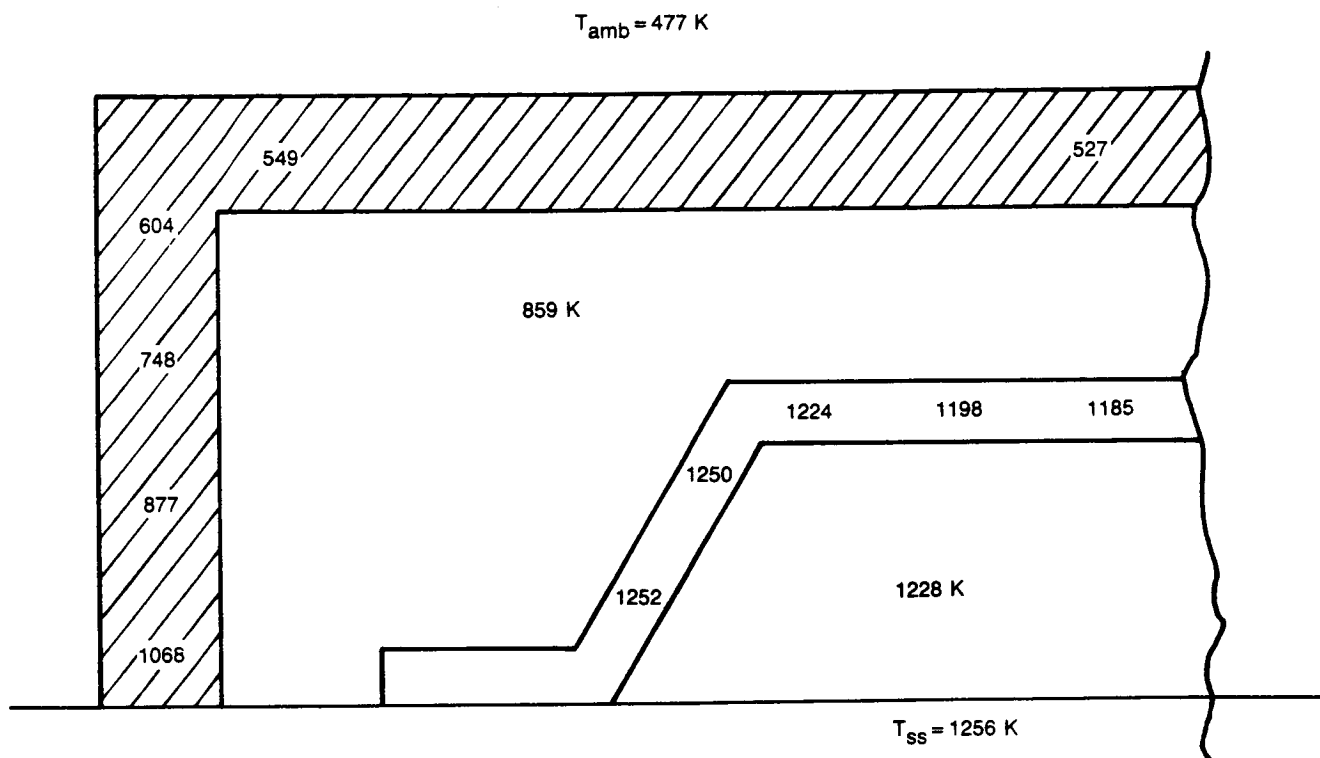


Figure 44. Temperature Distribution for Simple Radiation Shield

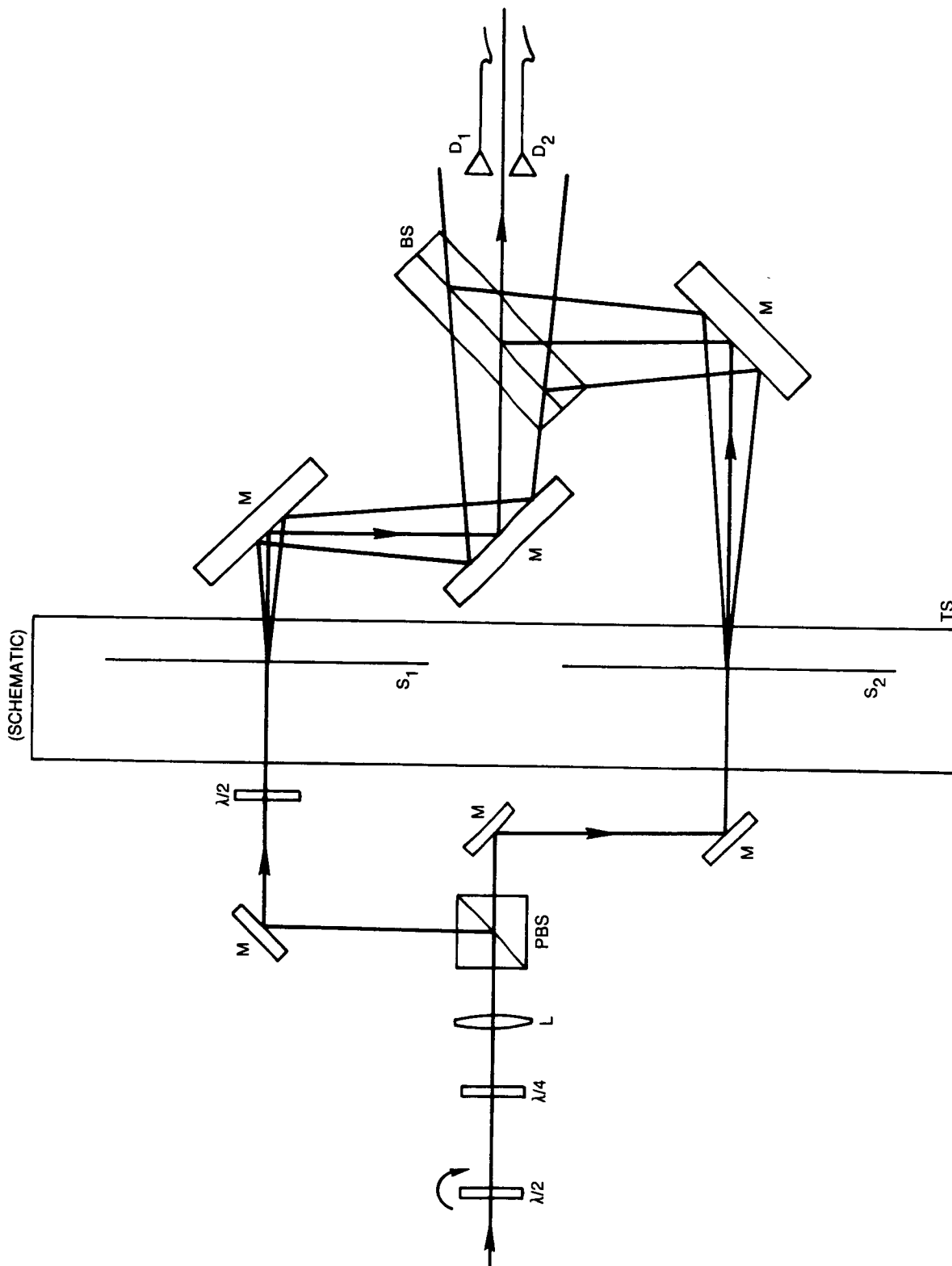


Figure 45. Specklegram Readout System

ORIGINAL PAGE IS
OF POOR QUALITY



Figure 46. Specklegram Readout System

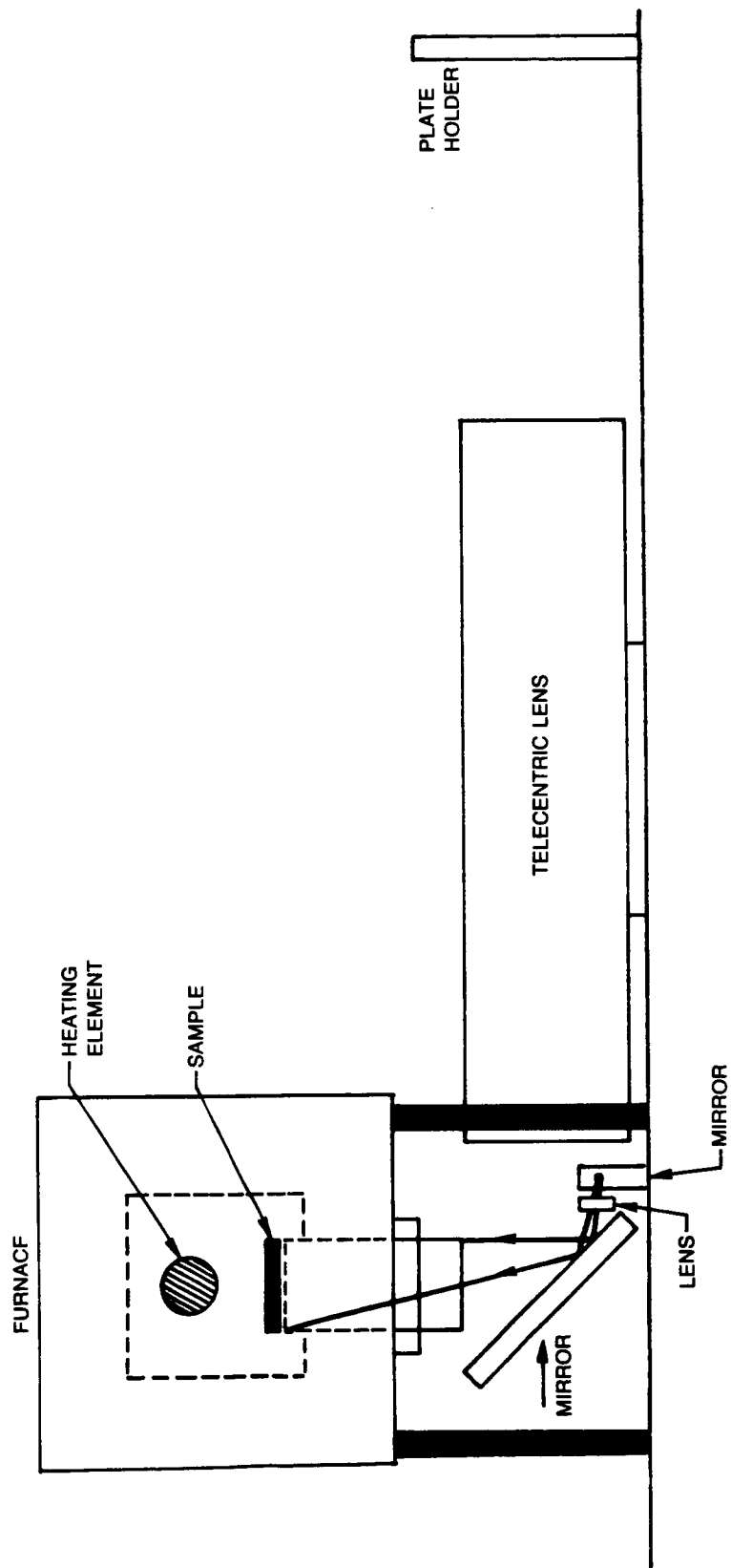


Figure 47. Elevated Temperature and Specklegram Recording Test Apparatus

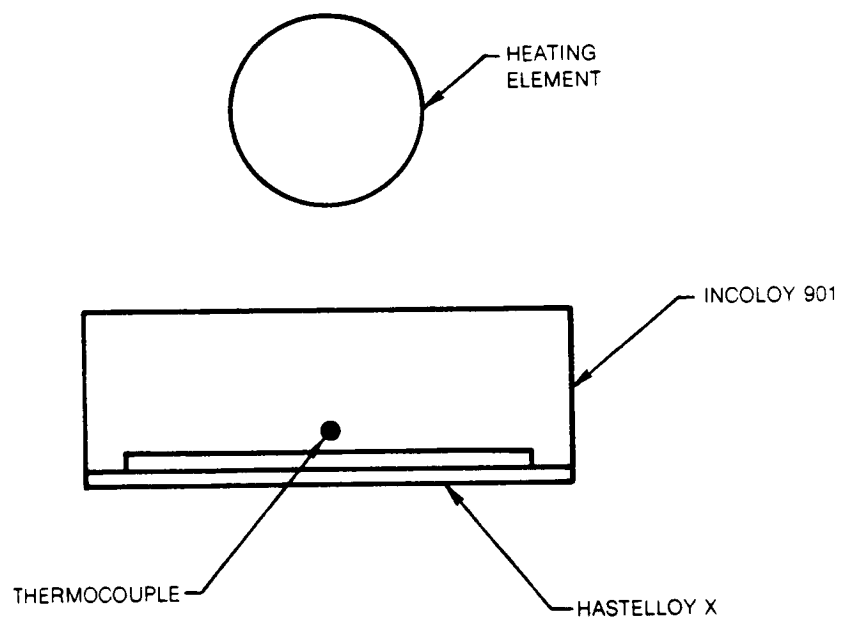


Figure 48. Schematic of Bimetallic Test Sample

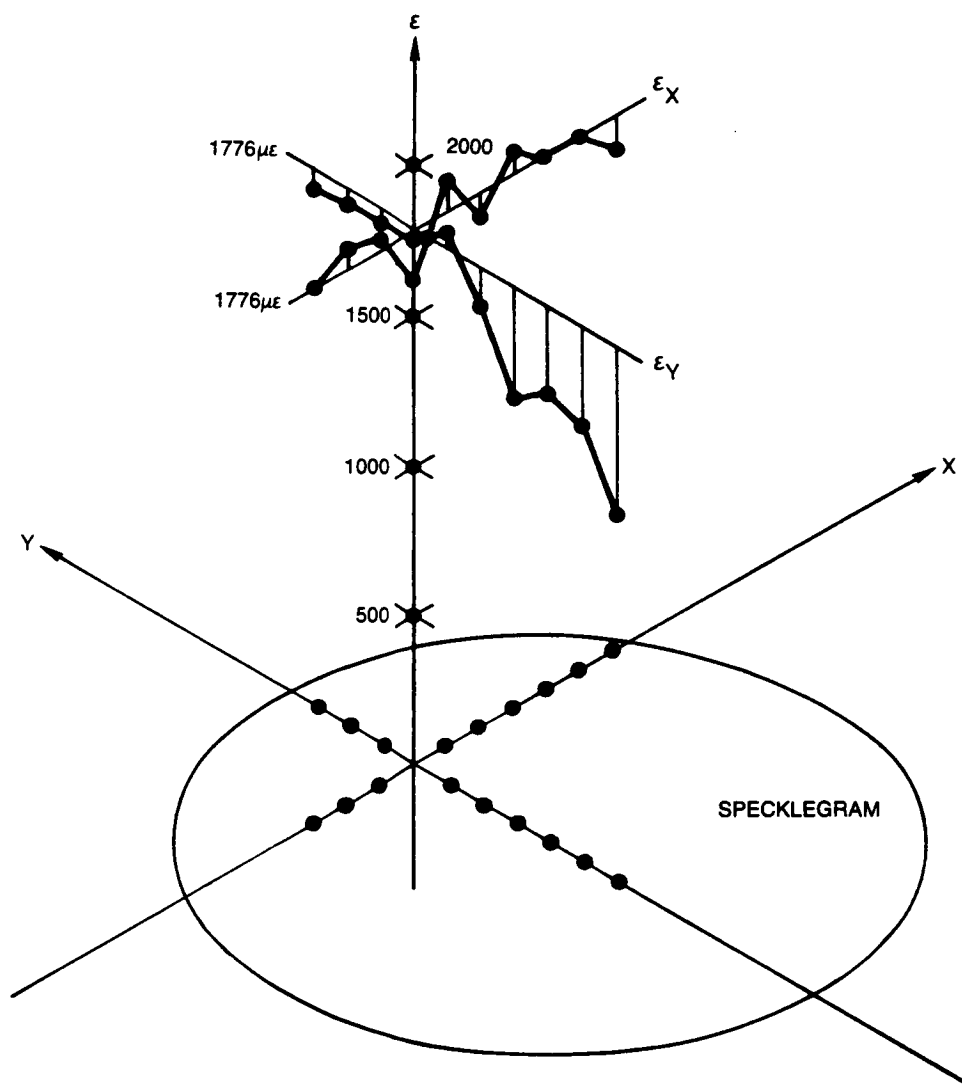


Figure 49. High Temperature Strain vs X and Y

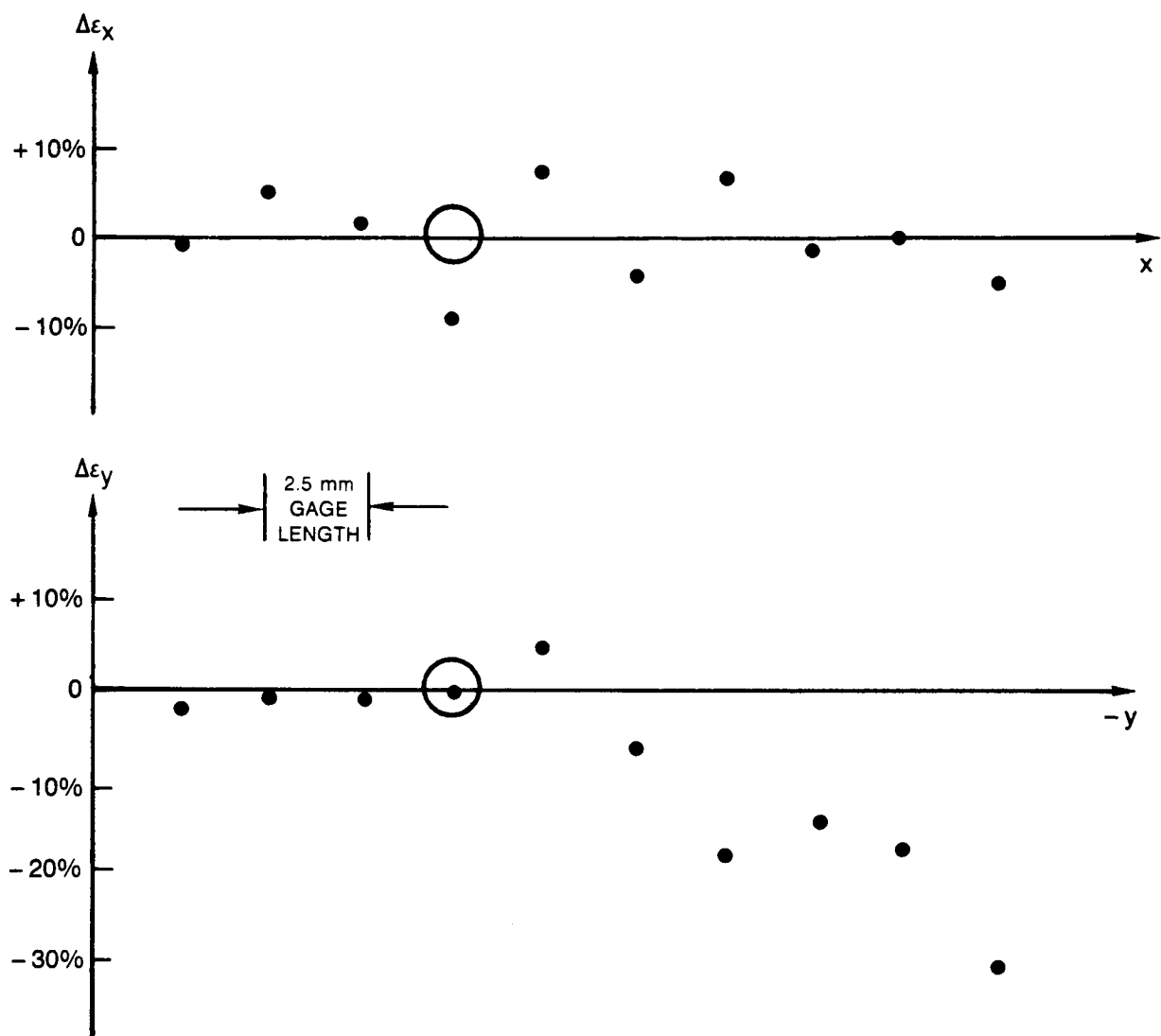


Figure 50. Percent Error — Measured vs Theoretical

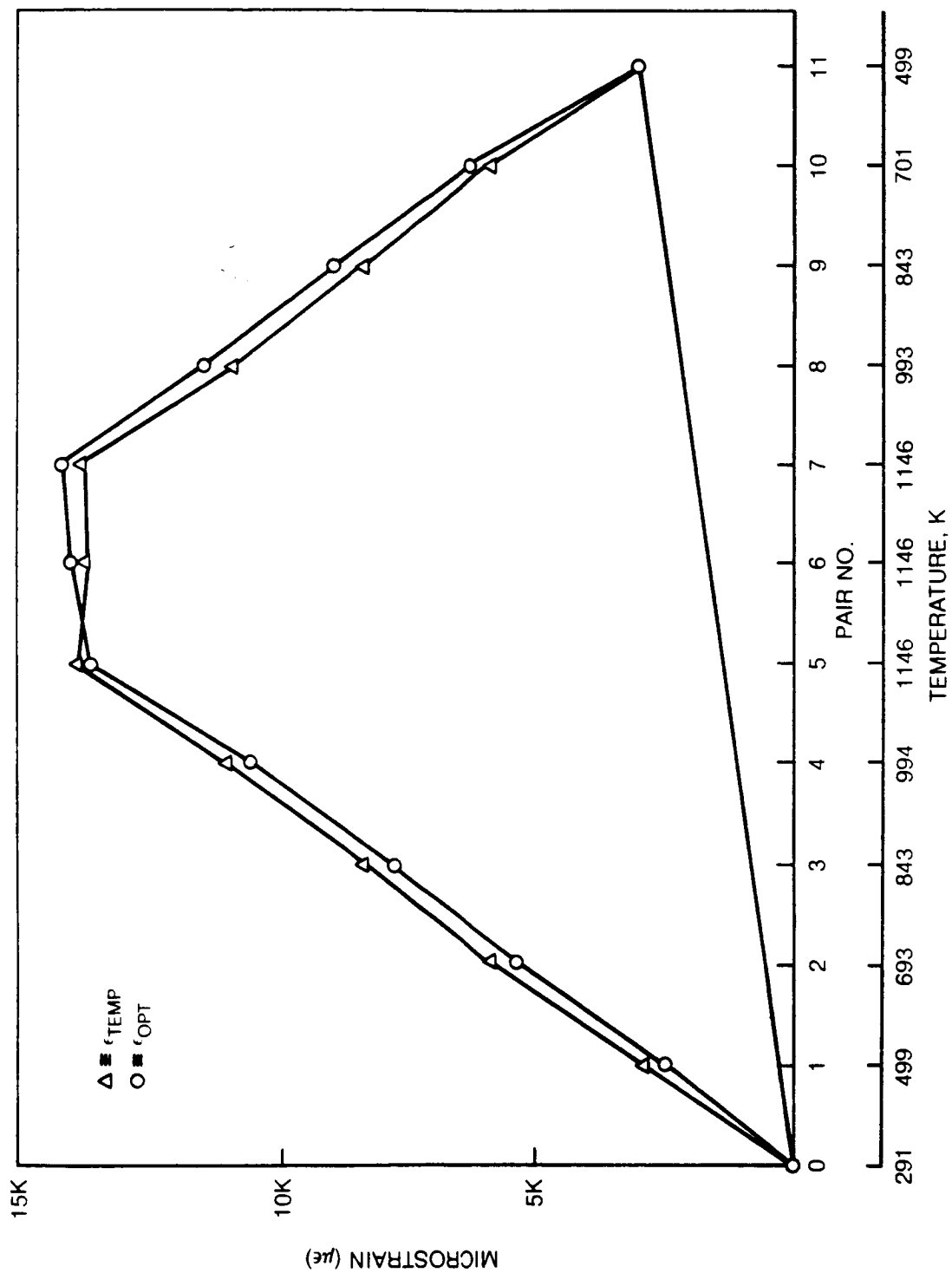


Figure 51. Thermally Induced Strain of Unstressed Hastelloy-X Sample

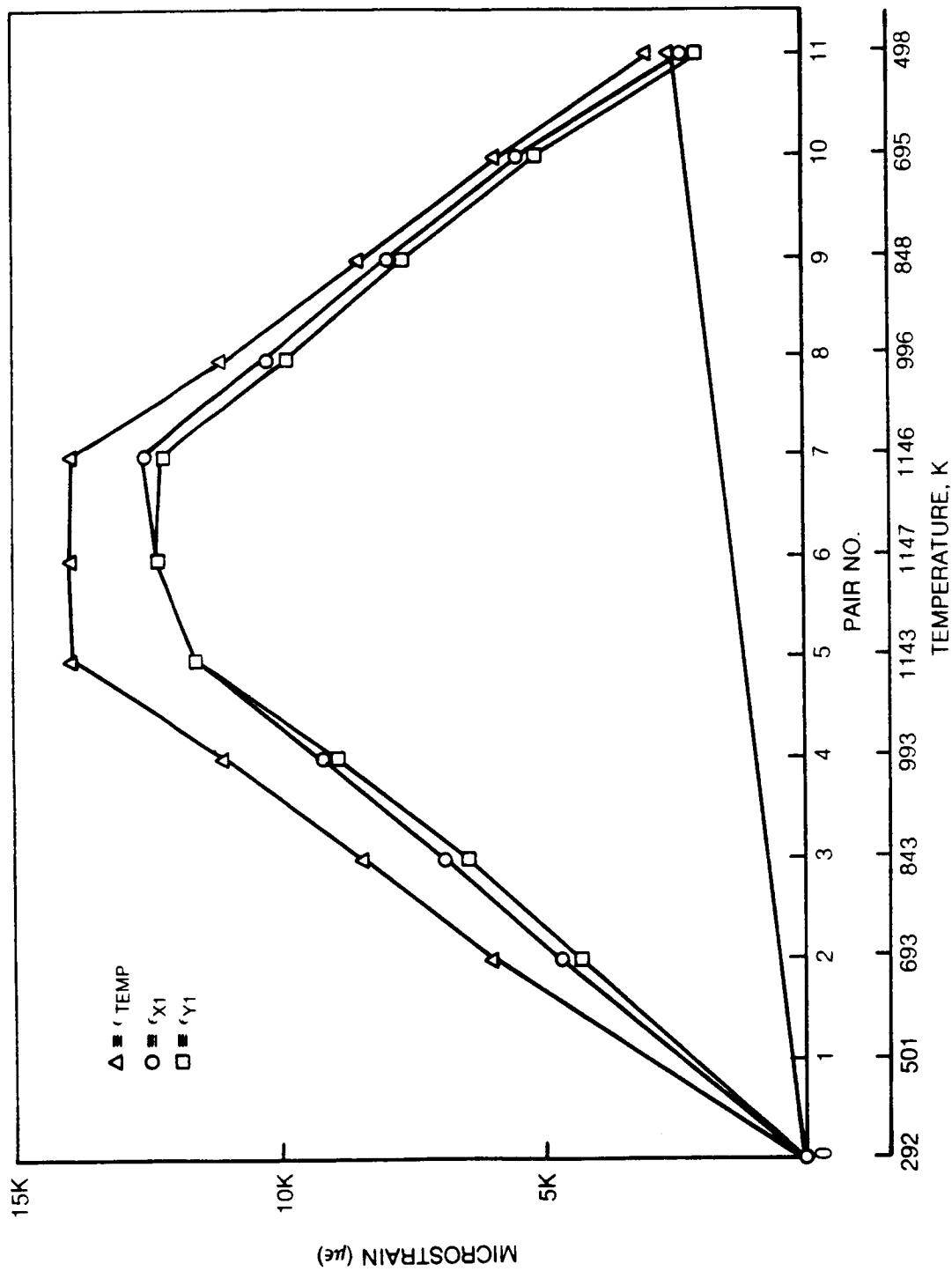


Figure 52. Thermally Induced Strain in Bimetallic Sample

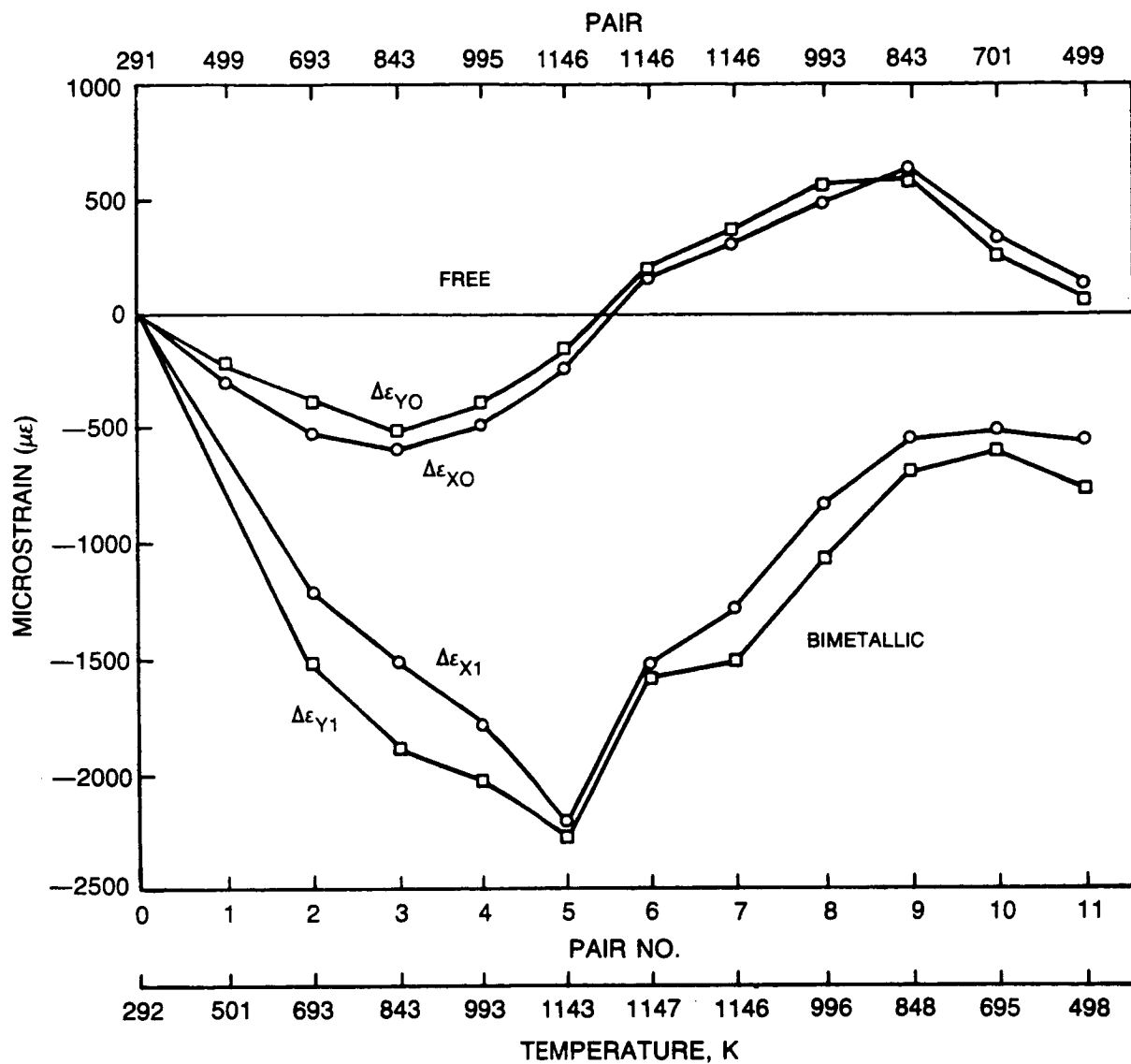


Figure 53. Difference in Strain Between that Measured by Speckle Technique and Calculated from Temperature

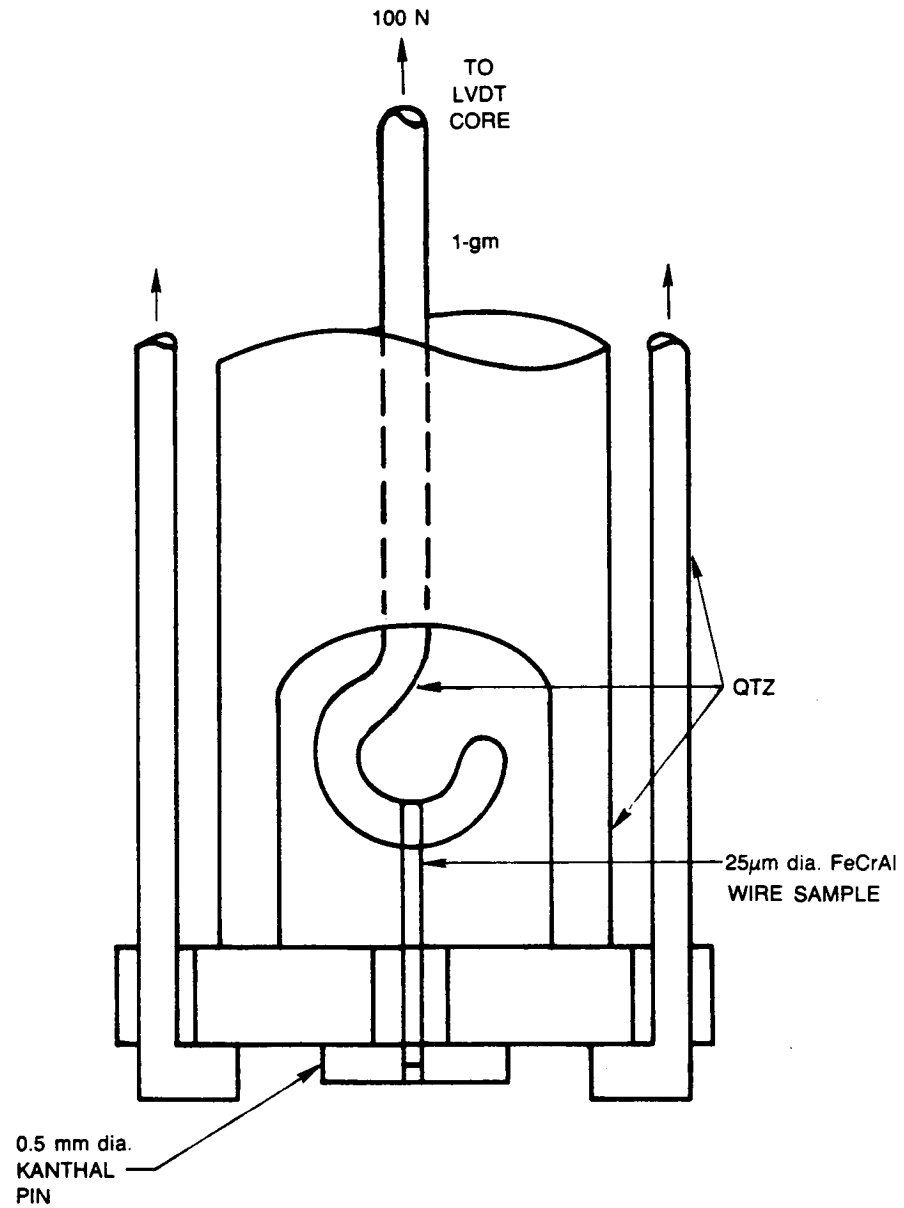


Figure 54. Thermal Expansion Experiment

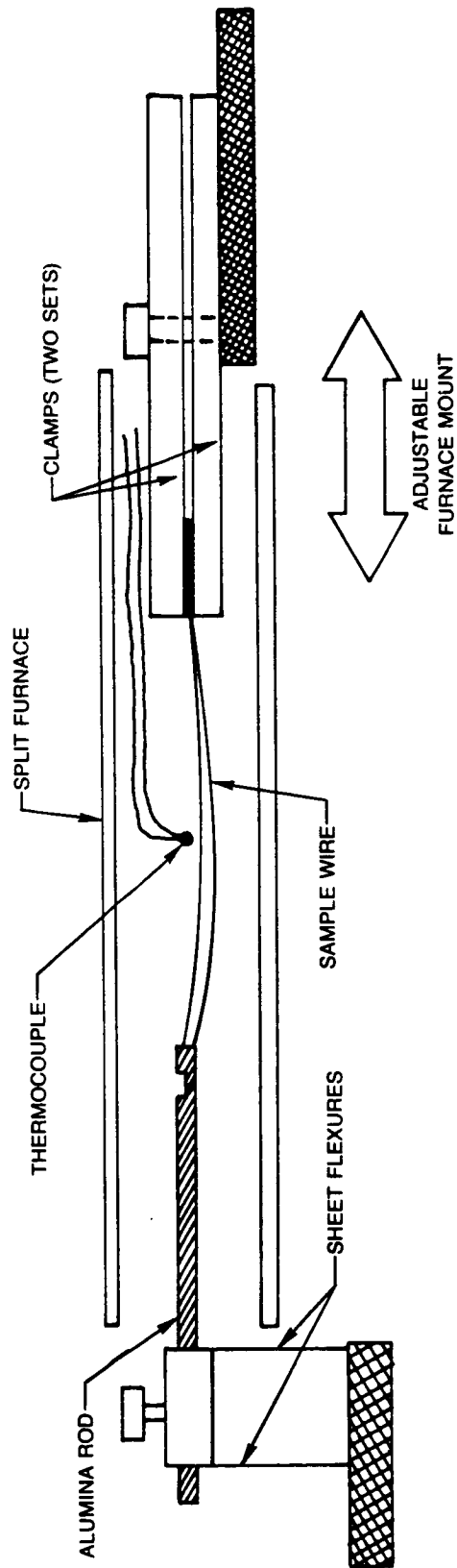


Figure 55. High-Speed Thermal Cycle/Drift Resistivity Measurement Apparatus

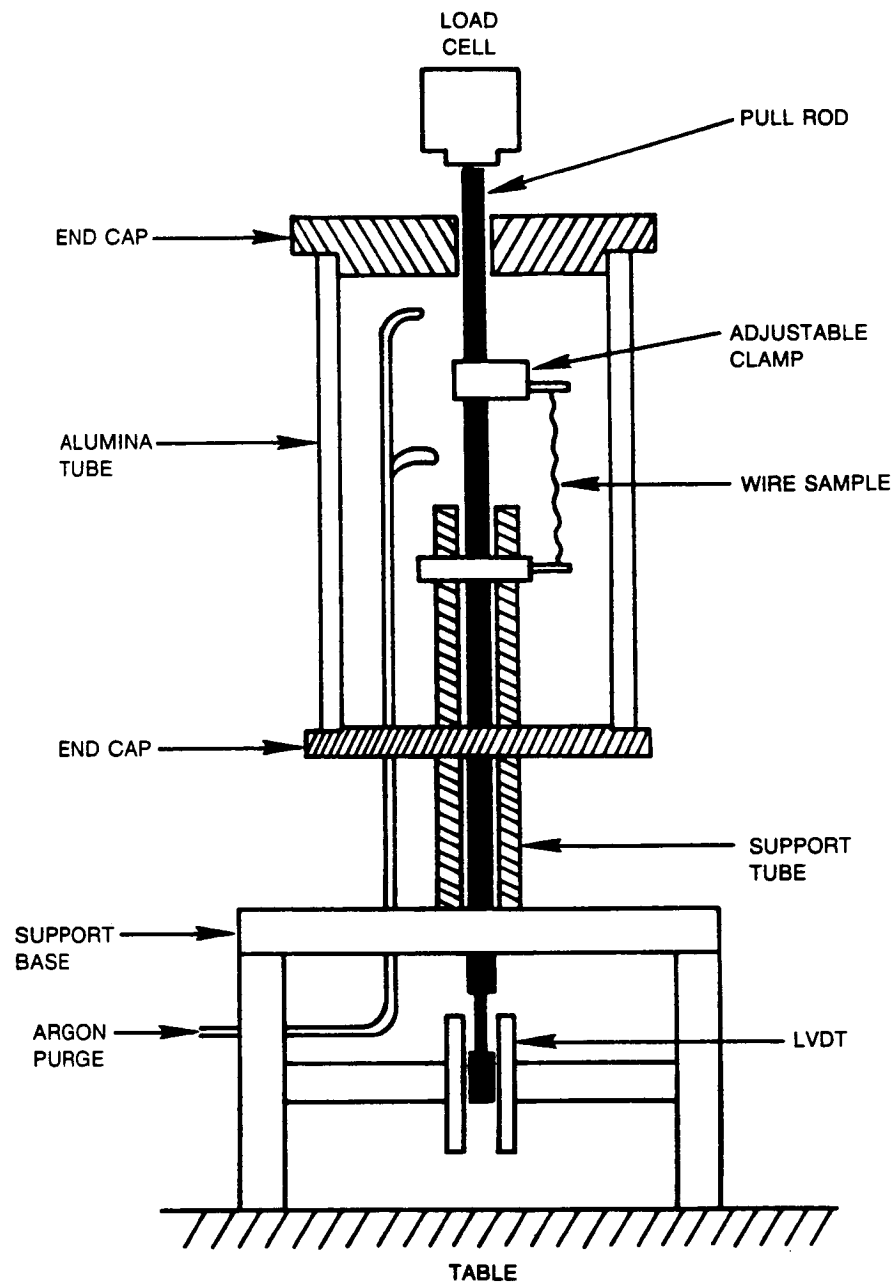


Figure 56. UTRC Wire Tensile Tester

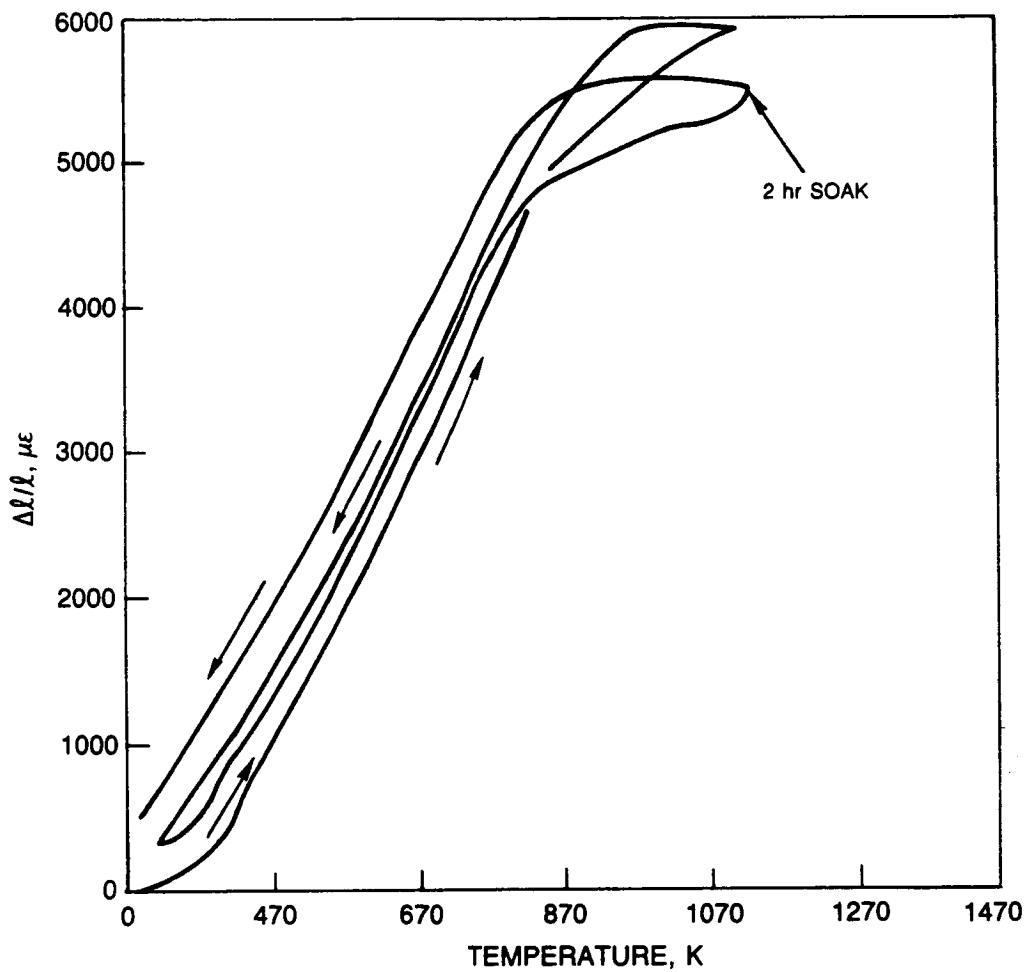


Figure 57. Thermal Expansion of Kanthal A-1 Wire, 25 μ m dia., Heated 2 K/min, In Air

(AS-RECEIVED, HEATED AND COOLED AT 250K/min)

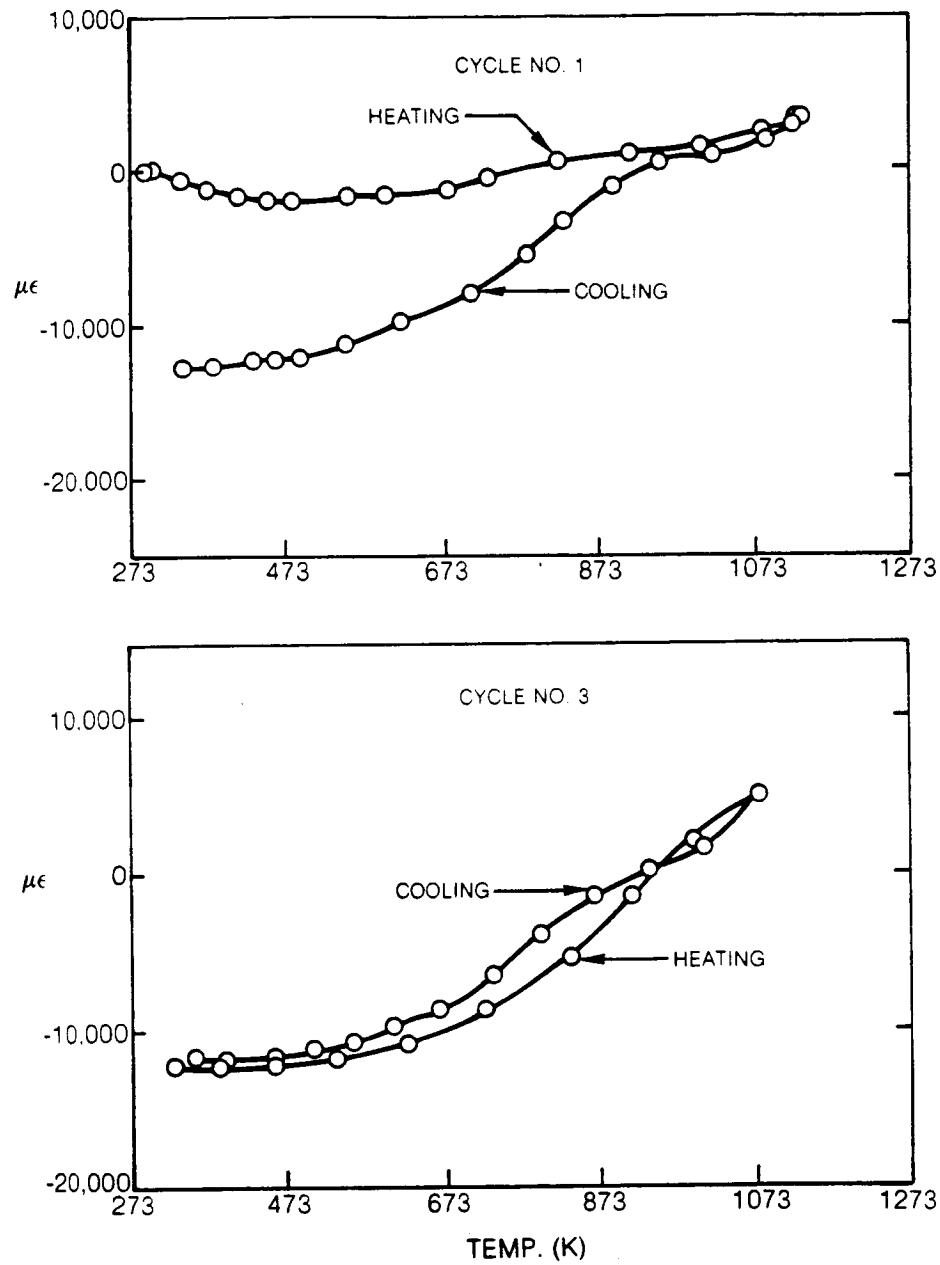


Figure 58. Apparent Strain of Kanthal A-1 Wire No. 1

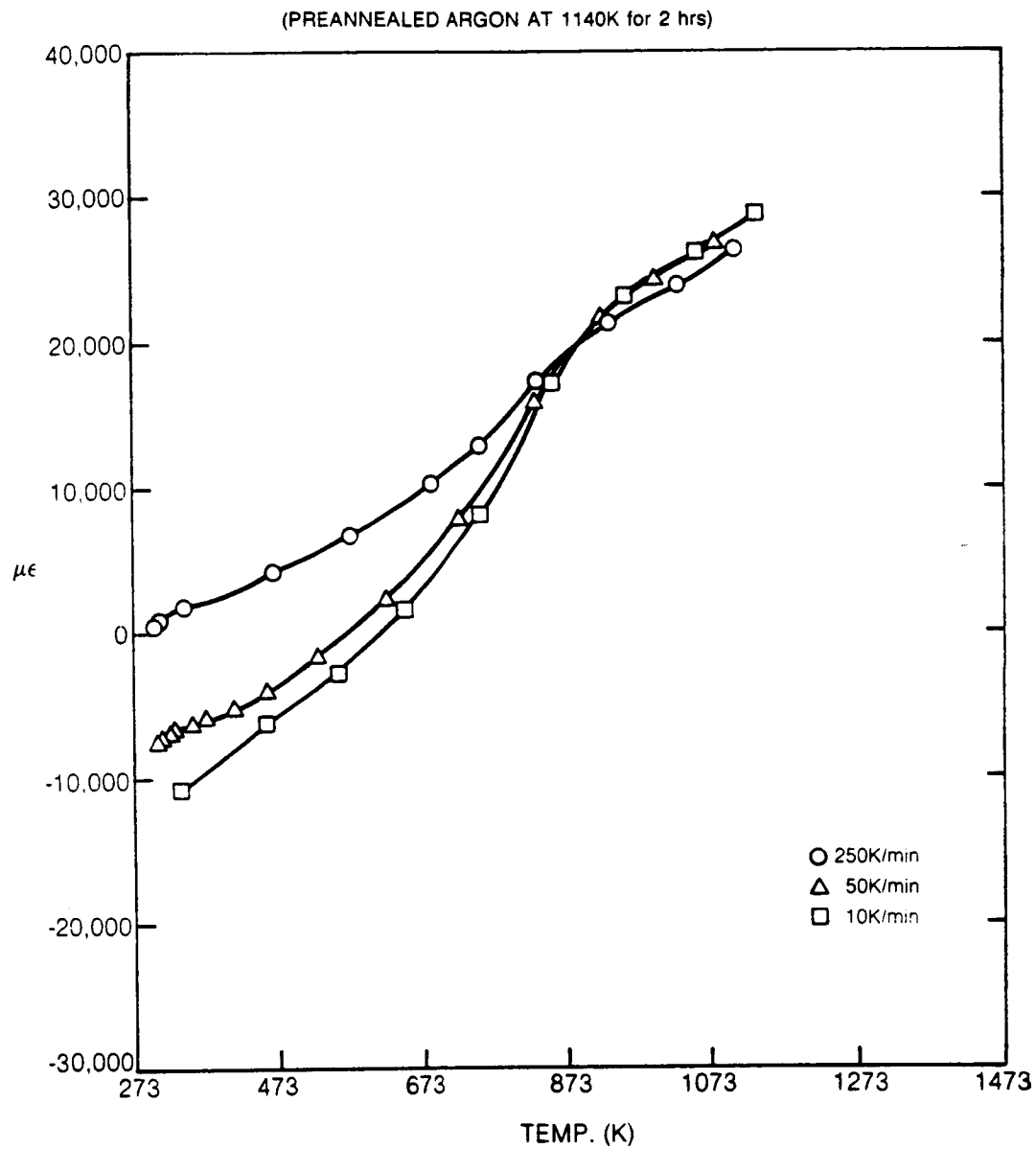


Figure 59. Cooling Rate Sensitivity of Apparent Strain of Kanthal A-1 Wire No. 2

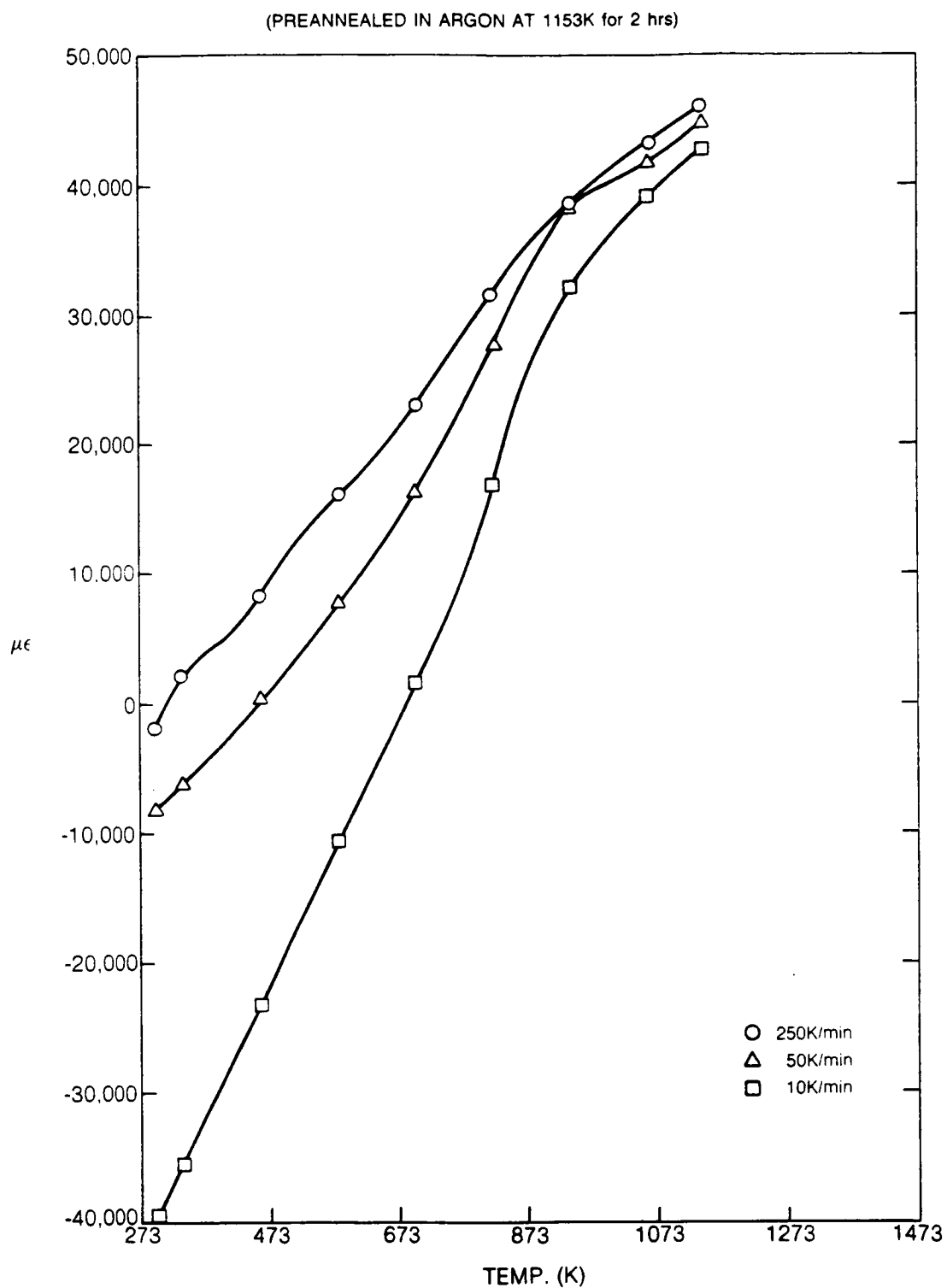


Figure 60. Cooling Rate Sensitivity of Apparent Strain of Kanthal A-1 Wire No. 3

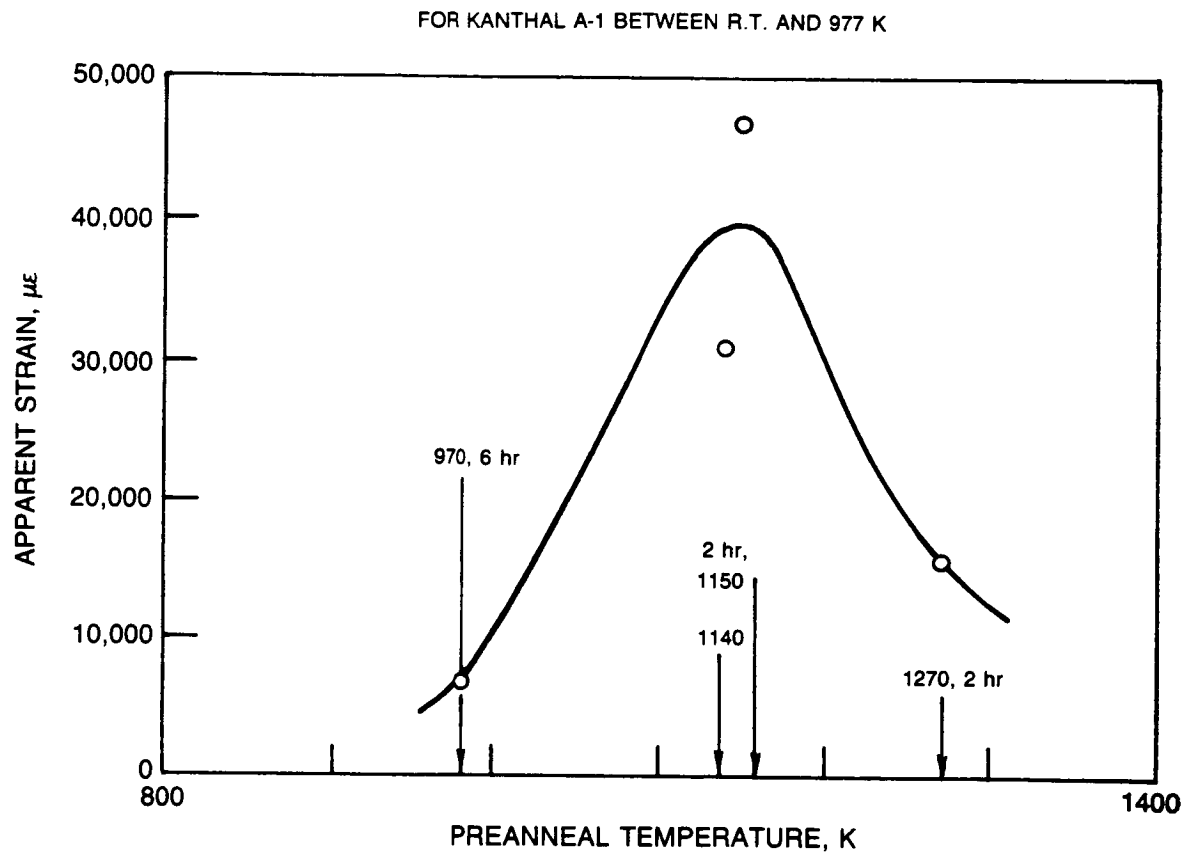


Figure 61. Effect of Temperature of Preannealing in Argon on Apparent Strain Change

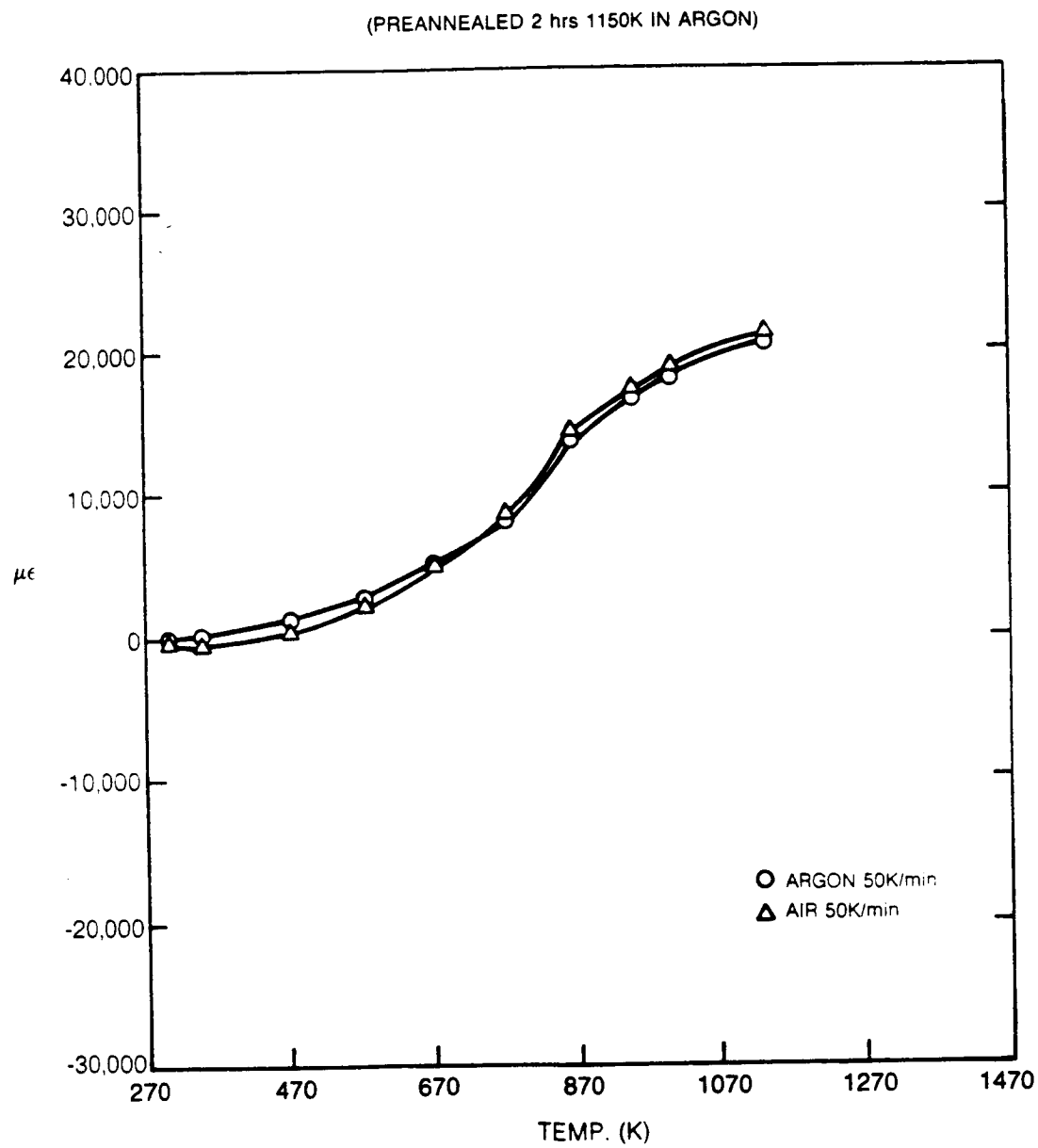


Figure 62. Change in Apparent Strain During Cooling In Air and Argon, Kanthal A-1 Wire No. 4

(KANTHAL A-1, WIRE NO. 7, PREANNEALED 6 hrs AT 970K IN ARGON)

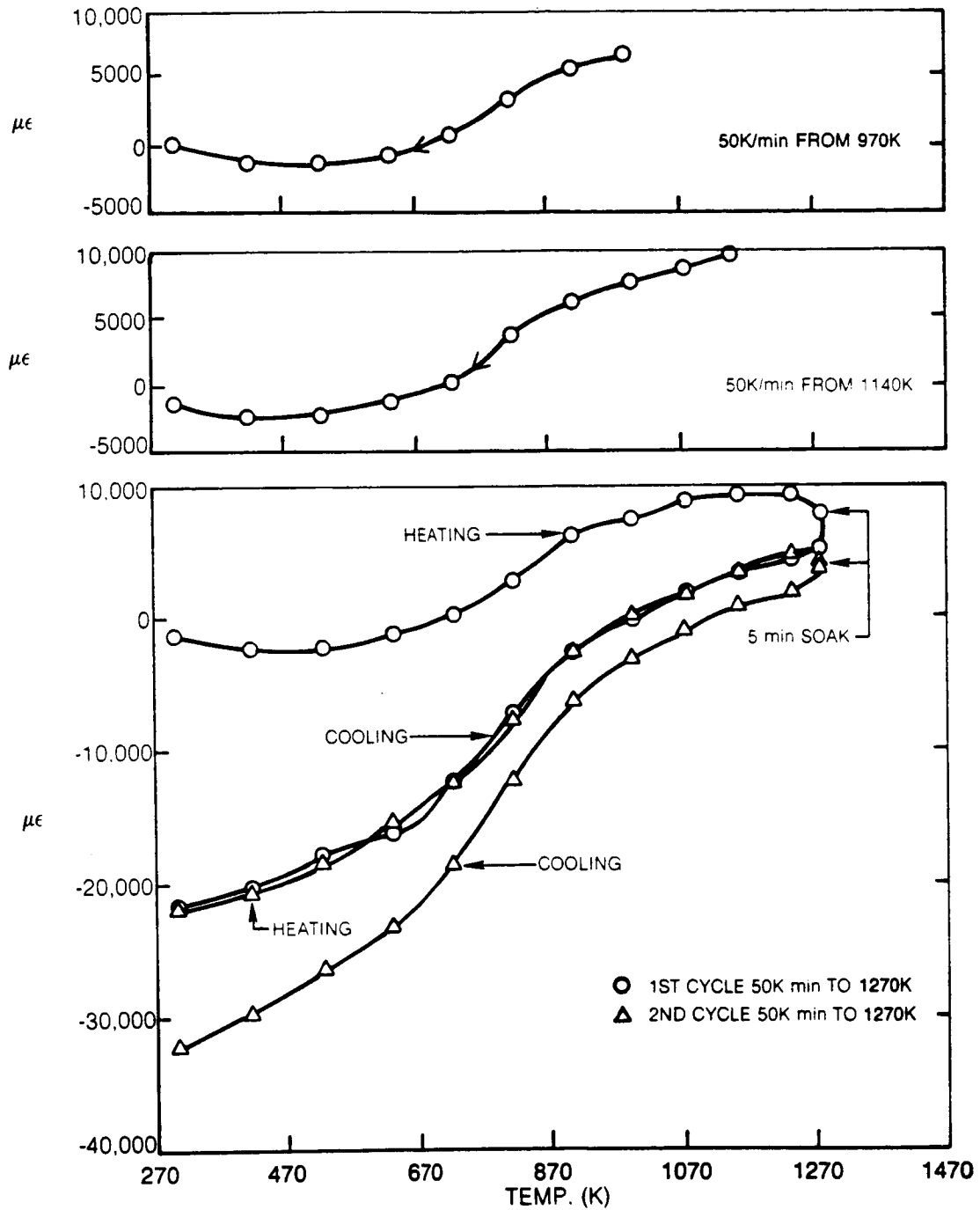


Figure 63. Change In Apparent Strain Upon Heating to Successively Higher Temperatures

(KANTHAL A-1, WIRE NO. 8, PREANNEALED IN ARGON 2 hrs AT 1270K)

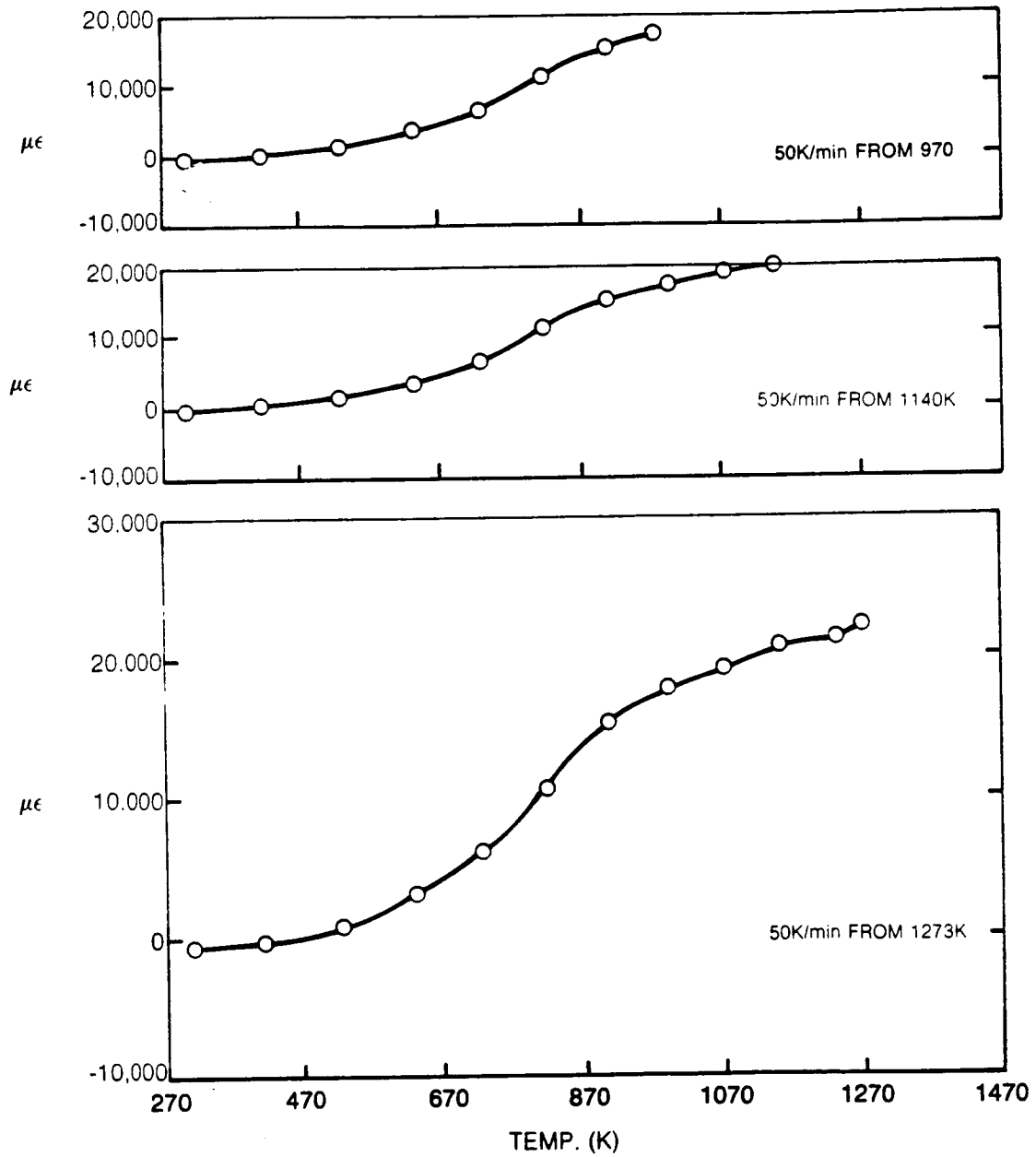


Figure 64. Change in Apparent Strain Upon Heating to Successively Higher Temperatures

(PREANNEALED 2 hrs IN ARGON AT 810K FOLLOWED BY STRAINING 4 PERCENT)

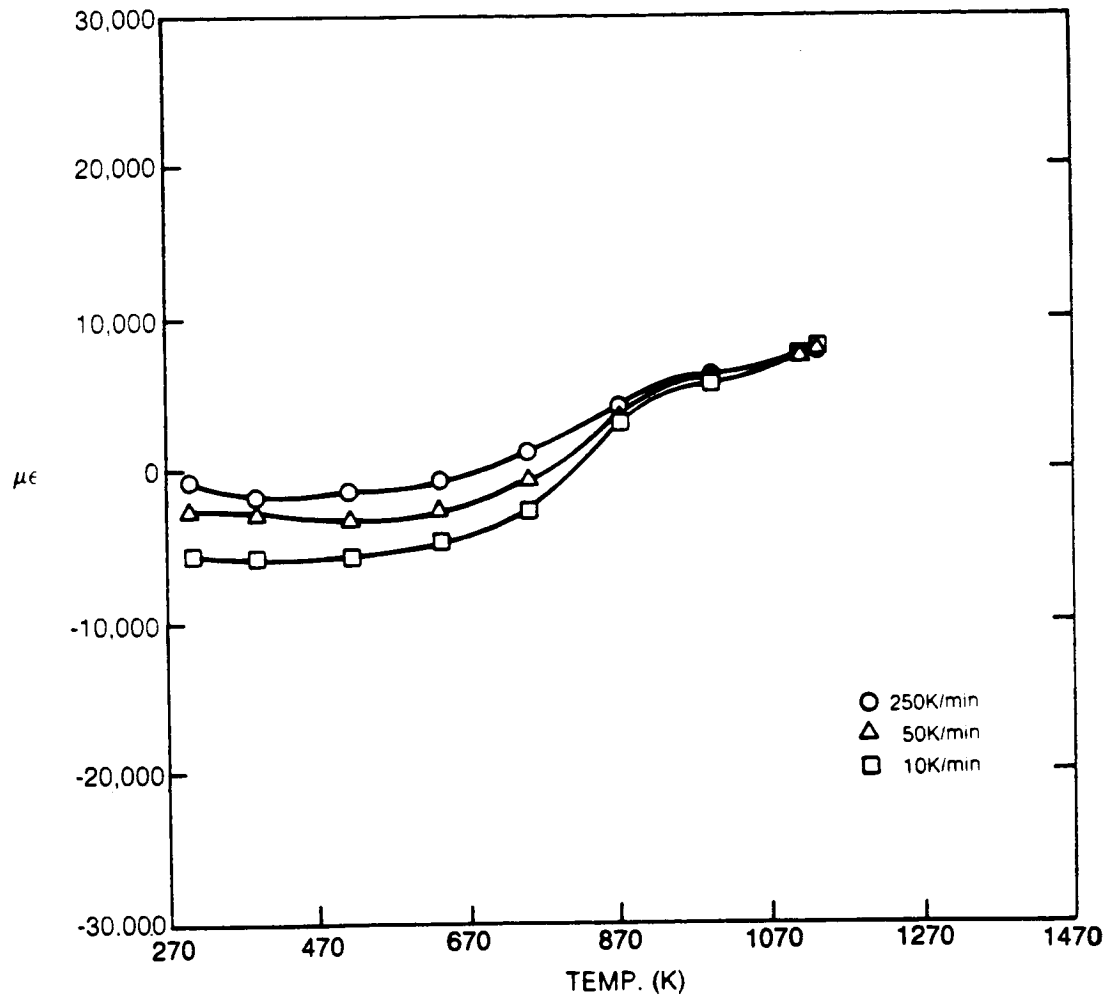


Figure 65. Change in Apparent Strain Upon Cooling Kanthal A-1 Wire No. 9

(PREANNEALED 2 hr IN ARGON AT 813K, STRAINED 4 PERCENT, ANNEALED 4 hrs 1200K)

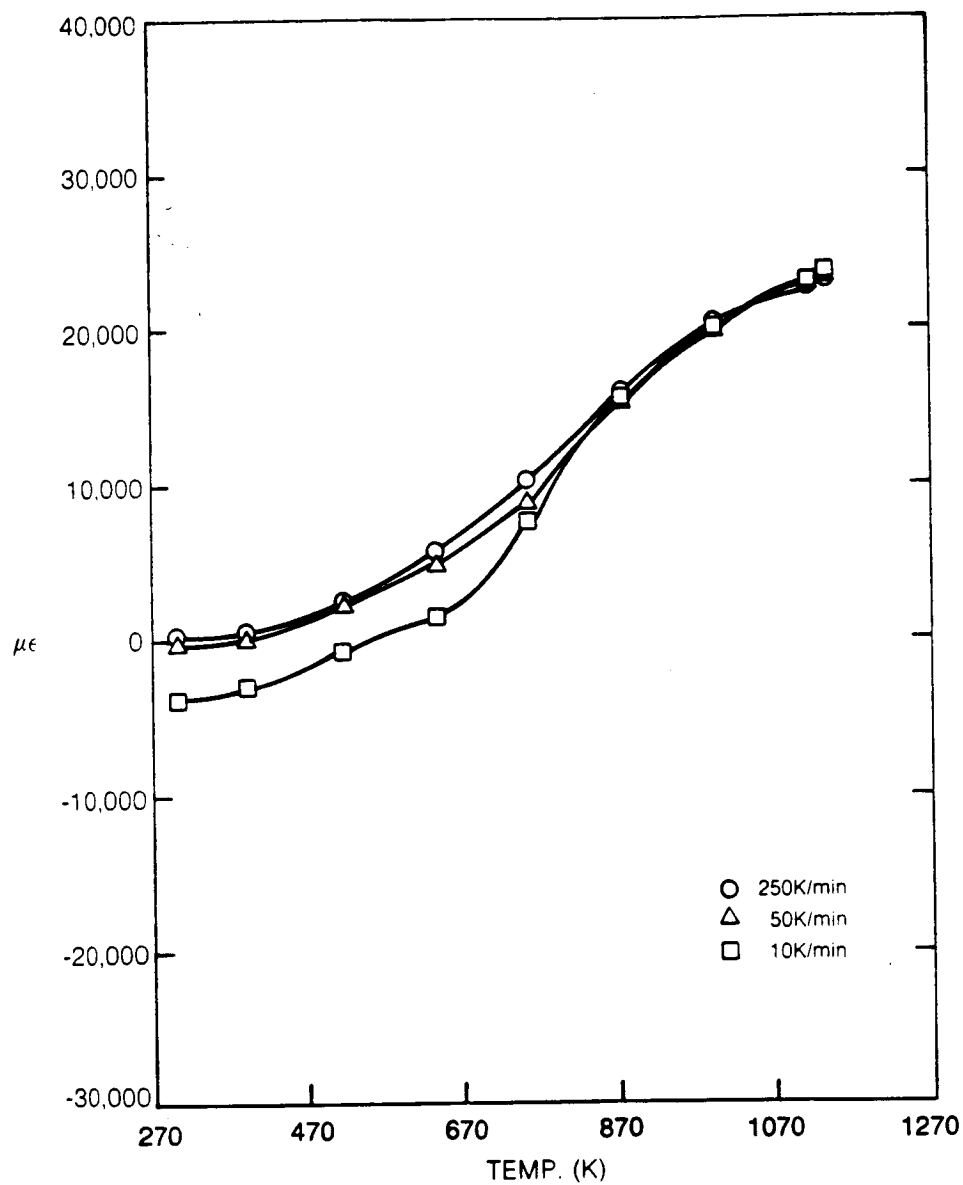


Figure 66. Change in Apparent Strain Upon Cooling Kanthal A-1 Wire No. 10

C-3

(PREANNEALED 2 hr IN ARGON AT 810K, STRAINED 4 PERCENT, ANNEALED 4 hrs 1200K)

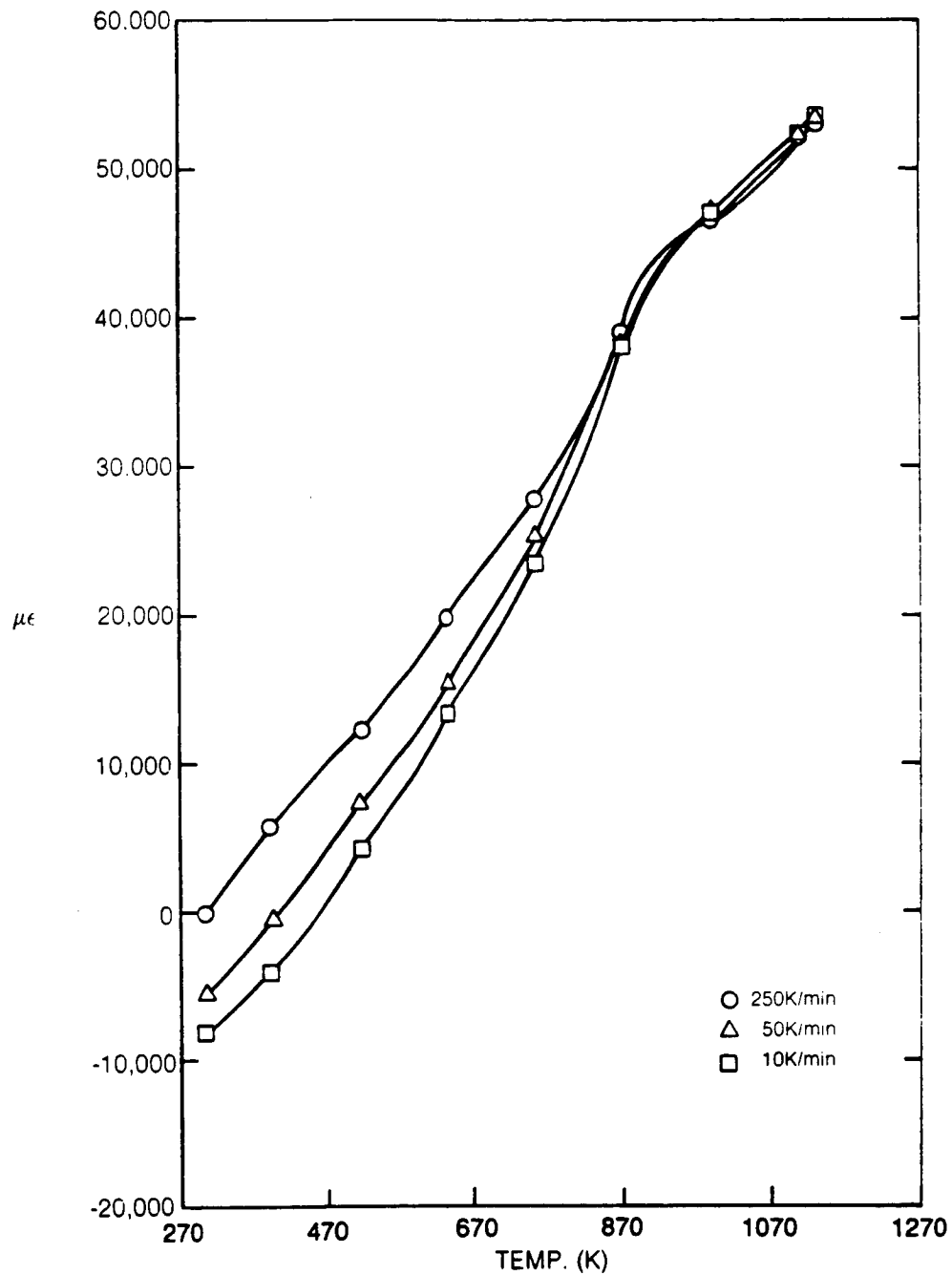


Figure 67. Change in Apparent Strain Upon Cooling Kanthal A-1 Wire No. 11

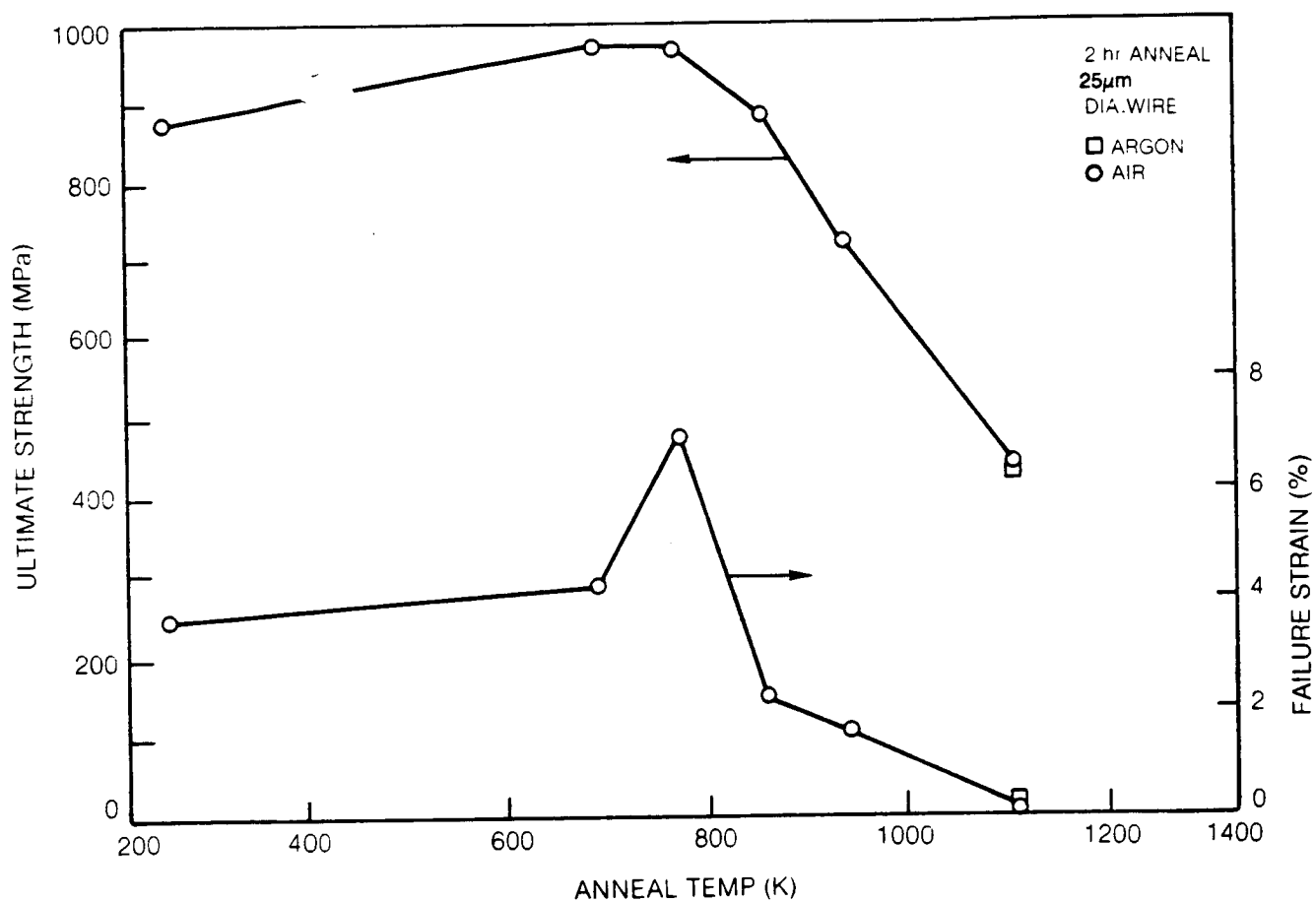


Figure 68. Room Temperature Strength and Ductility of Annealed Kanthal A-1

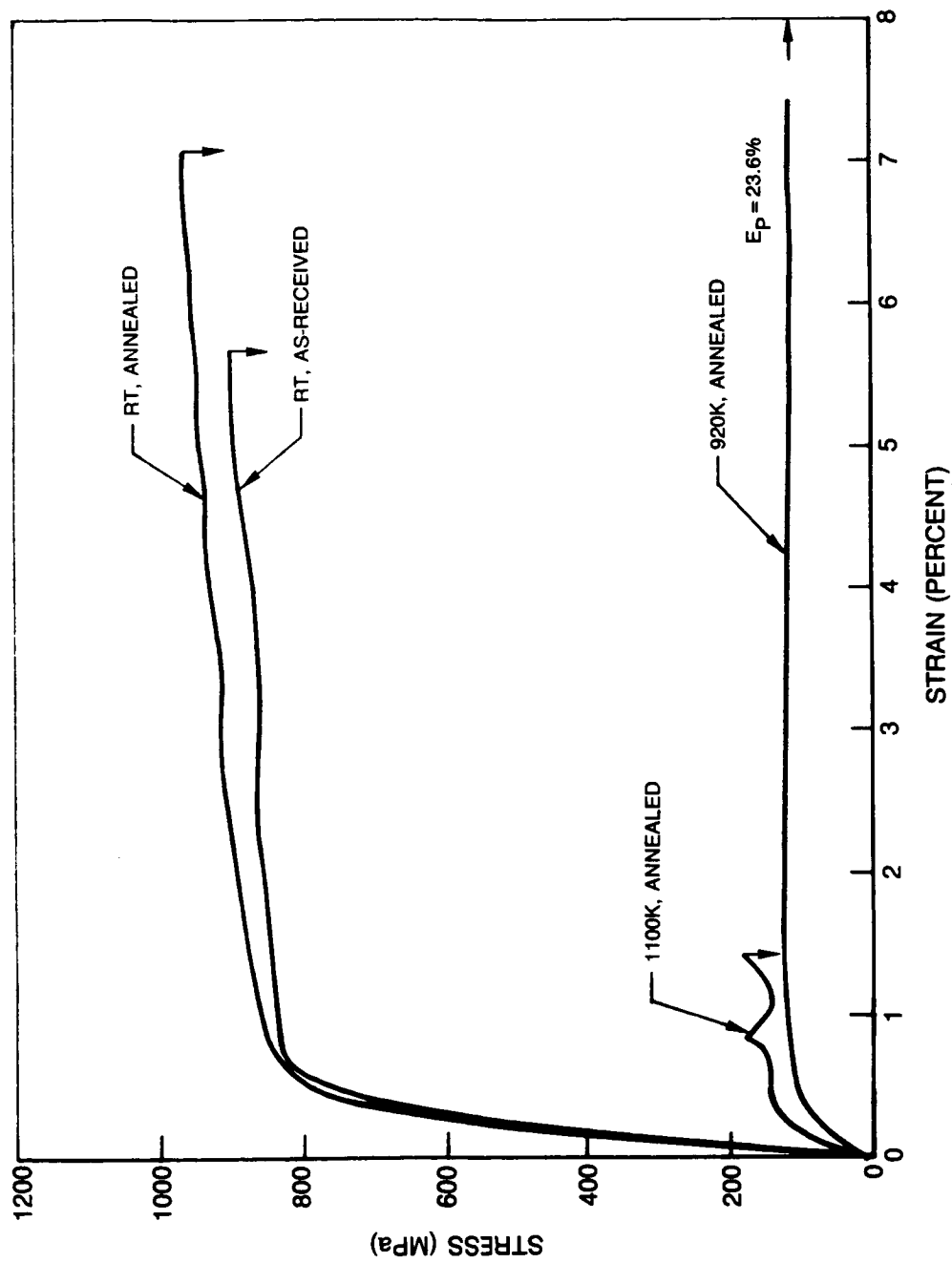


Figure 69. Stress Strain Curves of 25 μ m dia. Kanthal A-1 Wire at Different Temperatures After Preanneal for 2 hrs at 810K, Compared with As-Received Wire

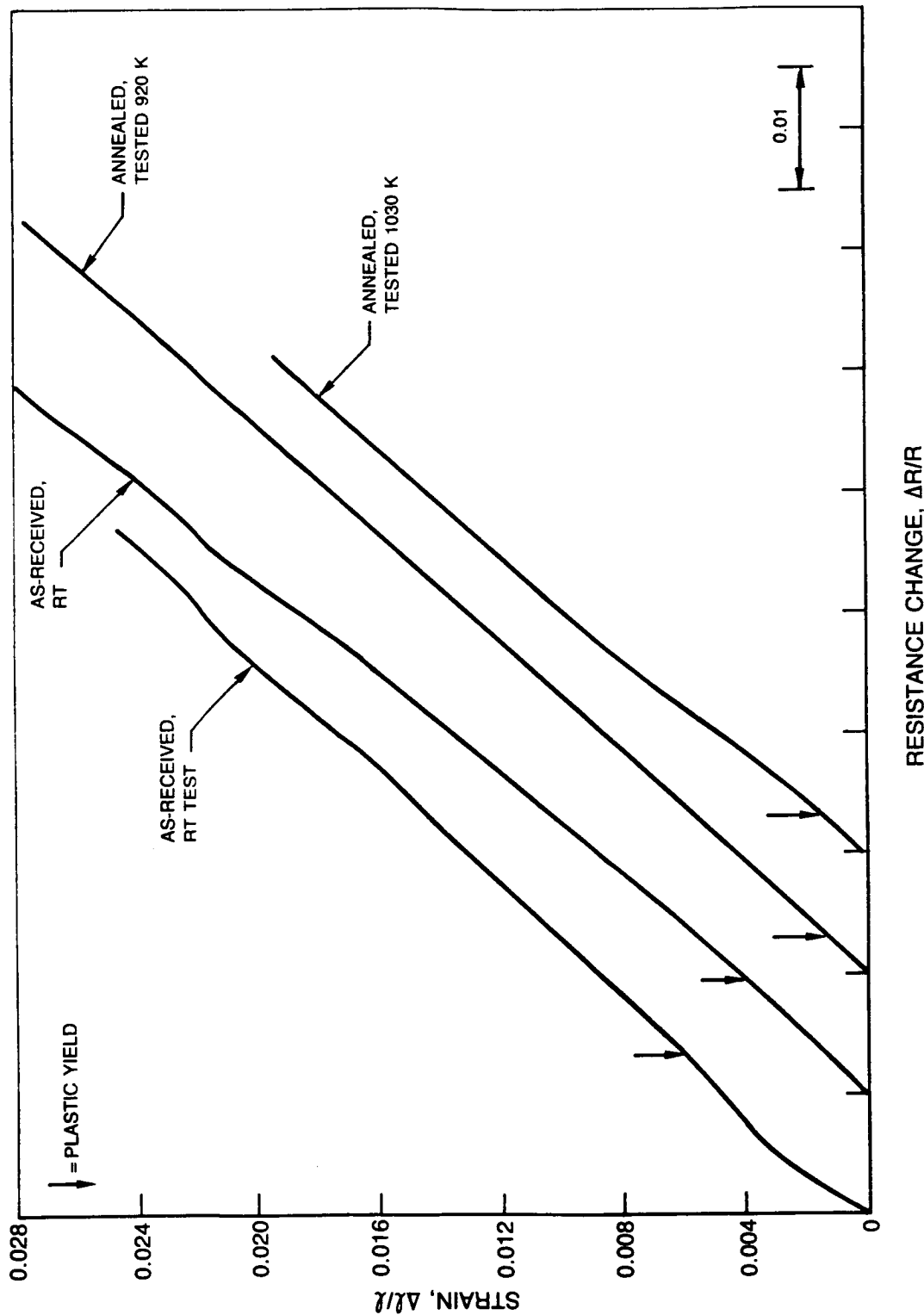


Figure 70. Comparisons of Strains from Length Change (LVDt) and Electrical Resistance Changes for 25 μ m dia. Kanthal A-1 Wires As-Received or Preannealed 2 hrs at 810 K

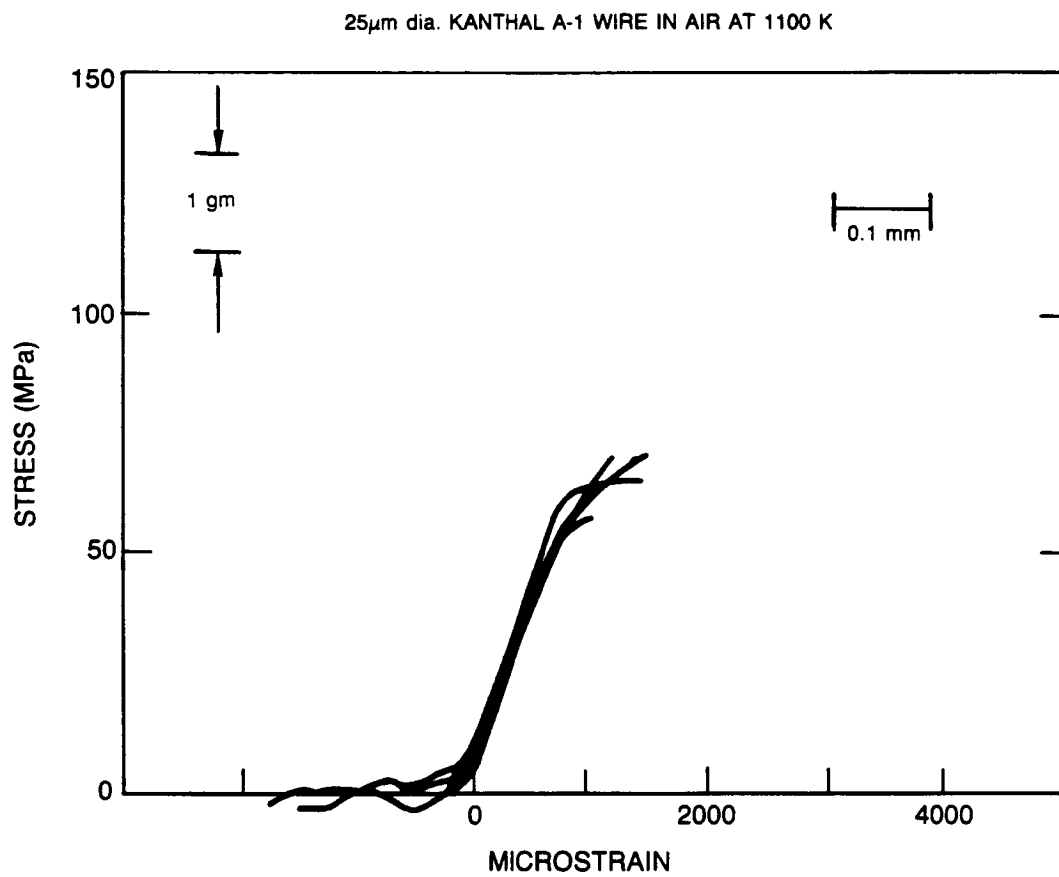


Figure 71. Reproducibility of Elastic Behavior

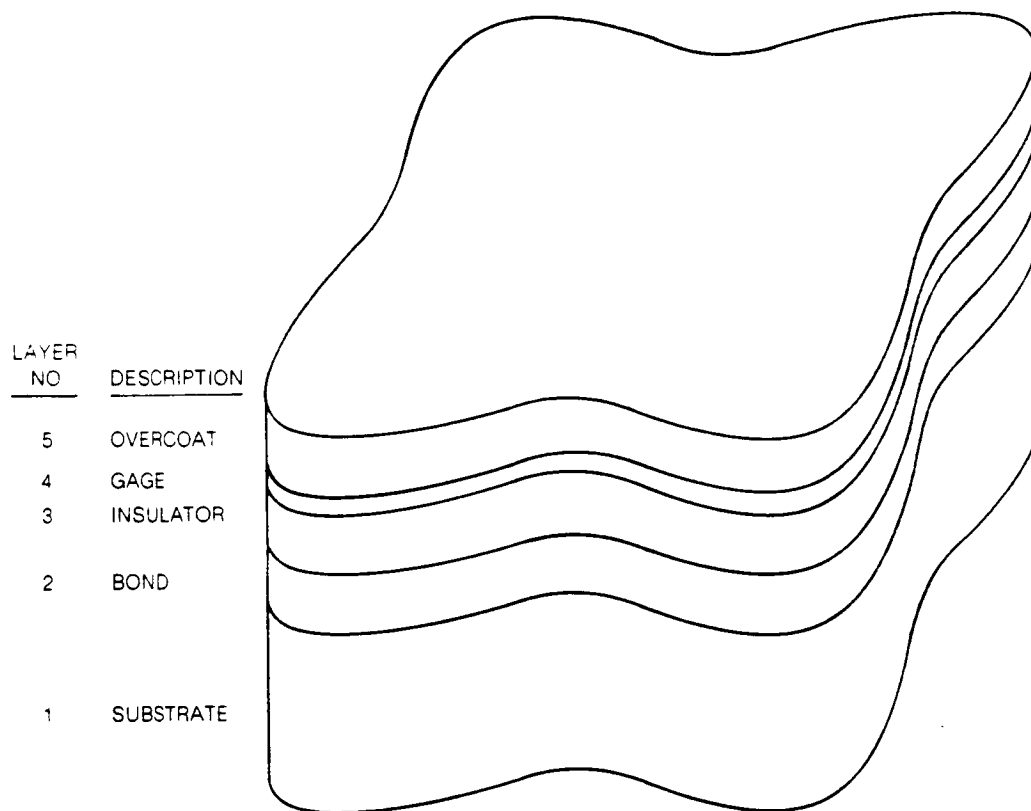


Figure 72. High Temperature Strain Gage Measurement Layup

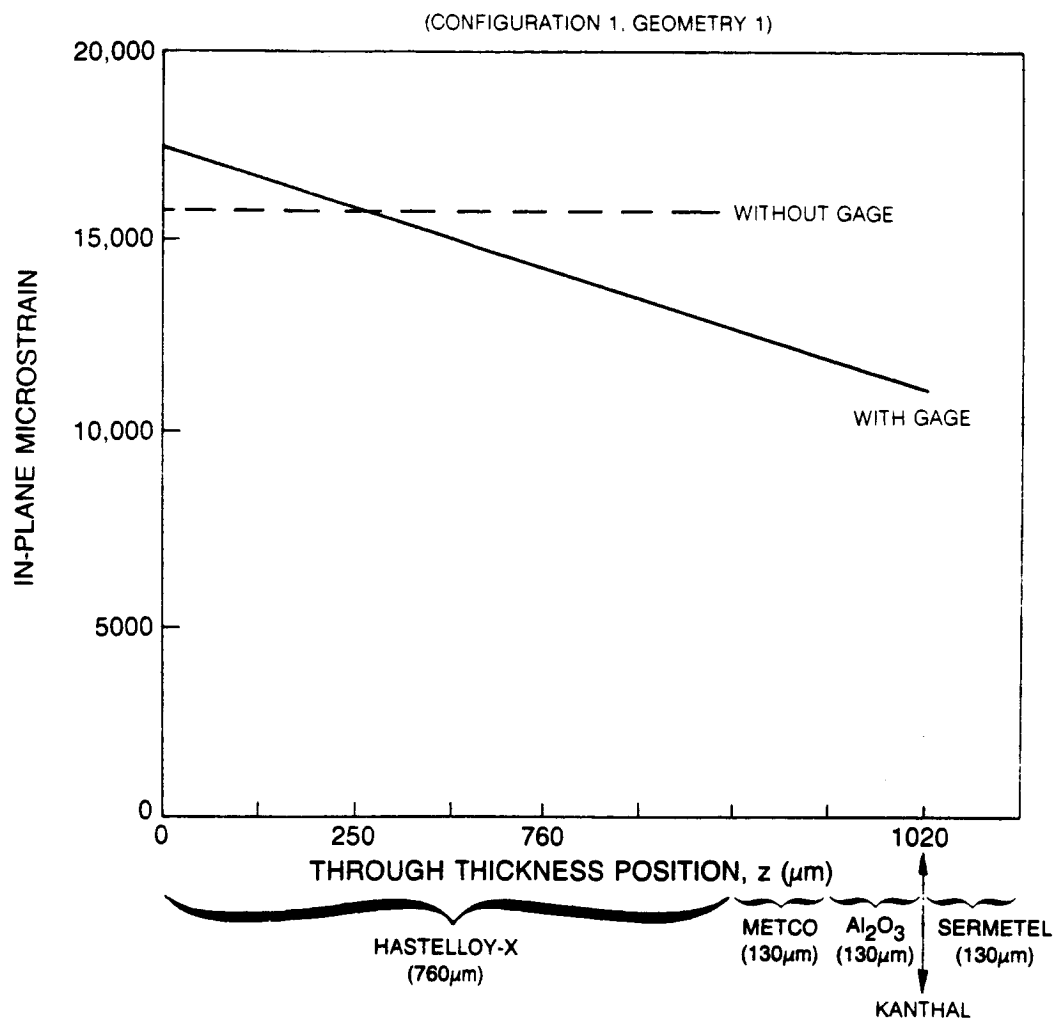


Figure 73. Strain Distribution at 1250K in a 0.76 mm Thick Hastelloy X Sheet With and Without Strain Gages

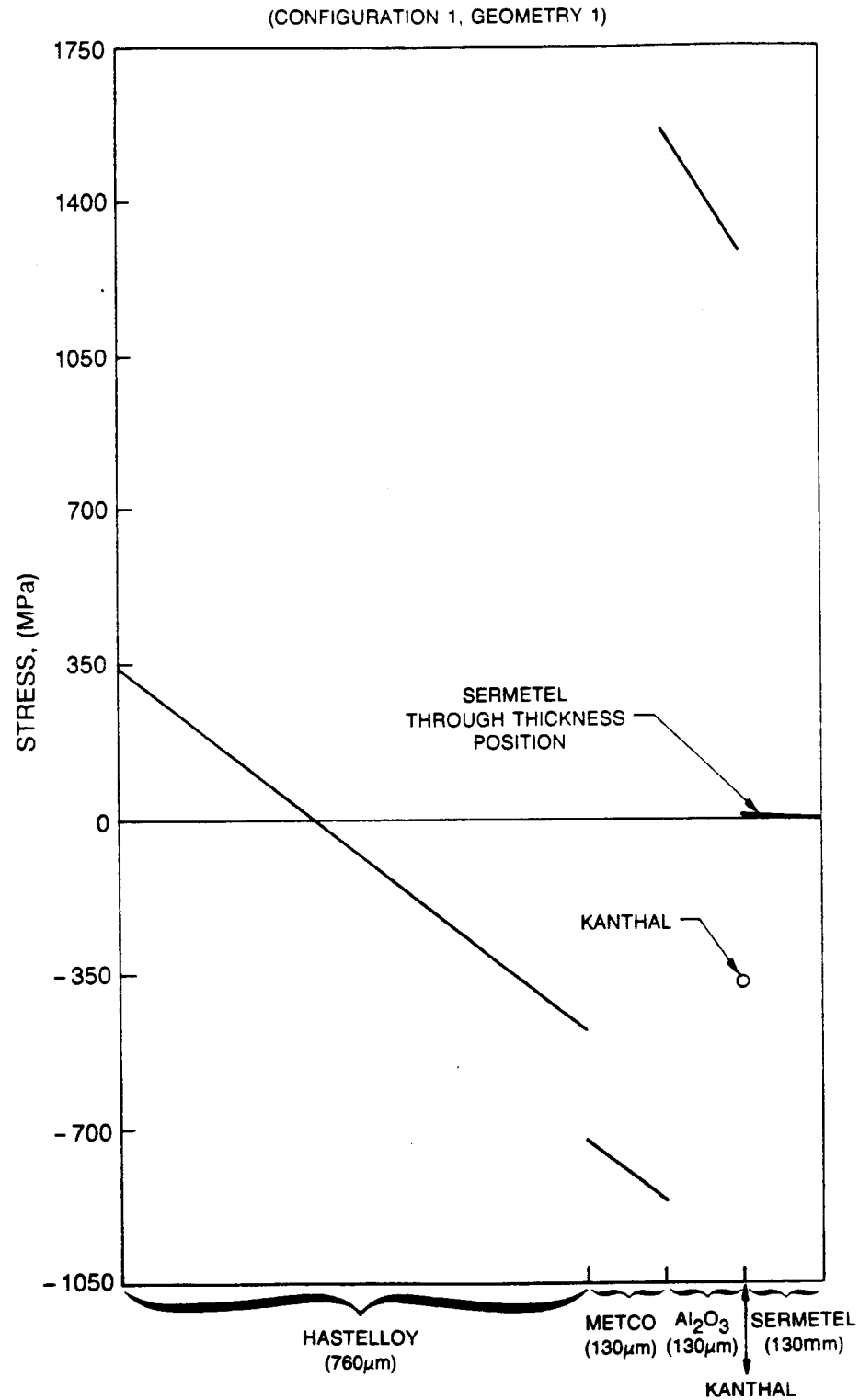


Figure 74. Stress Distribution at 1250K Due to a Typical Strain Gage Installation on a 0.76 mm Thick Hastelloy X Sheet

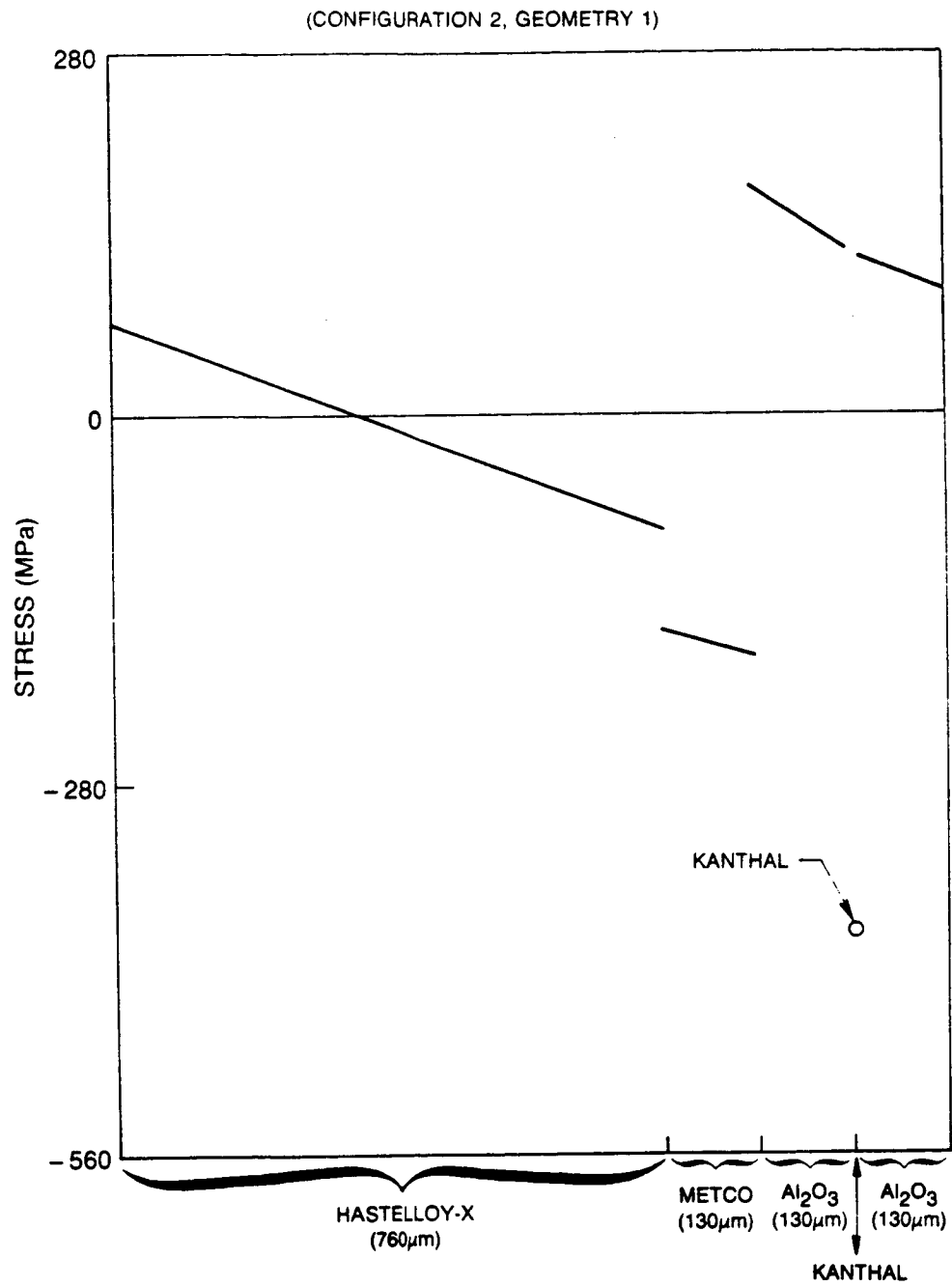


Figure 75. Stress Distribution at 420K Due to a Typical Strain Gage Installation on a 0.76 mm Thick Hastelloy X Sheet